

---

**Ground state and dynamical properties  
of the finite Kondo lattice model and  
transport through carbon based  
nanodevices**  
a numerical study

Sebastian Smerat

---



München 2011



---

**Ground state and dynamical properties of the  
finite Kondo lattice model and transport  
through carbon based nanodevices  
a numerical study**

**Sebastian Smerat**

---

Dissertation  
an der Fakultät für Theoretische Physik  
der Ludwig–Maximilians–Universität  
München

vorgelegt von  
Sebastian Smerat  
aus Leverkusen

München, den 08. Februar 2011

Erstgutachter: Prof. Dr. Ulrich Schollwöck

Zweitgutachter: Prof. Dr. Herbert Schoeller

Tag der mündlichen Prüfung: 25. März 2011

# Contents

<b>Zusammenfassung</b>	<b>ix</b>
<b>Summary</b>	<b>xi</b>
<b>Publication List</b>	<b>xiii</b>
<b>1 Introduction</b>	<b>1</b>
1.1 Motivation . . . . .	1
1.2 Aim of this thesis . . . . .	2
1.3 Outline . . . . .	3
<b>2 Matrix product states and DMRG</b>	<b>5</b>
2.1 Matrix product states . . . . .	6
2.1.1 General construction . . . . .	6
2.1.2 Matrix product state operations . . . . .	7
2.1.3 Compression of an MPS . . . . .	11
2.1.4 Matrix product operators . . . . .	15
2.2 DMRG . . . . .	15
2.2.1 Ground state calculation . . . . .	15
2.2.2 Time evolution . . . . .	20
2.2.3 Frequency space DMRG . . . . .	25
<b>3 The one-dimensional Kondo lattice model</b>	<b>35</b>
3.1 Introduction . . . . .	35
3.2 Derivation of the Kondo lattice model . . . . .	35
3.2.1 From the periodic Anderson model to the Kondo lattice model . . . . .	35
3.2.2 Two-band model . . . . .	37
3.3 Exactly solved cases . . . . .	37
3.3.1 One electron in the conduction band . . . . .	37
3.3.2 Half filling of the conduction band . . . . .	40
3.3.3 Strong coupling limit . . . . .	40
3.4 Effective interactions . . . . .	41
3.4.1 RKKY interaction . . . . .	42

3.4.2	Kondo singlet formation . . . . .	43
3.5	Phase diagram . . . . .	44
3.5.1	Phase diagram from bosonization . . . . .	44
3.5.2	Phase diagram from DMRG . . . . .	45
3.5.3	Quarter filling . . . . .	47
3.6	Fermi surface sum rules . . . . .	48
3.7	Application of the KLM to real materials . . . . .	49
3.7.1	Manganese perovskites . . . . .	50
3.7.2	Heavy fermion compounds . . . . .	50
<b>4</b>	<b>Quasiparticles in the Kondo lattice model at partial fillings of the conduction band</b>	<b>51</b>
4.1	Introduction . . . . .	51
4.2	Methods . . . . .	55
4.2.1	DMRG . . . . .	55
4.2.2	Correction vector method . . . . .	56
4.2.3	Quasiparticle lifetime . . . . .	57
4.3	Results . . . . .	59
4.3.1	Dispersion . . . . .	60
4.3.2	Life time estimations from spectral functions . . . . .	63
4.4	Summary . . . . .	66
<b>5</b>	<b>Coulomb interaction effects and electron spin relaxation in the 1d KLM</b>	<b>67</b>
5.1	Introduction . . . . .	67
5.2	Model . . . . .	70
5.3	Method . . . . .	70
5.3.1	DMRG . . . . .	70
5.3.2	Ground states . . . . .	70
5.3.3	Susceptibility . . . . .	71
5.3.4	Quasiparticle life-times . . . . .	71
5.3.5	Dispersion relation . . . . .	73
5.4	Results . . . . .	73
5.4.1	Phase diagram . . . . .	74
5.4.2	Susceptibilities . . . . .	75
5.4.3	Dispersion relation . . . . .	76
5.4.4	Quasiparticle life-times . . . . .	76
5.5	Discussion . . . . .	80
<b>6</b>	<b>Single electron transport in carbon nanotube quantum dots</b>	<b>83</b>
6.1	Single electron transport devices . . . . .	84
6.1.1	Single electron junction and quantum point contact . . . . .	84
6.1.2	Single electron box . . . . .	85
6.1.3	Single electron transistor . . . . .	86
6.1.4	Quantum dots . . . . .	89

---

6.2	Model Hamiltonian and master equations of single electron transport . . . . .	90
6.2.1	Model Hamiltonian . . . . .	90
6.2.2	Master equations of single electron transport . . . . .	91
6.3	Carbon nanotubes and carbon nanotube peapods . . . . .	92
6.3.1	Graphene . . . . .	92
6.3.2	Single-wall carbon nanotubes . . . . .	95
<b>7</b>	<b>Transport via coupled states in a C<sub>60</sub> peapod quantum dot</b>	<b>99</b>
7.1	Introduction . . . . .	99
7.2	Experimental results . . . . .	100
7.2.1	The device . . . . .	100
7.2.2	Transport measurements . . . . .	101
7.3	Peapod model and transport calculations . . . . .	103
7.3.1	Extended constant interaction model . . . . .	103
7.3.2	Transport calculation results . . . . .	106
7.4	Nature of the impurity state . . . . .	108
7.5	Conclusion . . . . .	109
<b>8</b>	<b>Spin-dependent electronic hybridization in a rope of carbon nanotubes</b>	<b>111</b>
8.1	Introduction . . . . .	111
8.2	The sample and the experiment . . . . .	113
8.3	Model, transport calculation and results . . . . .	115
8.4	Magnetic field measurements . . . . .	118
8.5	Discussion . . . . .	120
	<b>Acknowledgments</b>	<b>138</b>
	<b>Curriculum Vitae</b>	<b>141</b>
	<b>Erklaerung</b>	<b>142</b>



# Zusammenfassung

Die erste Studie in dieser Arbeit befasst sich mit Vielteilcheneffekten in einem eindimensionalen stark korrelierten elektronischen System - dem Kondogittermodell. Dieses System wird mit Hilfe der numerischen Dichtematrix Renormierungsgruppenmethode behandelt, da analytische Methoden, also störungstheoretische Methoden wegen annähernd gleich grossen Kopplungskonstanten, versagen. Das Kondogittermodell besteht aus einem Elektronenleitungsband, dass über eine Spinaustauschwechselwirkung an ein Gitter mit lokalisierten Spins gekoppelt ist.

Wir studieren insbesondere die spektralen Eigenschaften des eindimensionalen Kondogittermodells als Funktion der Austauschwechselwirkung, der Elektronenbandfüllung und des Quasiimpulses in der ferromagnetischen und paramagnetischen Phase. Wir berechnen die Dispersionsrelation der Quasiteilchen, ihre Lebensdauer und den Z-Faktor. Aus früheren Arbeiten ist der exakte Grundzustand und die Quasiteilchen-Dispersionsrelation für das Kondogittermodell mit nur einem Leitungselektron bekannt. Das Quasiteilchen konnte als Spinpolaron identifiziert werden. Wir finden dieses Quasiteilchen auch im Fall mehrere Elektronen. In unseren Rechnungen finden wir weiterhin, dass die Quasiteilchen-Lebensdauer um mehrere Größenordnungen in der paramagnetischen und ferromagnetischen Phase voneinander abweichen und sie hängt sehr stark von dem Quasiimpuls des Elektrons ab. Desweiteren studieren wir den Einfluss von Coulomb-Wechselwirkung auf das Phasendiagramm, die magnetische Suszeptibilität und die Elektronen-Spinrelaxation. Wir zeigen, dass eine lokale Coulomb-Wechselwirkung eine ferromagnetische Ausrichtung der lokalen Spins bewirkt und nächste-Nachbar Coulomb-Wechselwirkung, abhängig von der Füllung, eine paramagnetische oder ferromagnetische Ordnung fördert. Wir berechnen auch Quasiteilchen-Lebensdauern, die mit der Spinrelaxationszeit und Dekohärenzzeit der Elektronen in Bezug gebracht werden können und erklären ihre jeweilige Abhängigkeit von der Stärke der Wechselwirkungen und der Leitungselektronenfüllung, um die Kombination von Parametern zu ermitteln, für die die Relaxationszeit maximiert wird. Effektive Austauschwechselwirkungen zwischen den Elektronen dominieren dabei die Spinrelaxation und die Dekohärenz.

In der zweiten Studie dieser Arbeit berechnen wir numerisch den Elektronentransport durch Kohlenstoff-basierte Quantenpunkte. Dazu benutzen wir die Methode der Ratengleichungen mit einer Ankopplung in erster Ordnung an die Zuleitungen. Zur Modellierung der Quantenpunkte wird ein erweitertes konstante-Wechselwirkung Modell verwendet. Diese Arbeit wurde in Kollaboration mit zwei Arbeitsgruppen auf dem Gebiet der Experimentalphysik durchgeführt. Ein Vergleich zwischen den Messdaten dieser Gruppen mit den von uns numerisch erhaltenen Daten, zeigt eine überzeugende Übereinstimmung.

In der ersten Kollaboration wurde Elektronentransport durch eine Kohlenstoff-Nanoröhre, die

mit Fullerenen gefüllt ist, gemessen. Wir identifizieren eine kleine Hybridisierung zwischen den Fullerenen und der umgebenden Kohlenstoff-Nanoröhre als entscheidend für das Verstehen der Transportmessungen. In der zweiten Kollaboration wurde Elektronentransport durch ein Bündel von Kohlenstoffnanoröhren gemessen. Auch hier spielt die Hybridisierung, in diesem Fall zwischen den einzelnen Röhren eine entscheidende Rolle. Zusätzlich wird ein externes Magnetfeld angelegt, das es ermöglicht, den Spinzustand auf dem Quantenpunkt zu identifizieren. Dies hat potentielle Anwendungen in der spinabhängigen Elektronik.

# Summary

The first topic of this thesis is the study of many-body effects in an one-dimensional strongly correlated electronic system - the Kondo lattice model. This system is tackled numerically by means of the density matrix renormalization group, since analytic method, i.e., perturbation theory fail due to competing coupling constants. The Kondo lattice model consists of a conduction band of electrons which couple via a spin exchange coupling to a localized spin lattice.

We study the spectral properties of the one-dimensional Kondo lattice model as a function of the exchange coupling, the band filling, and the quasimomentum in the ferromagnetic and paramagnetic phases. We compute the dispersion relation of the quasiparticles, their lifetimes, and the Z factor. The exact ground state and the quasiparticle-dispersion relation of the Kondo lattice model with one conduction electron are well known. The quasiparticle could be identified as the spin polaron. Our calculations of the dispersion relation for partial band fillings give a result similar to the one-electron case, which suggests that the quasiparticle in both cases is the spin polaron. We find that the quasiparticle lifetime differs by orders of magnitude between the ferromagnetic and paramagnetic phases and depends strongly on the quasimomentum. Furthermore, we study the effects of the Coulomb interaction on the phase diagram, the static magnetic susceptibility and electron spin relaxation. We show that onsite Coulomb interaction supports ferromagnetic order and nearest neighbor Coulomb interaction drives, depending on the electron filling, either a paramagnetic or ferromagnetic order. Furthermore, we calculate electron quasiparticle life times, which can be related to electron spin relaxation and decoherence times, and explain their dependence on the strength of interactions and the electron filling in order to find the sweet spot of parameters where the relaxation time is maximized. We find that effective exchange processes between the electrons dominate the spin relaxation and decoherence rate.

In the second topic of this thesis, we numerically calculate the electron transport through carbon nanotube based quantum dot devices. We use a master equation's approach in first order of the tunneling rate to the leads and an extended constant interaction model to model the carbon nanotube system. This work has been done in collaboration with two experimental groups and we compare their respective experimentally obtained data to our numerical calculations. In both collaborations striking similarity between the numerical data and the experimental data is found.

In the first collaboration transport through a carbon nanotube peapod, i.e, a carbon nanotube filled with fullerenes, has been measured. We identify a small hybridization between a fullerene molecule and the surrounding carbon nanotube to be of crucial importance for the understanding of the transport data. In the second collaboration, electron transport through a carbon nanotube rope, i.e., a bundle of carbon nanotubes has been measured. Also here, hybridization between

the different nanotubes plays a crucial role. Furthermore, an external magnetic field is applied, which enables the identification of specific spin states of the compound quantum dot system. This might be important for future applications of such devices in spin-dependent electronics.

# Publication list

During the course of the work for this thesis several articles have been published or made available as preprints on arxiv.org.

- S. Smerat, U. Schollwöck, I. P. McCulloch and H. Schoeller  
*Quasiparticles in the Kondo lattice model at partial fillings of the conduction band using the density matrix renormalization group*  
Phys. Rev. B **79**, 235107 (2009)
- A. Eliassen, J. Paaske, K. Flensberg, S. Smerat, M. Leijnse, M. R. Wegewijs, H. I. Jørgensen, M. Monthieux, J. Nygård  
*Transport via coupled states in a  $C_{60}$  peapod quantum dot*  
Phys. Rev. B **81**, 155431 (2010)
- S. Smerat, H. Schoeller, I. P. McCulloch and U. Schollwöck  
*Coulomb interaction effects and electron spin relaxation in the 1d Kondo lattice model*  
accepted by Phys. Rev. B, arXiv:1011.3404
- K. Goß, S. Smerat, M. Leijnse, M. R. Wegewijs, C. M. Schneider, C. Meyer  
*Spin-dependent electronic hybridization in a rope of carbon nanotubes*  
submitted to Phys. Rev. Lett, arXiv:1011.4004



# Chapter 1

## Introduction

### 1.1 Motivation

In 1936 Alan Turing proposed an universal machine, known as the Turing machine, which should completely capture to perform a task by algorithmic means. This is, together with the invention of the first transistor by John Bardeen, Walter Brattain and Will Shockley in 1947, the cornerstone of a machine which revolutionized the twentieth century: the programmable computer. The evolution of the computer has been scorching and is in accord with the famous Moore's law, which was codified in 1965 by Gordon Moore and predicted an exponential growth of computational power, which still holds today, but voices raised already in the 1980's that the rapid evolution will find its end within the first two decades of the 21th century. However, the Church-Turing thesis cleaving to the efficiency of the universal Turing machine has been challenged several times and it had to be adopted to involve modern evolutions of computer science. Motivated by the question whether there is a stronger Church-Turing thesis, in 1985 David Deutsch attempted to develop a device, which could be used to simulate arbitrary physical systems and since the most fundamental laws of physics are provided by quantum mechanics his invention were quantum analogues of the machines defined by Turing and took the name quantum computers [200]. The quantum computer enables an exponential speed up of specific problems, e.g., the factorization of an integer into prime numbers.

Quantum computers demand for an entirely new class of materials, which especially involves miniaturizing electronic devices to the nanoscale. In the last two decades an immense support from experimental and theoretical physics has impelled the development in this area. In 1998 Daniel Loss and David DiVincenzo [171] defined the basic necessities to implement spin-based quantum computers and since then an ongoing effort has been made to fulfill these rules in various types of systems.

Among others, e.g., ionic traps and ultra-cold atomic gases, quantum dots [103], i.e., small and spatially confined regions in an electronic device, are especially promising to implement spin-based quantum computers in the future. In these devices one of the key issues is the control of the spin degree of freedom, i.e., flipping a dedicated spin or reading it out. Furthermore, in order to perform quantum computational algorithms the spins should not be influenced substan-

tially by the environment as long as the algorithm endures. This asks for long spin relaxation and decoherence times and methods have been invented to prolong these. One of the major sources of spin relaxation and decoherence is the interaction of the information carrying spin with spins in its neighborhood. To diminish or even exploit these interactions it is necessary to understand them in great detail on the microscopic side, which involves complicated many-body physics.

For the treatment and examination of spin dynamics of one-dimensional systems, realized in nature as carbon nanotube systems or quantum wires, a powerful numerical method exists: the density matrix renormalization group method, invented by Steven R. White in 1992 [318, 317]. It allows one to treat exceptionally long one-dimensional systems and makes the calculation of ground states, expectation values of observables, spectral properties, finite temperature and time-dependent properties possible.

On the mesoscopic side, which is the regime between microscopic and macroscopic, it is necessary to understand the physical properties of the employed nanoscale devices. As devices are shrunk to such small sizes physics requires a different description: First, the deBroglie wavelength of electrons must be taken into account and therefore their explicit quantum nature. Second, the quantization of charge becomes dominating due to a strong Coulomb interaction and this results in effects such as Coulomb blockade.

Quantum dots can be assembled from different materials, e.g., gallium arsenide, silicon based materials or carbon based materials, for example, carbon nanotubes or graphene [170, 40]. All of them have in common that as quantum dots they are embedded in an electrical circuit with three terminals, so called single-electron transistors. This allows for a fine-tuning of the electric charge on the quantum dot and enables electron transport through the quantum dot. Within such a configuration spectroscopic information of the quantum dot can be obtained and underlying physical mechanisms can be identified. Furthermore and besides applications in quantum computers, it has turned out that nanoscale devices also find applications in spin-dependent electronics, which makes use of the spin degree of freedom in conventional electronic circuits.

## 1.2 Aim of this thesis

The aim of this thesis is two-fold. First, we treat the microscopic side of one-dimensional electronic systems and elaborate the collective behavior of electrons in strong interaction with a surrounding spin bath. Second, we approach from the mesoscopic side and calculate the electronic transport in carbon nanotube systems in order to reveal the electronic level structure of these systems.

### Microscopic

We examine the interaction between conduction electrons in an one-dimensional lattice with an underlying lattice of spins. This model is widely known as the one-dimensional Kondo lattice model and is generally used to understand materials with atomic magnetic moments, so called  $f$ -spins. We use the density matrix renormalization group to calculate the ground state of the Kondo lattice model and furthermore examine the spectral properties of the conduction electrons.

This leads to the formulation of the spin polaron quasiparticle, which shows extraordinarily long life-times, which makes it especially interesting for further studies. Subsequently, we elaborate the influence of interactions between conduction electron on the phase diagram and the spin relaxation of the Kondo lattice model.

### Mesoscopic

We calculate the electronic transport in carbon nanotube systems in first order in the coupling to the attached leads. A systematic analysis of the numerical results and a comparison to experimentally obtained results enables the identification of hybridization between different constituents of the system to be of crucial importance. The carbon nanotube systems are described in a constant interaction model, where we have added interaction terms describing the interaction of electrons in different parts of the system.

## 1.3 Outline

The outline of this thesis is as follows:

- Chapter 2 introduces the density matrix renormalization group method in the language of matrix product states. The broad spectrum of the method is briefly reviewed, beginning with the basic manipulations of matrix product states. Further, time-evolution algorithms and the calculation of dynamical properties are explained.
- In Chapter 3 light is shed on the fundamental physics of the one-dimensional Kondo lattice model. A strong focus lies on the exactly solvable cases and the phase diagram of the Kondo lattice model. Exactly solvable are the limits of one electron in the conduction band, large coupling and half-filling of the conduction band. The determination of the phase diagram is illustrated by means of the bosonization method and the density matrix renormalization group method.
- Chapter 4 discusses quasiparticle properties of the Kondo lattice model at partial electron filling of the conduction band for various sets of parameters using the density matrix renormalization group. The quasiparticle dispersion relation at half-filling of the conduction band is obtained and compared to a perturbative method and this shows a striking similarity. The partial filling regime, inaccessible by the perturbative Ansatz, is accessed by the density matrix renormalization group method. The quasiparticle dispersion is calculated and interpreted in terms of a continuation of the limiting case of one electron in the conduction band. Furthermore, the quasiparticle is identified as the spin polaron and the calculation of its life-time in dependence of the available parameters shows that the life-time is extraordinarily long in the ferromagnetic phase of the Kondo lattice model.
- In Chapter 5 the Kondo lattice model is extended by onsite and nearest neighbor Coulomb interactions between electrons in the conduction band. This reveals a concurring influence

of onsite and nearest neighbor Coulomb interaction at low electron filling of the conduction band and a competitive influence at large electron filling. The spin susceptibility exposes a change from ferromagnetic order to a Ruderman-Kittel-Kasuya-Yosida ordering if Coulomb interaction becomes strong. Furthermore, the spin relaxation time of the conduction electrons is calculated in dependence of the available parameters and the sweet spot with an exceptionally long spin relaxation time is identified.

- Chapter 6 introduces single electron transport in nano-devices with a specific focus on carbon based devices, especially carbon nanotubes. Stability diagrams representing transport data, Coulomb blockade and master equations are explained.
- Chapter 7 reviews a transport experiment and corresponding transport calculations on carbon nanotube peapods, i.e, carbon nanotubes filled with fullerenes. It is shown that a simple model incorporating hybridization between fullerenes and the carbon nanotube can explain the experimentally observed features in a first order master equation transport calculation. The experimentally observed features contain additional transport signatures, which are not expected within a free single carbon nanotube transport experiment.
- In Chapter 8 a transport experiment on carbon nanotube ropes, i.e., bundled carbon nanotubes, and corresponding transport calculations are explained. As in Chapter 7 signs of hybridization between the different strands of the rope are found and can be explained in a first order master equation transport calculation. Additionally, an externally applied magnetic field allows for a differentiation of certain spin states of the quantum dot.

## Chapter 2

# Matrix product states and DMRG

Strong correlation effects in low dimensional quantum systems still belong to the most interesting issues in the physicists world. In one dimensional systems the Fermi liquid picture breaks down and the Tomonaga-Luttinger liquid becomes the valid picture at arbitrary interaction strength. The physics of the system is no longer governed by effective particles and collective excitations are dominating. Therefore classically simplifying the description of such systems becomes impossible, even though a few exact solutions of one dimensional systems, e.g., via Bethe-Ansatz exist. The full quantum nature of the respective system has to be taken into account and unfortunately in many physical systems, e.g., in lattice systems, the size of the Hilbert space grows exponentially<sup>1</sup> with the system size, which makes such systems intractable.

For one dimensional lattice systems, in 1992, Steven R. White invented a numerically exact method, the *density-matrix renormalization group* (DMRG) [317, 318], which enables its possessor to calculate ground states, expectation values and correlations efficiently. The success of the method is documented by an impressive number of reviews [228, 261, 101, 262]. Within the then following decade the method has been extended to the study of dynamic properties [100, 154, 284, 126], finite-temperature information [309, 278, 269], and time-evolutions far from equilibrium [306, 307, 52, 319, 304, 234, 12, 104].

The DMRG can be formulated very efficiently [66, 123, 178, 217, 250, 305, 182] by means of *Matrix-Product states* (MPS) [11, 141, 140, 2, 66], which have been invented earlier than and separate from DMRG. However, it turns out that most of the DMRG algorithms have a quite natural formulation in the language of MPS. By now, it has become a well know fact that DMRG performs exceptionally well on one dimensional lattice systems. This has been shown in many works [227, 166, 62, 264, 289, 43, 4, 303], most of them related to MPS.

In this chapter we will first introduce Matrix-Product states starting with the general construction and explaining the basic manipulation schemes. Then, on the basis of MPS, we focus on the DMRG used to calculate ground states, time evolutions and dynamical properties of ground states.

---

<sup>1</sup>In a spin-1/2 chain with  $L$  sites  $2^L$  states are possible.

## 2.1 Matrix product states

### 2.1.1 General construction

Imagine an one dimensional lattice system with open boundary conditions and length  $L$ . To each physical site  $i$  a local Hilbert space  $\mathcal{H}_i$  is assigned with the local dimension  $d$ . The total Hilbert space is a tensor product  $\mathcal{H} = \bigotimes_{i=1}^L \mathcal{H}_i$ . We can now write an arbitrary state  $|\Psi\rangle$  in the Hilbert space  $\mathcal{H}$  as

$$|\Psi\rangle = \sum_{a_{L-1}} \sum_{\sigma_L=1}^d A_{a_{L-1},1}^{\sigma_L} |a_{L-1}\rangle |\sigma_L\rangle, \quad (2.1)$$

where  $A_{a_{L-1},1}^{\sigma_L} = \langle a_{L-1} \sigma_L | \Psi \rangle$ , the sum over  $a_{L-1}$  runs over the complete Hilbert space describing sites 1 to  $L-1$  and  $|\sigma_i\rangle$  are the states of the local Hilbert space at site  $i$ .  $|a_{L-1}\rangle$  is called a *left block* and correspondingly we can also define right blocks. Repeating the decomposition for  $|a_{L-1}\rangle$  and subsequently all further left blocks we arrive at

$$|\Psi\rangle = \sum_{a_1} \cdots \sum_{a_{L-1}} \sum_{\sigma_1} \cdots \sum_{\sigma_L} A_{1,a_1}^{\sigma_1} A_{a_1,a_2}^{\sigma_2} \cdots A_{a_{L-2},a_{L-1}}^{\sigma_{L-2}} A_{a_{L-1},1}^{\sigma_L} |\sigma_1\rangle \cdots |\sigma_L\rangle \quad (2.2)$$

$$= \sum_{\sigma_1} \cdots \sum_{\sigma_L} \hat{A}^{\sigma_1} \hat{A}^{\sigma_2} \cdots \hat{A}^{\sigma_{L-2}} \hat{A}^{\sigma_L} |\sigma_1\rangle \cdots |\sigma_L\rangle, \quad (2.3)$$

whereas for the  $\hat{A}^\sigma$ -matrices  $A_{a_{i-1},a_i}^{\sigma_i} = \langle a_{i-1} \sigma_i | a_i \rangle$  applies. This last eq. (2.3) defines a so called *matrix product state* (MPS) with  $\sigma_i$  being the physical indices and  $a_i$  the bond indices. The connection between two  $\hat{A}^\sigma$ -matrices is a *bond*. For open boundary conditions it naturally turns out that the  $\hat{A}^\sigma$ -matrices at site 1 and site  $L$  have the shape  $1 \times D_1$  and  $D_L \times 1$ , respectively, since there are no further matrices to the left and the right of the system and consequently the matrix product of Eq. (2.3) gives a scalar. The matrix product state as given in Eq. (2.3) is formally exact, but for numerical and efficiency reasons the dimension of a general  $A$ -matrix will be limited to the maximal bond dimension  $D$  by some effective truncation scheme, which will be defined below and is essential for nearly all matrix product algorithms.

Furthermore  $\hat{A}^\sigma$ -matrices and consequently also MPS can be represented in a pictorial way, as shown in Fig. 2.1 and 2.2. This representation is a rigorous one and can not just be used to illustrate MPS operations, but also to proof statements.

### Singular value decomposition

Throughout this chapter the *singular value decomposition* (SVD) will be needed for most of the MPS related algorithms.<sup>2</sup> Therefore we will give its definition right here:

**Singular value decomposition:** To every matrix  $\hat{A} \in \mathbb{C}^{m \times n}$  there exist matrices  $\hat{U} \in \mathbb{C}^{m \times p}$ ,  $\hat{V}^\dagger \in \mathbb{C}^{p \times n}$  with orthonormal columns and rows, respectively, and a diagonal matrix

$$\hat{S} := \text{diag}(s_1, \dots, s_p) \in \mathbb{R}^{m \times n}, \quad p = \min\{m, n\} \quad (2.4)$$

<sup>2</sup>SVD could also bare the name *method almighty* in the context of MPS.

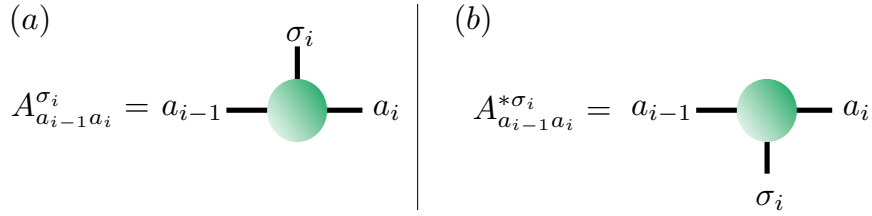


Figure 2.1: Representation of a single  $\hat{A}^\sigma$ -matrix. In (a) we see  $A_{a_{i-1}a_i}^{\sigma_i}$  and in (b) its canonical conjugate. The usefulness of drawing the canonical conjugate matrix upside down will become clear from the main text.

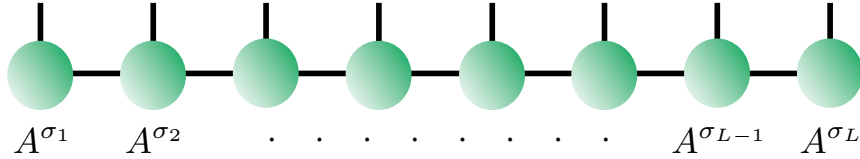


Figure 2.2: An arbitrary matrix product state constructed from the  $\hat{A}^\sigma$ -matrices of Fig. 2.1. Closed bonds imply a summation over the corresponding indices.

with

$$s_1 \geq s_2 \geq \dots \geq s_p \geq 0, \quad (2.5)$$

such that

$$\hat{A} = \hat{U} \hat{S} \hat{V}^\dagger. \quad (2.6)$$

For a rigorous proof of the singular value decomposition, see [50].

## 2.1.2 Matrix product state operations

To understand how matrix product states work in practice we will explain some basic operations in this section. We start with the normalization of a MPS, calculate overlaps of two different MPS and expectation values of some arbitrary observable.

### Orthonormalized MPS basis sets

For several MPS operations it is beneficial, when the MPS follows a certain type of orthonormalization. Building up a MPS from the left to the right, we request all left blocks to be orthonormalized, i.e.,  $\langle a'_j | a_j \rangle = \delta_{a'_j, a_j} \forall j$ . At an arbitrary site  $l$ , assuming that all blocks for sites left of  $l$  are already orthonormalized, we find the condition:

$$\delta_{a'_l a_l} = \langle a'_l | a_l \rangle = \sum_{\sigma_l} \sum_{a'_{l-1} a_{l-1}} A_{a'_{l-1} a'_l}^{*\sigma_l} A_{a_{l-1} a_l}^{\sigma_l} \langle a'_{l-1} \sigma_l | a_{l-1} \sigma_l \rangle = \sum_{\sigma_l} \left( A^{\sigma_l \dagger} A^{\sigma_l} \right)_{a'_l, a_l}, \quad (2.7)$$

which is the condition for *left-normalized*  $\hat{A}^\sigma$ -matrices. If all matrices of a MPS are left-normalized the MPS is called *left-canonical*. The same can be done for right blocks, leading in total to the

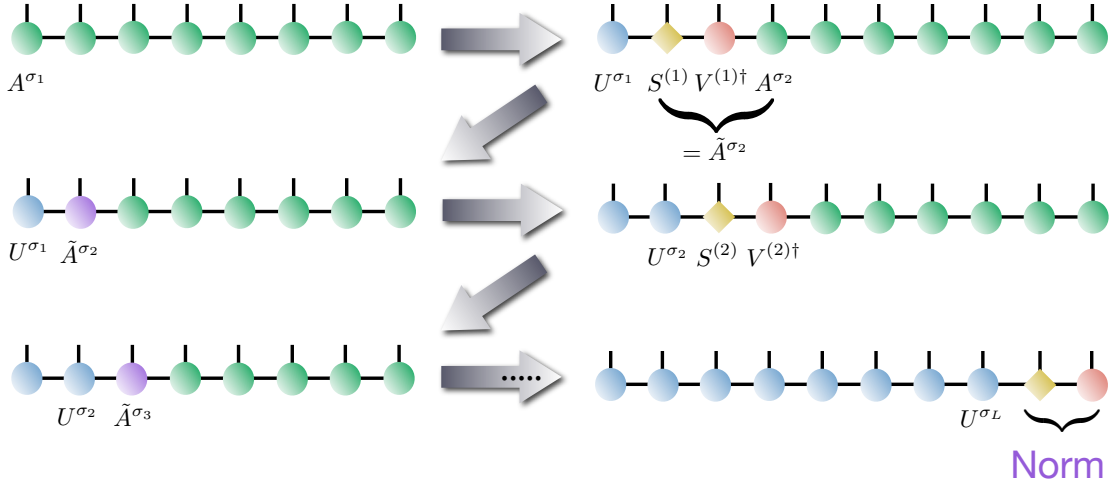


Figure 2.3: Left-canonicalization scheme for a MPS. In the last step, when all matrices are canonized, there is a left over constituting of a  $\hat{S}$ -matrix and a  $\hat{V}^\dagger$ -matrix. The multiplication of these two results is a simple scalar, which is the norm of the state.

two definitions:

$$\sum_{\sigma_i} A^{\sigma_i \dagger} A^{\sigma_i} = \mathbb{I} \quad \text{left-normalization} \quad (2.8)$$

$$\sum_{\sigma_i} A^{\sigma_i} A^{\sigma_i \dagger} = \mathbb{I} \quad \text{right-normalization.} \quad (2.9)$$

In practice, if an arbitrary MPS is present without any normalization one applies the SVD for this purpose. We illustrate this for the case of left-canonicalization, which can also be beautifully represented in the graphical notation as shown in Fig. 2.3. Note that the graphical representation takes care of the correct contraction and matrix multiplications. We start now with the arbitrary MPS

$$|\Psi\rangle = \sum_{a_1} \cdots \sum_{a_{L-1}} \sum_{\sigma_1} \cdots \sum_{\sigma_L} A_{1,a_1}^{\sigma_1} A_{a_1,a_2}^{\sigma_2} \cdots A_{a_{L-2},a_{L-1}}^{\sigma_{L-2}} A_{a_{L-1},1}^{\sigma_L} |\sigma_1\rangle \cdots |\sigma_L\rangle, \quad (2.10)$$

where all  $\hat{A}^\sigma$ -matrices are typically not normalized. Reshaping and applying an SVD to  $\hat{A}^{\sigma_1}$  leads to:

$$A_{1,a_1}^{\sigma_1} = A_{\sigma_1,1,a_1} \stackrel{SVD}{=} \sum_s U_{\sigma_1,1,s} S_{s,s} V_{s,a_1}^\dagger = \sum_s U_{1,s}^{\sigma_1} \tilde{V}_{s,a_1}^\dagger, \quad (2.11)$$

where  $U^{\sigma_1}$  has orthonormal columns and therefore fulfills Eq. (2.8). The kind of reshaping we use is essential here, since it relegates the local character of the  $\hat{A}^\sigma$ -matrix expressed by the  $\sigma$ -index to the  $\hat{U}$ -matrix. Plugging this into Eq. (2.10) we find

$$|\Psi\rangle = \sum_{s_1} \sum_{a_2} \cdots \sum_{a_{L-1}} \sum_{\sigma_1} \cdots \sum_{\sigma_L} U_{1,s_1}^{\sigma_1} \sum_{a_1} \left( \tilde{V}_{s_1,a_1}^\dagger A_{a_1,a_2}^{\sigma_2} \right) A_{a_2,a_3}^{\sigma_3} \cdots A_{a_{L-2},a_{L-1}}^{\sigma_{L-2}} A_{a_{L-1},1}^{\sigma_L} |\sigma_1\rangle \cdots |\sigma_L\rangle \quad (2.12)$$

$$= \sum_{s_1} \sum_{a_2} \cdots \sum_{a_{L-1}} \sum_{\sigma_1} \cdots \sum_{\sigma_L} U_{1,s_1}^{\sigma_1} \tilde{A}_{s_1,a_2}^{\sigma_2} A_{a_2,a_3}^{\sigma_3} \cdots A_{a_{L-2},a_{L-1}}^{\sigma_{L-2}} A_{a_{L-1},1}^{\sigma_L} |\sigma_1\rangle \cdots |\sigma_L\rangle, \quad (2.13)$$

where we defined  $\tilde{A}_{s_1, a_2}^{\sigma_2} := \sum_{a_1} (\tilde{V}_{s_1, a_1}^\dagger A_{a_1, a_2}^{\sigma_2})$ . This procedure has to be repeated for all sites to reach a fully left-canonical state. The last SVD on site  $L$  results in a scalar number  $\hat{S}\hat{V}^\dagger$ , which is the norm of the state and has to be saved separately.

By *sweeping* through the system, which means going through the system site by site and performing local operations, we canonized the whole MPS. Here only one sweep (from the first to the last site) is needed (see Fig. 2.3), but as we will get to know throughout this chapter, algorithms exist, where sweeping back and forth several times is an important element of the algorithm in order to reach in some sense an optimized MPS.

For right-canonization of an MPS one has to start at site  $L$  and basically go through the same steps as for left-canonization, but from right to left (reverse sweep). The only difference occurs during the reshaping procedure, because the local index  $\sigma$  has to be attached to the  $\hat{V}^\dagger$ -matrix this time.

## Overlap

Consider two MPS

$$|\Psi\rangle = \sum_{\sigma_1} \cdots \sum_{\sigma_L} \hat{A}^{\sigma_1} \cdots \hat{A}^{\sigma_L} |\sigma_1\rangle \cdots |\sigma_L\rangle \quad (2.14)$$

$$|\Phi\rangle = \sum_{\sigma_1} \cdots \sum_{\sigma_L} \hat{B}^{\sigma_1} \cdots \hat{B}^{\sigma_L} |\sigma_1\rangle \cdots |\sigma_L\rangle, \quad (2.15)$$

whose overlap  $\langle\Phi|\Psi\rangle$  we want to calculate. In a naive approach one would simply perform

$$\langle\Phi|\Psi\rangle = \sum_{\sigma_1} \cdots \sum_{\sigma_L} \left( \hat{B}^{\sigma_1} \cdots \hat{B}^{\sigma_L} \right)^* \hat{A}^{\sigma_1} \cdots \hat{A}^{\sigma_L}, \quad (2.16)$$

which asks for the calculation of  $d^{2(L-1)}$  matrix products, which is numerically exponentially costly and for large  $L$  even impossible to calculate. With only a slight modification, meaning a reordering of the sums, we can cast the same operation with only a linearly increasing number of matrix products:

$$\langle\Phi|\Psi\rangle = \sum_{\sigma_1} \cdots \sum_{\sigma_L} \hat{B}^{\sigma_L \dagger} \cdots \hat{B}^{\sigma_1 \dagger} \hat{A}^{\sigma_1} \cdots \hat{A}^{\sigma_L} \quad (2.17)$$

$$= \sum_{\sigma_L} \hat{B}^{\sigma_L \dagger} \cdots \sum_{\sigma_2} \left( \hat{B}^{\sigma_2 \dagger} \sum_{\sigma_1} \left( \hat{B}^{\sigma_1 \dagger} \hat{A}^{\sigma_1} \right) \hat{A}^{\sigma_2} \right) \cdots \hat{A}^{\sigma_L}. \quad (2.18)$$

This scheme needs the computation of  $d \cdot (2L - 1)$  matrix products, which grows only linearly with  $L$ . The graphical representation directly suggests this method, see Fig. 2.4.

## Norm

The norm is simply a special case of the overlap, namely  $\langle\Psi|\Psi\rangle$ . If  $|\Psi\rangle$  is already in the left- or right-canonized form, life even gets simpler, because from Eq. (2.18) and Eq. (2.8) we directly

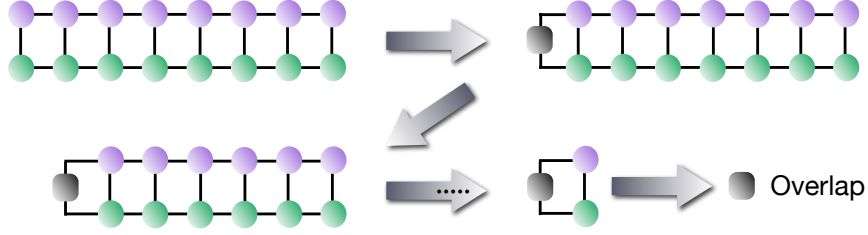


Figure 2.4: Overlap scheme for two MPS. The procedure is optimally carried out like a zipper. In the last step the contractions result in a scalar (black box without any lines), which is the overlap.

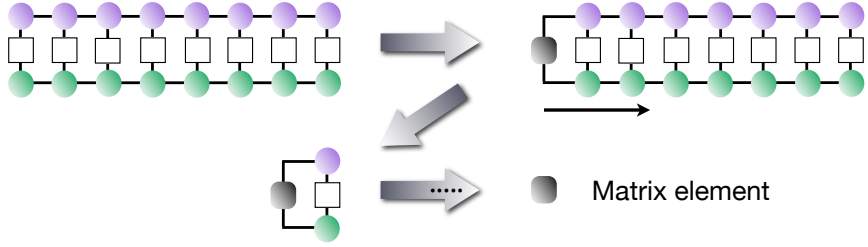


Figure 2.5: Matrix element calculation scheme of an operator  $\langle \Phi | \hat{O} | \Psi \rangle$ . The white squares between the  $\hat{A}^\sigma$ -matrices represent the local operator matrix elements.

find for left-canonized MPS that all matrix products give an identity  $\mathbb{I}$ . The norm of the state is either one or it has been saved separately. For right-canonized MPS we basically find the same result after doing some reordering in Eq. (2.18).

### Matrix elements

A local operator  $\hat{O}$  is defined as

$$\hat{O} = \sum_i \sum_{\sigma_i \sigma'_i} O^{\sigma'_i \sigma_i} |\sigma'_i\rangle \langle \sigma_i|, \quad (2.19)$$

where in practice most of the  $O^{\sigma'_i \sigma_i}$  will be identities. A general matrix element of the operator  $\hat{O}$  is then given by

$$\langle \Phi | \hat{O} | \Psi \rangle = \sum_{\sigma'_1} \dots \sum_{\sigma'_L} \sum_{\sigma_1} \dots \sum_{\sigma_L} \hat{B}^{\sigma'_L \dagger} \dots \hat{B}^{\sigma'_1 \dagger} O^{\sigma'_1 \sigma_1} \dots O^{\sigma'_L \sigma_L} \hat{A}^{\sigma_1} \dots \hat{A}^{\sigma_L}, \quad (2.20)$$

which we will directly rewrite in the efficient way (see Fig. 2.5)

$$\langle \Phi | \hat{O} | \Psi \rangle = \sum_{\sigma'_L \sigma_L} O^{\sigma'_L \sigma_L} \hat{B}^{\sigma'_L \dagger} \dots \sum_{\sigma'_2 \sigma_2} \left( O^{\sigma'_2 \sigma_2} \hat{B}^{\sigma'_2 \dagger} \sum_{\sigma'_1 \sigma_1} \left( O^{\sigma'_1 \sigma_1} \hat{B}^{\sigma'_1 \dagger} \hat{A}^{\sigma_1} \right) \hat{A}^{\sigma_2} \right) \dots \hat{A}^{\sigma_L}. \quad (2.21)$$

Expectation values are a special case of matrix elements with  $|\Phi\rangle = |\Psi\rangle$ .

### Addition of two MPS

Assume we have an MPS  $|\Phi\rangle$  we want to add another MPS  $|\Psi\rangle$  to. The states read

$$|\Psi\rangle = \sum_{\sigma_1} \cdots \sum_{\sigma_L} \hat{A}^{\sigma_1} \cdots \hat{A}^{\sigma_L} |\sigma_1\rangle \cdots |\sigma_L\rangle \quad (2.22)$$

$$|\Phi\rangle = \sum_{\sigma_1} \cdots \sum_{\sigma_L} \hat{B}^{\sigma_1} \cdots \hat{B}^{\sigma_L} |\sigma_1\rangle \cdots |\sigma_L\rangle. \quad (2.23)$$

The addition of the two MPS results in

$$|\Psi\rangle + |\Phi\rangle = \sum_{\sigma_1} \cdots \sum_{\sigma_L} \hat{C}^{\sigma_1} \cdots \hat{C}^{\sigma_L} |\sigma_1\rangle \cdots |\sigma_L\rangle, \quad (2.24)$$

with

$$\hat{C}^{\sigma_i} = \hat{A}^{\sigma_i} \oplus \hat{B}^{\sigma_i} = \begin{pmatrix} \hat{A}^{\sigma_i} & 0 \\ 0 & \hat{B}^{\sigma_i} \end{pmatrix} \quad \text{for sites 2 to L-1} \quad (2.25)$$

$$\hat{C}^{\sigma_1} = \hat{A}^{\sigma_1} \oplus \hat{B}^{\sigma_1} = \begin{pmatrix} \hat{A}^{\sigma_1} & \hat{B}^{\sigma_1} \end{pmatrix} \quad \text{for site 1} \quad (2.26)$$

$$\hat{C}^{\sigma_L} = \hat{A}^{\sigma_L} \oplus \hat{B}^{\sigma_L} = \begin{pmatrix} \hat{A}^{\sigma_L} \\ \hat{B}^{\sigma_L} \end{pmatrix} \quad \text{for site L,} \quad (2.27)$$

where the special shape of  $\hat{C}^{\sigma_1}$  and  $\hat{C}^{\sigma_L}$  takes care of the correct matrix dimensions at the boundaries of the chain. It is important to note here that this is different for periodic boundary conditions.

The addition of two MPS therefore significantly increases the necessary matrix dimensions and in computational applications it will not be possible to repeat this procedure arbitrarily often. Therefore, already for this simple procedure it might be useful to have an algorithm at hand, which compresses an MPS approximately. We will introduce this algorithm in the next section, regarding the fact that there are MPS algorithms still to be discussed in this chapter making exhaustive use of MPS compression.

### 2.1.3 Compression of an MPS

Many MPS operations expand the matrix dimensions of a given MPS substantially. Since classical computers provide natural bounds an algorithm may simply break down at the point, when the matrix dimensions surmount a certain threshold and this raises the desire to approximately compress the given MPS. Assume we have such a given MPS with a maximal bond dimension  $D'$ . There exist two common truncation schemes of MPS approximation. First, we will discuss the SVD compression, for which we have to understand the notion of Schmidt decomposition. Here we make use of the fact that the relative magnitude of the schmidt coefficients decides, whether a certain state is important to describe the MPS or not. Second, we examine the variational compression, which simply varies every  $\hat{A}$ -matrix such that it becomes optimal in the sense that the newly compressed MPS approximates the original MPS optimally.

### Schmidt decomposition

A completely arbitrary state  $|\Xi\rangle$  can be decomposed into a bipartite system as

$$|\Xi\rangle = \sum_{ij} \xi_{ij} |i\rangle_L |j\rangle_R, \quad (2.28)$$

where  $\{|i\rangle_L\}$  and  $\{|j\rangle_R\}$  are orthonormal basis sets. The Schmidt decomposition [10, 200] enables us by means of the SVD to write  $|\Xi\rangle$  in two bases, which share the same reduced density matrix eigenvalue spectrum. The Schmidt decomposition reads

$$|\Xi\rangle = \sum_{ij} \sum_{\tau=1}^{r'} U_{i\tau} S_{\tau} V_{\tau j} |i\rangle_L |j\rangle_R \quad (2.29)$$

$$= \sum_{\tau=1}^{r'} S_{\tau} \sum_i U_{i\tau} |i\rangle_L \sum_j V_{\tau j} |j\rangle_R \quad (2.30)$$

$$= \sum_{\tau=1}^{r'} S_{\tau} |s_{\tau}\rangle_L |s_{\tau}\rangle_R, \quad (2.31)$$

where the *Schmidt rank*  $r'$  is the number of singular values or *Schmidt numbers* and where we have represented the singular values in an one dimensional array  $S$ . Remember that from the definition of the SVD, Eq. (2.5), the singular values are decreasingly ordered. The reduced density matrices for the Hilbert spaces  $L$  and  $R$ , respectively, are given by

$$\rho_L = \sum_{\tau=1}^{r'} S_{\tau}^2 |s_{\tau}\rangle_L \langle s_{\tau}| \quad (2.32)$$

$$\rho_R = \sum_{\tau=1}^{r'} S_{\tau}^2 |s_{\tau}\rangle_R \langle s_{\tau}|. \quad (2.33)$$

From these expressions we directly see, that the size of the singular value  $S_{\tau}$  determines how important the state  $|s_{\tau}\rangle_{L/R}$  is to describe the system state  $|\Xi\rangle$  properly. By reducing  $r'$  to  $r < r'$  and neglecting the corresponding states in the sum in Eq. (2.31) we can truncate  $|\Xi\rangle$  in a controlled fashion, disregarding only the unimportant constituents. We will use this result in the next section on *SVD compression*.

### SVD compression

Assume we have an MPS

$$|\Psi\rangle = \sum_{\sigma_1} \cdots \sum_{\sigma_L} \hat{A}'^{\sigma_1} \cdots \hat{A}'^{\sigma_L} |\sigma_1\rangle \cdots |\sigma_L\rangle \quad (2.34)$$

given with a maximal bond dimension  $D'$  and we desire to truncate the bond dimension to  $D < D'$ . Furthermore, we assume  $|\Psi\rangle$  is right-canonical and therefore that all right blocks of the MPS

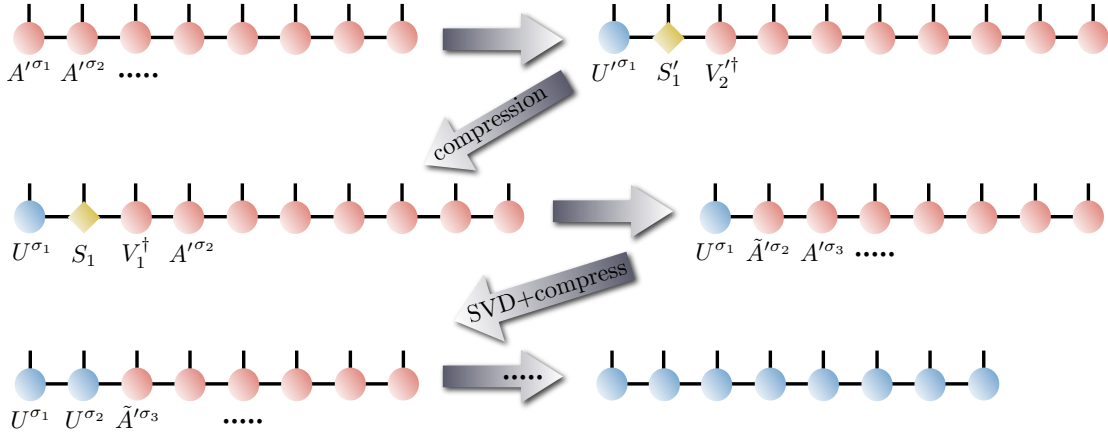


Figure 2.6: SVD compression of an MPS. Blue matrices correspond are left normalized and red matrices are right normalized. Starting with a right normalized state one ends up with a left normalized.

have orthonormal basis sets. This enables us to Schmidt decompose the MPS by means of SVD on the first site:

$$|\Psi\rangle = \sum_{\sigma_1} \dots \sum_{\sigma_L} \hat{U}^{\sigma_1} \hat{S}'_1 \hat{V}_1^{\dagger} \hat{A}'^{\sigma_2} \dots \hat{A}'^{\sigma_L} |\sigma_1\rangle \dots |\sigma_L\rangle. \quad (2.35)$$

The Schmidt numbers on the diagonal of  $S'_1$  are decreasingly ordered. In order to truncate the basis on the first site we simply cut away the last  $D' - D$  Schmidt numbers, if the size makes it necessary.  $\hat{S}'_1$ , a  $D' \times D'$ -matrix becomes  $\hat{S}_1$ , a  $D \times D$ -matrix. Accordingly, we have to adopt  $\hat{U}'^{\sigma_1}$  by cutting away the last  $D' - D$  columns and  $\hat{V}'^{\sigma_1}$  by cutting away the last  $D' - D$  rows. This leads to

$$|\Psi\rangle = \sum_{\sigma_1} \dots \sum_{\sigma_L} \hat{U}^{\sigma_1} \hat{S}_1 \hat{V}_1^{\dagger} \hat{A}'^{\sigma_2} \dots \hat{A}'^{\sigma_L} |\sigma_1\rangle \dots |\sigma_L\rangle \quad (2.36)$$

$$= \sum_{\sigma_1} \dots \sum_{\sigma_L} \hat{U}^{\sigma_1} \tilde{\hat{A}}'^{\sigma_2} \dots \hat{A}'^{\sigma_L} |\sigma_1\rangle \dots |\sigma_L\rangle. \quad (2.37)$$

The right block starting on site 2 is still in an orthonormal basis, since  $\hat{V}_1^{\dagger}$  has orthogonal rows and therefore conserves orthogonality.<sup>3</sup> After the first step we have a *mixed canonical* state. The left block with site 1 is left canonical, while all right blocks starting with site 2 are right canonized. We repeat this procedure for every following site, sweeping from left to right, see Fig. 2.6. In the end, the state is approximately compressed with a maximal bond dimension  $D$  and is left canonical. If we start with a left canonical state, we have to do the procedure in a reversed way, starting from the right end of the system.

### Variational compression

No proof exists that the SVD compression executed as described above is optimal, but it turns out in practice that it works quite well. However, if one wants to be sure to compress the state

<sup>3</sup>It simply rotates the basis of the right block.

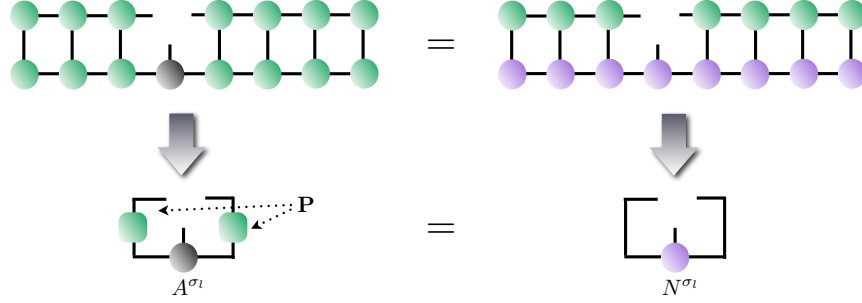


Figure 2.7: Variational compression of an MPS. The grey shaded matrix is the unknown and to be optimized matrix.

optimally one has to use the *variational compression* method. Again we assume, we have a MPS

$$|\Psi'\rangle = \sum_{\sigma_1} \dots \sum_{\sigma_L} \hat{A}'^{\sigma_1} \dots \hat{A}'^{\sigma_L} |\sigma_1\rangle \dots |\sigma_L\rangle, \quad (2.38)$$

which has a bond dimension  $D'$  and we desire to compress to a state  $|\Psi\rangle$  with bond dimension  $D$ . The difference between the two states is quantified by the norm of their difference  $\| |\Psi\rangle - |\Psi'\rangle \|$ . One has to find a state with bond dimension  $D$  to start with, which can, e.g., be the SVD compressed state, which should be a good approximation to the uncompressed state. To optimize  $\| |\Psi\rangle - |\Psi'\rangle \| = \langle \Psi | \Psi \rangle - \langle \Psi' | \Psi \rangle - \langle \Psi | \Psi' \rangle + \langle \Psi' | \Psi' \rangle$  for, e.g., the  $\hat{A}^{\sigma_l}$ -matrix we simply derivate the norm with respect to  $A_{a_{l-1}a_l}^{\sigma_l*}$  and set it equal zero:

$$\begin{aligned} \frac{\partial}{\partial A_{a_{l-1}a_l}^{\sigma_l*}} \| |\Psi\rangle - |\Psi'\rangle \| &= \sum_{\sigma'} \left( \hat{A}^{\sigma_1*} \dots \hat{A}^{\sigma_{l-1}*} \right)_{1,a_{l-1}} \left( \hat{A}^{\sigma_{l+1}*} \dots \hat{A}^{\sigma_L*} \right)_{a_l,1} \hat{A}^{\sigma_1} \dots \hat{A}^{\sigma_l} \dots \hat{A}^{\sigma_L} \\ &\quad - \sum_{\sigma'} \left( \hat{A}^{\sigma_1*} \dots \hat{A}^{\sigma_{l-1}*} \right)_{1,a_{l-1}} \left( \hat{A}^{\sigma_{l+1}*} \dots \hat{A}^{\sigma_L*} \right)_{a_l,1} \hat{A}'^{\sigma_1} \dots \hat{A}'^{\sigma_l} \dots \hat{A}^{\sigma_L} \\ &= \sum_{\tilde{a}_{l-1}\tilde{a}_l} \sum_{\sigma'} \left( \hat{A}^{\sigma_{l-1}\dagger} \dots \hat{A}^{\sigma_1\dagger} \right)_{a_{l-1},1} \left( \hat{A}^{\sigma_1} \dots \hat{A}^{\sigma_{l-1}} \right)_{\tilde{a}_{l-1},1} \hat{A}_{\tilde{a}_{l-1},\tilde{a}_l}^{\sigma_l} \times \\ &\quad \times \left( \hat{A}^{\sigma_{l+1}} \dots \hat{A}^{\sigma_L\dagger} \right)_{\tilde{a}_l,1} \left( \hat{A}^{\sigma_L\dagger} \dots \hat{A}^{\sigma_{l+1}\dagger} \right)_{1,\tilde{a}_l} - N_{a_{l-1},a_l}^{\sigma_l} = 0 \end{aligned}$$

where  $\sum_{\sigma'}$  is the sum over all  $\sigma_i$  except  $\sigma_l$ . Keeping  $\hat{A}^{\sigma_l}$  explicit, because we want to optimize this matrix, we can rewrite this equation as a linear equation system:

$$\sum_{\tilde{a}_{l-1}\tilde{a}_l} P_{a_{l-1}a_l,\tilde{a}_{l-1}\tilde{a}_l} A_{\tilde{a}_{l-1}\tilde{a}_l}^{\sigma_l} = N_{a_{l-1}a_l}^{\sigma_l} \quad (2.39)$$

$$\hat{P} A^{\sigma_l} = N^{\sigma_l}, \quad (2.40)$$

where  $\hat{P}$  is a matrix of dimension  $D^2 \times D^2$  and  $A^{\sigma_l}$  and  $N^{\sigma_l}$  are vectors. From the graphical representation it becomes quite clear, how to solve the equation system optimally, see Fig. 2.7. The scheme is iterative, meaning that starting with site 1 one has to sweep several times through the system until the approximated state does not change anymore.

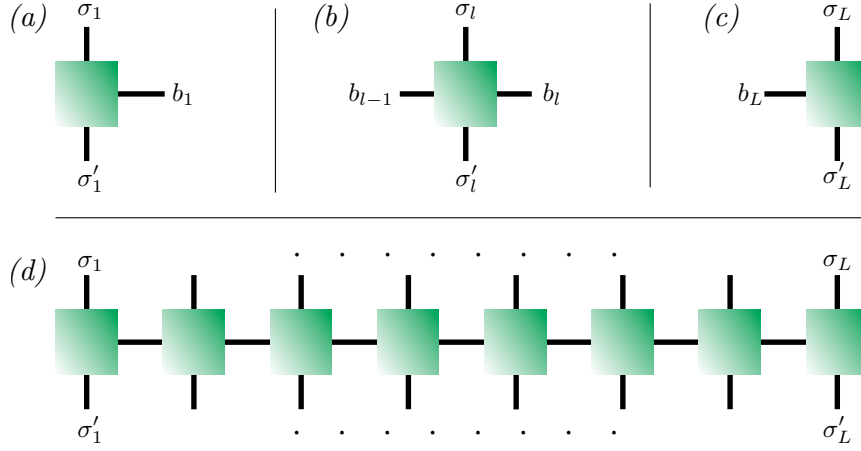


Figure 2.8: Matrix product operator. (a) Matrix product operator matrix on the first site. (b) Matrix product operator matrix on sites 2 to  $L - 1$ . (c) Matrix product operator matrix on the last site. (d) Matrix product operator representation.

### 2.1.4 Matrix product operators

The MPS representation can be extended straightforwardly to the *matrix-product operator* (MPO) representation.

$$\hat{O} = \sum_{\sigma_1 \sigma'_1} \dots \sum_{\sigma_L \sigma'_L} \hat{D}^{\sigma_1 \sigma'_1} \dots \hat{D}^{\sigma_L \sigma'_L} |\sigma_1\rangle \dots |\sigma_L\rangle \langle \sigma'_1| \dots \langle \sigma'_L| \quad (2.41)$$

Its pictorial representation is given in Fig. 2.8. Applying an MPO to an MPS is also simple:

$$\hat{O}|\Psi\rangle = \sum_{\sigma_1 \sigma'_1} \dots \sum_{\sigma_L \sigma'_L} \hat{D}^{\sigma_1 \sigma'_1} \dots \hat{D}^{\sigma_L \sigma'_L} \hat{A}^{\sigma'_1} \dots \hat{A}^{\sigma'_L} |\sigma_1\rangle \dots |\sigma_L\rangle \quad (2.42)$$

$$= \sum_{\sigma \sigma' \mathbf{a}, \mathbf{b}} \hat{D}_{1, b_1}^{\sigma_1 \sigma'_1} \hat{D}_{b_1, b_2}^{\sigma_2 \sigma'_2} \dots \hat{D}_{b_{L-1}, 1}^{\sigma_L \sigma'_L} \hat{A}_{1, a_1}^{\sigma'_1} \hat{A}_{a_1, a_2}^{\sigma'_2} \dots \hat{A}_{a_{L-1}, 1}^{\sigma'_L} |\sigma_1\rangle \dots |\sigma_L\rangle \quad (2.43)$$

$$= \sum_{\sigma} \sum_{\mathbf{a}, \mathbf{b}} \sum_{\sigma'_1} \left( \hat{D}_{1, b_1}^{\sigma_1 \sigma'_1} \hat{A}_{1, a_1}^{\sigma'_1} \right) \sum_{\sigma'_2} \left( \hat{D}_{b_1, b_2}^{\sigma_2 \sigma'_2} \hat{A}_{a_1, a_2}^{\sigma'_2} \right) \dots \sum_{\sigma'_L} \left( \hat{D}_{b_{L-1}, 1}^{\sigma_L \sigma'_L} \hat{A}_{a_{L-1}, 1}^{\sigma'_L} \right) |\sigma_1\rangle \dots |\sigma_L\rangle \quad (2.44)$$

$$= \sum_{\sigma} \sum_{\mathbf{a}, \mathbf{b}} \hat{C}_{(1,1), (b_1 a_1)}^{\sigma_1} \hat{C}_{(b_1 a_1), (b_2 a_2)}^{\sigma_2} \dots \hat{C}_{(b_{L-1} a_{L-1}), (1,1)}^{\sigma_L} |\sigma_1\rangle \dots |\sigma_L\rangle, \quad (2.45)$$

which leads as expected to a new MPS with larger bond dimensions in general.

## 2.2 DMRG

### 2.2.1 Ground state calculation

In this section we explain how ground states can be calculated variationally by means of MPS and MPOs. For this purpose we will first introduce the notion of writing a Hamiltonian in MPO form. Then we describe the variational procedure.

### Writing a Hamiltonian in MPO form

Writing a Hamiltonian in MPO representation can be done by simple construction [182, 262]. The MPO shall be given by

$$\hat{H} = \sum_{\sigma_1 \sigma'_1} \dots \sum_{\sigma_L \sigma'_L} \hat{W}^{\sigma_1 \sigma'_1} \dots \hat{W}^{\sigma_L \sigma'_L} |\sigma_1\rangle \dots |\sigma_L\rangle \langle \sigma'_1| \dots \langle \sigma'_L|. \quad (2.46)$$

The matrices  $\hat{W}^i$  have to be constructed in such a way that the right operators are connected to each other. For local operators  $X_i$  we find

$$\hat{W}^1 = \begin{pmatrix} X_1 & \mathbb{I} \end{pmatrix} \quad \hat{W}^i = \begin{pmatrix} \mathbb{I} & 0 \\ X_i & \mathbb{I} \end{pmatrix} \quad \hat{W}^L = \begin{pmatrix} \mathbb{I} \\ X_L \end{pmatrix}. \quad (2.47)$$

This readily leads to a tensor product of single local operators. The extension to nearest neighbor interaction,  $X_i \otimes Y_j$  (where  $X_i$  always acts left to  $Y_j$ ) is given by

$$\hat{W}^1 = \begin{pmatrix} 0 & X_1 & \mathbb{I} \end{pmatrix} \quad \hat{W}^i = \begin{pmatrix} \mathbb{I} & 0 & 0 \\ Y_i & 0 & 0 \\ 0 & X_i & \mathbb{I} \end{pmatrix} \quad \hat{W}^L = \begin{pmatrix} 0 \\ \mathbb{I} \\ Y_L \end{pmatrix}. \quad (2.48)$$

The extension to  $N$ -body interactions is straightforward. A mixture of local and nearest neighbor interactions would give non-zero entries in  $\hat{W}^1$  and  $\hat{W}^L$  in Eq. (2.48) instead of 0 and in  $\hat{W}^i$  for the matrix entry at  $(3, 1)$ .

### Iterative ground state search

We now use the MPS formalism developed in the preceding sections to iteratively search the ground state to a given Hamiltonian. The energy of a certain MPS  $|\Psi\rangle$  with respect to some Hamiltonian  $\hat{H}$  is given by

$$E = \frac{\langle \Psi | \hat{H} | \Psi \rangle}{\langle \Psi | \Psi \rangle}. \quad (2.49)$$

We explain the so called *on-site* algorithm in detail. Starting by optimizing the  $\hat{A}$ -matrix on the first site and then optimizing the second, third and so on, we lower the energy of  $|\Psi\rangle$  with each optimized  $\hat{A}$ -matrix a bit further. In each step we keep all matrices except the one to be optimized fixed. As soon as we have reached the last site, we reverse the direction, sweeping back and optimizing all matrices with another background of fixed  $\hat{A}$ -matrices. This procedure has to be repeated - in some cases up to several hundred times - until the energy has converged to some fixed value, which is then close to the ground state energy. However, the difference between the calculated and the true ground state energy only depends on the number of truncated states and therefore on the bond dimension  $D$ . If we would allow for arbitrary bond dimensions the result would be exact.<sup>4</sup>

<sup>4</sup>At least exact up to machine precision.

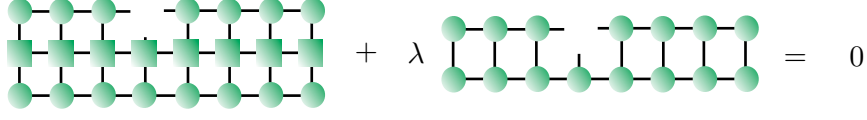


Figure 2.9: Pictorial representation of Eq. (2.52).

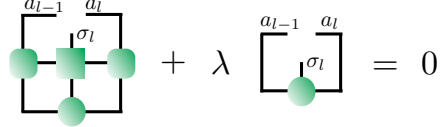


Figure 2.10: Pictorial representation of Eq. (2.56).

The optimization of  $|\Psi\rangle$  can be formulated as a Lagrangian optimization problem. We aim for minimizing  $f(\hat{A}^{\sigma_l^*}) = \langle \Psi | \hat{H} | \Psi \rangle$  under the condition  $g(\hat{A}^{\sigma_l^*}) = \langle \Psi | \Psi \rangle = 1$ . The Lagrangian function is then given as

$$\Lambda(\hat{A}^{\sigma_l^*}, \lambda) = f(\hat{A}^{\sigma_l^*}) + \lambda (g(\hat{A}^{\sigma_l^*}) - 1) \quad (2.50)$$

$$= \langle \Psi | \hat{H} | \Psi \rangle + \lambda (\langle \Psi | \Psi \rangle - 1). \quad (2.51)$$

We find the first Lagrange equation to be

$$\frac{\partial}{\partial \hat{A}_{a_{l-1}a_l}^{\sigma_l^*}} \Lambda(\hat{A}^{\sigma_l^*}, \lambda) = \frac{\partial}{\partial \hat{A}_{a_{l-1}a_l}^{\sigma_l^*}} \langle \Psi | \hat{H} | \Psi \rangle + \lambda \frac{\partial}{\partial \hat{A}_{a_{l-1}a_l}^{\sigma_l^*}} \langle \Psi | \Psi \rangle = 0, \quad (2.52)$$

which is depicted in Fig. 2.9. The second Lagrange equation is simply the normalization condition of  $|\Psi\rangle$ .

We write the constituents of Eq. 2.52 now explicitly and resort them as we need it. Assuming that  $|\Psi\rangle$  is left normalized for all  $i < l$  and right normalized for all  $i > l$  we find for  $g(\hat{A}^{\sigma_l^*})$ :

$$\langle \Psi | \Psi \rangle = \sum_{\sigma_l} \sum_{a_l a_{l-1}} \hat{A}_{a_{l-1}a_l}^{\sigma_l} \hat{A}_{a_{l-1}a_l}^{\sigma_l^*}. \quad (2.53)$$

For  $f(\hat{A}^{\sigma_l^*})$  we find:

$$\begin{aligned}
\langle \Psi | \hat{H} | \Psi \rangle &= \sum_{\sigma \sigma'} \hat{A}^{\sigma_1^*} \dots \hat{A}^{\sigma_L^*} \hat{D}^{\sigma_1 \sigma'_1} \dots \hat{D}^{\sigma_L \sigma'_L} \hat{A}^{\sigma'_1} \dots \hat{A}^{\sigma'_L} \\
&= \sum_{a_{l-1} a'_{l-1} d_{l-1}} \left( \sum_{\sigma_{l-1} \sigma'_{l-1}} \hat{A}^{\sigma_{l-1}^\dagger} \dots \sum_{\sigma_1 \sigma'_1} \hat{A}^{\sigma_1^\dagger} \hat{D}^{\sigma_1 \sigma'_1} \hat{A}^{\sigma'_1} \dots \hat{D}^{\sigma_{l-1} \sigma'_{l-1}} \hat{A}^{\sigma'_{l-1} \dagger} \right)_{a_{l-1}, d_{l-1}, a'_{l-1}} \\
&\times \sum_{d_l} \sum_{a_l a'_l} \sum_{\sigma_l \sigma'_l} \hat{A}_{a_{l-1} a_l}^{\sigma_l^*} \hat{D}_{d_{l-1} d_l}^{\sigma_l \sigma'_l} \hat{A}_{a'_{l-1} a'_l}^{\sigma'_l} \\
&\times \left( \sum_{\sigma_{l+1} \sigma'_{l+1}} \hat{D}^{\sigma_{l+1} \sigma'_{l+1}} \hat{A}^{\sigma'_{l+1}} \dots \sum_{\sigma_L \sigma'_L} \hat{D}^{\sigma_L \sigma'_L} \hat{A}^{\sigma'_L} \hat{A}^{\sigma_L \dagger} \dots \hat{A}^{\sigma_{l+1} \dagger} \right)_{a'_l d_l, a_l} \\
&= \sum_{\sigma_l \sigma'_l} \sum_{a_{l-1} a_l} \sum_{d_l} \sum_{a'_{l-1} a'_l} \hat{L}_{d_{l-1}, a'_{l-1}}^{a_{l-1}} \hat{D}_{d_{l-1} d_l}^{\sigma_l \sigma'_l} \hat{R}_{d_l, a_l}^{a'_l} \hat{A}_{a_{l-1} a_l}^{\sigma_l^*} \hat{A}_{a'_{l-1} a'_l}^{\sigma'_l},
\end{aligned}$$

where  $\hat{L}_{d_{l-1}, a'_{l-1}}^{a_{l-1}}$  and  $\hat{R}_{d_l, a_l}^{a'_l}$  abbreviate the expressions in the brackets.

Hence

$$\frac{\partial}{\partial \hat{A}_{a_{l-1} a_l}^{\sigma_l^*}} \langle \Psi | \hat{H} | \Psi \rangle + \lambda \frac{\partial}{\partial \hat{A}_{a_{l-1} a_l}^{\sigma_l^*}} \langle \Psi | \Psi \rangle = 0 \quad (2.54)$$

$$\Rightarrow \sum_{\sigma'_l} \sum_{d_l} \sum_{a_{l-1} a'_l} \hat{L}_{d_{l-1}, a'_{l-1}}^{a_{l-1}} \hat{D}_{d_{l-1} d_l}^{\sigma_l \sigma'_l} \hat{R}_{d_l, a_l}^{a'_l} \hat{A}_{a_{l-1} a_l}^{\sigma_l^*} + \lambda \hat{A}_{a_{l-1} a_l}^{\sigma_l} = 0, \quad (2.55)$$

which can be reshaped to a linear equation system and we find a simple eigenvalue equation

$$(\hat{\mathbf{H}} + \lambda \mathbb{I}) \hat{\mathbf{A}}^l = 0. \quad (2.56)$$

We have to keep in mind that this simple form is only possible due to the restriction of optimizing only one matrix at a time and that  $|\Psi\rangle$  is mixed canonized.<sup>5</sup> Pictorially, the equation in Fig. 2.9 simplified to Fig. 2.10. Solving this equation, using an eigensolver, will give the new matrix  $\hat{\mathbf{A}}^l$  and the corresponding eigenvalue  $\lambda$ , which is the approximation to the ground state energy. The matrix dimensions of  $\hat{\mathbf{H}}$  is of the order of  $D^2 d \times D^2 d$ , which is in general large. Therefore, a numerical method like the Lanczos iterative solver [160, 188, 253], seeking for the lowest eigenvalue of the system, is used. Implementing the eigensolver efficiently is very important, since this operation occurs quite often in a single ground state search: *Number of solved eigenequations* = *Sweeps*  $\times$  *Sites*  $\approx \mathcal{O}(10^5 - 10^6)$  times.

Convergence with respect to a fixed bond dimension  $D$  is reached, when the ground state energy does not change anymore. However, a better criterion is to check, whether the calculated ground state is an eigenstate of  $\hat{H}$  by considering  $\langle \Psi | \hat{H}^2 | \Psi \rangle - \langle \Psi | \hat{H} | \Psi \rangle^2$ . This expression has to become as small as possible.

<sup>5</sup>Otherwise Eq. 2.56 would be a generalized eigenvalue system.

The initial state used for ground state calculations is generally chosen in two different ways. First, the state can be build up site by site by means of *infinite size DMRG* [183]. This has the benefit that we are already in an eigenstate of the Hamiltonian most probably close to the ground state. Second, we can start with a random state, which is far of the ground state at the beginning. Both methods carry the risk to get stuck in a local minimum during the ground state search, i.e., finding an eigenstate, which is not the ground state. This is an artifact of the above described *one-site* algorithm, in which only one  $\hat{A}$ -matrix is varied at a time, which has the consequence that the rank of the varied matrix never exceeds the chosen bond dimension. The simplest way trying to get around this is given by gradually increasing the bond dimension, where it has turned out that one should start with a large number of sweeps and small bond dimension and then move to smaller numbers of sweeps with larger bond dimensions. However, one should never do a ground state calculation with only a single bond dimension. Another way to avoid local minima is provided by the *two-site DMRG* [290, 183]. Optimization of two  $\hat{A}$ -matrices at a time leads to an increased matrix rank of  $dD$ , which leads to a reshuffling of states during the truncation procedure.

This state reshuffling [314, 262] can also be forced in the one-site algorithm. For this purpose one has to make a state prediction and mix the old states with the predicted states. The density matrix of the left block and the matrix to be optimized is defined as

$$\rho^{L,l} = \text{Tr}_R |\Psi\rangle\langle\Psi|, \quad (2.57)$$

where the trace runs over all states of the right block. By applying the Hamiltonian to the left block plus the site to be optimized, we generate states targeted by the Hamiltonian, but which might have been missed in the ground state algorithm. In terms of the density matrix this mixing is

$$\rho^{L,l} = \text{Tr}_R |\Psi\rangle\langle\Psi| + \alpha \sum_{d_l} \text{Tr}_R \hat{H}_{d_l}^{L,l} |\Psi\rangle\langle\Psi| \hat{H}_{d_l}^{L,l}, \quad (2.58)$$

where  $\alpha$  is the mixing factor. In general, one chooses  $\alpha \approx 10^{-4}$ .

## Symmetries

The eigenvalue problem in Eq. (2.56) can be reduced further by taking symmetry properties of the Hamiltonian into account, i.e., accounting for conserved quantum numbers. Typical examples of conserved quantum numbers are the total particle number or the total quantized spin, whose irreducible representation of the symmetry group is Abelian. The corresponding operators commute with the Hamiltonian and are generators of the  $U(1)$  algebra.

Within the language of MPS Abelian symmetries are implemented in a simple bookkeeping scheme. Quantum numbers can be attached to every  $\hat{A}$ -matrix,  $\hat{A}_{Q_l, Q_r}^{Q_\sigma}$  and only those blocks of the matrix, which fulfill  $Q_\sigma + Q_l + Q_r = Q_{\text{tot}}$  are non-zero.

By making use of the Wigner-Eckart theorem [60, 321, 322] one can expand quantum number conservation to non-Abelian symmetry groups, like  $SU(2)$ . All MPS calculations have then to be performed in the suitable non-Abelian basis. Details of the implementation would exceed the scope of this thesis, but can be found in [181, 22, 184].

### 2.2.2 Time evolution

DMRG performs excellent in ground state calculations [261], but at the latest when optical lattices in ultra-cold atomic gases [27] began to play an important role in physics a strong desire in the DMRG community arose to calculate non-equilibrium and time-dependent properties. Recently, it has become possible to manipulate and detect single atoms in an optical lattice [268], which opens up the path to construct arbitrary initial states. Then a Hamiltonian pre-designed by the superimposed lattice acts on the system and expectation values or correlations of observables can be measured in time. Furthermore, nanoelectronics [103] is a huge and lively field, where time-dependent calculations are needed, e.g., in electron transport calculations.

The challenge to implement time dependent algorithms in a DMRG scheme is to use the limited set of DMRG states and adequately describe the time evolved state within this given set of states and ensure that the Hilbert space used still involves the most important states. The first attempt to calculate the time evolution of a DMRG state was made by Cazalilla and Marston [41]. Their method belongs to the class of static time dependent DMRG methods, or *static TD-DMRG*, in which they blow up the local Hilbert space without changing it in time. It turns out that this method is numerically very costly and therefore limited to very small time scales. Luo et al. [173] proposed to define the density matrix from the time-dependent wave function to retain the information on the relevant excitation states, which performs more reliably, but still costly.

A milestone of the development was reached with the invention of adaptive time-dependent DMRG schemes, so called *adaptive TD-DMRG*, which was first proposed in [52, 319, 307]. Both approaches are efficient implementations of an algorithm for the classical simulation of the time evolution of weakly entangled quantum states, *TEBD* [306, 307]. After each time step the Hilbert space is adapted to describe the time evolved state efficiently. As we will show in this section this can easily be implemented within the language of MPS.

Up to now, without being exhaustive, the adaptive TD-DMRG has been applied to many different problems: Electron transport in nanoscale systems [108, 57, 32, 3, 110]; Transport in spin chains [316, 164]; Simulation of time dependent Hamiltonians [133, 98]; Finite temperature calculations [68] and the calculation of spectral densities from real-time evolutions [16]. The method has been most extensively used within the large class of atomic gases and optical lattices: Properties of Fermi gases [109, 111]; Local relaxation of cold atoms in optical superlattices [49, 74]; Realization of the Bose-Hubbard model [251]; Spin-charge separation [138, 139, 143]; Bose-Fermi mixtures [232]; Simulation of magnetism in optical lattices [15, 133] and the realization of resonating valence bond states (RVB) [294].

In this section we will first introduce the time evolution using Trotter decomposition. Then we will explain a different approach, the Krylov subspace method. Finally, we will show how to use the time evolution schemes to do finite temperature calculations, or imaginary time evolutions.

#### Trotter time evolution

The implementation of the time evolution algorithm by means of the Suzuki-Trotter decomposition is especially simple in the MPS representation. We assume a time-independent Hamiltonian

$\hat{H}$  with nearest-neighbor interactions. We seek for a possibility to write the time evolution as an MPO. The time evolution operator can then be written as

$$e^{-i\hat{H}t} = e^{-i(\hat{H}_{\text{odd}} + \hat{H}_{\text{even}})t}, \quad (2.59)$$

with  $\hat{H}_{\text{odd}} = \hat{h}_1 + \hat{h}_3 + \dots$  and  $\hat{H}_{\text{even}} = \hat{h}_2 + \hat{h}_4 + \dots$  and  $\hat{h}_i$  the bond Hamiltonian on sites  $i$  and  $i+1$ . Since  $[\hat{h}_i, \hat{h}_{i+2}] = 0$  due to nearest neighbor interactions, only, the time evolution for odd or even bonds, respectively, could be performed bond-wise. However,  $[\hat{H}_{\text{odd}}, \hat{H}_{\text{even}}] \neq 0$  and therefore we have to approximately decompose the odd and even terms. This can be done by means of the Trotter-Suzuki decomposition. For this purpose we divide the time  $t$  into  $N$  pieces with a length of  $\Delta t$ , such that  $\Delta t \cdot N = t$  stays fixed for any choice of  $N$ , especially for  $N \rightarrow \infty$ , where the decomposition becomes exact again. The time evolution operator<sup>6</sup> can then be rewritten as

$$e^{-i(\hat{H}_{\text{odd}} + \hat{H}_{\text{even}})t} = e^{-i(\hat{H}_{\text{odd}} + \hat{H}_{\text{even}})N\Delta t} \quad (2.60)$$

$$= \left( e^{-i\hat{H}_{\text{even}}\Delta t} \cdot e^{-i\hat{H}_{\text{odd}}\Delta t} + \mathcal{O}(\Delta t^2) \right)^N. \quad (2.61)$$

To keep the error due to the Trotter decomposition small,  $\Delta t$  has to be chosen small. We can now write the time evolution operators for even and odd bonds as MPOs.  $e^{-i\hat{h}_1\Delta t}$  generally has the form  $\sum_{\sigma_1\sigma_2\sigma'_1\sigma'_2} O^{\sigma_1\sigma_2,\sigma'_1\sigma'_2} |\sigma_1\sigma_2\rangle \langle \sigma'_1\sigma'_2|$ , which is non-local. Using an SVD we can rewrite this as

$$O^{\sigma_1\sigma_2,\sigma'_1\sigma'_2} = \tilde{O}^{\sigma_1\sigma'_1,\sigma_2\sigma'_2} \quad (2.62)$$

$$= \sum_k U_{\sigma_1\sigma'_1,k} S_{k,k} \left( V^\dagger \right)_{k,\sigma_2\sigma'_2} \quad (2.63)$$

$$= \tilde{U}^{\sigma_1\sigma'_1} \left( \tilde{V}^\dagger \right)^{\sigma_2\sigma'_2}, \quad (2.64)$$

where  $\sqrt{S_{k,k}}$  has been absorbed in  $\tilde{U}^{\sigma_1\sigma'_1}$  and  $(\tilde{V}^\dagger)^{\sigma_2\sigma'_2}$ , respectively. We have derived a local representation of the time evolution operator and we can write them as MPOs.

The time evolution algorithm, see Fig. 2.11, proceeds now as follows: (1) Apply the odd and then (2) the even bonds time evolution operator to the initial state  $|\Psi\rangle$ . (3) This will enlarge the bond dimension of the MPS, which has to be compressed to its original dimension  $D$ , again. (4) Repeat these steps (1) - (3) as often as needed, or possible, until the desired time  $t = N\Delta t$  is reached. At each time step, observables can be evaluated in the standard way,  $\langle \hat{O}(t) \rangle = \langle \Psi(t) | \hat{O} | \Psi(t) \rangle$ .

The two errors in the time evolution by means of Trotter decomposition are well controllable. The truncation error is determined by the number of states kept in each time evolutionary step and the Trotter error or *time evolution error*<sup>7</sup> is overcome by reducing the time step width  $\Delta t$  or by choosing higher orders of the Trotter decomposition [75, 137]. A detailed error analysis using the Trotter decomposition can be found in [90].

<sup>6</sup>The time evolution operator has in general the form  $\sum_{\sigma} O^{\sigma_1 \dots \sigma_L, \sigma'_1 \dots \sigma'_L} |\sigma_1 \dots \sigma_L\rangle \langle \sigma'_1 \dots \sigma'_L|$  and is highly non-local.

<sup>7</sup>The time evolution error is the error, which is due to the method chosen.

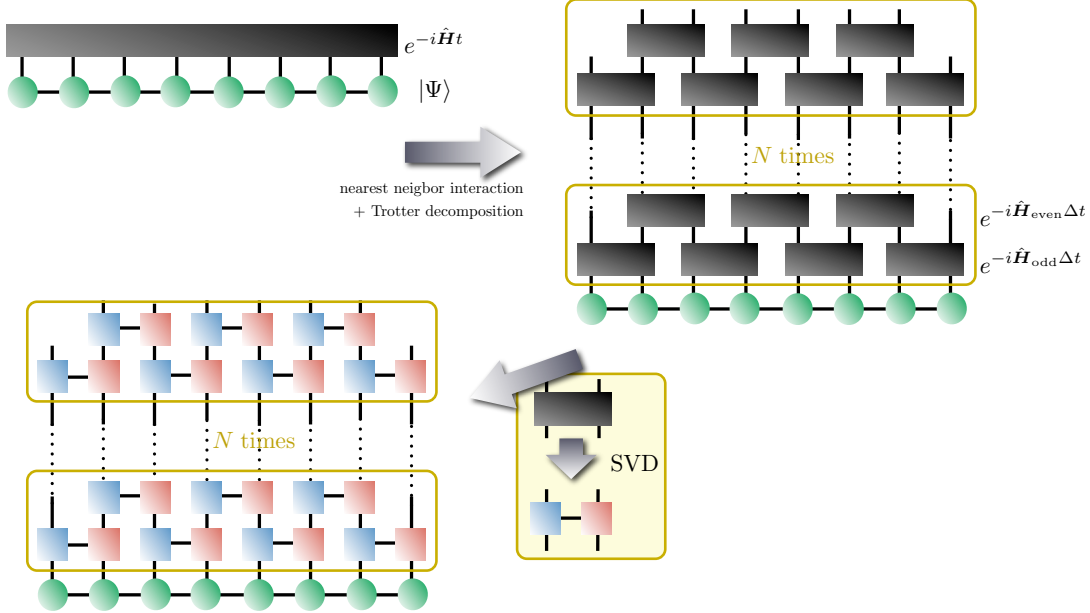


Figure 2.11: Time evolution by means of the Trotter decomposition.

### Krylov subspace method

Even if the time evolution in terms of the Trotter decomposition is favorable in most cases it has two disadvantages. First, the time evolution is limited to nearest neighbors. A generalization to wider ranged interactions is not trivial and incorporates an increasing number of SVDs for larger and larger matrices. Second, in the end the time evolution error can only be decreased by choosing smaller time steps  $\Delta t$ , which might not be desirable in all cases, since more and more time steps become necessary. To overcome these issues, several different time evolution methods have been tested [75, 68] and among them the *Krylov subspace method* [260], which we present in this section. The idea of the Krylov time evolution method is to approximately represent the given Hamiltonian in a new and extraordinarily suitable basis, which is much smaller than the original DMRG basis. The time evolution is performed within this basis and therefore is enormously simplified.

The  $k$ -dimensional *Krylov subspace* [188] is spanned by repeatedly applying the Hamiltonian  $\hat{H}$  on the state to be time evolved  $|\Psi(t)\rangle$ :

$$K_k = \left\{ \hat{H}^0 \Psi(t), \hat{H}^1 \Psi(t), \dots, \hat{H}^{k-1} \Psi(t) \right\}, \quad (2.65)$$

where  $|k_i\rangle = \hat{H}^i |\Psi(t)\rangle$ ,  $i \in \{0, 1, 2, \dots, k-1\}$  denote the *Krylov vectors*.

These vectors have to be ortho-normalized via the recursion relation (Lanczos iteration [188])

$$\beta_{n+1} |K_{n+1}\rangle = \hat{H} |K_n\rangle - \alpha_n |K_n\rangle - \beta_n |K_{n-1}\rangle \quad (2.66)$$

with  $\beta_j^2 = \langle K_j | K_j \rangle$ ,  $\langle K_i | K_j \rangle = 0$  for  $i \neq j$  and  $\alpha_j = \langle K_j | \hat{H} | K_j \rangle$ . A detailed error analysis of the Krylov subspace approximation (including upper estimates of the error) is given in Refs. [288, 114]. From the recursion relation it is obvious that the Hamiltonian is a tridiagonal  $k \times k$  matrix in the basis of the Krylov vectors and therefore easily diagonalizable. The time evolution proceeds then as follows:

$$e^{-i\hat{H}\Delta t} |\Psi(t)\rangle \approx \sum_{ij} |K_i\rangle \langle K_i | e^{-i\hat{H}\Delta t} |K_j\rangle \langle K_j | \Psi(t)\rangle \quad (2.67)$$

$$= \sum_i c_i |K_i\rangle. \quad (2.68)$$

This form of the time evolution is unitary and therefore conserves the normalization. Note that the time evolution is only approximate due the Krylov subspace approximation, which projects the full Hamiltonian  $\hat{H}$  on some effective Hamiltonian  $(\hat{H}_{\text{eff}})_{ij} = \langle K_i | \hat{H} | K_j \rangle$ , which is possible due to the choice of a suitably small time step  $\Delta t$ .

Note further that from an MPS point of view the dimension of each next higher Krylov vector significantly increases, since we apply  $\hat{H}$  another time. For each Krylov vector we use an own MPS, which makes the implementation much more efficient, especially compared to classical DMRG, where a set of target states had to be chosen to optimally represent all Krylov vectors in the same enlarged basis, see for example [68]. The MPS representation is much more efficient, since the numerical cost of the algorithm scales cubic with the number of states.

The number of needed Krylov vectors is restricted to 3 – 10 providing a Krylov error of  $10^{-10}$  or even smaller. The small number of Krylov vectors also guarantees that the bond dimension of the higher Krylov vectors is not too large and further since higher Krylov vectors tend to be more and more linearly dependent one avoids instabilities in the orthogonalization procedure. The coefficients  $c_i$  are used for estimating the convergence of the Krylov approximation. If  $c_{k-1}$  drops below a certain threshold the Krylov approximation has converged. If this does not happen for a presetted limit of Krylov vectors, one has to repeat the calculation for a smaller time step.

Again, we have two sorts of errors involved. First, the truncation error, set by the number of DMRG states taken into account and second the time evolution error, set by the error given by the Krylov approximation. Typically, the truncation error starts to dominate the whole error at very short times, compared to the whole time scale [75]. There is no *target error* in the MPS formulation of the algorithm. This is only relevant to classical DMRG algorithms, where the target Hilbert space had to be build up before performing the time evolution.

### Natural limitation of time evolution

The Lieb-Robertson theorem states that entanglement  $S$  of an out of equilibrium evolution can grow according to  $S(t) \leq S(0) + ct$ , where  $c$  is a constant proportional to the speed of propagation of the excitations in the system. From [213] it follows that the bond dimension needed to describe the system with a constant error is  $D(t) \propto 2^t$  and therefore exponentially growing in time. Naturally, the calculation will end when the number of states needed to describe the physical system exceeds the computational resources. Still, a lot of interesting physics can be explored with time evolution methods before entanglement explodes. Recent developments in

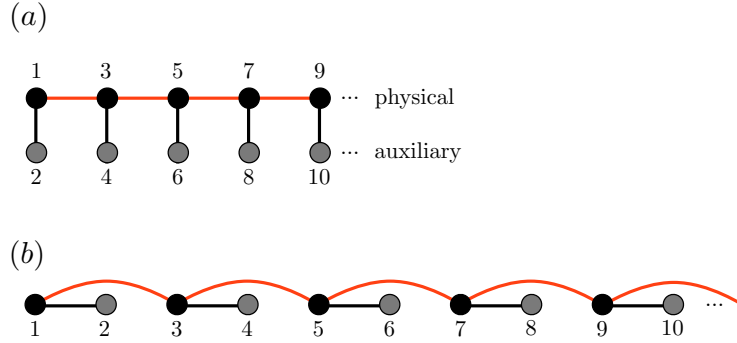


Figure 2.12: Purification of an MPS with nearest neighbor interaction. Black discs are physical sites, grey discs auxiliary sites, black solid lines symbolize the maximal entanglement between two sites at  $\beta = 0$  and red solid lines are the interaction between two sites. (a) In the ladder view. (b) In the 1d chain view.

the field of time evolution methods focus on limiting the spread of information or entanglement in the system. Just to name two of the recent developments, there is the time evolution in the Heisenberg picture [234, 104], where not the state is time evolved, but the observable and the other method is the *transverse folding algorithm* [12], where the MPS tensor network is folded in an efficient way, such that entanglement becomes more localized.

### Finite temperature DMRG

By means of purification of a mixed state [304] we can also perform temperature dependent calculations. Using Schmidt decomposition we can write an arbitrary mixed state  $\hat{\rho}_P = \sum_{a=1}^r s_a^2 |a\rangle_P \langle a|$  in Hilbert space  $P$  (physical Hilbert space) as a pure state by taking an auxiliary Hilbert space  $Q$  into account:

$$|\Psi\rangle = \sum_{a=1}^r s_a |a\rangle_P |a\rangle_Q. \quad (2.69)$$

Hence we find

$$\hat{\rho}_P = \text{Tr}_Q \hat{\rho}, \quad (2.70)$$

where  $\hat{\rho}$  is the density matrix of the whole system  $P \otimes Q$ . The mixed state density matrix at the inverse temperature  $\beta = 1/T$  is given by

$$\hat{\rho}_{P,\beta} = \frac{1}{Z(\beta)} e^{-\beta \hat{H}} = \frac{1}{Z(\beta)} e^{-\beta \hat{H}/2} \cdot \hat{\mathbb{1}} \cdot e^{-\beta \hat{H}/2}, \quad (2.71)$$

<sup>8</sup> $k_B$  is set to 1.

where  $Z(\beta) = \text{Tr}_P \exp(-\beta \hat{H})$  and with  $\hat{\mathbb{I}} = Z(0) \hat{\rho}_{P,\beta=0}$ , which is the factorized mixed state at infinite temperature, we find

$$\hat{\rho}_{P,\beta} = \frac{Z(0)}{Z(\beta)} e^{-\beta \hat{H}/2} \cdot \text{Tr}_Q |\Psi_0\rangle \langle \Psi_0| \cdot e^{-\beta \hat{H}/2} \quad (2.72)$$

$$= \frac{Z(0)}{Z(\beta)} \text{Tr}_Q e^{-\beta \hat{H}/2} \cdot |\Psi_0\rangle \langle \Psi_0| \cdot e^{-\beta \hat{H}/2} \quad (2.73)$$

$$= \frac{Z(0)}{Z(\beta)} \text{Tr}_Q |\Psi_\beta\rangle \langle \Psi_\beta|, \quad (2.74)$$

where  $|\Psi_0\rangle$  is the purified state and the trace over  $Q$  could be commuted with the exponential, since  $\hat{H}$  only acts on Hilbert space  $P$ . An arbitrary expectation value of an operator  $\hat{O}$  can be computed as  $\langle \hat{O} \rangle_\beta = \langle \Psi_\beta | \hat{O} | \Psi_\beta \rangle / \langle \Psi_\beta | \Psi_\beta \rangle$ .

The state at infinite temperature factorizes on each site. Therefore, it is enough to purify a single site as follows:

$$\frac{1}{d} \hat{\mathbb{I}} = \frac{1}{d} \sum_{\sigma} |\sigma\rangle_P \langle \sigma| = \frac{1}{d} \text{Tr}_Q \left( \sum_{\sigma} |\sigma\rangle_P |\sigma\rangle_Q \right) \left( \sum_{\sigma} \langle \sigma|_P \langle \sigma|_Q \right), \quad (2.75)$$

which naturally leads to a ladder structure for a one dimensional system, where the physical sites live on the upper bar and the auxiliary sites on the lower bar, see Fig. 2.12(a). The system is then maximally entangled on every rung and not entangled at all on the bars. Using imaginary time evolution we act only on the physical part of the system. Translated to a one dimensional system, see Fig. 2.12(b), it can be formulated as a chain with next nearest neighbor interaction. Trotter decomposition becomes more sophisticated now, since we have to perform time evolution on four sites simultaneously: First we evolve the odd plaquettes with site numbers  $(1, 2, 3, 4), (5, 6, 7, 8), \dots$  and then the even plaquettes  $(3, 4, 5, 6), (7, 8, 9, 10), \dots$ . Via applying SVD two times instead of only one time, we can bring the imaginary time-evolution operator into MPO form.

### 2.2.3 Frequency space DMRG

So far, we have seen that DMRG can be used to calculate ground state properties, see Sec. 2.2.1, and time evolution of arbitrary initial non-equilibrium states, see Sec. 2.2.2. Furthermore, DMRG can also be used to calculate dynamical ground state properties, like Greens functions and spectral densities, of a physical system. The fermionic<sup>9</sup> retarded real-time Greens function of an operator  $\hat{A}$  is defined as

$$G_C^R(t' - t) = -i \Theta(t' - t) \left\langle \left[ \hat{C}(t'), \hat{C}^\dagger(t) \right]_+ \right\rangle, \quad (2.76)$$

<sup>9</sup>Identical to the bosonic Greens function up to a sign.

where  $[\cdot, \cdot]$  denotes the anti-commutator and further we define

$$G_C^>(t' - t) = -i \langle \hat{C}(t') \hat{C}^\dagger(t) \rangle \quad t' > t \quad (2.77)$$

$$G_C^<(t' - t) = -i \langle \hat{C}^\dagger(t') \hat{C}(t) \rangle \quad t \geq t' \quad (2.78)$$

Assuming a time-independent Hamiltonian we find in frequency space

$$G_C^>(\omega) = \langle 0 | \hat{C} \frac{1}{E_0 + \omega - \hat{H} + i\eta} \hat{C}^\dagger | 0 \rangle \quad (2.79)$$

$$G_C^<(\omega) = \langle 0 | \hat{C}^\dagger \frac{1}{E_0 - \omega - \hat{H} - i\eta} \hat{C} | 0 \rangle, \quad (2.80)$$

with  $G_C^R(\omega) = G_C^>(\omega) - G_C^<(\omega)$ . The spectral density is defined via

$$C_C(\omega) = -\frac{1}{\pi} \lim_{\eta \rightarrow 0} G_C^R(\omega). \quad (2.81)$$

The finite broadening factor  $\eta$  has a three-fold meaning: First, it ensures causality. Second, it provides a finite lifetime of the excitations in the system  $\tau \propto \frac{1}{\eta}$  and therefore damps finite size effects, since  $\eta$  in frequency space corresponds to an exponential damping term  $\exp -\eta t$  in real-time space. Third,  $\eta$  causes a Lorentzian broadening of the spectral density, as will be seen in Sec 3.

By now, several approaches to calculate Greens functions and spectral densities by means of DMRG, exist. Most of them rely on the evaluation of Eq. 2.79. In this chapter, we first present the *continued-fraction Lanczos dynamics*, which has first been implemented in Ref. [100] and calculates time-efficient, but comparatively rough approximations to dynamical quantities. Then, we introduce the *correction vector method*<sup>10</sup>, see Ref. [154], which is numerically precise, but costly. A reformulation of the correction vector method is the so called *dynamical DMRG* in Ref. [126].

With the breakthrough of TD DMRG, calculating frequency space properties by fourier transforming real-time observables became attractive. Even though there exist other linear prediction techniques [315, 226], we present here the recent *linear time prediction* method by T. Barthel et al. [16].

The most recent success in calculating spectral properties has been achieved by a *Chebychev expansion* method [115, 116].

The applications of frequency space DMRG are thematically widely spread and so numerous that it is not possible to mention them all. However, those works can be classified by the method used: Continued fraction dynamics, correction vector or very similar the dynamical DMRG and real-time methods. The first application of the numerically efficient, but limited in its precision continued fraction dynamics has been on  $S = 1/2$  antiferromagnetic Heisenberg chains [100]. Furthermore it has been applied to the spin-boson model [205], the Holstein model [337] and

<sup>10</sup>In this thesis, we make extensive use of this method.

spin-orbit chains in external fields [334]. The dispersion relation of a spin chain has been calculated in [211] and in [80] a self-consistent impurity solver for dynamical mean-field theory [191, 82] is provided.

The numerically costly and exact correction vector method and dynamical DMRG have first been applied to calculate nonlinear optical coefficients of Hubbard chains and similar models [223]. The AC conductivity of the Bose-Hubbard model with nearest-neighbor interaction could be determined in [153]. In [237] it could be shown that the method can also be applied to dynamic correlations of single-impurity Anderson models. For quasiparticles in metallic grains, it could be shown in [91] that pair breaking excitations of the BCS ground state [14], surprisingly have infinite life times. In [20] very precise spectral functions of the Hubbard model have been calculated. It could be shown that dynamical DMRG can be applied to impurity problems [203] and further that it is possible to precisely calculate Greens functions of a single impurity Anderson model [202]. This has been extended later to the calculation of the spectral density of the two-impurities Anderson model [204]. The spin and charge separation of the one dimensional extended Hubbard model at half-filling with onsite and nearest neighbor interaction has been calculated in [19]. Edge singularities could be found in high-energy spectra of  $S = 1$  Heisenberg chains in strong external magnetic fields [76]. It could be demonstrated that one of the most striking effects of Luttinger liquids, the bosonic spin charge separation, is available in an interacting two-component Bose Hubbard model [139, 138]. In [201] the authors examined spin and charge separation of the Hubbard model with next nearest neighbor hopping. Spectral properties of a two-channel fermion-boson transport model have been calculated in [63]. The Hubbard model in infinite dimensions has been examined in [236]. The electronic spectral density, dispersion relation and for the first time the electron life-time in a Kondo lattice model has been calculated in [280, 279]. Further examination of fermi-boson mixtures has taken place in [61]. Recently, also spectral properties of the Hubbard model near a Mott transition [142] and of the Hubbard model with spin polarization [301] have been calculated.

### Continued fraction dynamics

The *continued-fraction dynamics* method has first been exploited in Ref. [79], but the formalization of the method goes back to Lanczos, see Refs. [7, 162, 161]. A very clear presentation of the iterative procedure for generating continued fractions in terms of Greens functions can be found in Ref. [87]. We do not provide the derivation of the continued fraction method in full detail and restrict ourselves to the main results.

Within the continued-fraction algorithm the Hamiltonian  $\hat{H}$  is iteratively tridiagonalized by generating a Krylov subspace, spanned by the vectors:

$$|f_{n+1}\rangle = \frac{1}{b_{n+1}} (\hat{H}|f_n\rangle - a_n|f_n\rangle - b_n^2|f_{n-1}\rangle), \quad (2.82)$$

where  $b_{n+1}$  is determined by the normalization condition of  $|f_{n+1}\rangle$ . Furthermore,

$$|f_0\rangle = \hat{C}|0\rangle \quad (2.83)$$

$$a_n = \langle f_n | \hat{H} | f_n \rangle, \quad (2.84)$$

the Greens function can be written as

$$G_C^<(z) = \langle f_0 | \frac{1}{z - \hat{H}} | f_0 \rangle, \quad (2.85)$$

where  $z = E_0 + \omega - i\eta$ . Projecting the Hamiltonian on the Krylov vectors iteratively, we finally end with a continued-fraction expression for the Greens function (see [87]):

$$G_C^<(z) = \frac{1}{z - a_0 - \frac{b_1^2}{z - a_1 - \frac{b_2^2}{z - a_2 - \dots}}}. \quad (2.86)$$

Thinking in the language of MPS and MPO, we can calculate the Greens function by spanning the Krylov space and calculating all relevant factors  $a_i$  and  $b_i$ :

1. Calculate the ground state  $|0\rangle$ ;
2. Apply  $\hat{C}$  on the ground state to get  $|f_0\rangle$ ;
3. Calculate the Krylov subspace by performing a Lanczos tridiagonalization of  $\hat{H}$  and making use of Eq. 2.82;
4. Calculate the Greens function from the obtained factors in step 3.

There are severe numerical limitations to this algorithm, concerning the Lanczos part. For convergence of the Lanczos iteration scheme  $\mathcal{O}(100)$  iterations are needed. However, for large numbers of iterations, global orthogonality is lost, since the algorithm orthogonalizes only locally. The generation of new coefficients has to be stopped before this happens. In Ref. [154] the authors developed the criterion  $\langle f_0 | f_n \rangle > \varepsilon$ , when fulfilled, the Lanczos iteration is stopped. If the Lanczos algorithm has converged at that point one can successfully calculate the Greens functions, otherwise it is not reliably possible.

### Correction vector method

The *correction vector method* [284] was proposed in 1989 even before DMRG was invented. Its first applications were realized in Refs. [239, 154].

The correction vector is defined as a part of the Greens function:

$$|c(\omega, \eta)\rangle = \frac{1}{E_0 + \omega + i\eta - \hat{H}} \hat{C}^\dagger |0\rangle \quad (2.87)$$

and therefore the Greens function can be obtained from

$$G_C^>(\omega, \eta) = \langle 0 | \hat{C} | c(\omega, \eta) \rangle. \quad (2.88)$$

The solution of the linear equation system

$$(E_0 + \omega + i\eta - \hat{H}) |c(\omega, \eta)\rangle = \hat{C}^\dagger |0\rangle, \quad (2.89)$$

provides the correction vector and is the numerical challenge of the method. Solving this equation can be done by several different approaches. The Ansatz by Kühner and White [154] solves the real and imaginary part separately. A slight variation of this method is provided by the *dynamical DMRG* [126], where Eq. 2.89 is reformulated into a minimization problem. We will present here a MPS related method, where the equation is solved by local updates of  $\hat{A}$ -matrices. For this purpose we multiply Eq. 2.89 from the left by the conjugated correction vector and obtain

$$\frac{\partial}{\partial A_{a_{i-1}a_i}^{\sigma_i^*}} \left( \langle c(\omega, \eta) | (E_0 + \omega + i\eta - \hat{H}) | c(\omega, \eta) \rangle - \langle c(\omega, \eta) | \hat{C}^\dagger | 0 \rangle \right) = 0, \quad (2.90)$$

which is similar to the equations depicted in Fig. 2.9 and Fig. 2.10. Sweeping through the system updating one matrix after another will finally lead to the correction vector. However, there is a peculiarity, since the operator  $E_0 + \omega - i\eta - \hat{H}$  is non-hermitian<sup>11</sup> and therefore the Lanczos algorithm can not be used to solve the linear equation system. Instead, one uses the GMRES method [188] or the biconjugated gradient method [254, 188]. The initial MPS for  $|c(\omega, \eta)\rangle$  is typically  $\hat{C}|0\rangle$ , which is the only good guess one can make here.

The drawback of this method is that the correction vector for each  $(\omega, k)$ -point, where  $k$  is a global index for all quantum numbers characterizing a state of a system has to be calculated separately. The numerical cost is much higher than in the continued-fraction method, but the precision can be driven to machine precision, in principal.

### Convergence properties of the correction vector method

In this section we briefly examine convergence properties of the correction vector method of a specific model, the one dimensional Hubbard chain. We will not be able to derive completely generic rules out of this, but allows us to mention some of the known peculiarities performing correction vector calculations.

We specifically choose the Hubbard model with open boundaries, whose Hamiltonian reads

$$\hat{H}_{\text{Hub}} = -t \sum_{i\sigma}^{L-1} \left( \hat{c}_{i\sigma}^\dagger \hat{c}_{i+1\sigma} + \hat{c}_{i+1\sigma}^\dagger \hat{c}_{i\sigma} \right) + U \sum_{i=1}^L \hat{n}_{i\uparrow} \hat{n}_{i\downarrow}, \quad (2.91)$$

where  $t$  is the hopping constant,  $\sigma = \uparrow, \downarrow$  the electron spin index,  $L$  the lattice length,  $\hat{c}_i^{(\dagger)}$  the electron annihilation (creation) operator,  $U$  the onsite Coulomb interaction constant and  $\hat{n}_{i\sigma} = \hat{c}_{i\sigma}^\dagger \hat{c}_{i\sigma}$ . We fix  $L = 64$ ,  $t = 1$  and  $U = 1$  and we calculate the ground state  $|0\rangle$  with  $N = 4$  electrons and spin in  $z$ -direction  $S_{\text{tot}}^z = 0$  using a maximal bond dimension of  $D_{\text{gs}} = 140$  states. The truncation error of the converged ground state approximately reached  $10^{-10}$ .

Using the correction vector method, we calculate  $G_{\hat{c}_{k\sigma}}^>(\omega, \eta)$ , where

$$\hat{c}_{k\sigma} = \sqrt{\frac{2}{L+1}} \sum_{i=1}^L \hat{c}_i \sin\left(\frac{ik\pi}{L+1}\right) \quad (2.92)$$

<sup>11</sup>In DMRG calculations  $\eta$  has to be kept finite

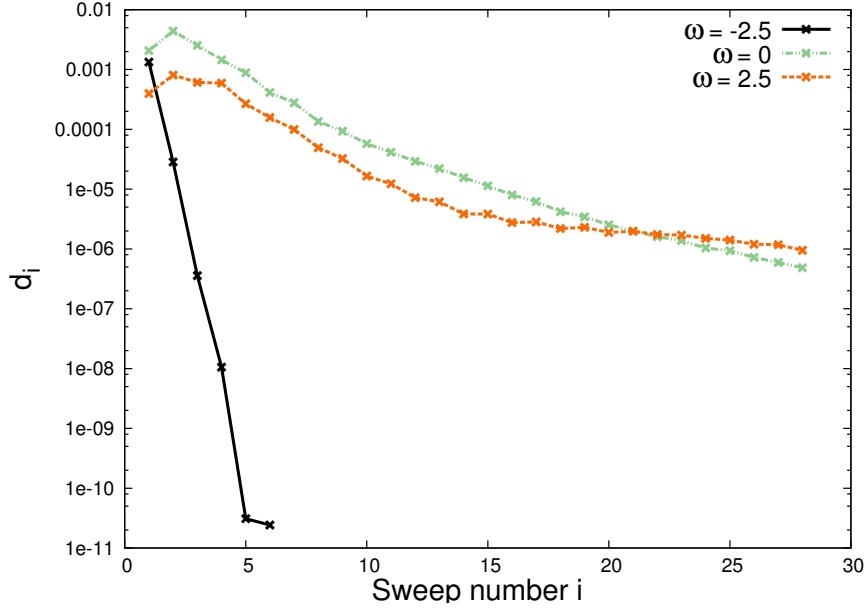


Figure 2.13: Correction vector calculation for a Hubbard model with  $L = 64$ ,  $t = 1$ ,  $U = 1$ ,  $N = 4$  and quasimomentum  $k = 1$  with finite broadening  $\eta = 0.1$  at three different frequencies. The number of used DMRG states during the correction vector calculation is fixed to  $D_{\text{GMRES}} = 500$ . On the y-axis, we plot the relative difference in the overlap of the two wavefunctions of subsequent sweeps.

is the electron annihilation operator in momentum space. For  $U = 0$  the states  $\hat{c}_{k\sigma}^\dagger$  are exact eigenstates of  $\hat{H}_{\text{Hub}}$ . Therefore,  $\hat{c}_{k\sigma}^\dagger|0\rangle$  might be close to an exact eigenstate also for finite  $U$  and  $N \ll L$ .

Calculating  $G_{\hat{c}_{k=1\uparrow}}^>(\omega, \eta = 0.1)$  for many values of  $\omega$ , we find a resonance of the system at  $\omega \approx \omega_1 = -2.5$ . Furthermore, we chose a value on the tail of the resonance at  $\omega_2 = 0$  and an off-resonant value  $\omega_3 = 2.5$ . We restrict our error and convergence analysis to these three points. The accuracy or error of the GMRES calculation is given by the maximal bond dimension  $D_{\text{GMRES}}$  taken into account and therefore the truncation error  $\epsilon_{\text{GMRES}}$ . Here, we determine the quality of the result from the overlap of two wave functions after subsequent sweeps. We define

$$d_{i+1} = |\langle \Psi_{i+1} | \Psi_i \rangle| - |\langle \Psi_i | \Psi_{i-1} \rangle|, \quad (2.93)$$

where  $\Psi_i$  is the wave function after the  $i$ th GMRES sweep. For  $i \rightarrow \infty$  we should find  $d_i \rightarrow 0$ .

For a fixed bond dimension  $D_{\text{GMRES}} = 500$  we find for  $\eta = 0.1$  the convergence behavior as shown in Fig. 2.13. For  $\omega_1$  the correction vector has a relative error of  $10^{-10}$  after the first few sweeps, which is due to the fact that  $\hat{c}_{k\sigma}^\dagger|0\rangle$  is nearly an eigenstate<sup>12</sup> and  $\omega_1$  is close to a resonance. Far off the resonance, the error shrinks much slower and does not converge in the sense that it reaches a fixed point. A criterion for stopping the algorithm would simply be, to preset a threshold, e.g.,  $10^{-7}$ , when reached the algorithm is stopped.

<sup>12</sup>It is not generically the case that  $\hat{c}_{k\sigma}^\dagger|0\rangle$  is close to an eigenstate in a fermionic system, e.g., for large fillings and large  $U$ , or other models, like the Kondo lattice model.

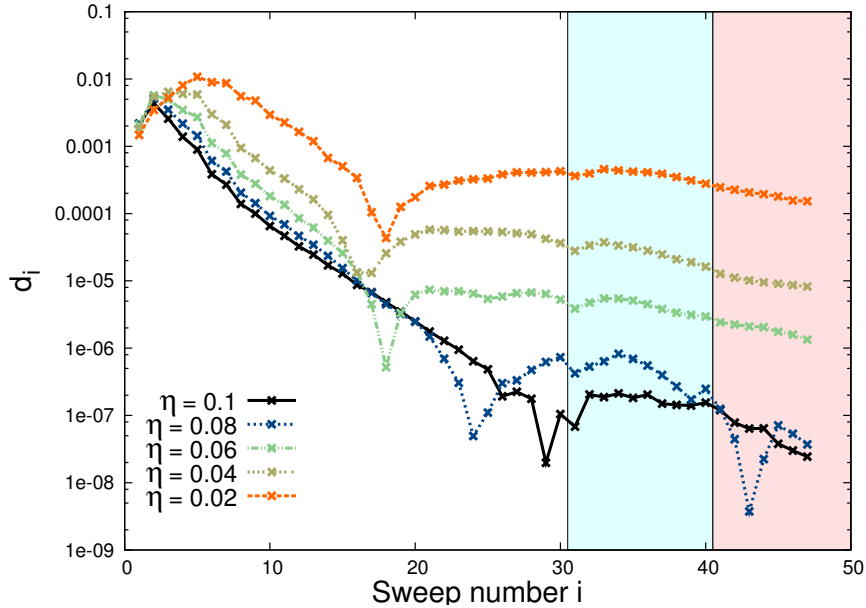


Figure 2.14: Correction vector calculation for a Hubbard model with  $L = 64$ ,  $t = 1$ ,  $U = 1$ ,  $N = 4$  and quasimomentum  $k = 1$  with  $\omega = 0$  and at different finite broadening  $\eta = 0.1$ . The number of used DMRG states during the first 30 sweeps is fixed to  $D_{\text{GMRES}} = 500$  and increased to 750 at sweep 31 (blue region) and increased to 1000 at sweep 41 (red region). On the  $y$ -axis, we plot the relative difference in the overlap of the two wavefunctions of subsequent sweeps.

Not only the frequency  $\omega$  is decisive, but also the magnitude of  $\eta$  has a recognizable influence on the truncation error and convergence properties of the correction vector method. As shown in Fig. 2.14 the change in the overlap  $d_i$  becomes much larger for smaller  $\eta$  at the same number of states and also the truncation error, which is about  $\mathcal{O}(10^{-10})$  for  $\eta = 0.1$  in the last sweep, grows up to approximately  $\mathcal{O}(10^{-8})$  for  $\eta = 0.02$ . Therefore the accuracy of the method sensitively depends on the finite broadening factor  $\eta$  and for smaller  $\eta$  a significantly higher number of states is necessary to reach the same accuracy as for larger  $\eta$ .

For ground state calculations it is beneficial to begin with a small bond dimension  $D$  and increase it in every subsequent sweep until the needed accuracy is achieved, converging the state at the final number of states. However, it is not clear whether this is the procedure of choice for correction vector calculations. In Fig. 2.15 we compare the case of a fixed bond dimension with the one of an increasing bond dimension in the first sweeps. In the blue area the number of states is increased by 50 for the dashed brown line. The solid black line, which represents the calculation at a fixed number of states, approaches the final value much faster. Within the red area, the number of states is in both cases 500, but there is a notable difference between both curves. Therefore, the numerical effort is at least the same, but more likely it is even higher, which is confirmed in [137]. Within this thesis we found the same result for the Kondo lattice model.

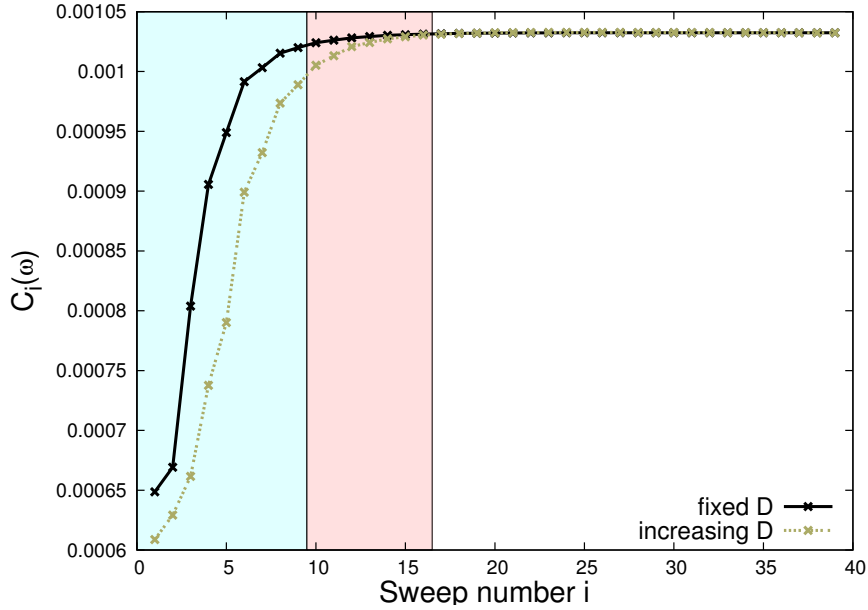


Figure 2.15: Spectral density of a Hubbard model with  $L = 64$ ,  $t = 1$ ,  $U = 1$ ,  $N = 4$  and quasimomentum  $k = 1$  with  $\omega = 0$  and at finite broadening  $\eta = 0.1$ . The solid black line shows the result of a calculation with 500 DMRG states in all sweeps. For the dotted brown line 50 DMRG states are used in the first sweep and in every subsequent sweep the number of states is increased by 50 up to 500. From sweep 10 onwards, the number of states is fixed at 500 states.

### Spectral densities from real-time dynamics and the time prediction method

The calculation of frequency space observables from real-time calculations goes straight forward. First, one performs the time evolution of a state, e.g.,  $\hat{C}|0\rangle$  and then fourier transforms the resulting real-time Greens function to the frequency space. However, time evolution is restricted to finite times and similar to algorithms in frequency space, one has to use efficient methods in order to get reliable data. One of these techniques is the so called *time prediction method* [16] relying on the prediction method introduced early in Refs. [177, 335], which predicts terms  $d_{N+1}, d_{N+2}, \dots$  of a time series from the already calculated terms  $d_0, d_1, \dots, d_N$  at times  $t_0, t_1, \dots, t_N$ .

Assume, we have given the time series  $d_0, d_1, \dots, d_N$  and we make a prediction Ansatz

$$\tilde{d}_n = - \sum_{i=1}^p a_i d_{n-i}. \quad (2.94)$$

This means we assume that  $d_n$  can be predicted from the  $p$  preceding values. From minimizing the least square error  $\sum_{n \in \mathcal{N}_{\text{fit}}} |\tilde{d}_n - d_n|^2$  for known  $d_i$  the coefficients  $a_i$  can be determined and can be used to predict values of the time series  $d_n$  with  $n > N$ . The final Fourier transformation gives much better quality data with time prediction than using an abruptly ending time series.

This method is suited for situations close to equilibrium, where only a few pole frequencies are involved. For strong non-equilibrium cases the method will fail, since too many Greens functions' poles are involved leading to irregular non-predictable behaviour. In [16] the method

is successfully applied to the  $XX$  model in order to compute the observable

$$S(l, t) = \frac{1}{2\pi} \left\langle \left[ \hat{S}_l^-(t), \hat{S}_l^+(0) \right] \right\rangle$$

up to infinite times.



# Chapter 3

## The one-dimensional Kondo lattice model

### 3.1 Introduction

The one-dimensional Kondo lattice model is one of the models in condensed matter physics to describe the interaction of conduction electrons with a lattice of localized impurity spins.

In this chapter we will first derive the Kondo lattice model as a special case of the periodic Anderson model and point out its connection to a general two-band electron model. Then, we discuss the basic physical properties, which contains several exactly solved cases and the phase diagram obtained via bosonization and DMRG. Finally, we describe the application of the Kondo lattice model to real materials. However, the results on the Kondo lattice model obtained in this thesis, see Chapters 4 and 5, are not strictly connected to these applications. Therefore, we give separate introductions to the Kondo lattice model with a special view at the beginning of Chapters 4 and 5.

### 3.2 Derivation of the Kondo lattice model

#### 3.2.1 From the periodic Anderson model to the Kondo lattice model

The Kondo lattice model (KLM) can be derived from the more general periodic Anderson model [298]. The latter describes an electron conduction band with additional local orbitals on each lattice site. For historic reasons we denote these additional orbitals by the term  $f$ -orbitals. The electrons can either move from site to site in the conduction band or hop from one of the lattice sites of the conduction band to the  $f$ -orbital and back. The Hamiltonian of the orbitally non-degenerate periodic Anderson model (PAM) is given by

$$H_{\text{PAM}} = -t \sum_{i\sigma} \left( c_{i\sigma}^\dagger c_{i+1\sigma} + h.c. \right) + \sum_{i\sigma} \varepsilon_f n_{i\sigma}^f + V \sum_{i\sigma} \left( c_{i\sigma}^\dagger f_{i\sigma} + f_{i\sigma}^\dagger c_{i\sigma} \right) + U \sum_i n_{i\uparrow}^f n_{i\downarrow}^f, \quad (3.1)$$

where  $\sigma = \uparrow, \downarrow$  is the spin index,  $n_{i\sigma} = c_{i\sigma}^\dagger c_{i\sigma}$ ,  $n_{i\sigma}^f = f_{i\sigma}^\dagger f_{i\sigma}$ , and the sum  $\sum_i$  is taken over all  $L$  lattice sites. The first term describes the hopping process inside the conduction band,  $\varepsilon_f$  is

the atomic energy of the  $f$  level,  $V$  is the matrix element of the local hybridization between conduction band and local  $f$ -orbital.  $U$  is the Coulomb interaction in the  $f$ -orbital.

The Kondo limit of the PAM is defined as the case, where the energy of the  $f$ -orbital is chosen such that it is occupied by a single electron, and further the Coulomb interaction  $U$  prohibits double occupation in first order processes. This is achieved by choosing

$$\varepsilon_f < \varepsilon_F \quad (3.2)$$

$$\varepsilon_f + U > \varepsilon_F \quad (3.3)$$

$$U \gg V, \quad (3.4)$$

where  $\varepsilon_F$  is the Fermi energy.

Schrieffer and Wolff [263] could show that in the Kondo limit the PAM can be mapped on the Kondo lattice model. Instead of using their result we will use a simple Brillouin-Wigner perturbation theory [243] with the small parameter  $U/V$ . We then involve a simple projection of the Hamiltonian, which is the essential idea of Schrieffer and Wolff. Further, we consider only a single site:

$$H_{\text{eff}} = PH_0P + PH_V \frac{1}{E - H_0} H_V P, \quad (3.5)$$

with  $H_0 = U n_{i\uparrow}^f n_{i\downarrow}^f + \varepsilon_f \sum_{\sigma} f_{\sigma}^{\dagger} f_{\sigma}$  and  $H_V = V \sum_{\sigma} (c_{\sigma}^{\dagger} f_{\sigma} + f_{\sigma}^{\dagger} c_{\sigma})$ . The subspace of the  $f$ -orbital is spanned by the states

$$|0\rangle, |\uparrow\rangle, |\downarrow\rangle, |\uparrow\downarrow\rangle. \quad (3.6)$$

The projector  $P$  is defined as

$$P = |\uparrow\rangle\langle\uparrow| + |\downarrow\rangle\langle\downarrow| \quad (3.7)$$

Making use of

$$S^z = \frac{1}{2} (|\uparrow\rangle\langle\uparrow| - |\downarrow\rangle\langle\downarrow|) \quad (3.8)$$

$$S^+ = |\uparrow\rangle\langle\downarrow| \quad (3.9)$$

$$S^- = |\downarrow\rangle\langle\uparrow|, \quad (3.10)$$

we finally arrive at

$$2V^2 \left( \frac{1}{\varepsilon_f + U} - \frac{1}{\varepsilon_f} \right) (\hat{s} \cdot \hat{S}), \quad (3.11)$$

where  $\hat{s}$  is the conduction electron spin operator and  $\hat{S}$  is the  $f$ -orbital spin operator. Setting

$$J = 2V^2 \left( \frac{1}{\varepsilon_f + U} - \frac{1}{\varepsilon_f} \right) \quad (3.12)$$

and re-introducing the full lattice structure, we obtain the Hamiltonian of the Kondo lattice model

$$H_{\text{KLM}} = -t \sum_{i\sigma} \left( c_{i\sigma}^\dagger c_{i+1\sigma} + h.c. \right) + J \sum_i \hat{s}_i \cdot \hat{S}_i, \quad (3.13)$$

where  $J$  is generally denoted as the *Kondo coupling constant*,  $\hat{s}_i$  is the electron spin operator at site  $i$  and  $\hat{S}_i$  is the spin operator of the localized spin at site  $i$ . Note that  $J$  is in general positive and therefore mediates an antiferromagnetic exchange.

The strong Coulomb interaction limit of the PAM corresponds to the weak coupling limit of the KLM. Nevertheless, we will see that it is interesting to consider not only small  $J$ , but arbitrary  $J$ , see Chapters 4 and 5.

### 3.2.2 Two-band model

The periodic Anderson model and further the Kondo lattice model are special cases of a general lattice with two bands and the electron-electron interaction

$$V = \frac{1}{2} \sum_{n_1, \dots, n_4} \sum_{j_1, \dots, j_4} \sum_{\sigma, \sigma'} V_{\sigma\sigma'}(n_1 j_1, \dots, n_4 j_4) c_{n_1 j_1 \sigma}^\dagger c_{n_2 j_2 \sigma'}^\dagger c_{n_3 j_3 \sigma'} c_{n_4 j_4 \sigma}, \quad (3.14)$$

where  $n_i = c, f$  labels the band the  $j_i$ 's label the lattice site [96]. In order to obtain the Kondo lattice model from this general model one has to make the following assumptions:

1. There is exactly one localized  $f$ -electron at each lattice site, which corresponds to the Kondo limit, see Eqs. 3.2, 3.3 and 3.4.
2. Only on-site interactions are considered, similar to the Hubbard interaction.
3. Electron-electron interactions between electrons in the same band may be neglected.

## 3.3 Exactly solved cases

Up to now the Kondo lattice model with  $J > 0$  refuses to be solved up to a few special cases. It can be solved for only one electron in the conduction band, at half filling of the conduction band and in the strong coupling limit, i.e., for  $J \rightarrow \infty$ .

### 3.3.1 One electron in the conduction band

We consider now the case of only one conduction electron in the conduction band of the KLM for antiferromagnetic exchange  $J > 0$ , see Fig. 3.1. This case has been considered by Sigrist et al. in 1991 [273] and they have been able to determine the exact ground state and some of its properties.

The general basis state of the KLM with one electron is

$$|j, \sigma; \sigma_1 \dots \sigma_L\rangle = \sigma |j, \sigma\rangle \otimes |\sigma_1 \dots \sigma_L\rangle, \quad (3.15)$$

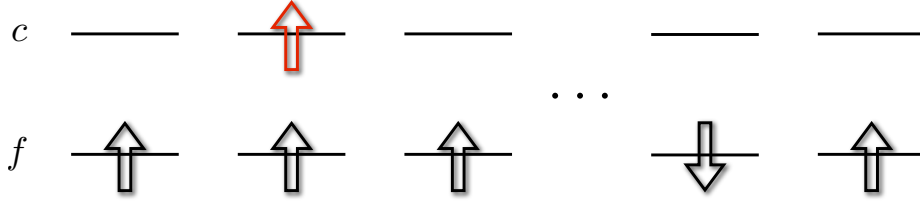


Figure 3.1: The Kondo lattice model with one electron in the conduction band.

where  $|j, \sigma\rangle$  denotes the electron on site  $j$  with spin  $\sigma \in \{\uparrow, \downarrow\}$ , the factor  $\sigma$  is a phase factor, which is used to keep the off-diagonal matrix element negative and is necessary for the applicability of the Perron-Frobenius matrix theorem.  $|\sigma_1 \dots \sigma_L\rangle$  denotes the local spins on sites 1 to  $L$ .

Applying  $H \equiv H_{\text{KLM}}$ , see Eq. 3.13, we obtain

$$H|j, \sigma; \sigma_1 \dots \sigma_L\rangle = -t \sum_a |j+a, \sigma; \sigma_1 \dots \sigma_L\rangle \quad (3.16)$$

$$+ \frac{1}{4} J \sigma \sigma_j |j, \sigma; \sigma_1 \dots \sigma_L\rangle \quad (3.17)$$

$$- \frac{1}{4} J (1 - \sigma \sigma_j) |j, -\sigma; \sigma_1 \dots \sigma_j \dots \sigma_L\rangle. \quad (3.18)$$

The sum  $\sum_a$  is taken over nearest neighbors of  $j$ . Hence,  $\exists n \in \mathbb{N}$  such that  $\langle a | H^n | b \rangle \neq 0$  for two arbitrary basis states  $|a\rangle$  and  $|b\rangle$  and therefore all basis states are connected. This allows the application of the Perron-Frobenius matrix theorem, which states that the lowest energy eigenstate  $|\Psi_g(M)\rangle$  has a strictly positive wavefunction and is non-degenerate.

We will prove the following theorem: *The total spin of the ground state of the KLM with antiferromagnetic coupling between local spins and conduction electrons and with one electron in the conduction band is  $(L-1)/2$ , where  $L$  is the number of lattice sites in the system.*

Since we know that states with different total spin  $S_{\text{tot}}$  are orthogonal to each other, a wave function  $|\Phi\rangle$  with a finite overlap with  $|\Psi_g(M)\rangle$  lives in the same total spin sector. The idea of Sigrist et al. [273] has been to choose an arbitrary wave function  $|\Phi\rangle$  as a superposition of the basis states and to prove that the overlap with  $|\Psi_g(M)\rangle$  is finite:

$$|\Phi(\frac{L-1}{2})\rangle = |j, \uparrow; \downarrow, \uparrow, \dots, \uparrow\rangle + |j, \downarrow; \uparrow, \dots, \uparrow\rangle. \quad (3.19)$$

This state has a Kondo singlet at site 1 and the total spin of this state is  $(L-1)/2$ . Repeatedly applying  $S^-$  on  $|\Phi((L-1)/2)\rangle$  we can construct a wavefunction with a  $z$ -component  $M$  matching the  $z$ -component of  $|\Psi_g(M)\rangle$ . We arrive at

$$|\Phi(M)\rangle = (S^-)^{\frac{L-1}{2}-M} |\Phi(\frac{L-1}{2})\rangle \quad (3.20)$$

$$= \left[ \frac{L-1}{2} - M \right]! \sum_{\sigma_2 + \dots + \sigma_L = M} (|j, \uparrow; \downarrow, \uparrow, \dots, \uparrow\rangle + |j, \downarrow; \uparrow, \dots, \uparrow\rangle). \quad (3.21)$$

This is a strictly positive wavefunction, hence

$$\langle \Phi(M) | \Psi_g(M) \rangle \neq 0 \quad (3.22)$$

and the overlap is finite. Therefore the total spin of the ground state is  $(L-1)/2$ . q.e.d.

With this knowledge we can directly write down the exact wavefunction of the KLM:

$$|\Phi\rangle = \sum_{i=1}^L \left( A^i c_{i\downarrow}^\dagger + \sum_{j=1}^L B^{ij} c_{i\uparrow}^\dagger S_j^- \right) |\text{FM}\rangle, \quad (3.23)$$

where  $|\text{FM}\rangle$  is the state of the KLM where all localized spins are polarized upwards ( $|\uparrow \dots \uparrow\rangle$ ) and the conduction band is empty. The coefficients  $A^i$  and  $B^{ij}$  are still to be determined. Applying the Hamiltonian  $H$  to this state we obtain the equations

$$EA^i = -t \sum_a A^{i+a} - \frac{1}{4} J A^i + \frac{1}{2} J B^{ij} \quad (3.24)$$

$$EB^{ij} = -t \sum_a B^{i+a,j} + \frac{1}{2} J \delta_{ij} A^i - \frac{1}{4} J (2\delta_{ij} - 1) B^{ij}. \quad (3.25)$$

$E$  is the energy of the state. The system of equations can be solved employing a Fourier transformation

$$\tilde{A}^k = \frac{1}{\sqrt{L}} \sum_{j=1}^L A^j e^{-ikj} \quad (3.26)$$

$$\tilde{B}^{kq} = \frac{1}{L} \sum_{j,l=1}^L B^{jl} e^{-ikj} e^{-iq(j-l)}, \quad (3.27)$$

which results in

$$\frac{1}{L} \sum_q \frac{1}{2E_k - \varepsilon_q - J/2} = -\frac{E_k - \varepsilon_k + J/2}{E_k - \varepsilon_k - J/4}, \quad (3.28)$$

where  $E_k$  are the eigenenergies. The coefficients are determined from

$$\tilde{B}^{kq} = -\frac{1}{\sqrt{L}} \frac{E - \varepsilon_1 - J/4}{E - \varepsilon_{k+q} - J/4} \tilde{A}^k \quad (3.29)$$

and the normalization condition  $|\tilde{A}^k|^2 + \sum_q |\tilde{B}^k|^2 = 1$ . Sigrist et al. find in their rigorous analysis that the ground state has spin  $(L-1)/2$  and momentum  $k=0$  and that a *massive spin polaron* is formed, see also Chapter 4.

### 3.3.2 Half filling of the conduction band

The Kondo lattice model at half-filling of the conduction band is believed to be an appropriate model for Kondo insulators [332, 310]. Kondo insulators are semiconductors with a very small gap from hybridization between conduction electrons and  $f$ -orbitals [73, 1]. However, some people doubt that Kondo insulators are in the local moment regime [323, 113] and it is not clear whether one should use the KLM or better the PAM.

Half-filling of the conduction band in the KLM is defined as  $n = N/L = 1$ , where  $N$  is the number of electrons in the conduction band. An important theorem has been proven in [298, 267]: *In any dimension on a bipartite lattice of the KLM, for  $J > 0$ , the unique ground state is a spin singlet. For  $J < 0$ , the same conclusion holds as long as the number of lattice sites is the same on both sub-lattices.* If  $J$  is very large, the model shows a spin gap and the ground state becomes a spin liquid.

Here, we consider only  $J > 0$ . If  $J \rightarrow \infty$  the ground state consists out of  $L$  Kondo singlets, one on each lattice site. The ground state energy is

$$E_{gs,hf} = -\frac{3J}{4}L. \quad (3.30)$$

Two basic excitations are possible. First, a single spin can be flipped, which transforms a Kondo singlet into a triplet and lets the energy increase by  $J$ . Second, a charge can be moved by one lattice site. This will lead to one doubly occupied and one empty site in the conduction band and the now vacant  $f$ -orbitals can either form a singlet or triplet, whose energy is degenerate for  $J = \infty$ . The spin and charge gap found prevails down to  $J \rightarrow 0$ . This has been found from a mapping to the Hubbard model [129], exact diagonalization [296] and DMRG [332]. These numerical calculations have been assisted by approximate analytic methods, like the Gutzwiller-projected mean-field solution [310] and a projection to the non-linear sigma model [299]. For  $J \gg 1$  the gap is linear in  $J$  and for  $0 < J \ll 1$  the gap behaves as  $\Delta E \sim e^{-a/J}$ .

### 3.3.3 Strong coupling limit

The strong coupling limit at partial filling of the conduction band has been widely considered. For  $J \rightarrow \infty$  Kondo singlets will be formed. Two neighboring Kondo singlets will be changed during a hopping process of one of their electrons to an empty and a doubly occupied conduction site. The energy cost of this process is  $3J/2$ . For  $J \rightarrow \infty$  and  $N$  electrons in the conduction band there will be  $L - N$  empty sites, only, and double occupation will be prohibited. This enables one to perform a mapping of the Kondo lattice model in the strong coupling limit on the Hubbard model with  $U = \infty$ . The sites occupied by a Kondo singlet will be mapped to an empty site of the Hubbard model, and empty sites of the Kondo lattice are mapped either to an occupied spin up or spin down electron site of the Hubbard model. Double occupation is forbidden, see Fig. 3.2.

Lacroix [157] has proven this mapping and the corresponding Hubbard Hamiltonian is

$$H_{\text{Hubbard}} = \frac{t}{2} \sum_{i\sigma} \left( \tilde{f}_{i\sigma}^\dagger \tilde{f}_{i+1\sigma} + \text{h.c.} \right) + \frac{3J}{4} \sum_i (1 - n_i) \quad (3.31)$$

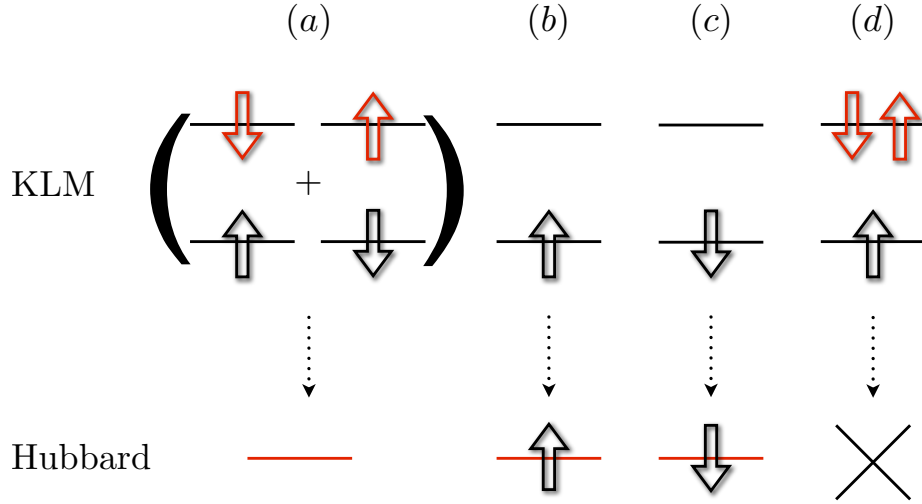


Figure 3.2: Mapping of the Kondo lattice site to the Hubbard site. (a) The Kondo singlet is mapped on the empty site of the Hubbard model. (b) The empty conduction band site with an up local spin is mapped to the Hubbard model with a spin up. (c) The empty conduction band site with a down local spin is mapped to the Hubbard model with a spin down. (d) The doubly occupied conduction band site is mapped out.

under the constriction  $n_i = \sum_{\sigma} \tilde{f}_{i\sigma}^{\dagger} \tilde{f}_{i\sigma} \leq 1$ .

An ordering once given cannot be changed anymore, since the electrons cannot pass each other, because double occupation is forbidden. Furthermore no spin-flips are possible. Spin is totally degenerate and this results in a total independence of spin and charge [209].

A perturbation theory in  $t/J$  [274] has revealed that the degeneracy of the state at  $J \rightarrow \infty$  is lifted to the benefit of the completely polarized state, where all local spins point in one direction and the conduction electron spins in the opposite direction. The total spin of this state is therefore  $S_{\text{tot}} = (L - N)/2$ . This is furthermore the maximal spin possible, because a higher spin value would require a Kondo singlet to be changed to a triplet and this is energetically not affordable due to  $J \rightarrow \infty$ . A true gap in the system is only available if  $J$  is larger than all other singlet excitations.

The KLM with onsite Coulomb interaction in the strong coupling limit has been considered in [328]. In this case it could be shown that the  $f$ -spins are aligned ferromagnetically and that the Hubbard term adds an energy penalty of  $U/2$  to each doubly occupied conduction band site.

### 3.4 Effective interactions

Basically, two regimes with different types of interaction can be distinguished in the KLM. At weak coupling  $J/t \ll 1$  an effective interaction between the localized spins mediated by the conduction electrons dominates the KLM. It is the so called *Ruderman-Kasuya-Yosida (RKKY) interaction* [252, 132, 331]. At strong coupling  $J/t \gg 1$  Kondo singlet formation dominates the KLM.

### 3.4.1 RKKY interaction

For  $J = 0$  the  $f$ -spin system is completely decoupled from the conduction electrons and all possible  $f$ -spin configurations are totally degenerate. In this case, the electrons behave like a non-interacting electron gas doubly occupying all orbitals with  $k < k_F$ . The wave function can be written as a tensor product

$$|\Psi\rangle = |0\rangle \otimes |\sigma\rangle \quad (3.32)$$

$$|\sigma\rangle = \sum_{\sigma_1 \dots \sigma_L} \psi_{\sigma_1 \dots \sigma_L}^\sigma |\sigma_1 \dots \sigma_L\rangle, \quad (3.33)$$

where  $|0\rangle$  is the ground state of the free electron system with  $L$  sites and  $N$  electrons. The degeneracy of the  $f$ -spin system will be lifted perturbatively, if  $J$  is switched on to small values. In a Rayleigh-Schrödinger perturbation theory we find

$$E = E_0 + \langle \Psi | V | \Psi \rangle - \sum_{n \neq 0} \frac{|\langle n, \sigma | V | 0, \sigma \rangle|^2}{E_n - E_0} + \dots, \quad (3.34)$$

where  $V$  is the local interaction between the  $f$ -spins and the conduction electrons and  $|n\rangle$  are the excited states of the non-interacting electron system fulfilling  $H_0|n\rangle = E_n|n\rangle$ . The only non-vanishing matrix elements are generated from  $c_{k\sigma}^\dagger c_{k'\sigma}$  where  $k' < k_F < k$  due to the complete occupation of the electron band up to  $k_F$ . In second order perturbation theory we obtain

$$E = E_0 + \sum_{ij} J_{\text{RKKY}}(i-j) \langle \sigma | \hat{S}_i \cdot \hat{S}_j | \sigma \rangle \quad (3.35)$$

$$J_{\text{RKKY}} = \frac{J^2}{2L^2} \sum_{k' < k_F < k \leq \frac{\pi}{a}} \frac{e^{i(k'-k)(i-j)a}}{\varepsilon(k) - \varepsilon(k')}, \quad (3.36)$$

where  $a$  is the lattice constant. The degeneracy of the  $f$ -spin configurations is now lifted and the local spins take their order such that the energy will be minimized, corresponding to the effective interaction between the local spins, which is given by  $J_{\text{RKKY}}(i-j)$  and is called *RKKY*-interaction.

The summation over the  $k$ -indices is different for different dimensions and one obtains [9]

$$J_{\text{RKKY}}(r) = \begin{cases} \frac{mJ^2}{2\pi} (\text{Si}(2k_F r) - \frac{\pi}{2}) & \text{1D} \\ \frac{mk_F^2 J^2}{8\pi} (J_0(k_F r) Y_0(k_F r) + J_1(k_F r) Y_1(k_F r)) & \text{2D} \\ \frac{mk_F J^2}{16\pi^3 r^3} \left( \cos(2k_F r) - \frac{\sin(2k_F r)}{2k_F r} \right) & \text{3D} \end{cases}, \quad (3.37)$$

where  $r = |i-j|a$  and  $m$  is the electron mass. The special function  $\text{Si}$  is the sine integral function and  $J_n$  and  $Y_n$  are the first and second Bessel functions of order  $n$ , respectively.  $J_{\text{RKKY}}(r)$  for the one dimensional case is shown in Fig. 3.3.

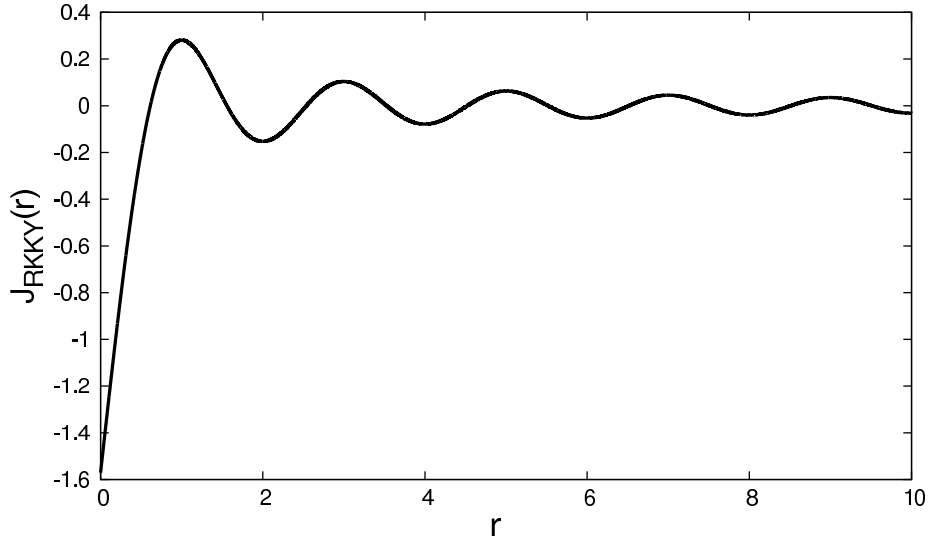


Figure 3.3: RKKY interaction for the one-dimensional case according to Eq. 3.37. We choose  $mJ^2/2\pi = 1$  and  $k_F = \pi/2a$ , which corresponds to quarter-filling of the conduction band. The period of the oscillations is therefore 2.

The characteristic of the RKKY interaction is the determination of the ordering by the wave vector  $2k_F$  in any dimension. In three dimensions the interaction decays proportional to  $1/r^3$ , in two dimensions proportional to  $1/r$ . In one dimension the interaction is divergent, which can be seen from a Fourier transformation:

$$J_{\text{RKKY}}(k) = \frac{1}{2\pi} \int_{-\infty}^{\infty} J_{\text{RKKY}}(r) e^{-ikr} dk \propto \frac{1}{k} \ln \left| \frac{2k_F + k}{2k_F - k} \right|. \quad (3.38)$$

This expression diverges logarithmically for  $k \rightarrow 2k_F$ , which is a typical result if perturbation theory is applied to one-dimensional systems. From this result it is expected that the local spins order according to the wave vector  $2k_F$  RKKY-like for small  $J/t \ll 1$ . For infinite systems the RKKY interaction diverges in one dimension at  $k = 2k_F$ , which demands for other methods than perturbation theory. In a bosonization Ansatz [117] and in a numerical Ansatz using DMRG [197] (see also Chapter 5) the RKKY ordering could be confirmed.

### 3.4.2 Kondo singlet formation

The mechanism of Kondo singlet formation is very important in the strong coupling limit  $J/t \gg 1$  of the KLM. As has been shown by Sigrist et al. [274] in perturbation theory in  $t/J$  the KLM orders ferrmagnetically in this case. The RKKY interaction and the Kondo singlet formation act highly competitively. This interplay leads to a phase transition at intermediate values of  $J/t$ .

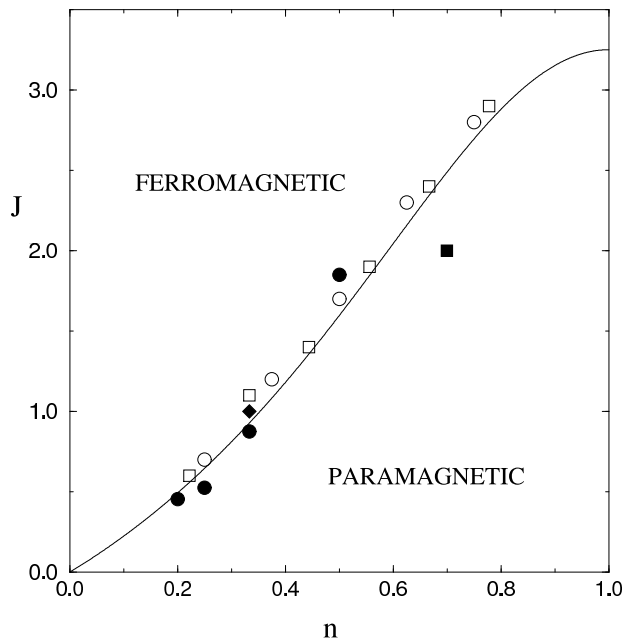


Figure 3.4: Phase diagram as obtained from the bosonization solution taken from [118]. The solid line is the bosonization solution fitted to the numerical data available at that time. The open circles and squares are exact diagonalization data from [297], the solid squares are from a Monte-Carlo calculation in [295] and the solid diamonds and solid circles are DMRG data from [197] and [39], respectively.

## 3.5 Phase diagram

Up to 1997, much effort has been spent to determine the phase diagram of the one dimensional Kondo lattice model, which has been summarized in the review of Tsunetsugu et al. [298]. But only after the press date of [298] a rigorous analytic solution by means of bosonization has been found by Honner and Gulacsi [117, 118]. In the following years, the phase diagram could be justified in extensive numerical DMRG calculations [181, 186, 185].

In this section, we will briefly review the phase diagram obtained by bosonization and then we will compare these results to the numerical DMRG calculations.

### 3.5.1 Phase diagram from bosonization

The bosonization Ansatz [86] provides both the phase diagram of the one dimensional KLM and a non-perturbative explanation of the  $2k_F$  oscillations due to the effective RKKY interaction [117, 118]. The bosonization method transforms the basic fermionic excitations of the non-interacting model to bosonic spin and density excitations. It has to be assumed that the dispersion relation of the conduction electrons can be linearized close to  $k_F$ . Bosonization is only possible for the conduction electrons and not for the  $f$ -spins, because the  $f$ -spins are fully localized and do not move, and therefore provide a vanishing Fermi velocity. One has to keep in mind that bosonization is expected to work well for small and strong coupling  $J/t$ , but not so well for the intermediate coupling regime.

In [117, 118] justified approximations and the assumption that the expectation value of the bosonic fields can be taken as zero as they are for the non-interacting case lead to an effective Hamiltonian

$$\begin{aligned}
H_{\text{eff}} = & - \mathcal{J} \sum_j S_j^z S_{j+1}^z \\
& + A \frac{Ja}{\alpha} \sum_j \{ \cos [K(j)] + \cos [2k_F ja] \} \\
& - A \frac{Ja}{\alpha} \sum_j \{ \sin [K(j)] \sin [2k_F ja] \},
\end{aligned} \tag{3.39}$$

for the KLM, where

$$\mathcal{J} = \frac{J^2 a^2}{2\pi^2 v_F} \int_0^\infty dk \cos(2ka) \Lambda_\alpha^2(k), \tag{3.40}$$

$a$  is the lattice constant and  $A$  is a dimensionless parameter which depends on the cutoff function  $\Lambda_\alpha(k)$ . The cutoff function is necessary to restrict the bosonization to short wave-length  $\alpha \sim \frac{1}{k_F}$ . A typical choice for  $\Lambda_\alpha(k)$  is a gaussian  $\exp(-\alpha^2 k^2/2)$ . The function  $K(j)$  appearing in the second and third term is zero if the ground state is ferromagnetic.

For large  $J$  the first term dominates over the other terms, because it is proportional to  $J^2$ . It causes a ferromagnetic ordering of the local spins, which corresponds to numerical and analytical findings. In the ferromagnetic phase  $K(j) = 0$ , hence, only the second term can destroy the ferromagnetic ordering and close to the phase transition a transverse-field Ising model describes the physics of the Kondo lattice model. The transverse-field Ising model is extensively known [72, 71, 231], especially the phase transition from a ferromagnetic phase to a paramagnetic phase and the corresponding critical coupling constant  $J_c$ . For the KLM one obtains the critical coupling in dependence of the electron filling  $n$ :

$$\frac{J_c}{t} = \frac{8\pi^2 A \sin(\pi n/2)}{\alpha \int_0^\infty dk \cos(ka) \Lambda_\alpha^2(k)}. \tag{3.41}$$

Fitting this function to the numerical data obtained from publications at that time results in the phase diagram shown in Fig. 3.4.

### 3.5.2 Phase diagram from DMRG

The phase diagram of the Kondo lattice model has been calculated numerically using the DMRG method [181, 186, 185] with high precision for a lattice size of 60 sites at partial fillings of the conduction band. This exceeds lattice sizes used in previous numerical calculation using exact diagonalization or less sophisticated DMRG algorithms by a factor of 3 and more. This has been possible due to the exploitation of the  $SU(2) \times SU(2)$  symmetry available in the KLM. The result of this calculation is shown in Fig. 3.5. The bosonization solution nicely fits to the numerical data.

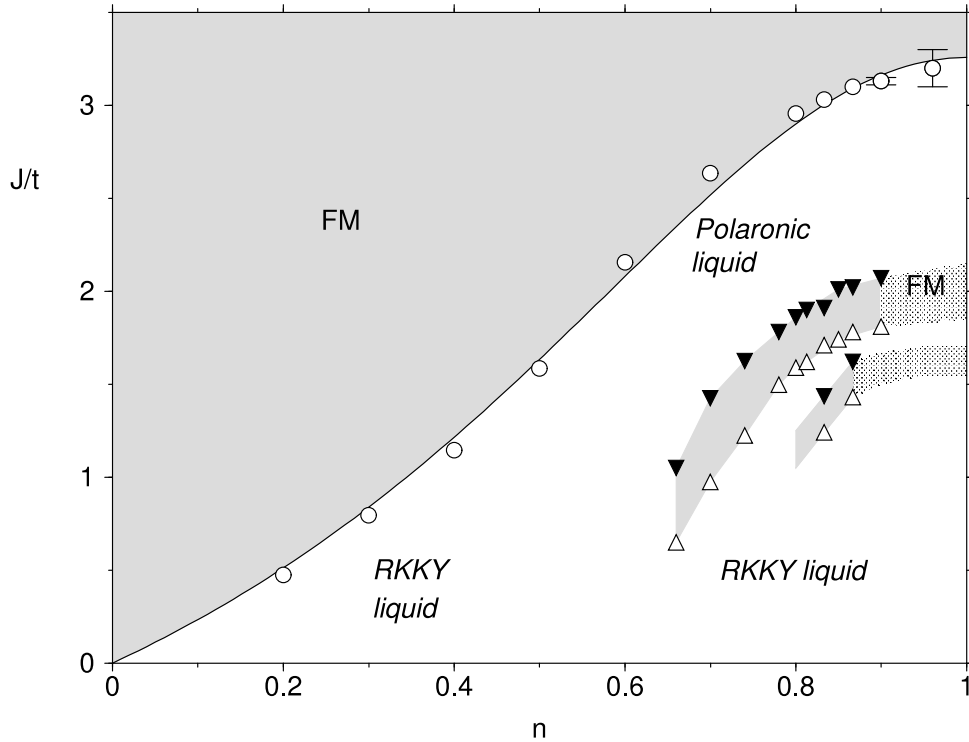


Figure 3.5: Phase diagram obtained from the DMRG calculations in [181, 186, 185]. The solid line is the bosonization solution from [118] fitted to the numerical data.

Furthermore, for intermediate couplings and high fillings additional ferromagnetic phase appear. These additional phases are very weak in the numerical calculations and demand for an extreme numerical precision and accuracy. There are several possible explanations for this:

1. The calculations have been performed on finite size clusters of 60 sites. This introduces finite size gaps in the system, which might result in findings which differ from the thermodynamic limit, even qualitatively.
2. In this regime numerics are highly sensitive to the chosen truncation error due to numerical instabilities. Especially, it is very difficult to achieve energy convergence. Therefore one can not clearly exclude that the appearing ferromagnetic phases resemble an artifact occurring due to finite-size effects and insufficient precision.
3. However, there are some hints that these phases also appear in infinite lattices. From a bosonization [336] approach, where the KLM has been mapped to a sine-Gordon model, it turns out that for non-zero Bose fields such additional phase might appear at intermediate couplings and high fillings. These indications are, however, not clear and it is hard to fit the analytics to the numerics.

However, the phase line separating the ferromagnetic and the paramagnetic phase in Fig. 3.5 is still the most precise calculation performed up to today.

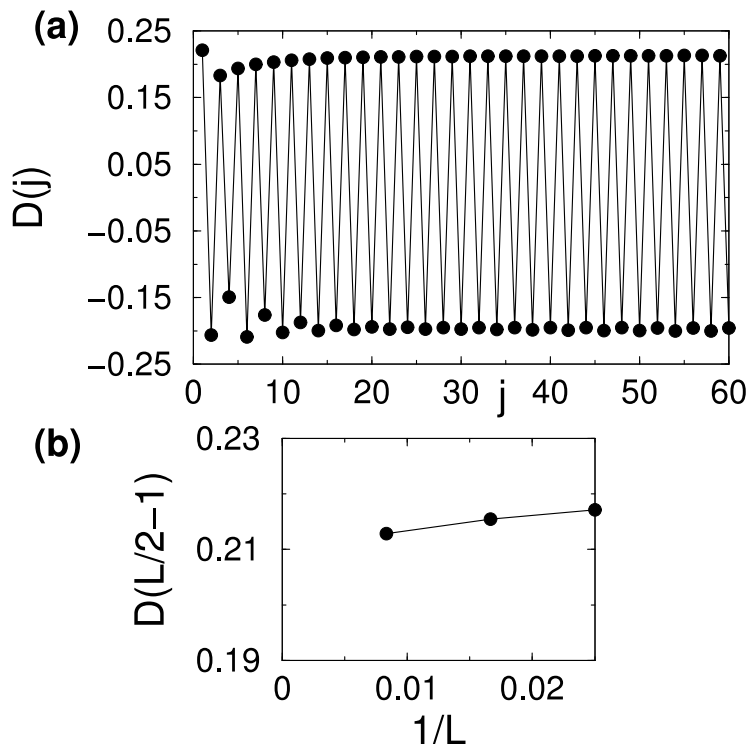


Figure 3.6: (a) The dimer order parameter  $D(j)$  vs lattice site for  $J = 0.5$ ,  $L = 120$  and  $n = 0.5$ . Only half the chain is shown here. (b) Finite-size extrapolation:  $D(L/2 - 1)$  vs  $1/L$  for  $J = 0.5$ ,  $L = 120$  and  $n = 0.5$ . Figure is taken from [327].

### 3.5.3 Quarter filling

The special case of quarter-filling  $n = 1/2$  has been escaped from scientists' attention until 2003, when Xavier et al. [327] performed a DMRG study of the Kondo lattice model at quarter-filling and later confirmed their own results in another high accuracy calculation in [324]. The uniqueness of the filling manifests in the availability of exactly two local spins per conduction electron. Another case where such a matching occurs is at half-filling, where a unique antiferromagnetic phase is found. In [327] a cluster of  $L = 120$  is examined at  $J = 0.5$  and a dimerization phase is found, which is described by the correlation  $D(j) = \langle \hat{S}_j \cdot \hat{S}_{j+1} \rangle$  showing strong oscillations with a period of 2, see Fig. 3.6. Furthermore, this dimerized phase has a charge gap, where there is no charge gap for  $n \neq 0.5$ .

The quarter-filled KLM is believed to describe the quasi one-dimensional organic compounds  $(\text{Per})_2\text{M}(\text{mnt})_2$ , where per stands for perylene, mnt stands for maleonitriledithiolate and M can either be Pd, Pt or Au. These compounds show a metal-insulator transition at a temperature of a few Kelvin [112, 179]. The charge gap found in the dimerized phase provides a suitable mechanism to explain the metal-insulator transition.

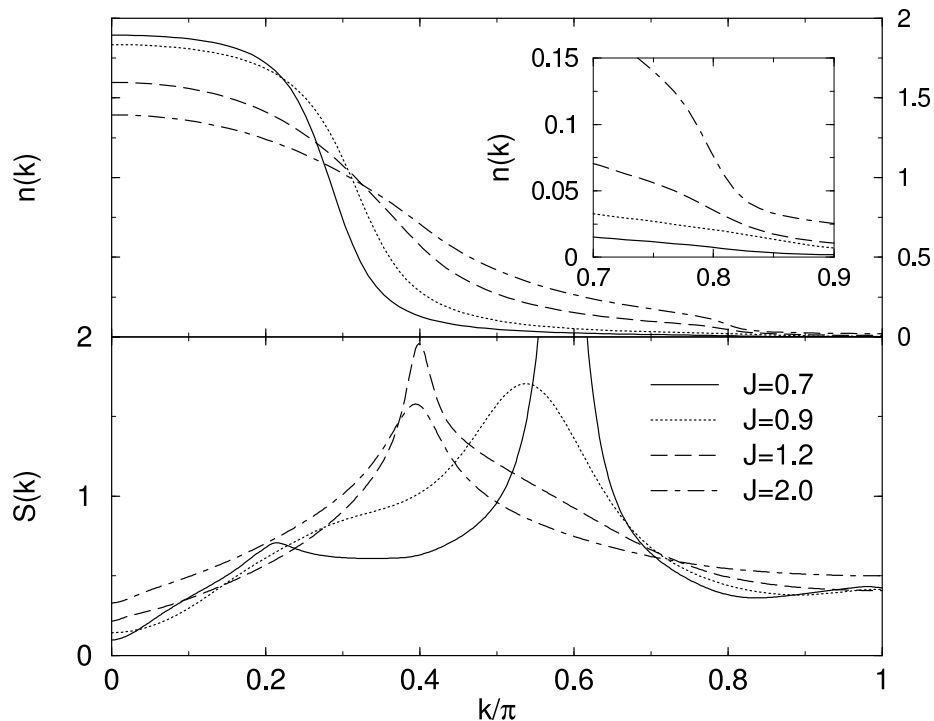


Figure 3.7: The electron momentum distribution  $n(k)$  in the (*upper panel*) and the spin structure factor  $S(k)$  in the (*lower panel*) for  $n = 0.6$ . The picture is taken from [186].

### 3.6 Fermi surface sum rules

The position of the Fermi point<sup>1</sup>  $k_F$  in the KLM has raised many controversial discussions and publications. According to the Luttinger theorem [174] the position of the Fermi point does not change when a coupling constant is changed as long as no phase transition occurs. Luttinger proved his statement perturbatively showing that order by order the corrections to the Fermi volume vanish. However, the prove breaks down, if non-perturbative effects play an essential role, which is the case in most one-dimensional systems.

One would suppose that the Fermi point of the one-dimensional KLM lies at

$$k_{F_{\text{small}}} = \frac{\pi}{2}n, \quad (3.42)$$

which is frequently denoted as the *small Fermi surface*.  $n$  is the filling of the conduction band and therefore only the conduction electrons contribute to the Fermi volume<sup>2</sup>. However, the KLM is derived from the PAM. In the PAM the  $f$ -electrons are not strictly local, even in the Kondo limit and therefore they contribute to the Fermi volume and this raises the question whether the

<sup>1</sup>Strangely, the KLM community frequently uses the term Fermi surface in one dimension, adopted from three dimensions. However, what is meant by Fermi surface in one dimension is the position of the Fermi point  $k_F$ .

<sup>2</sup>Another confusing term adopted from three dimensional systems, which means the position of the Fermi point.

local  $f$ -spins of the KLM contribute to the Fermi volume leading to a *large Fermi surface* with

$$k_{F_{\text{large}}} = \frac{\pi}{2}(n+1) \quad (3.43)$$

and whether the size of the Fermi volume changes when  $J$  is changed. This question is of great interest to the whole condensed matter community since it provides an implicit confirmation or rejection of the validity of the Luttinger theorem in one dimension.

By means of exact diagonalization considering very small clusters it has been stated [297] that the KLM in the weak coupling limit describes a paramagnetic Luttinger liquid with spin and charge correlations at  $2k_F$ , where  $k_F = k_{F_{\text{small}}}$ . Furthermore, in [197] using DMRG and [295] using the Monte-Carlo method for  $n = 0.7$  a small Fermi surface has been found at arbitrary coupling strengths. In a KLM with frustrating next-nearest neighbor interaction [300] a large Fermi surface has been observed raising the question whether this result holds also when this additional interaction has been switched of, since it breaks the  $SO(4)$  invariational symmetry and the bipartite structure of the model. In a refinement of [197] the same authors found again in a DMRG study [198] that an  $f$ - $f$ -spin interaction  $J_H$ , stabilizing the paramagnetic order, leads to a large Fermi surface for large  $J$  in the paramagnetic phase. This result has been extracted from the  $f$ -spin structure factor and the electron momentum distribution. However, small values of  $J$  could not be reached due to numerics. In [271] the DMRG is employed to study Friedel oscillations in the KLM and from their analysis a large Fermi surface could be found for large values of  $J$  in the paramagnetic phase.

It is generally accepted that at  $k_F$  a gap should appear in the electron momentum distribution  $n(k)$  of the conduction electrons. This has been studied by [186], where a transition from a small Fermi surface at small  $J$  to a large Fermi surface at large  $J$  in the paramagnetic phase of the KLM could be identified. The result is shown in Fig. 3.7, where the electron momentum distribution is shown in the upper panel. At the value of the large Fermi surface a kink appears for large  $J$ , while there is no kink for small  $J$ . These results have been confirmed in independent calculations in [326] and later in [17]. Furthermore, these findings give an additional reasoning for the ferromagnetic phases in the large paramagnetic phase, which separate regimes with a different Fermi surface size and therefore conserve the validity of the Luttinger theorem.

### 3.7 Application of the KLM to real materials

Although the focus of applications of the KLM in this thesis, see Chapters 4 and 5, lies not on the field of classical condensed matter, we would like to review briefly the corresponding applications. Systems where conduction electrons interact via a direct spin interaction with localized magnetic moments may possibly be described by the KLM. To this class of systems belong the manganese oxide perovskites on the one hand and the heavy fermion compounds on the other hand. These materials are typically two- or three-dimensional. However, only the one-dimensional KLM is successfully tractable on a theoretical level and it is tried to make predictions from the one-dimensional case for the higher dimensional case. For the future one hopes that methods evolve, which make the higher dimensional KLM tractable.

### 3.7.1 Manganese perovskites

Today, every hard-disc write/reading head makes use of the giant magnetoresistance (GMR) [24], which is necessary to achieve the high data storage densities. Similar to this effect is the colossal magnetoresistance (CMR) [127]. The magnetoresistance is described by

$$\frac{\Delta\rho}{\rho(0,T)} = \frac{\rho(H,T) - \rho(0,T)}{\rho(0,T)}, \quad (3.44)$$

where  $H$  is an externally applied magnetic field,  $T$  is temperature and  $\rho$  is the resistivity. Manganese oxide perovskite show the CMR effect and have the form  $R_{1-x}A_xMnO_3$ , where R can be substituted by the trivalent elements La, Nd or Pr and A by the divalent elements Ca, Sr, Ba, Cd or Pb.

The applicability of the KLM to these perovskites is possible due to the properties of the  $3d$  shell electrons in  $Mn^{3+}$ . In  $RMnO_3$  the triply ionized Mn atoms contain four  $3d$  electrons. In perovskites the  $3d$  band splits and  $Mn^{3+}$  has the following properties: Three electrons occupy the lower three-fold degenerate  $t_{2g}$  orbitals and one of electron occupies the two-fold degenerate delocalized  $e_g$  orbital. Doping of R with A leads to a mixture of  $Mn^{3+}$  and  $Mn^{4+}$  ions. The  $Mn^{3+}$  ions contribute the  $e_g$  electrons which form the delocalized conduction electrons. In the  $Mn^{4+}$  the  $e_g$  electron is missing and a strong Hund's rule coupling forces the  $t_{2g}$  spins to align in the same direction forming localized spins  $3/2$ . The coupling between the localized and the conduction electrons is again via Hund's rule coupling. Therefore, the system can in principle be described by the KLM except for an approximation of the local spins as spin  $1/2$ . However, it turned out that neglecting the coupling to the phonons may lead to predictions wrong by an order of magnitude [193].

### 3.7.2 Heavy fermion compounds

The interesting material class of *heavy fermion compounds* is characterized at low temperature  $T$  by an especially small energy scale of a few tens of Kelvin in the specific heat  $C$  and the spin susceptibility  $\chi$ . The linear coefficients in  $C/T$  and  $\chi/T$  are extremely large, larger by a factor of 100-1000 compared to conventional metals. The Wilson ratio, which is proportional to  $C/\chi$  stays at the order of 1. In a Fermi liquid picture this can be interpreted with a very large effective electron mass  $m^*$ , which is by a factor of 100-1000 larger than the bare electron mass. Therefore, these materials are called heavy fermion materials. The corresponding materials can have very different ground states.  $CeAl_2$  and  $U_2Zn_{17}$  have a magnetically ordered ground state,  $CeCu_2$  and  $UBe_{13}$  have a non-BCS superconducting ground state and  $CeAl_3$  and  $UAl_2$  have an unordered and non-superconducting ground state. The conduction band of these materials is formed by  $s$ -,  $p$ - and  $d$ - orbitals, while the inner  $f$ -orbitals are localized. The two classes of orbitals only weakly hybridize and a strong Hund's rule coupling of  $f$ -electrons on the same site form an effective local  $f$ -spin. This can be modeled either by the PAM or in the Kondo limit of the PAM also by means of the KLM.

# Chapter 4

## Quasiparticles in the Kondo lattice model at partial fillings of the conduction band

In this chapter we review DMRG calculations of ground state and dynamical properties of the Kondo lattice model. The content of this chapter has been published in

*S. Smerat, U. Schollwöck, I. P. McCulloch and H. Schoeller*  
"Quasiparticles in the Kondo lattice model at partial fillings of the conduction band using the density matrix renormalization group"  
*Phys. Rev. B* **79**, 235107 (2009).

The focus in this work lies on the *spin polaron* quasiparticle of the Kondo lattice model. From a careful analysis of the spectral density we find that it has an extraordinarily long life-time.

### 4.1 Introduction

The Kondo lattice model (KLM) has been a matter of constant interest for more than the last three decades. In two and three dimensions it is one of the common models to describe heavy-fermion [48] physics and is also a possible candidate for high- $T_c$  superconductivity.[298] Our motivation to study the one-dimensional KLM [298] is threefold. Firstly it has been shown [244] that the spin polaron, which is a quasiparticle of the KLM, plays an important role in nonequilibrium transport in a quantum wire coupled to a ferromagnetic spin chain; our method provides the possibility to investigate the quasiparticles of the model. The spin polaron might also play an important role in the electron spin decay process [259] in quantum dots induced by the hyperfine interaction due to nuclear spins. Secondly it might be helpful to understand the one-dimensional model in greater detail to assist investigations in higher dimensions. And lastly the model has become interesting for the description of mesoscopic systems, like carbon nanotubes filled with fullerenes or endohedral fullerenes, so called peapods.[149] The aim of this work is to expand on the understanding of the spectral properties of the 1d KLM. We show, by means of the density-matrix renormalization group [317, 261] (DMRG), that persistent quasiparticle states exist, which are likely to be the spin polaron states, and extrapolate their lifetimes and their

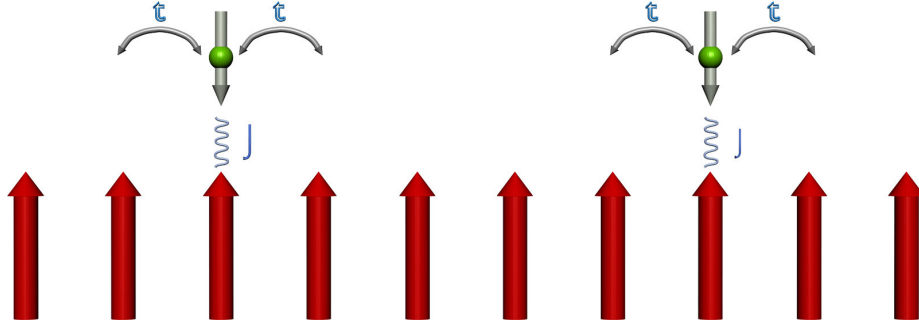


Figure 4.1: (*Color online*) The Kondo lattice model. The conduction electrons are depicted in the upper row (green) and the localized electrons are depicted as bolt arrows in the lower row (red).

spectral weights. Furthermore we calculate the quasiparticle dispersion relation. For the case of half-filling we show that our results qualitatively agree with the results of a strong coupling expansion in Ref. [293]. We compare dispersion relations and confirm the existence of a critical coupling constant at which the effective quasiparticle mass diverges for large momenta.

The KLM (Fig. 4.1) consists of a lattice with one localized f-electron on every of the  $L$  lattice sites, which do not interact with each other and a band of itinerant conduction electrons of finite filling  $n$ , coupled to the localized electrons by an on-site Heisenberg exchange interaction. The Hamilton operator of the 1d KLM is given by

$$H = -t \sum_{i=1}^L \sum_{\sigma=\uparrow,\downarrow} \left( c_{i\sigma}^\dagger c_{i+1\sigma} + \text{h.c.} \right) + J \sum_{i=1}^L \hat{S}_i \cdot \hat{s}_i, \quad (4.1)$$

where  $t$  is the hopping parameter,  $c_{i\sigma}^\dagger$  generates an electron at site  $i$  with spin  $\sigma$  and  $\hat{S}_i$  ( $\hat{s}_i$ ) are the spin operators of the localized (conduction) electrons at site  $i$ , respectively.  $J$  is the Kondo coupling constant; we will consider only  $J > 0$  here, i.e. the antiferromagnetic coupling case. With  $k$  we denote the quasimomentum in the following.

In principle, the 1d KLM supports three phases, depending on the filling  $n$  and on the coupling  $J$ : A ferromagnetic, a paramagnetic and, at half-filling ( $n = 1$ ) only, a spin liquid phase, see Fig. 4.9. At half-filling of the conduction electron band the model is best understood and early works using large- $N$ -methods [240, 241] and the Gutzwiller approximation [245, 246] revealed that the magnetic properties are due to the competition of the RKKY interaction and the formation of Kondo singlets, where such a singlet is a conduction electron forming a spin singlet with a localized electron. Due to half-filling, the electrons induce an effective RKKY interaction between the localized spins, which forces antiferromagnetic power-law correlations in the ground state. The occurrence of RKKY oscillations or  $2k_F$ -oscillations could be confirmed in Ref. [332] using DMRG. By means of exact diagonalization [296] and quantum Monte Carlo [78] it was shown that the ground state is spin- and charge-gapped and that it is a singlet of total spin. Therefore the ground state can be associated for all  $J$  with the universality class of spin liquids. There has been a controversial discussion about the size of the Fermi volume (which is a single line in one dimension), whether it is small and therefore the Fermi wave vector is  $k_F = \frac{\pi}{2}n$  or

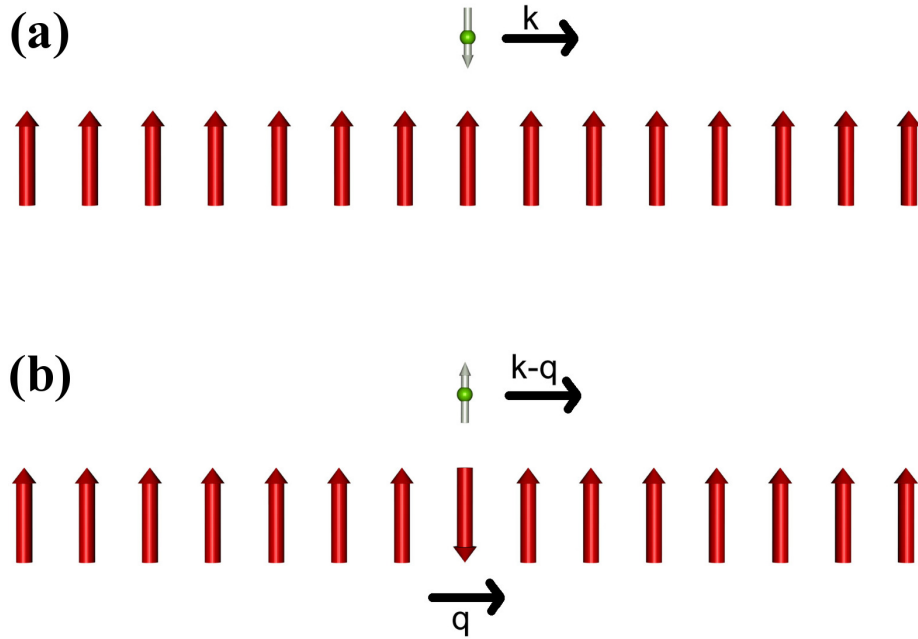


Figure 4.2: (*Color online*) Representatives of the constituent elements of the spin polaron: a) Electron spin down; b) Electron spin up and one of the lattice spins down.

whether it is large and therefore  $k_F = \frac{\pi}{2}(n+1)$ . While a small Fermi volume would correspond to only conduction electrons contributing to the Fermi volume, a large Fermi volume would mean that the localized electrons also contribute to the Fermi volume. The idea of a large Fermi volume is borrowed from the periodic Anderson model.[298] There the f-electrons can move back to the conduction band and therefore contribute to the Fermi volume. The KLM can be derived from the periodic Anderson model [263] in the case of large Coulomb interaction, where only one localized electron per site is allowed and other occupations are fully suppressed. This gives rise to the question whether the Fermi volume is also large in the KLM. Lately the authors of Ref. [293] could argue within a strong coupling expansion and from the evaluation of the conduction electron density that the Fermi volume in the case of half-filling is small. In the same work, Ref. [293], the quasiparticle dynamics of the half filled KLM have been examined as well. It has been possible to calculate the quasiparticle dispersion relation to good accuracy, where the quasiparticle mass has been found to diverge around  $k \approx \pi$  for  $t/J > t/J_c \approx 0.50 \pm 0.02$ . Therefore the quasiparticles behave like nearly localized f-electrons due to the strong correlation of the conduction and localized electrons. This is consistent with an early large-N approach, [241, 298] where it could be shown, that the effective electron mass is by magnitudes larger than the bare electron mass. Although the large-N approach is valid for arbitrary filling its application is best at half-filling due to an intrinsic small energy scale, which can be brought into relation with a spin gap. [298]

In the limiting case of vanishing conduction electron density it could be rigorously shown [273] by both applying the Perron-Frobenius theorem and later exact diagonalization [274] that

the KLM is ferromagnetic for all  $J$ . Importantly, Sigrist et al. [273] could show, that the quasiparticle of the Kondo lattice model is the spin polaron, which corresponds to an excited state separated from a continuum of scattering states. Representatives of the constituent elements of the spin polaron are shown in Fig. 4.2. In Fig. 4.2(a) the localized spin lattice is completely ferromagnetic and the electron spin is oriented in the opposite direction. Due to the antiferromagnetic exchange interaction the electron energy for quasimomentum  $k$  is reduced. Via spin-flip processes, this state is coupled to the states shown in Fig. 4.2(b), where the electron spin and one of the localized spins are flipped and the momentum  $q$  has been transferred to the spin lattice. These are states of higher energy since the antiferromagnetic interaction can only reduce the energy if the two flipped spins are at the same site. The coupling leads to a level repulsion between the states of Fig.4.2(a) and Fig.4.2(b), the energetically lower one corresponding to the spin polaron state and the higher ones forming the scattering states band. As proposed in Ref. [244], the spin polaron state is expected to have a very long lifetime if its energy lies outside the band of scattering states, so that it is protected against magnon absorption and emission processes.

At partial band fillings  $n$ , ferromagnetism also survives in the strong-coupling limit,[274] where the KLM can be mapped to an effective Heisenberg model with a ferromagnetic exchange coupling. In this limit the formation of Kondo singlets, which move through the lattice, is sufficient to explain the occurrence of ferromagnetism, but this does not exclude RKKY interaction, which might still play an important role. From exact diagonalization studies [297] it follows that the KLM is ferromagnetic for  $J \gtrsim 0.5$  at  $n \approx 0.25$ . The critical  $J$  increases roughly linear to  $J \approx 3$  at  $n \approx 0.75$ . This raises the question, which mechanism drives ferromagnetism at couplings  $J$  of  $\mathcal{O}(1)$  and one proposal [117] is that double exchange might be the crucial mechanism, where one conduction electron is responsible for screening several localized electrons. Screening lowers the total energy in the antiferromagnetic KLM as long as  $J$  surmounts a critical value and forces the localized spins to align in the same direction.

At a certain  $J$  the KLM approaches a second order transition [186] by lowering  $J$  to a paramagnetic phase, where the spin polaron [190] might play an important role. The transition line has been calculated using exact diagonalization [297] and has been refined later by means of bosonization.[117] The destruction of the ferromagnetic phase is described by a quantum random transverse-field Ising Hamiltonian.[117] Approaching the transition line from high  $J$  it has been proposed [117, 185] that the large ferromagnetic cluster splits up in several small clusters each corresponding to one spin polaron. Just below the transition line the small clusters' direction of magnetization is not the same anymore for all clusters and leads to zero net magnetization. By means of DMRG the spin structure factor of the localized electrons could be calculated [185] and it has been found that the size of the Fermi volume is small for very low  $J$  and becomes large approaching the transition line from lower  $J$ . From this one can conclude that near the transition line, the localized electrons are incorporated in the Fermi volume and therefore spin polarons are formed. Lowering  $J$  the spin polarons are destroyed. In another proposal [326] using DMRG the size of the Fermi surface for small  $J$  has been calculated from the spin correlation function and found to be small. The corresponding authors find for  $J \gtrsim 1$  that strong boundary charge perturbations mash the true bulk behaviour and therefore a small Fermi surface is not distinguishable from a large Fermi surface. The Fermi surface size is left as an open question. The paramagnetic KLM has also been argued [270] to belong to the class of Tomonaga-Luttinger liquids.[99] This

is motivated by the gapless spin and charge excitation,[298] which also makes the model difficult to handle with numerical methods using finite system sizes in this regime. From an analysis of Friedel oscillations, which are  $2k_F$  or  $4k_F$  oscillations, the Luttinger parameters could be determined for  $J > 1.8$  and the Fermi volume has been found to be large. For very low  $J$ , RKKY or  $2k_F$  oscillations dominate the correlation functions of the KLM. This could be attributed [117] to the backscattering of the conduction electrons at the localized electrons. In a recent work [325] the Luttinger parameter has been calculated for many values of  $J$  and  $n$  in the paramagnetic phase. Using a logarithmic correction the spin correlation function can be fitted perfectly to DMRG data.

In this chapter we consider the spectral properties of the Kondo lattice model at partial band fillings. We will calculate the dispersion relation in the ferromagnetic phase for different Kondo couplings  $J$  and various fillings  $n$  and find a well-defined quasiparticle band. Comparing the one conduction electron case of Ref. [273] with the partial band filling case here, the latter seems to be a direct continuation of the former, meaning that the quasiparticle dispersion relation is found to be similar in both cases. Therefore it is likely that the spin polaron picture used in Ref. [273] suits here as well. We are able to confirm the results of Ref. [293] at half-filling. In a second step we will show from the width of the spectral densities that the lifetime of the spin polaron is very long and therefore the quasiparticle is persistent. We also examine the spectral densities in the paramagnetic phase and find unexpectedly, that a quasiparticle excitation visible in the spectral density, exists and can be fitted reasonably good by a Lorentzian function. It has been argued [117] that this quasiparticle also might be of the spin polaron type. Its lifetime is smaller by several orders of magnitude than in the ferromagnetic phase but the ratio depends very sensitively on the values of  $J$ ,  $n$  and the quasimomentum  $k$ . An interesting effect is found that the lifetime is maximal in the ferromagnetic phase if the quasimomentum is close to the Fermi points.

The chapter is outlined as follows: In section 4.2 we will discuss the method, particularly how we calculate spectral densities, how we extract the lifetimes and how we extrapolate them. In section 4.3 we will present our results. We will end up in a brief summary in section 4.4.

## 4.2 Methods

In this section we describe the methods used in our calculations. First of all we briefly discuss our DMRG algorithm. Secondly we describe the correction vector method, which we use to calculate Green's functions. At last we show how to calculate the lifetime of quasiparticles using the spectral functions we obtained from the Green's functions.

### 4.2.1 DMRG

For the calculation of ground states, we use a *DMRG* algorithm with abelian and non-abelian symmetries, whose implementation is based on a matrix-product formulation (see Ch. 2). We use open boundary conditions for all calculations. We kept up to 1800 DMRG ansatz states in our calculations setting the discarded weight typically smaller than  $10^{-5}$ .

### 4.2.2 Correction vector method

Applying the *correction vector* method as introduced in Sec. 2.2.3 we obtain the spectral functions  $A(\omega)$ , where  $\omega$  is the energy. To calculate  $A(\omega)$ , we need the retarded Green's function  $G_A(\omega + i\eta) = G_A^+(\omega + i\eta) + G_A^-(\omega + i\eta)$ , where

$$G_A^+(\omega + i\eta) = \langle 0 | A^\dagger \frac{1}{\omega + E_0 + i\eta - H} A | 0 \rangle \quad (4.2)$$

$$G_A^-(\omega + i\eta) = \langle 0 | A \frac{1}{\omega - E_0 + i\eta + H} A^\dagger | 0 \rangle \quad (4.3)$$

are the two branches of the retarded Green's function and  $A$  is an arbitrary operator,  $|0\rangle$  is the ground state with energy  $E_0$  and  $\eta > 0$  is an artificial broadening factor, which is needed to lower the lifetime of the excitation to avoid boundary effects due to the finite system size. The basic rule is to choose  $\eta > \frac{c}{L}$ , where  $c$  is the velocity of the excitation, but the minimal  $\eta$  is strongly depending on the model.

In principle one would need to compute both branches of the Green's function to obtain the complete spectral properties. For the determination of life times the spectral weight of the quasiparticle is nearly completely concentrated in one of the branches. Therefore we can neglect the other branch in this case. From now on, we will base all our arguments concerning the Green's function on the  $+$ -branch. Concerning the spectral density the calculations for the  $-$ -branch can be done similarly except for a minus sign.

The correction vector is defined as

$$|c(\omega + i\eta)\rangle = \frac{1}{\omega + E_0 + i\eta - H} A | 0 \rangle \quad (4.4)$$

and hence

$$(\omega + E_0 + i\eta - H) |c(\omega + i\eta)\rangle = A | 0 \rangle, \quad (4.5)$$

where the groundstate  $|0\rangle$  is obtained from the preceding DMRG calculation. This leads to a non-hermitian system of linear equations for real and imaginary parts, which can be solved using the GMRES method [254]. The outcome is  $|c(\omega + i\eta)\rangle$ , which allows to calculate the Green's function as

$$G_A(\omega + i\eta) = \langle 0 | A |c(\omega + i\eta)\rangle. \quad (4.6)$$

The spectral density can then be obtained by applying the standard formula

$$A(\omega + i\eta) = -\frac{1}{\pi} \text{Im} G_A(\omega + i\eta), \quad (4.7)$$

where  $\omega$  is assumed to be real.

### 4.2.3 Quasiparticle lifetime

For the calculation of *quasiparticle lifetimes* we will limit ourselves to electronic systems. It is useful to transform the Hamiltonian into the fourier space according to

$$c_{i\sigma} = \frac{1}{\sqrt{N}} \sum_k c_{k\sigma} e^{ikr_i}. \quad (4.8)$$

Hence we obtain

$$H = \sum_k \sum_{\sigma=\uparrow,\downarrow} \left( \varepsilon_0(k) c_{k\sigma}^\dagger c_{k\sigma} \right) + J \sum_k \hat{S}_k \cdot \hat{s}_{-k} \quad (4.9)$$

with  $\varepsilon_0(k) = -2t \cos ka$ , where  $a$  is the lattice spacing. The one electron Green's function is then defined as

$$G_{k\sigma}(\omega + i\eta) = \langle 0 | c_{k\sigma} \frac{1}{\omega + E_0 + i\eta - H} c_{k\sigma}^\dagger | 0 \rangle. \quad (4.10)$$

The self-energy  $\Sigma_\sigma(k, \omega)$  is implicitly defined for the interacting system  $H$  as

$$G_{k\sigma}(\omega + i\eta) = \frac{1}{\omega + i\eta - (\varepsilon_0(k) - \mu + \Sigma_\sigma(k, \omega + i\eta))},$$

with  $\mu$  the chemical potential. Note that  $\eta$  appears also in the self-energy. This is necessary, because  $\lim_{\eta \rightarrow 0}$  will not be carried out in the numerical calculations. In general, the self-energy is a complex function  $\Sigma_\sigma(k, \omega) = R_\sigma(k, \omega) + iI_\sigma(k, \omega)$ . Separation of real and imaginary part leads to

$$G_{k\sigma}(\omega + i\eta) = \frac{1}{\omega - (\varepsilon_0(k) - \mu + R_\sigma(k, \omega + i\eta)) + i(\eta - I_\sigma(k, \omega + i\eta))}. \quad (4.11)$$

We now assume, that the self-energy is continuous and only weakly depending on  $\omega$  in the vicinity of a resonance  $\omega_{i\sigma} = \varepsilon_0(k) - \mu + R_\sigma(k, \omega)|_{\omega=\omega_{i\sigma}}$ , where  $\omega_{i\sigma}$  is one out of several resonances, which are well separated to provide the correct determination of the lifetime of the quasiparticles (see the end of this section for the explicit extrapolation scheme). In addition we assume  $|I_\sigma(k, \omega)| \ll |\varepsilon_0(k) - \mu + R_\sigma(k, \omega)|$  near to the resonance we are interested in, i.e. we assume long lifetimes, because we are interested in these. This leads to

$$I_\sigma(k, \omega + i\eta) \approx I_\sigma^{(i)}(k), \quad (4.12)$$

in the vicinity of the  $i$ th resonance. For the real part of the self-energy we apply a Taylor expansion at the resonance  $\omega_{i\sigma}$ . We find

$$\begin{aligned} \omega - (\varepsilon_0(k) - \mu + R_\sigma(k, \omega + i\eta)) &\approx \\ \approx (\omega - \omega_{i\sigma}) \left( 1 - \frac{dR_\sigma(k, \omega + i\eta)}{d\omega} \Big|_{\omega+i\eta=\omega_{i\sigma}} \right) - i\eta \frac{dR_\sigma(k, \omega + i\eta)}{d\omega} \Big|_{\omega+i\eta=\omega_{i\sigma}} \end{aligned} \quad (4.13)$$

and define

$$\alpha_{i\sigma} = \left( 1 - \frac{dR_\sigma(k, \omega)}{d\omega} \Big|_{\omega=\omega_{i\sigma}} \right)^{-1}. \quad (4.14)$$

Substituting this to Eq. (4.11) the Green's function in the vicinity of resonance  $\omega_{i\sigma}$  is given by

$$G_{k\sigma}(\omega + i\eta) = \alpha_{i\sigma} \frac{1}{\omega - \omega_{i\sigma} + i \left( \eta + \alpha_{i\sigma} \left| I_\sigma^{(i)}(k) \right| \right)} \quad (4.15)$$

and the spectral function obtains the form

$$A_{k\sigma}(\omega + i\eta) = \sum_i \frac{\alpha_{i\sigma}}{\pi} \frac{\eta + \alpha_{i\sigma} \left| I_\sigma^{(i)}(k) \right|}{(\omega - \omega_{i\sigma})^2 + \left( \eta + \alpha_{i\sigma} \left| I_\sigma^{(i)}(k) \right| \right)^2}, \quad (4.16)$$

which corresponds to a sum of Lorentz distributions at the resonances  $\omega_{i\sigma}$  with a broadening of

$$B^{(i)}(\eta) = \eta + \alpha_{i\sigma} \left| I_\sigma^{(i)}(k) \right|. \quad (4.17)$$

Hence the broadening computed with the correction-vector method is essentially the sum of the natural broadening  $\alpha_{i\sigma} \left| I_\sigma^{(i)}(k) \right|$  and the artificially introduced broadening  $\eta$  and therefore  $B(\eta)$  linearly depends on  $\eta$ . Note that from the Lehmann representation of the spectral density one can find that  $I_\sigma^{(i)}(k) \leq 0$ .

The broadened spectral density  $A_{k\sigma}(\omega + i\eta)$  is a convolution of the non-broadened spectral density  $A_{k\sigma}(\omega)$  with a Lorentzian of width  $\eta$ . We now assume, that the spectral density consists of a sum of Lorentz distributions, which are separated by non-lorentzian regions. The outcome of the convolution of two Lorentzians again is a Lorentzian, where the broadenings behave additively. As the broadening corresponds to an inverse lifetime, we can define the lifetime of the quasiparticle corresponding to the  $i$ th resonance as

$$\tau = \lim_{\eta \rightarrow 0} \frac{1}{\eta + \alpha_{i\sigma} \left| I_\sigma^{(i)}(k) \right|} = \frac{1}{\alpha_{i\sigma} \left| I_\sigma^{(i)}(k) \right|}. \quad (4.18)$$

The limitations of this method are obvious. First of all the excitation must cause a lorentzian shaped peak in the spectral density. To be able to extract the broadening of such a peak all other peaks must be energetically separated from this one. Thus we have to check, whether the conditions of our theory are fulfilled or not. We can check whether the spectral density has a lorentzian shape (see Fig. 4.8) and  $B(\eta)$  has to depend linearly on  $\eta$  (see Fig. 4.3). In eq. (4.12) we only take zeroth order in  $\omega + i\eta$  of the imaginary part of the self-energy into account. The first order leads to a small additional linear  $\eta$ -dependent contribution in  $B(\eta)$  in eq. (4.17), which is the reason for the small finite slope of  $B(\eta) - \eta$  in Fig. 4.3.

We have now two possible estimates for the lifetime of a quasiparticle:

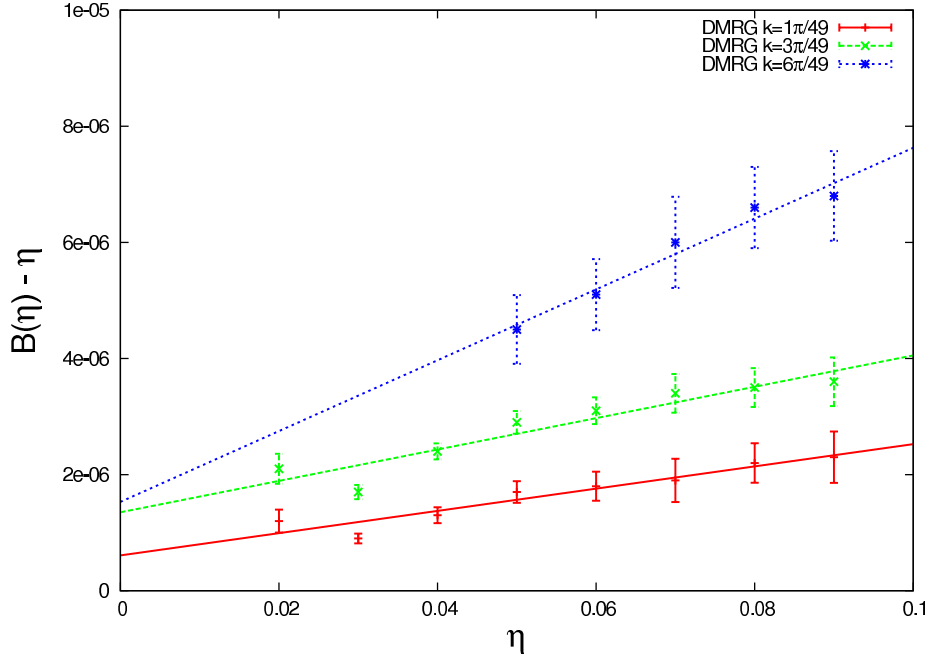


Figure 4.3: (Color online) The linear fit of  $B(\eta)$  vs  $\eta$  is shown for three different quasimomenta, for a system with 48 sites,  $n = 0.125$ ,  $t = 1$  and Kondo coupling  $J = 1$ . The data has been offset by  $\eta$ .

1. Lower estimate: Use the inverse broadening  $B(\eta)^{-1}$  directly (without  $\eta \rightarrow 0$ ). With (4.18)  $B(\eta)^{-1}$  is smaller than  $B(0)^{-1}$ , this is therefore a reliable lower estimate.
2. Extrapolation: Calculate the broadening for several different  $\eta$ . From this one can extract the linear dependence of  $B(\eta)$  on  $\eta$  and  $B(0)^{-1}$  gives the extrapolated lifetime. See also Fig. 4.3.

It turns out that due to long lifetimes only extrapolated lifetimes are meaningful. Therefore in the next section we will discuss the results obtained by the second method only.

From the Lorentzian fit of a single resonance peak of the spectral function in Eq. (4.16) one can also estimate the spectral weight  $\alpha_{i\sigma}$  of the corresponding excitation.

## 4.3 Results

In this section we will present the results obtained using the methods we discussed in the last section. First we will show the calculated dispersion relations considering a Kondo lattice model at half-filling and at partial filling. Our half-filling results show a qualitative agreement with the results in Ref. [293]. In the second part we show several spectral functions and the calculated lifetimes, which leads to the conclusion that we find a bound polaron state. The hopping parameter  $t$  is set to  $t = 1$  in all calculations.

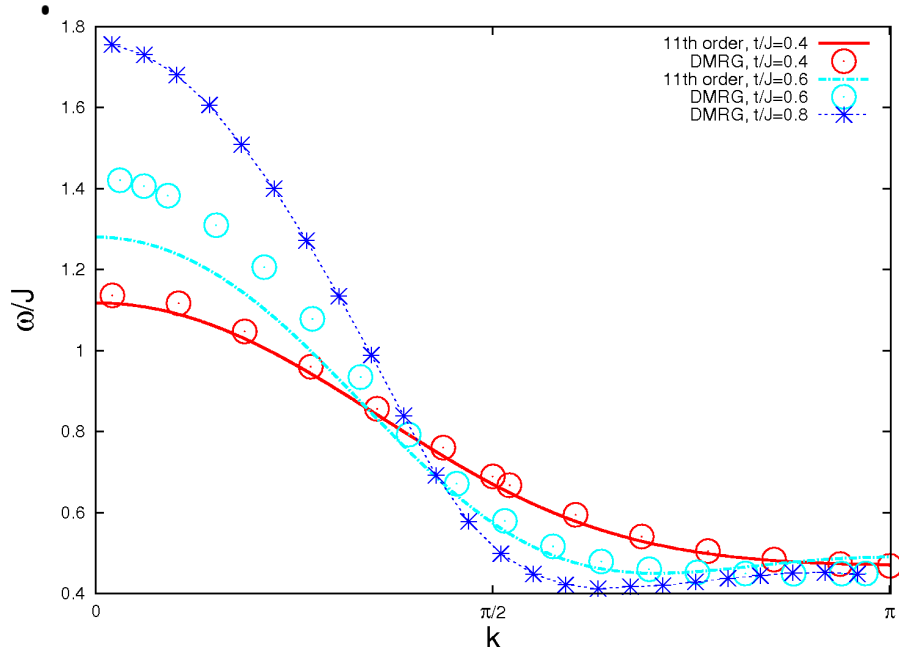


Figure 4.4: (*Color online*) Dispersion relations of the half-filled KLM. The comparison to 11th order perturbation theory is taken from [293]. The line for  $t/J = 0.8$  is meant only as a guide to the eye.

### 4.3.1 Dispersion

The half filled KLM serves as the touchstone of our method, where we can compare our results to those of Trebst et al. [293], who did a strong coupling expansion up to 11th order in  $t/J$ . We calculated the dispersion relation for different values of  $t/J$ , see Fig. 4.4 and used lattice sizes of 32 and 48 sites. The calculations have converged in the sense that we could not find any deviations between calculations of different system sizes. The dispersion relations are a compound of the single spectral densities, or in other words, the dispersion relation can be obtained by glueing all the spectral densities for all values of  $k$  together. Our results show very well agreement to the results in Ref. [293] for  $t/J = 0.4$  with small deviations for small  $k$ . By strong coupling expansion it is found that the band flattens out for  $k \rightarrow \pi$  around  $t/J_c \approx 0.50 \pm 0.02$  and therefore the effective quasiparticle mass diverges. This is also found by DMRG for a higher value of  $t/J_c \approx 0.576 \pm 0.002$ . As one can see, in Fig. 4.4, the strong coupling expansion dispersion relation has a pronounced minimum at  $k \approx 0.7\pi$  for  $t/J = 0.6$ . This minimum is not visible by eyes only in the DMRG data, still it is there at  $k \approx 0.9\pi$ . The minimum becomes easily visible also in the DMRG data for  $t/J = 0.8$  as shown in Fig. 4.4. Summarizing, the DMRG results match very well to the strong coupling expansion for low  $t/J$  but the agreement becomes worse for  $t/J \geq 0.6$ . Qualitatively, the same things happen, but for a larger value of  $t/J$  in the DMRG calculations. DMRG is the more reliable method in that regime, because it is non-perturbative and the error can be easily controlled by very small DMRG truncation errors. In this case it is easy to keep the truncation error reasonably low. We can confirm the physical picture established

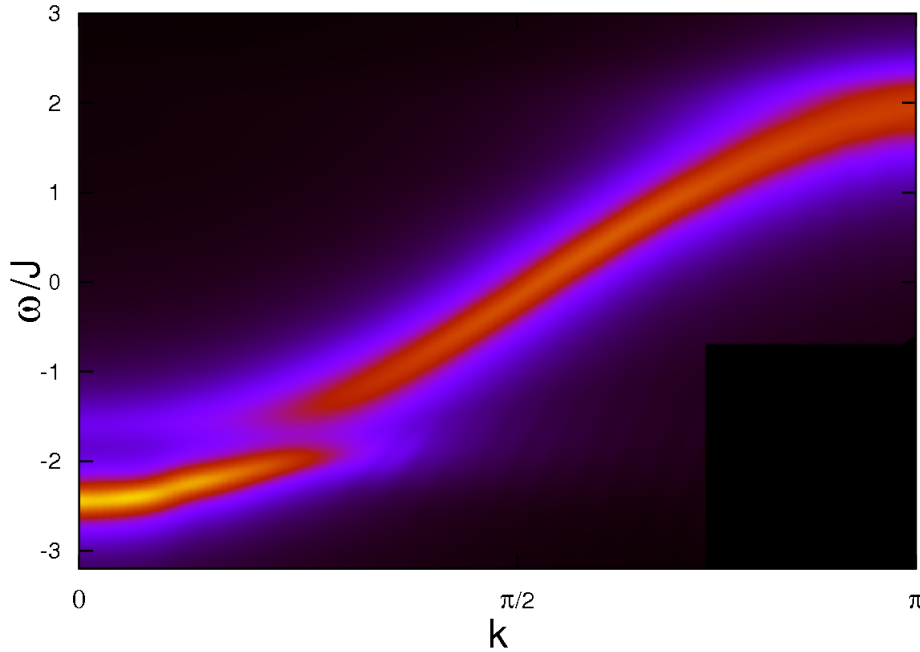


Figure 4.5: (*Color online*) Dispersion of a KLM with 48 Sites,  $n = 0.125$ ,  $J = 1$  and  $t = 1$  compounded of spectral densities for all values of  $k$ . The colorscale corresponds to the height of the spectral density. The broadening is  $\eta = 0.2$ . The lower band is the bound quasiparticles band, while the upper one is the scattering states band.

by Trebst et al., namely that the quasiparticles gain an enormously high mass, which is due to a growing correlation between the conduction and the f-electrons. The quasiparticles with high momenta therefore behave like almost localized f-electrons.

Now we consider the dispersion relation of the KLM for partial band filling, see Fig. 4.5. For the ground state calculation of the KLM with 48 sites, a filling of  $n = 0.125$  and  $J = 1$  we used about 100 DMRG ansatz states. The calculation of the correction vectors needed 800 DMRG states to reach good convergence. In Fig. 4.5 and all other figures of dispersion relations we neglected the chemical potential, which would shift the lower band edge to nearly zero. One can distinguish two different bands. The higher one behaves like  $-2t \cos k$  (up to a constant offset) and can therefore be attributed to free electrons, which do not form bound states with the localized spins. From now on, this band will be referred to as the *scattering states band* in the sense that these excited states rapidly decay. The lower one of the two bands represents the states of the system which are formed by the conduction electrons bound to the localized spins, from now on referred to as *quasiparticle or Spin-polaron band*. Contrary to the scattering states band this band consists only of one state, which is separated from the continuum (for large  $L$ , where  $L$  is the lattice size) of scattering states and has a Lorentzian shape from which the lifetime can be extracted, which is very long in most of the cases, see Sec. 4.3.2. Even on lowering  $\eta$  the excitation peak does not differ from its Lorentzian shape, therefore we can be sure that only one excitational state can be responsible for this. In contrast to the Spin-polaron band the scattering states band does not change its width linearly with  $\eta$ . Keeping

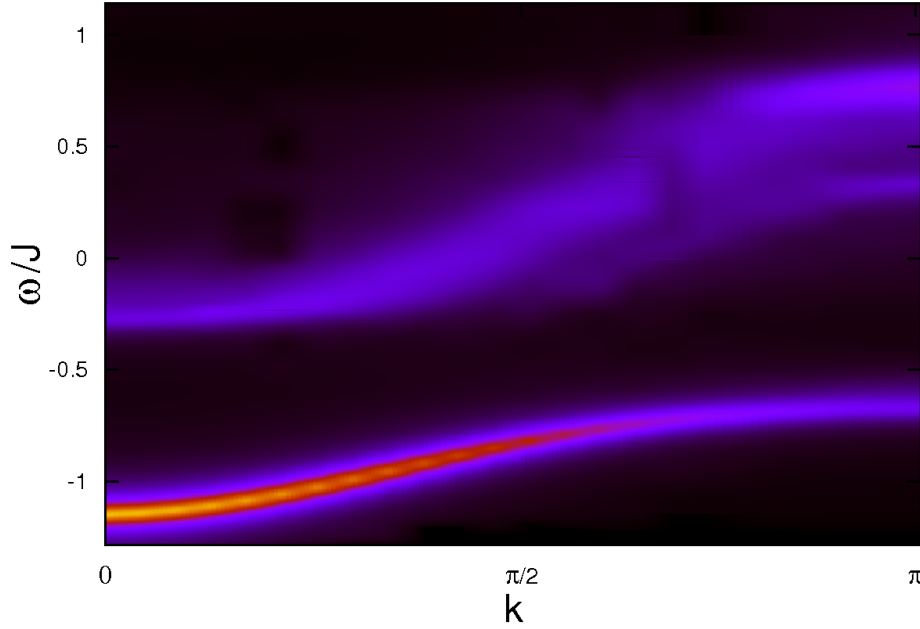


Figure 4.6: (*Color online*) Dispersion relation (as in Fig. 4.5) of a KLM with  $n = 0.125$ ,  $J = 3.5$  and  $t = 1$ . The lower band is the bound quasiparticles band, while the upper one is the scattering states band.

the same filling  $n = 0.125$ , but raising the Kondo coupling constant  $J$  to 3.5, see Fig. 4.6, the quasiparticle band becomes more separated from the scattering states, because the quasiparticle state is now energetically lowered. This can be understood by a simple physical picture. For that we rewrite the exchange coupling of the Hamiltonian as  $\sum_i^L \left[ J^z S_i^z s_i^z + \frac{J_\perp}{2} (S_i^+ s_i^- + S_i^- s_i^+) \right]$  and we now set  $J_\perp = 0$ . The quasiparticle state of the KLM almost only consist of an electron with spin antiparallel to the localized spins. With respect to our modified exchange coupling this results in a lowered energy of  $J^z/4$  per electron. The scattering states also contain important contributions with an electron spin oriented parallel to the localized spins. This leads to a higher energy of  $J^z/4$ . Therefore the energy difference between quasiparticle and scattering states is  $J^z/2$  and scales with  $J^z$ . Taking also a finite  $J_\perp$  into account the quasiparticle energy is even lowered more due to spin flip processes. The scattering states band has a similar shape as before, as expected. The weight of the quasiparticle states band is also increasing with  $J$ . This is also expected, because the state becomes energetically more favorable with increasing  $J$ .

In Fig. 4.7 we show the dispersion relation of the quasiparticle of a system with  $J = 3.5$  for three different fillings,  $n = 0.125$ ,  $n = 0.25$  and  $n = 0.75$ . The ground state is ferromagnetic in all cases. We conclude that even in the presence of many electrons the spin polaron state can be clearly identified.

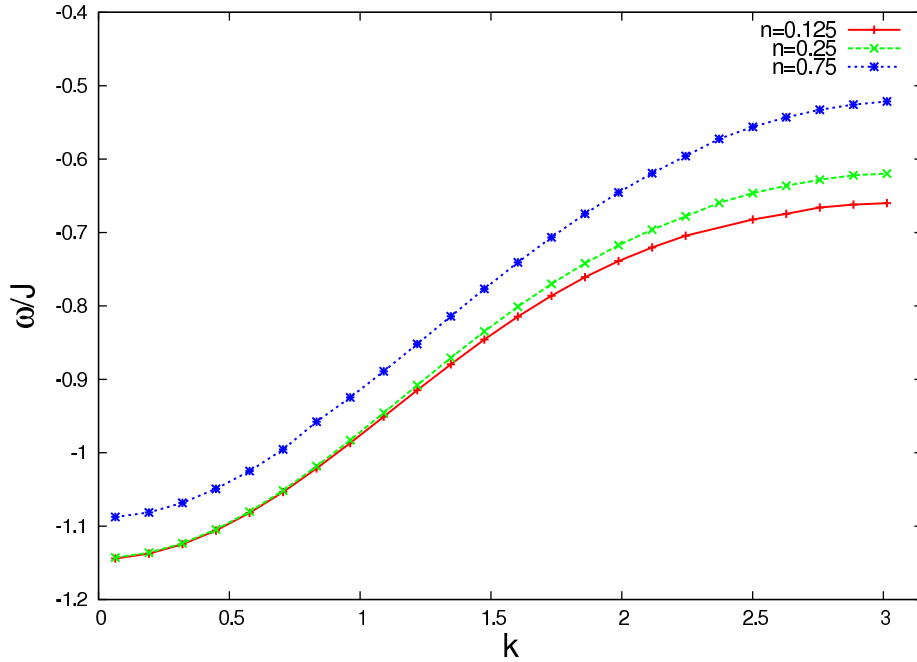


Figure 4.7: (Color online) Dispersion relations of a KLM with  $J = 3.5$ ,  $t = 1$  and three different fillings,  $n = 0.125$ ,  $n = 0.25$ , and  $n = 0.75$  extracted of the spectral densities.

### 4.3.2 Life time estimations from spectral functions

In a further step we take a look at single spectral densities for fixed quasimomentum  $k$ , which provides the possibility to calculate quasiparticle lifetimes of the bound quasiparticles and prove the existence of bound polaron states. We consider only the calculation of the extrapolated lifetimes, as described in section 4.2.3 and whose extrapolation scheme is shown in Fig. 4.3. Calculating extrapolated lifetimes this way we have to be very careful due to the assumption that the spectral density complies a lorentzian distribution. For the spectral density being a lorentzian the imaginary part of the self-energy has to be very small compared to the energy of the resonance and it should not vary too much in the vicinity of the resonance. The expansion of the self energy leads then to a lorentzian function. Thus the spectral density is not lorentzian shaped in higher orders of the expansion and it has to be checked, see for example Fig. 4.8, whether it is good enough. Fig. 4.8 shows a spectral density for a KLM with 48 Sites,  $n = 0.125$ ,  $J = 1$  and quasimomentum  $k = \frac{\pi}{49}$ . The artificial broadening is set to  $\eta = 0.02$ . The number of data points obtained provides the possibility of a very precise fit of the lorentz distribution. Fig. 4.8 sharply supports the assumption made in sec. 4.2.3 that the spectral density has a lorentzian shape, which is necessary to calculate quasiparticle lifetimes.

We would like to make a comment concerning the lifetimes in the paramagnetic phase, which is supposed to be of Luttinger liquid type. In a Luttinger liquid we would not expect to have well defined quasiparticles. Therefore the approximation of Lorentzian shaped excitations in the spectral density is crude in the paramagnetic regime of the KLM. Then it is even more surprising

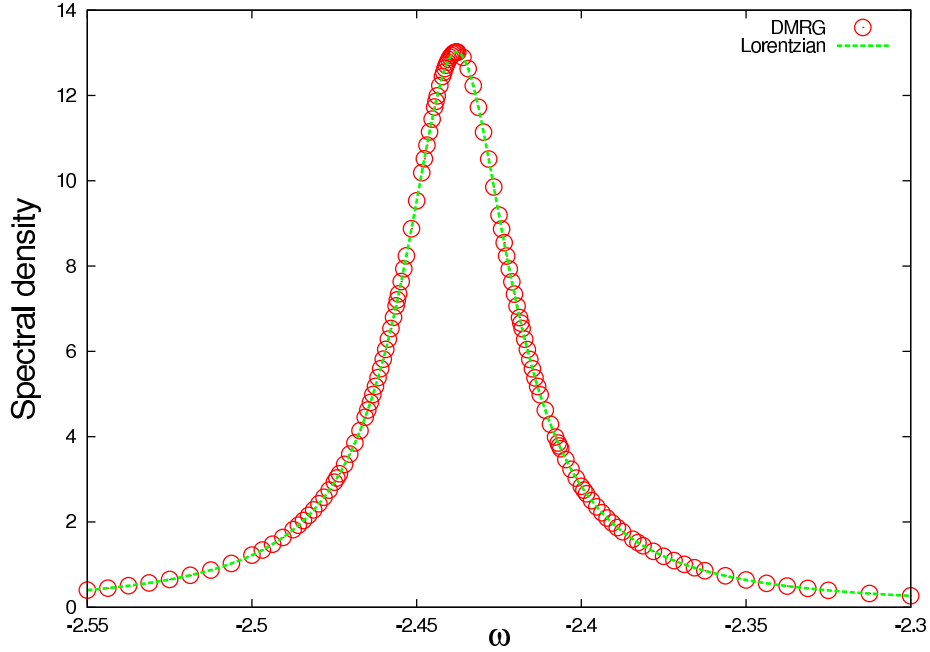


Figure 4.8: (*Color online*) Spectral function of a KLM with 48 Sites,  $n = 0.125$ ,  $J = 1$ ,  $t = 1$ ,  $k = \frac{\pi}{49}$  and  $\eta = 0.02$ . The green line is obtained by fitting a Lorentzian to the DMRG data.

that this approximation fits the DMRG data relatively well. But we also find that those excitations in the paramagnetic phase decay fast compared to the ferromagnetic phase (where we do not expect a Luttinger liquid, because of a finite spin gap) and this would be expected.

The extrapolated lifetimes are summarized in Fig. 4.9 and Tab. 4.1. There we can see, that the lifetime strongly depends on the parameters filling  $n$  and Kondo coupling constant  $J$  as well as on the quasimomentum  $k$ . The lifetimes in the ferromagnetic phase (this concerns the  $[n, J]$ -pairs  $\{[0.125, 0.5], [0.125, 1], [0.25, 1], [0.29, 1], [0.75, 3.5]\}$ ) decrease by approaching the paramagnetic phase by either lowering  $J$  or increasing  $n$ . For fixed and low quasimomentum  $k$  it seems that the lifetime decreases by increasing  $n$  (even if  $J$  is increased at the same time so that the distance to the paramagnetic phase is still large, compare e.g. the pairs  $[0.125, 1]$  and  $[0.75, 3.5]$ ). This indicates that the lifetime is influenced by the presence of other quasiparticles, probably by an effective interaction between the quasiparticles mediated via the coupling to the localized spins. This is further substantiated by the dependence of the quasiparticle lifetime on the quasimomentum  $k$  in the ferromagnetic phase. For  $k$  approaching the Fermi level, the lifetime increases, which is consistent with the fact that the phase space for quasiparticle interaction becomes smaller close to the Fermi level. In contrast, electron-magnon interaction is expected to be more important for quasiparticles close to the Fermi-level because the energy of the spin polaron comes closer to the scattering band. This effect can be seen in the paramagnetic phase for the pairs  $[0.375, 0.5]$  and  $[0.75, 2.5]$ , where the lifetime decreases with increasing quasimomentum. Thus, in the paramagnetic phase, we conclude that electron-magnon interaction limits the lifetime of the spin polaron. Deep inside the paramagnetic phase at  $[n = 0.375, J = 0.5]$  the

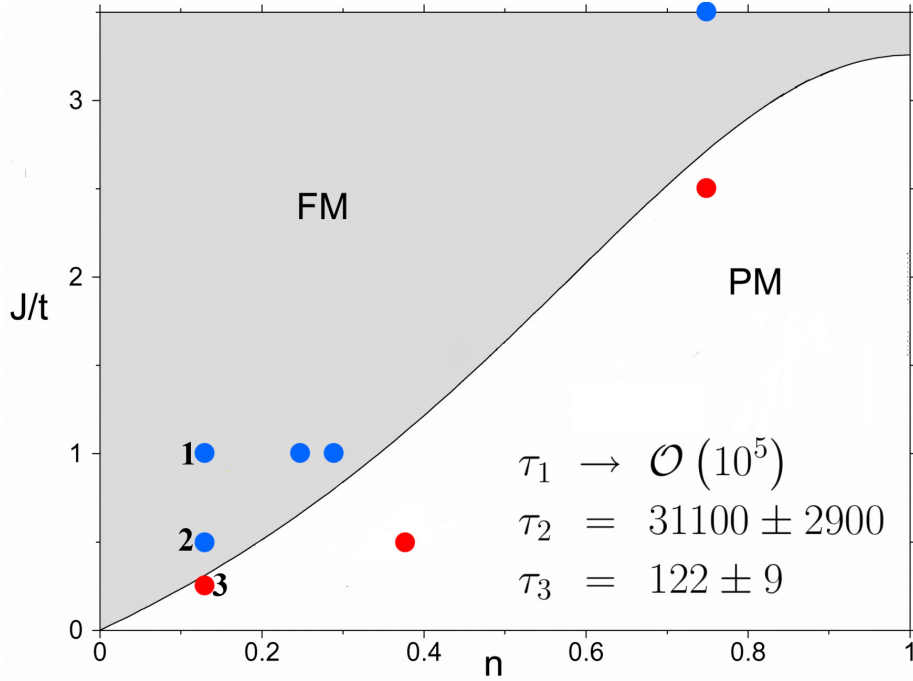


Figure 4.9: (*Color online*) Simplified phase diagram of the 1D Kondo lattice model taken from [185]. The points mark the parameters at which extrapolated lifetimes have been calculated. The lifetimes for points 1 ( $J = 1$ ), 2 ( $J = 0.5$ ) and 3 ( $J = 0.25$ ) and quasimomentum  $k = \frac{\pi}{49}$  are given directly in the picture by  $\tau_1$ ,  $\tau_2$  and  $\tau_3$ , the lifetimes for the other points are listed in tab. 4.1

lifetime is short for all determined values of  $k$ . Therefore, as predicted earlier in Refs. [117, 186] there exist no persistent quasiparticles in this regime.

We also extracted the spectral weight of the spin polaron excitation from the Lorentzian fit and summarized them in Tab. 4.1 in the second row of the respective  $k$  value. Considering the three numbered points of Fig. 4.9 we calculated the spectral weights

1.  $0.818004 \pm 0.000001$

2.  $0.87119 \pm 0.00003$

3.  $0.588 \pm 0.001$ ,

which do fulfill the expectation that the spectral weight should be significantly lower in the paramagnetic phase. The calculated weights are independent of  $\eta$  within the error bounds. They show a strong dependence on the quasimomentum (decreasing for growing  $k$ ) in the ferromagnetic as well as in the paramagnetic phase. This is expected because the spin polaron states with higher value of  $k$  have higher energy and come closer to the scattering states. However, it is unexpected that the spectral weight is large for  $[0.375, 0.5]$  and this still has to be explained.

## 66 4. Quasiparticles in the Kondo lattice model at partial fillings of the conduction band

Table 4.1: Summarization of extrapolated lifetimes (first row of the respective  $k$  value) and spectral weight of the spin polaron excitation (second row of the respective  $k$  value) for different fillings of the system, different coupling constants and different quasimomenta. The  $k$  values in paranthesis correspond to  $[0.75, 2.5]$ , only.

$k \backslash [n, J]$	$[0.25, 1]$ (fm)	$[0.29, 1]$ (fm)	$[0.375, 0.5]$ (pm)	$[0.75, 3.5]$ (fm)	$[0.75, 2.5]$ (pm)
$\frac{1\pi}{49} \left( \frac{1\pi}{33} \right)$	$831 \pm 16$	$183 \pm 3$	$67 \pm 9$	$38.6 \pm 0.8$	$25.7 \pm 1.6$
	$0.8211 \pm 0.0004$	$0.8292 \pm 0.0008$	$0.951 \pm 0.006$	$0.714 \pm 0.008$	$0.674 \pm 0.005$
$\frac{3\pi}{49}$	$2540 \pm 84$				
$\frac{8\pi}{49}$			$14.7 \pm 1.5$		
			$0.82 \pm 0.01$		
$\frac{11\pi}{49}$	$\mathcal{O}(10^5)$	$2850 \pm 600$			
	$0.6244 \pm 0.0001$	$0.6375 \pm 0.0005$			
$\frac{18\pi}{49} \left( \frac{12\pi}{33} \right)$				$\mathcal{O}(10^3)$	$5.29 \pm 0.14$
				$0.5580 \pm 0.0008$	$0.3391 \pm 0.0005$
$\frac{36\pi}{49} \left( \frac{24\pi}{33} \right)$				$\mathcal{O}(10^3)$	$12.76 \pm 0.62$
				$0.3391 \pm 0.0005$	$0.190 \pm 0.006$

### 4.4 Summary

In this chapter, we have studied the one-dimensional Kondo lattice model at half-filling and at partial band fillings for various Kondo couplings  $J$ . At half-filling we could verify the results of Ref. [293]. This includes the dispersion relation and the divergence in the effective quasiparticle mass. At partial band fillings we were able to show that in the case of ferromagnetism long living quasiparticle states exist and we have suggested that these are spin polaron quasiparticles as used in Ref. [273]. The lifetime exceeds the lifetime of quasiparticle excitations deep inside the paramagnetic phase by several orders of magnitude. From the dependence on the quasimomentum we conclude that the dominant decay process is the spin polaron-spin polaron interaction in the ferromagnetic phase, and the interaction between electrons and spin waves in the paramagnetic phase. The weight of the spin polaron state is very close to one even for special points in the paramagnetic phase. The results motivate the speculation that spin coherence can be significantly enhanced by coupling of electrons to magnons in the ferromagnetic phase of the localized spins. Even if the localized spins have a negligible exchange interaction, the itinerant electrons can mediate an effective exchange interaction (long ranged RKKY), which drives the local spins into a ferromagnetic like state due to long range correlations at low enough temperatures (the temperature, below which the long range correlations lead to a ferromagnetic like ordering, has been estimated recently for the two dimensional KLM and is within experimental reach.[276, 33] For a one dimensional Kondo lattice formulation with large localized spins it could be shown, that long range correlations lead to a helical ordered like state persisting to the experimentally reachable temperature regime [34].) As we have seen in this chapter, the spin excitations in the ferromagnetic phase can in turn form spin polaron bound states with the itinerant electrons, increasing their lifetime considerably. This effect persists in the presence of many electrons and becomes more efficient for quasimomenta close to the Fermi level. It is an interesting question for future research to investigate the consequences for the spin relaxation and dephasing rates in the Kondo lattice model by studying the spin-spin correlation functions.

# Chapter 5

## Coulomb interaction effects and electron spin relaxation in the 1d KLM

In this chapter we calculate ground state properties of the Kondo lattice model with onsite and nearest neighbor Coulomb interaction. Furthermore, we examine the spin life-time in dependence of the electron filling, the Kondo coupling and onsite Coulomb interaction. The content of this chapter has been published in

*S. Smerat, H. Schoeller, I. P. McCulloch and U. Schollwöck*  
"Coulomb interaction effects and electron spin relaxation in the 1d Kondo lattice model"  
*accepted by Phys. Rev. B (2011).*

The focus of this chapter lies on the applicability of the Kondo lattice model to real nano-devices, like carbon nanotube peapod systems, see e.g. Chapter 7, which is manifested in the explicit consideration of finite lattice length.

### 5.1 Introduction

Recently, the interest in nanoscale systems has been rapidly increasing. Among them are  $^{13}\text{C}$  carbon nanotubes, [45, 34] nanowires [244, 248] and carbon nanotubes filled with endohedral fullerenes or molecular magnets [149]. The above mentioned systems have in common, that they consist of local spins (electron or nuclear spins) which interact via exchange interaction with itinerant conduction electrons. These are exactly the constituents of the one dimensional Kondo lattice model [263, 298] (*KLM*). To make these materials available for spin electronics or quantum information processing it is necessary to understand their properties in detail: ground state (e.g. magnetic order), spectral (e.g. dispersion relation of electrons) and dynamical (e.g. non-equilibrium, spin relaxation/decoherence) properties.

Interaction between the local spins in the KLM is generated effectively due to the hopping  $t$  of electrons and an onsite direct spin exchange  $J$  between the itinerant and localized spins, see Fig. 5.1. This interaction is a result of the competition of onsite singlet formation and an effective RKKY (Ruderman-Kittel-Kasuya-Yosida) interaction [252]. The order of the local spins due to

the interaction is captured in the phase diagram of the KLM, [297, 298, 117, 185, 186] which is basically divided into three phases depending on  $J/t$  and the electron filling  $n$  ( $n = 1$  is half filling). At  $n = 1$  the system turns out to order anti-ferromagnetically for arbitrary coupling strength. A ferromagnetic (FM) phase is established, if either  $J$  is large enough or  $n$  is small enough. [273] Otherwise the local spin lattice is in the paramagnetic (PM) phase, because then the effective RKKY interaction dominates the system.

The mechanism of ferromagnetism in the KLM can also be understood in terms of an electron quasiparticle picture, where the quasiparticle is the so called *spinpolaron*[247, 266], see Fig. 5.2a. For a given FM order of the local spins in a 1d system it was shown that the itinerant electrons and the magnons of the local spin bath form a bound spinpolaron state which is detectable in transport measurements and was proposed as a long-living correlated many-body spin state [244] forming possibly one part of a many-body spin qu-bit. In Ref. [273] it was shown for the case of a single conduction electron that a spinpolaron develops with a huge extent over the whole lattice leading to FM order in the ground state. In Chapter 4 this was extended to finite electron fillings and it was shown that long quasiparticle life times are connected with FM order of the local spins. In Ref. [293], the quasiparticle dynamics of the half filled KLM ( $n=1$ ) have been examined as well. By means of a strong coupling expansion up to 11th order it has been possible to calculate the quasiparticle dispersion relation to good accuracy and it could be shown that the quasiparticles behave like nearly localized f-electrons due to the strong correlation of the conduction and localized electrons.

It is known that the main relaxation and decoherence source of single electron spins in semiconductor based quantum dots arises from interactions with the nuclear spin background. [171, 103, 70] An appropriate path to diminish the relaxation is the application of a large magnetic field, whereas the decoherence rate is reduced by state distribution narrowing. [47, 46] However, the initial preparation of the nuclear bath in a pure state (e.g. full polarization) is an experimental challenge. Recently, the idea was proposed to consider the nuclear bath at very low temperatures in the FM phase, which is mediated by many itinerant electrons via the RKKY-interaction. [244, 277, 34] In Ref. [34] it was shown that the Coulomb interaction in a 2d electron gas leads to an increased critical temperature of order  $T \sim 1mK$  for the nuclear spins, which might be feasible in experiments. In Ref. [277] a  $C^{13}$  carbon nanotube was studied. By approximating the conduction electrons by a Luttinger liquid and treating the large effective nuclear spins classically, the transition temperature between a helically ordered (FM for finite systems) and unordered spin lattice was calculated. [277] It could be shown that a finite long-ranged Coulomb interaction is required to have a finite transition temperature, [34] which is consistent with the Mermin-Wagner Theorem [189] and its recent extension.[35] Taking backaction effects of the nuclear lattice on the electron spins into account increases the transition temperature by another order of magnitude. This makes the KLM interesting for experiments, which are always performed at finite temperature.

These developments motivate the study of the KLM in the presence of a finite Coulomb interaction between the itinerant electrons. The simplest extension to the KLM in terms of lattice models is the onsite Coulomb interaction  $U$ . In the case of half-filling a finite  $U$  leads to the opening of a spin and charge gap. [271] This work has been extended within a continuum Luttinger liquid approach to arbitrary fillings solved by bosonization. [97] Lattice effects have

been accounted for by means of a phononic field and therefore there is no real lattice involved in those calculations. Still, the authors of Ref. [97] find the interesting result of a shift of the phase boundary between FM and PM phase, as expected.

In this chapter, we use the density matrix renormalization group method [317, 318, 261, 262] (DMRG) to study ground state and dynamical properties of the one dimensional KLM for local spins with spin 1/2 including onsite and nearest neighbor Coulomb interaction. Our method benefits from being numerically exact, acting in the lattice space without any approximations and taking all backaction effects of the local spin lattice on the conduction electrons automatically into account. Furthermore it allows for calculations in a broad parameter regime and works especially well for one dimensional systems with open boundary conditions and finite lattices. Here we are particularly interested in finite lattices, since nanoscale systems have finite sizes and show corresponding effects.

From ground state calculations we show that onsite Coulomb interaction lowers the value of  $J$  required for a transition from a PM to a FM ground state. For small  $n \lesssim 0.4$  nearest neighbor Coulomb interaction  $V$  acts the same way on the magnetic order as  $U$  does. For  $n \gtrsim 0.4$  they compete with each other. As a different sensor of magnetic order we utilize the static electron spin susceptibility. For the PM phase a peak at  $2k_F$  is expected (which diverges for  $L \rightarrow \infty$ ), while for the FM order a minimum at the smallest possible quasimomentum  $q$ , which is finite for finite lattices, should emerge. This was stated similarly in Refs. [34],[277] for small coupling constants  $J$ .

Finally, we calculate the quasiparticle life-time broadening  $\Gamma_+$  of an electron, its spin oriented in the opposite direction than that of all other electrons in the ground state. In Chapter 4 it has been shown in the FM phase and for electronic densities below half-filling that the effective interaction between spinpolaron states is weak proving that spinpolaron (spin-down) states are indeed well-defined quasiparticles with small life-time broadening  $\Gamma_-$  even in the presence of many electrons. However we will show here that the spin relaxation and decoherence rates will be dominated by the life-time broadening  $\Gamma_+$  of the opposite spin-up state, which is higher in energy. We will consider a single spin-up electron with quasimomentum  $k$  on top of the FM ground state of the 1d KLM. Although this spin has the same direction as the underlying local spins and, thus, can not decay by direct exchange with the local spins, we find that  $\Gamma_+$  is dominated by the effective exchange interaction with the sea of spinpolaron spin-down states in the system. As a consequence,  $\Gamma_+$  turns out to be much larger than  $\Gamma_-$  and dominates the spin relaxation as well as the spin decoherence rate (the pure dephasing term arising from the life-time broadening  $\Gamma_-$  of the spin down spinpolaron state is negligible). We analyze the life-time broadening  $\Gamma_+$  depending on  $J$ ,  $U$ ,  $n$  and the quasimomentum  $k$  and give explanations for the observations. Although the spin relaxation rate increases significantly in the presence of many electrons we will show in appropriate parameter regimes that the spin relaxation rate can be several order of magnitudes smaller in the FM phase compared to the PM phase.

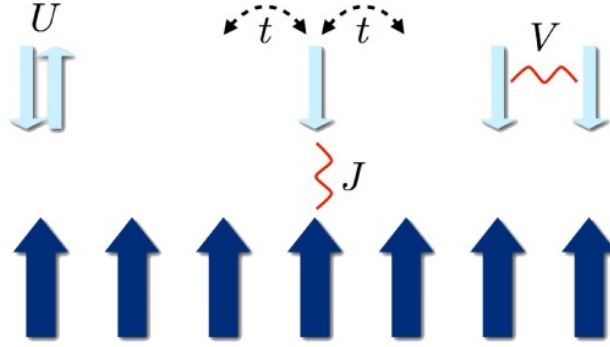


Figure 5.1: (Color online) The Kondo lattice model. The conduction electrons are depicted in the upper row (red) and the localized electrons are depicted as bold arrows in the lower row (grey).

## 5.2 Model

The Hamiltonian of the KLM with Coulomb interaction is sketched in Fig. 5.1 and defined as

$$H = -t \sum_{\sigma, i=1}^{L-1} \left( c_{i\sigma}^\dagger c_{i+1\sigma} + c_{i+1\sigma}^\dagger c_{i\sigma} \right) + J \sum_{i=1}^L \hat{S}_i \cdot \hat{s}_i + U \sum_{i=1}^L n_{i\uparrow} n_{i\downarrow} + V \sum_{i=1}^{L-1} n_i n_{i+1} \quad (5.1)$$

where  $t$  is the hopping integral,  $L$  the lattice size,  $c_{i\sigma}^{(\dagger)}$  the electron annihilation (creation) operator at site  $i$  with spin  $\sigma$ ,  $J > 0$  the antiferromagnetic Kondo exchange coupling,  $\hat{S}_i$  the spin operator of the local spin at site  $i$ ,  $\hat{s}_i$  the spin operator of the conduction electron at site  $i$ ,  $U$  the onsite Coulomb interaction constant,  $n_{i\sigma} = c_{i\sigma}^\dagger c_{i\sigma}$ ,  $V$  the nearest neighbor Coulomb interaction constant and  $n_i = n_{i\uparrow} + n_{i\downarrow}$ . All spins are considered to be spin 1/2. We define the filling by  $n = N/L$ , where  $N$  denotes the total number of itinerant electrons ( $n = 1$  corresponds to half-filling).

## 5.3 Method

### 5.3.1 DMRG

The DMRG method is a well established numerically exact method for the calculation of ground states, dynamical properties and time evolution of one dimensional lattice systems. Our algorithm is formulated in a matrix-product language and makes use of Abelian, e.g. particle number conservation ( $U(1)$ ) and non-Abelian, e.g., total spin conservation ( $SU(2)$ ), symmetries, see Chapter 2. Depending on the symmetry sector, the use of  $SU(2)$  symmetries in addition to  $U(1)$  symmetries allows for computations up to 10 times faster.

### 5.3.2 Ground states

Calculating the ground state of a given system is synonymous to finding the symmetry sector with its corresponding quantum numbers, where the energy is minimal. The ground state phase

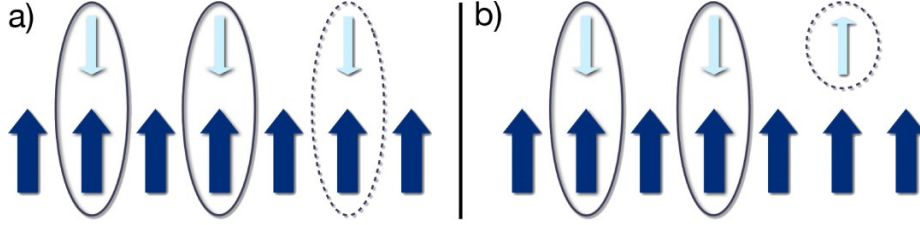


Figure 5.2: (Color online) (a) Sketch of a configuration with three spinpolarons, each consisting of a delocalized spin singlet state with the local spins. (b) Sketch of a configuration with two spinpolarons and one spin up electron.

diagram of the KLM is shown in Fig. 5.3 in dependence of the Kondo constant  $J$  and the filling  $n$ . Fixing  $J$  and  $n$  leaves the total spin quantum number  $S$  as the only free parameter, which distinguishes the order of the ground state, i. e.,  $S = (L - N)/2$  complies with FM order of local spins and  $S = 0$  with PM order. We choose  $SU(2)$  symmetry for the spin here, first for computational reasons and second it has the benefit that the states with different total spin quantum numbers are non-degenerate in this case, whereas in  $U(1)$  symmetry a partial degeneracy in the total spin in the direction of quantization exists. Considering Coulomb interaction in addition, we have another two variables that have to be fixed in advance and this means we have a quadruple of variables  $\{n, J, U, V\}$ , or a four dimensional phase diagram.

### 5.3.3 Susceptibility

We calculate the static electron spin susceptibility  $\chi(\omega = 0)$  by means of Green's functions and the application of dynamical DMRG [154, 126] with *GMRES*, see Sec. 2.2.3. Details of our implementation can be found in Chapter 4.

The definition of the spin susceptibility is

$$\chi_q^{+-}(\omega) = -\frac{1}{L} \left[ \langle 0 | \tilde{s}_q^+ \frac{1}{H - E_0 + \omega - i\eta} \tilde{s}_q^- | 0 \rangle + \langle 0 | \tilde{s}_q^- \frac{1}{H - E_0 - \omega + i\eta} \tilde{s}_q^+ | 0 \rangle \right] \quad (5.2)$$

with (for open boundary conditions)

$$\tilde{s}_q = \sum_{l=1}^L s_l \sin\left(\frac{ql\pi}{L+1}\right),$$

where  $H$  is the Hamiltonian given in Eq. (5.1),  $|0\rangle$  is the ground state of the system, and  $E_0$  the ground state energy.  $\eta$  is a finite artificial broadening factor, needed to avoid finite size effects [261] and which can be chosen smaller with larger lattice size.

### 5.3.4 Quasiparticle life-times

In Chapter 4 the quasiparticle life-time of the spinpolaron has been calculated (cf. Fig. 5.2a), by evaluating the electronic Green's function in momentum and frequency space

$$G_{k\sigma}(\omega + i\eta) = \frac{1}{\omega + i\eta - (\varepsilon_0(k) - \mu + \Sigma_\sigma(k, \omega + i\eta))}, \quad (5.3)$$

where  $\omega$  is the energy,  $\varepsilon_0(k)$  the free electron dispersion relation,  $\mu$  the electrochemical potential (which does not play a role in the calculation of broadenings of spectral densities) and  $\Sigma_\sigma(k, \omega + i\eta)$  the complex self-energy. From the imaginary part of the self-energy, which is given by the broadening of the Lorentzian shaped peak in the spectral density  $A_\sigma(k, \omega) = -(1/\pi) \text{Im} G_{k\sigma}(\omega)$  we can determine the quasiparticle life-time in dependence of all parameters. On the technical side, we use again the above mentioned GMRES method and calculate spectral densities as described in Chapter 4 and Sec. 2.2.3.

Basically, there exist four different scenarios for which the electronic quasiparticle life-time broadenings can be calculated assuming that in the FM ground state the local spins point up and the conduction electron spins point down (for large  $J$  the most dominant part of a spinpolaron state consists of a conduction electron pointing down with a small admixture of the spin up state plus a local magnon):

- **1** In the FM phase for a spin down electron (cf. Fig. 5.2a);
- **2** In the FM phase for a spin up electron (cf. Fig. 5.2b);
- **3** and **4** are the corresponding cases for the PM phase.

**1** corresponds to the spinpolaron life-time broadening  $\Gamma_-$  and **2** to its natural counter part  $\Gamma_+$ . **3** and **4** are identical, since the spins in the PM ground state have no specific direction.

In addition to Chapter 4 we calculate here the life-time broadening  $\Gamma_+$ . As shown in this chapter this rate is very large in the presence of many electrons,  $\Gamma_+ \gg \Gamma_-$ , and, as a consequence, dominates the spin relaxation and decoherence rates, as can be understood from the following qualitative analysis. The two many-body spin states  $|\pm\rangle$  depicted in Fig. 5.2 are not exact eigenstates but are expected to be part of a sharp many-body continuum with long lifetimes. The spin down state  $|-\rangle$  is protected from magnon absorption and emission processes since the spinpolarons can lower their energy by the entanglement with the local spins in a singlet state. Only virtual processes and weak spinpolaron-spinpolaron interactions lead to a small broadening  $\Gamma_-$  of this state, as shown in detail in Chapter 4. The spin-up state  $|+\rangle$  is protected due to the spin polarization of the local spins. Due to effective exchange interaction between the spinpolarons and the spin-up electron mediated by the magnons, as discussed in detail in this chapter in section 5.4.3, this state has a life-time broadening  $\Gamma_+ \gg \Gamma_-$ . Denoting the quasienergies of the two spin states by  $E_\pm$ , we get a decay according to  $\langle \pm | e^{-iHt} | \pm \rangle \sim e^{-iE_\pm t} e^{-(\Gamma_\pm/2)t}$ . To define the spin relaxation and decoherence rates, we introduce pseudo-spin operators  $P_z = (1/2)(|+\rangle\langle +| - |-\rangle\langle -|)$  and  $P_\pm = |\pm\rangle\langle \mp|$ . Using spin conservation, we obtain after a straightforward calculation that  $\langle P_z(t) \rangle = (1/2)|\langle + | e^{-iHt} | + \rangle|^2$ , if the system is prepared at  $t = 0$  in the state  $|+\rangle$ , and  $\langle P_+(t) \rangle = (1/2)\langle + | e^{-iHt} | + \rangle^* \langle - | e^{-iHt} | - \rangle$ , if the system is prepared in the state  $(1/\sqrt{2})(|-\rangle + |+\rangle)$  initially. As a result we find for the two different initial preparations that  $\langle P_z(t) \rangle \sim e^{-\Gamma_1 t}$  and  $\langle P_+(t) \rangle \sim e^{i\Delta t} e^{-\Gamma_2 t}$ , where  $\Delta = E_+ - E_-$  is the quasienergy splitting and the spin relaxation/decoherence rates are given by

$$\Gamma_1 = \Gamma_+ \quad , \quad \Gamma_2 = \frac{1}{2}\Gamma_+ + \frac{1}{2}\Gamma_- \quad . \quad (5.4)$$

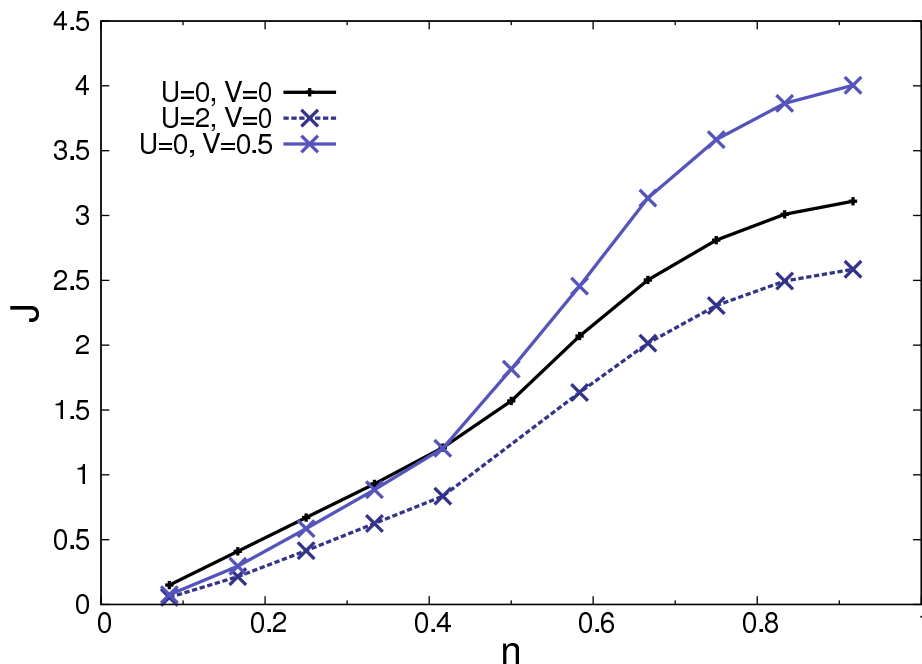


Figure 5.3: (*Color online*) Phase boundary between the FM (upper part) and the PM (lower part) ground state of the Kondo lattice model with  $L = 48$  for three different cases of Coulomb interaction.

This result shows that the dominant part to  $\Gamma_{1/2}$  is given by the broadening  $\Gamma_+$  of the spin-up state  $|+\rangle$ , whereas the broadening  $\Gamma_-$  of the spinpolaron state  $|-\rangle$  enters only into the pure dephasing term of longitudinal fluctuations and can be neglected.

### 5.3.5 Dispersion relation

The dispersion relation  $\omega_\sigma(k)$  can be constructed from the resonance of the single particle spectral density  $A_\sigma(k, \omega)$  at  $\omega = \omega_\sigma(k)$ . The number of  $k$  values is restricted by the lattice size  $L$ .

## 5.4 Results

In nearly all cases we have chosen  $L = 48$ , which is suitable from two different points of view. First, physically, we are especially interested in finite systems, which would more closely resemble, e.g., nanotubes in the real world. And second, from the point of view of computational cost, it is not convenient to take larger systems into account, since we already needed up to 3000 DMRG states in some of the calculations, which is a large number considering the number of executed calculations. All calculations are done with high computational precision, partly up to machine precision. We set  $t = 1$  in all calculations.

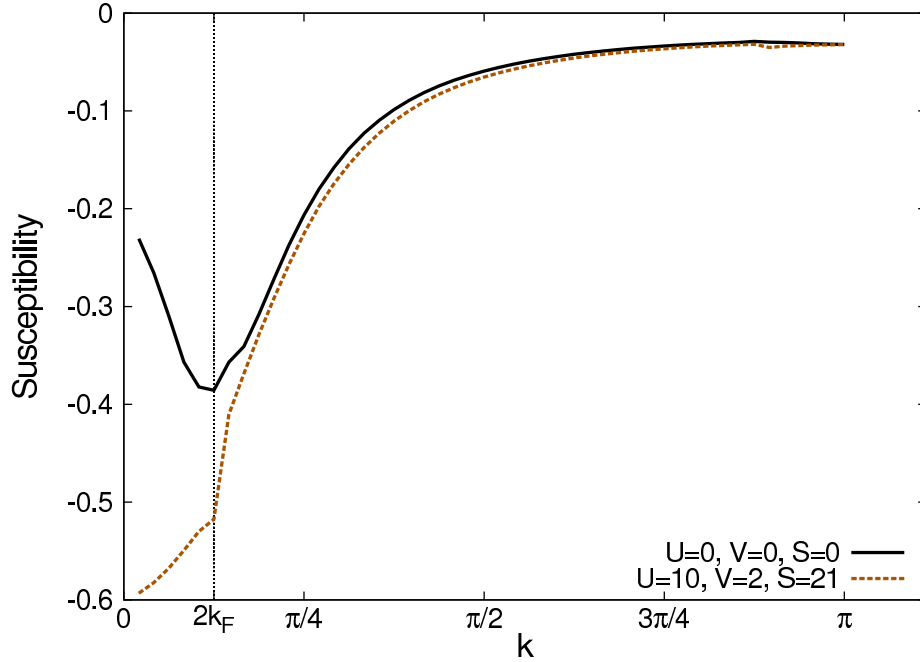


Figure 5.4: (*Color online*) Static electron spin susceptibility  $\chi(\omega = 0)$  for a Kondo lattice model with  $L = 48$ ,  $N = 6$  and  $J = 0.15$  with (dashed line) and without (solid line) Coulomb interaction. The thin vertical line marks  $2k_F$  in the PM phase.

### 5.4.1 Phase diagram

We will first investigate the influence of Coulomb interaction on the ground state of the Kondo lattice model. The phase diagram [298] of the KLM (without Coulomb interaction) is well established and shows two different phases, an FM and a PM one, see Fig. 5.3. The PM phase lies in the lower-right triangular of the phase diagram and for all other values of  $J$  and  $n < 1$  the KLM has an FM ground state. Especially for  $N = 1$  it was shown that the KLM is FM for any  $J$ . [273] As can be seen from Fig. 5.3, applying a finite onsite Coulomb interaction shifts the phase boundary downwards for all values of  $n$ . This is consistent with the analysis of [277], where a higher crossover temperature has been predicted in the presence of Coulomb interaction. However, we note that the two mechanism are quite different. Whereas in [277] the local nuclear spins have been treated quasiclassically due to their large effective spin, the present analysis is in the full quantummechanical regime of local spins with spin  $1/2$ . Roughly speaking the present result is consistent with the Stoner picture of ferromagnetism, where a finite Coulomb interaction leads to the preference of a fully spin-polarized state for the itinerant electrons. This state coincides with the qualitative picture of spinpolaron states pointing into the opposite direction of the local spins, see Fig. 5.2a.

For finite nearest neighbor Coulomb interaction  $V$  we find the qualitatively different result, that the phase boundary is shifted downwards for  $n \lesssim 0.4$  and upwards for  $n \gtrsim 0.4$  and therefore crosses the phase boundary of the KLM without Coulomb interaction. For small fillings this can be explained in the same way as for the onsite Coulomb interaction case. For filling  $n > 0.4$  the

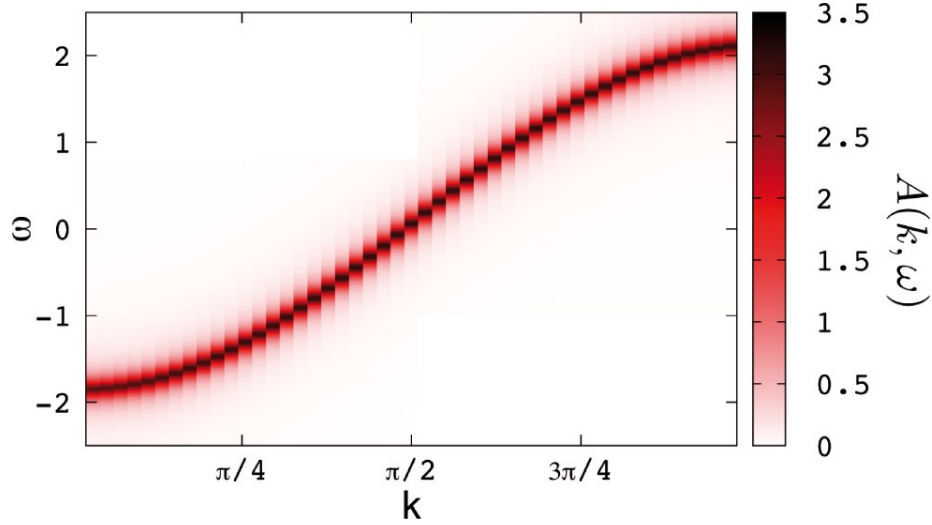


Figure 5.5: (Color online) Dispersion relation of a  $\uparrow$ -electron in a KLM with  $J = 0.5$ ,  $N = 4$  and  $U = V = 0$ .

electrons are relatively close to each other and therefore strongly influenced by  $V$ . The possibility to occupy the same site with two electrons of opposite spin does not lead to an increasing energy due to Coulomb interaction and increases the kinetic energy at the same time. Therefore, in this regime, the unordered state becomes more favorable.

Summarizing, the onsite and nearest neighbor Coulomb interaction are concurring for small  $n < 0.4$  and behave competitively for large  $n > 0.4$ . These results are pictured in Fig. 5.3: The solid blue line is the phase boundary of the non-interacting KLM. If Coulomb interaction is switched on, the phase boundary is lowered for all values of  $n$  (dashed dark blue line). For  $U = 0$  and  $V$  finite, the phase boundary is lowered for small  $n$  and raised above the non-interacting case phase boundary for larger  $n$ .

### 5.4.2 Susceptibilities

For small  $J$  the order of the local spins manifests itself also in the static electron spin susceptibility. As was shown in [277] the effective coupling between the local spins for small  $J$  is

$$J_{RKKY} \propto -\chi^{\pm}(\omega = 0, k, J, U). \quad (5.5)$$

Therefore the order of the local spin lattice should correspond to the absolute maximum of the static electron spin susceptibility. In Fig. 5.4 we show this for two extreme cases with  $L = 48$  and  $N = 6$ . The first case (solid black line in the figure) with  $U = 0$ ,  $V = 0$  has a PM ground state and shows the susceptibility in the non-interacting case. It has an absolute maximum at  $k = 2k_F$ . This evidences that for the chosen set of parameters the state indeed orders paramagnetically in a RKKY like fashion. If Coulomb interaction is switched on with  $U = 10$ ,  $V = 2$  (dashed brown line in the figure) the absolute maximum is at  $k = 0$ . In this case FM order becomes dominant.

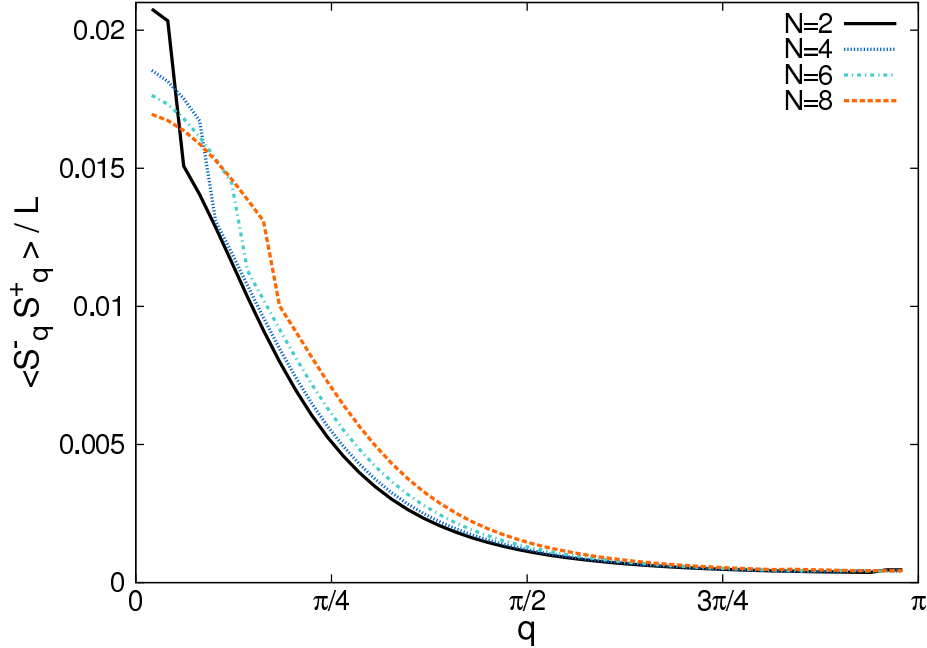


Figure 5.6: (Color online) Magnon density in the KLM with  $L = 48$ ,  $t = J = 1$ ,  $U = V = 0$  in dependence of the quasimomentum. The number of electrons is varied between 2 and 8 in steps of 2.

### 5.4.3 Dispersion relation

We calculated the dispersion relation of a  $\uparrow$ -electron in a KLM with  $L = 48$ ,  $N = 4$ ,  $J = 0.5$  and  $U = V = 0$ . The result is shown in Fig. 5.5. It shows a cosine shaped dispersion, which leads to the conclusion that the electron behaves more or less like a free electron, only slightly affected by the presence of the local spin lattice. This can be explained by the fact that a  $\uparrow$ -electron can not flip its spin directly by an exchange process with a local spin due to spin conservation. In contrast, a  $\downarrow$ -electron can do so, leading to the formation of spinpolarons, which can lower their energy by this process and obtain a larger effective mass leading to a sharper dispersion relation. However, as shown in the next section, the life-time broadening of  $\uparrow$ -electrons is generically larger than those of  $\downarrow$ -electrons, since the decay processes for spinpolarons start in higher order in  $J$  than those for  $\uparrow$ -electrons.

### 5.4.4 Quasiparticle life-times

From the electronic spectral density  $A_{\uparrow}(k, \omega)$  we obtain the quasiparticle life-time broadenings  $\Gamma_{\uparrow}$  in dependence of  $J$ ,  $U$ ,  $k$  and  $N$ . As we calculate the Green's function  $G_{\uparrow}(k, \omega)$  in frequency space, we obtain two branches: The  $c_{k\uparrow}^{\dagger}$ - and the  $c_{k\uparrow}$ -branch, respectively. The first one corresponds to an additional electron placed in a certain  $k$ -mode and interacting with the other electrons and the local spins. The second type addresses the spin up-part of the already existing electrons in the system. Therefore the two branches address two different sets of states in the spectrum of the Hamiltonian. Here we are interested in the first case only, since we would like

Table 5.1:  $k$ -dependence of relaxation rates for  $N = 2$  for different values of  $J$  and  $U$ .

$k [\pi/(L+1)]$	1	2	3	4
$J=0.5, U=0$	$0.00097 \pm 0.00003$	$0.00128 \pm 0.00002$	$0.00166 \pm 0.00003$	$0.00204 \pm 0.00005$
$J=0.5, U=0.2$	$0.00220 \pm 0.00009$	$0.00299 \pm 0.00005$	$0.00403 \pm 0.00005$	$0.0048 \pm 0.0001$
$J=0.3, U=0$	$0.00035 \pm 0.00001$	$0.000470 \pm 0.000004$	$0.00066 \pm 0.00002$	$0.00077 \pm 0.00002$
$J=0.3, U=0.2$	$0.00146 \pm 0.00006$	$0.00198 \pm 0.00004$	$0.00280 \pm 0.00007$	$0.00331 \pm 0.00008$

to know, what happens to a spin up electron brought into the system in addition to the other electrons.

### Decay rate dependence on $k$

In Tab. 5.1 we show decay rates of a spin up electron added to the  $N = 2$  ground state. For all sets of  $U$  and  $J$  we find that the decay rate increases with increasing  $k$  as long as  $k$  is smaller than  $2k_F$ . Here we give an explanation considering momentum conservation and phase space arguments. In the FM ground state the lowest electronic orbitals in  $k$  space are occupied up to  $2k_F$  by the available electrons all with spin down. A state with wave vector  $k$  has quasimomentum  $\pm k$  due to the open boundary conditions. An additionally superimposed spin up electron with a certain wave vector  $k_1$  has to change to the state  $k_2 > 2k_F$  in order to flip its spin, see Fig. 5.7a. This decay channel can only happen if a magnon is absorbed with wave vector  $q = |k_1 \pm k_2|$ . Such magnons are present in the ground state because each spinpolaron state consisting of a spin down electron with wave vector  $k$  has a small admixture of spin up states with wave vector  $|k \pm q|$  and a local magnon in state  $q$ . Smaller values of  $k_1$  decreases the number of magnons with small wave vector  $q = |k_1 - k_2|$  to enable this process. This can be quantified by the magnon density per electron  $m_q = \langle S_q^- S_q^+ \rangle / N$  (see Fig. 5.6) and further by the accumulated magnon density

$$\rho_{k_1} = \sum_{\sigma=\pm} \sum_{\substack{q=|k_1+\sigma k_2| \\ 0 < q < \pi, 2k_F < k_2 < \pi}} m_q \quad , \quad (5.6)$$

which is shown in Fig. 5.7b and clearly states that the number of suitable magnons increases with increasing  $k_1$  even above  $2k_F$  until it falls off finally. This result qualitatively reflects the decay rate for the spin up electron shown in Fig. 5.7c for a KLM with  $L = 48$ ,  $N = 4$ ,  $J = 0.5$  and  $U = V = 0$ . The decay rate first increases for small  $k$  as indicated by the accumulated magnon density. For values above  $2k_F$  the decay rate even surpasses the values at  $2k_F$  until it decreases finally for larger values of  $k$ . We note that this is only a qualitative explanation since other decay channels involving absorption of many magnons are present as well.

The discussed process for the decay of the spin up electron is essentially an exchange process between a spin up electron in state  $k_1$  and a spinpolaron in state  $k$ . The spinpolaron provides the magnon with wave vector  $q = |k_1 \pm k_2|$  to flip the spin up electron from state  $k_1 \rightarrow k_2$ , leaving the spinpolaron as a spin up electron in state  $|k \pm q|$ . As a result, by mediation of a local magnon, the spins of two electrons have been exchanged, whereas the local spin lattice is unaffected. This spin exchange process is the essential process leading to a large life-time broadening of the spin-up electrons if many electrons are present in the system. In contrast, the spinpolaron states have

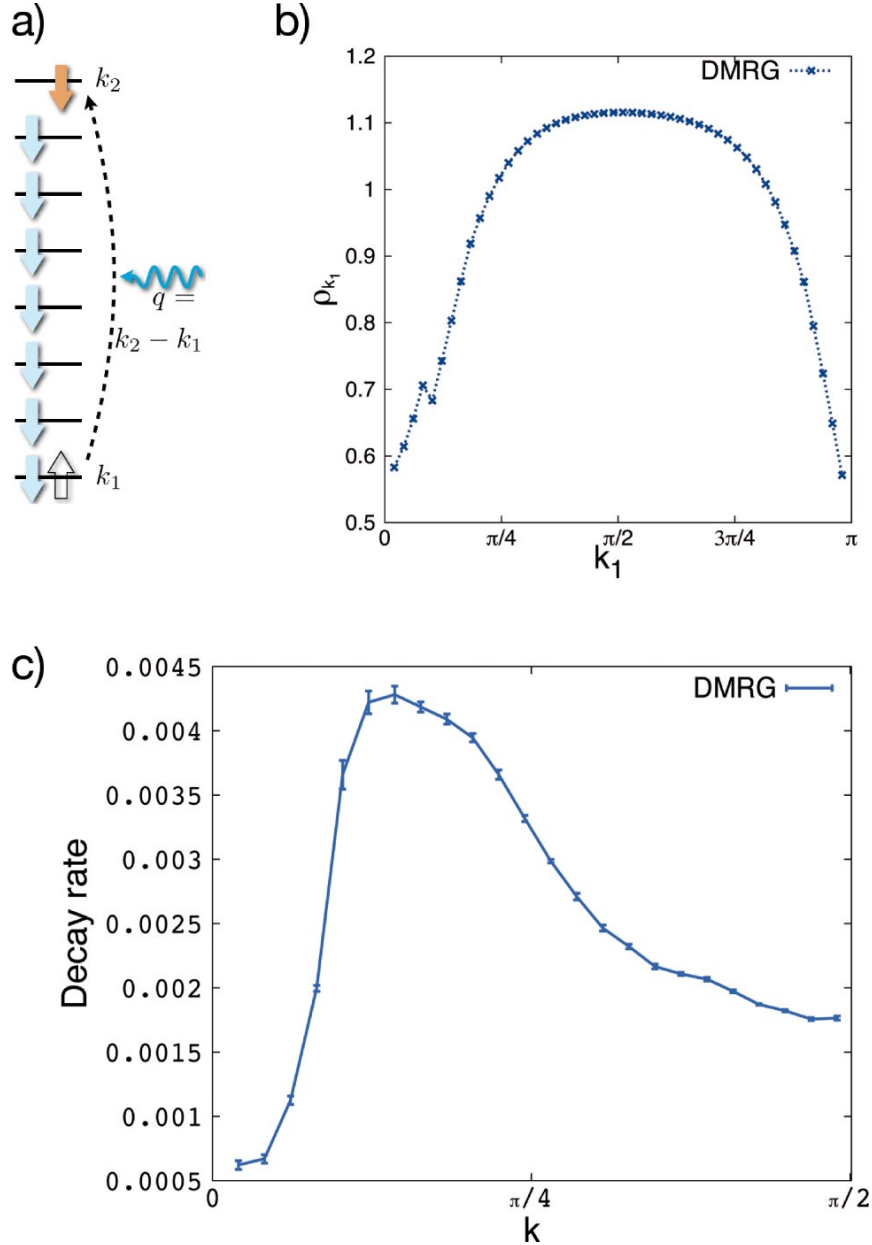


Figure 5.7: (Color online) (a) Simplified itinerant electron band structure in  $k$ -space. Light blue electrons on the left side are electrons initially in the ground state and electrons on the right side are additionally added to the ground state. The process shown correspond to a spin flip of the added electron at  $k = k_1$ . After the spin flip, the electron has opposite spin with  $k = k_2$  and has absorbed a magnon with  $q = k_2 - k_1$ . (b) Accumulated magnon density  $\rho_{k_1}$  as given in Eq. (5.6), for  $L = 48$ ,  $N = 4$  and  $J = 0.5$ . (c) Decay rates for  $L = 48$ ,  $N = 4$  and  $J = 0.5$  in dependence of  $k$ .

life-time broadenings, which are several orders of magnitude smaller compared to those of the spin-up states. The reason is that the spinpolaron-spinpolaron interaction is rather weak and can only be mediated via multi-magnon processes.

### Decay rate dependencies on $U, J, N$

In this section we will explain how the quasiparticle decay rate of the spin up state depends on  $U, J$  and  $N$  and why the found tendencies are to be expected. The results for these cases are shown in Tab. 5.2.

Let us first consider the  $J$ -dependency. Picking one of the columns and considering only one of the two  $U$ -values we immediately recognize that the decay rate shrinks with decreasing  $J$ . The exchange strength  $J$  determines the time scale on which spins will flip, therefore with decreasing  $J$  flipping will be suppressed and the rate decreases. We note that this is different for the decay rate of the spinpolaron, where an increasing  $J$  stabilizes each polaron and makes it insensitive to interactions with other electrons. For small  $J$  close to or even in the PM phase the decay rate of the spin up state increases notably, see  $N = 4$ . This is natural, since in a paramagnetically ordered system many additional decay channels will open up.

Considering the  $U$  dependence we find that with increasing  $U$  the rate increases in most cases. In section 5.4.1 we have found that an onsite Coulomb interaction has the tendency to order the local spins ferromagnetically. The additional spin up electron tries to align parallel to the other electrons to minimize interaction energy from the Coulomb potential. This infers a larger decay rate, if  $U$  becomes larger. Therefore this tendency here complies with the influence of the onsite Coulomb interaction found above. Only when a finite  $U$  triggers the crossover from the PM to the FM phase, the rate decreases with increasing  $U$ , see  $N = 4$  and  $J = 0.3$ . This is obvious since in the PM phase the phase space arguments presented in section 5.4.4 are no longer valid and many more decay channels are possible.

If we increase the number of electrons  $N$  in the system and keep the quasimomentum  $k$  fixed we find that the rates decrease with increasing  $N$ , for small  $N$  deep in the FM phase. This can be explained analog to the discussion in section 5.4.4. In the ground state, all initially available electrons fill the spinpolaron-band successively up to  $2k_F$  mainly in the spin down state. An additional spin up electron can be added to any  $k$ -mode. In Tab. 5.2 we considered the lowest state  $k = \pi/(L + 1)$  in all cases. Considering one of the rows the electron number is increased from left to right and with each electron more in the ground state the respectively next higher  $k$ -mode is occupied by this additional electron. As a consequence, as shown in section 5.4.4, by increasing  $N$  we decrease the number of magnons suitable for scattering processes and therefore the decay rate has to decrease. However, in competition to this effect, increasing  $N$  means also approaching the PM phase. Then we expect that different and also more decay channels open up, which should lead to an increasing decay rate. This can be seen in Tab. 5.2 for  $J = 0.8$  between  $N = 6$  and  $N = 12$ . We have also calculated lifetimes for  $N = 7, 9, 10, 11$  (not shown), showing that the decay rates are monotonically increasing with increasing  $N$  for large  $N$ . For values of  $N$  close to half-filling of the conduction band and large values of  $J$ , such that we can switch between PM and FM phase, we find decay rates of the order of 0.01. As a consequence, the decay rate depends nonmonotonically on  $N$ , it decreases for small values of  $N$  deep in the

Table 5.2: Relaxation rates in dependence of the electron number  $N$ ,  $J$  and  $U$ .  $k$  is set to the lowest possible value  $k = \pi/(L + 1)$ . The given number of  $N$  is the number of electrons taken into account during the ground state calculations, i.e., the spin up electron is in addition to this number. (p) mark parameters, which correspond to the paramagnetic phase.

N	1	2	3	4	6	12
J=1.0, U=0			0.00263 $\pm 0.00012$	0.00199 $\pm 0.00013$	0.00185 $\pm 0.00017$	0.00085 $\pm 0.00018$
J=1.0, U=0.2			0.00432 $\pm 0.00070$	0.00294 $\pm 0.00019$	0.00249 $\pm 0.00027$	0.0011 $\pm 0.0002$
J=0.8, U=0			0.00188 $\pm 0.00008$	0.00130 $\pm 0.00009$	0.00087 $\pm 0.00009$	0.00213 $\pm 0.00024$
J=0.8, U=0.2			0.00303 $\pm 0.00021$	0.00221 $\pm 0.00017$	0.00184 $\pm 0.00017$	0.00238 $\pm 0.00038$
J=0.6, U=0			0.00115 $\pm 0.00005$	0.00078 $\pm 0.00005$	0.00081 $\pm 0.00007$	(p)0.00508 $\pm 0.00031$
J=0.6, U=0.2			0.00239 $\pm 0.00012$	0.00156 $\pm 0.00012$		
J=0.5, U=0	0.00104 $\pm 0.00002$	0.00097 $\pm 0.00003$	0.00082 $\pm 0.00003$	0.00062 $\pm 0.00004$	0.00066 $\pm 0.00005$	
J=0.5, U=0.2	0.00233 $\pm 0.00004$	0.0022 $\pm 0.0001$	0.00205 $\pm 0.00008$	0.00126 $\pm 0.00011$	0.00141 $\pm 0.00013$	
J=0.5, U=0.4					0.00142 $\pm 0.00021$	
J=0.5, U=0.6					0.00245 $\pm 0.00018$	
J=0.5, U=0.8					0.00384 $\pm 0.00045$	
J=0.3, U=0	0.00041 $\pm 0.00001$	0.00035 $\pm 0.00001$	0.00033 $\pm 0.00001$	(p) 0.00144 $\pm 0.00010$	0.00150 $\pm 0.00020$	
J=0.3, U=0.2	0.00158 $\pm 0.0003$	0.00146 $\pm 0.000016$	0.00123 $\pm 0.00008$	0.00084 $\pm 0.00007$		
J=0.1, U=0.0	0.000030 $\pm 0.000001$		0.00004 $\pm 0.0000009$	(p) 0.00593 $\pm 0.00024$		
J=0.1, U=0.2			0.00061 $\pm 0.00003$	(p) 0.00460 $\pm 0.00011$		

FM phase and increases for larger values of  $N$  when the PM phase is approached.

Nonetheless we find the *sweet spot* of the system by *decreasing* the number of electrons going from  $N = 4$  to  $N = 3$  electrons at  $J = 0.1$ . There we find that the decay rate of the spin up electron decreases by two orders of magnitude when comparing the rates in the PM and FM phase. Still it is important to note that a minimum number of electrons in the system is important to maintain the FM order, especially at finite temperatures.

## 5.5 Discussion

In this chapter we discussed the phase diagram and the spin relaxation properties of the 1d spin-1/2 Kondo lattice model with Coulomb interaction. We found that a finite onsite or nearest

neighbor interaction favors a FM order of the local spin lattice for small enough electronic densities. This gives further strong support to the analysis of Refs. [34],[277], where similiar results have been found in 2d semiconductor systems and  $C^{13}$  carbon nanotubes. It provides a pathway to achieve a spontaneous and full polarization of the nuclear spins by lowering the temperature below the critical one. This configuration is desirable for applications in quantum information processing, since it reduces the spin relaxation and decoherence rates of the electronic spins. It is important to notice that a finite crossover temperature can only be expected, if the density of electrons is finite. Thus, many electrons are necessary to achieve the FM state. Once the FM state is achieved, one can in principle perform quantum information processing by realizing quantum dots with external gates on time scales which are small compared to the time the nuclear spins need to return to the PM phase. If this is possible one can effectively realize a system consisting of one single electron  $N = 1$  in contact with a ferromagnetically ordered nuclear spin lattice. In this case the spin up state and the spinpolaron are exact eigenstates, i.e., the ideal situation with  $\Gamma_{\pm} = 0$  is achieved. In this chapter we discussed the spin relaxation properties for  $N > 1$ , i.e. we analysed the question whether the spins in a many-body system could possibly be used as candidates for spin qu-bits. In Chapter 4 we already found that spinpolarons are indeed very long living states, indicating that the spinpolaron-spinpolaron interaction is rather weak. However, in this chapter we found that the spin up state is strongly influenced by exchange interaction between the spin up and spinpolaron states. This exchange process does not require any finite energy and, therefore, can not even be suppressed by application of a finite magnetic field. We analysed in detail the dependence of  $\Gamma_{+}$  on the Coulomb interaction  $U$ , the exchange interaction  $J$ , the particle number  $N$  and the quasimomentum  $k$ . In the FM phase we found that the rate decreases for smaller values of  $U$ ,  $J$ ,  $k$ , and larger values for  $N$ , unless we approach the PM phase. For appropriate parameter sets we have shown that the life-time of spin up states can be two orders of magnitude larger in the FM phase than in the PM phase. However, compared to the life-time of spin down spinpolaron states, their life-time is orders of magnitudes smaller, regardless of the chosen parameter regime in the FM phase.



# Chapter 6

## Single electron transport in carbon nanotube quantum dots

With the advances in microfabrication techniques in the early 1990s it became possible to construct nanostructure devices - *single electron transport devices* - so small that a single electron charge has a measurable influence in electron transport experiments. Up to this point it has been very difficult to spectroscopically resolve the discrete spectrum of an individual sample of condensed matter, which changed then, because the ability to fabricate nanoscale devices reveals this one of the most fundamental properties of quantum mechanics, namely, the fact that the energy spectrum of a system of particles confined to a small region is discrete or quantized.

The study of single electron effects has a long history starting with the famous experiment of Millikan [192], who observed the effects of single electrons on the falling rate of oil drops. In solids, single electron tunneling was first studied observing the electrical resistance in grained thin film materials [92]. This experiment was extended in Refs. [159, 85]. A first and detailed transport theory was developed by Kulik and Shekhter in 1975 [155]. The difference between today's devices and the samples of those former experiments is the averaging over many grains, while today it is standard technique to address only one single electron transport device. Modern theoretical predictions [5, 199, 169] boosted interest in single electronics and led to the discovery of many new transport phenomena. Fulton and Dolan [77] performed the first experiment on controlled single electron transport and observed the so called Coulomb oscillations. Since electron transport in nanoscale devices is one of the most popular topics in modern physics a lot of reviews have been published, see e.g. [55, 93, 6, 283, 148, 320, 69, 58].

In this chapter we will first explain briefly the basic single electron transport devices in order to give a simple introduction and understanding of the field and to explain the notation. We start with the *quantum point contact* and the *single electron junction*, which basically consists of only a capacitor and a resistor. Then we extend this by another capacitor, separating the junction from the voltage source and therefore generating an island - the *single electron box*, where the electron charges can be accumulated. The last device to be discussed is the *single electron transistor* consisting of two junctions and a capacitively coupled gate electrode, which offers nice tuneability of the island charge. From this we can define what is generally known as a *quantum dot*. Finally, we introduce graphene and carbon nanotubes.

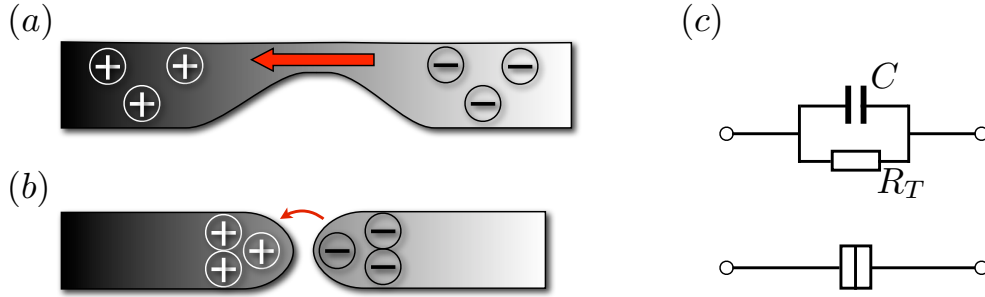


Figure 6.1: (a) Schematic drawing of a quantum point contact. (b) Schematic drawing of a tunnel junction. (c) An equivalent circuit of a tunnel junction. The lower drawing abbreviates the upper combination of a tunnel capacitance and resistance by one symbol.

## 6.1 Single electron transport devices

### 6.1.1 Single electron junction and quantum point contact

The simplest single electron transport devices are the quantum point contact and the single electron tunnel junction, see Fig. 6.1. The tunnel junction consists of two leads brought close to each other such that tunneling events occur. The setup naturally leads to a tunneling resistance  $R_T$  and a capacitance  $C$  between the two leads, as shown in Fig. 6.1(c). The first experiment on a tunnel junction by Fulton and Dolan [77] showed the effect of a discrete charge in the current-voltage characteristic. An electron passing across the tunneling barrier gains energy  $eV$ , where  $V = V_L - V_R$  and  $V_L$  is the voltage at the left electrode and  $V_R$  the voltage at the right electrode. The electrostatic energy of the junction is given by  $\int_0^Q dQ V = Q^2/2C$  and therefore the change in energy when a single electron tunnels is given by the so called *charging energy*

$$E_C = \frac{e^2}{2C}. \quad (6.1)$$

When  $C$  is sufficiently small and therefore  $E_C$  sufficiently large, the charging energy begins to play a significant role. Further, there are two generally accepted conditions [283, 148] for the occurrence of single electron charging effects. First, thermal fluctuations have to be suppressed, which is the case, if  $k_B T \ll E_C$ . From this we can deduce the magnitude of the capacitance. Let us assume that we can cool down our sample to the regime of  $\approx 1K$ . For  $k_B T = E_C$  we find  $C \approx 10^{-15}F$ . One could now think that this relation alone suffices to estimate the size of the sample, but one has to take into account that the separation of the electrodes is determined by the Fermi wavelength for tunneling events to be able to occur. Therefore the distance between the electrodes should be of the order of  $2\pi/k_F \approx 2\text{\AA}$ . Now we can estimate the approximate dimension of the tunnel electrodes, which has to be smaller than  $0.1 \mu\text{m}$ .<sup>1</sup> The second condition is given by the energy-time uncertainty relation  $\Delta E \cdot \Delta t \approx h$  and it is therefore related to the quantum fluctuations of the system. Using the  $RC$ -switching time  $\Delta t = R \cdot C$  and  $\Delta E = E_C$ , we find  $R_c \approx 26 \text{ k}\Omega$ . Therefore, the resistance of the tunnel junction has to be at least as large as

<sup>1</sup>Where we have used the formula of the capacitance of a parallel plate capacitor  $C = \epsilon_0 \epsilon_r A/d$ .

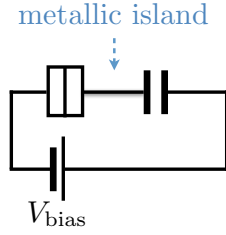


Figure 6.2: Replacement circuit of a single electron box. The box is defined by the metallic island between the junction and the capacitor.

$R_c$ . Then, quantum fluctuations are smaller than the charging energy. Hence, the current-voltage characteristic of the junction should show a Coulomb gap, i.e.,  $I = 0$  for  $-e/2C < V < e/2C$ .

However, single electron effects in tunnel junctions are typically not seen [58, 93], since we neglected the effect of the attached leads [56, 89]. The leads act like an electromagnetic environment with a capacitance, which exceeds the junction's capacitance by orders of magnitude and a finite impedance  $Z(\omega)$ , which is generally much smaller than the junction's resistance. It turns out that under these conditions a tunneling event is elastic and excites only electromagnetic modes in the external environment. Therefore, the electron charge of the tunneling event is directly transferred to the large capacitance of the leads and no change on the tunnel junction capacitance occurs.

The quantum point contacts [265] are constricted two-dimensional electron gases (2DEG), e.g., made from GaAs heterostructures [176], having a width and length much smaller than the mean free path of the conduction electrons and smaller than the Fermi wavelength. On top of the device there is a metal gate attached and applying a negative gate voltage depletes the conduction electrons such that the quantum point contact is defined by the electrostatic depletion. The gate voltage controls the width of the constriction. Transport through such a device [311, 313] becomes ballistic and is only determined by the geometry. Applying a finite bias voltage shows that the conductance of the device is quantized in units of

$$G = 2G_0 = \frac{2e}{h} \approx 26 \text{ (k}\Omega\text{)}^{-1}, \quad (6.2)$$

where 2 is due to the spin of the electrons.

### 6.1.2 Single electron box

The *single electron box*, depicted in Fig. 6.2, consists of a tunnel junction in series with a capacitor forming a metallic island separated from the voltage source. A voltage  $V_L$  can be applied to the junction and a voltage  $V_R$  to the capacitor.  $V(Q)$  is the voltage on the island, depending on the excess charge  $Q$  on the island. With  $C_r (V_r - V(Q)) = Q_r$  with  $r \in \{L, R\}$  and  $E_{\text{pot}} = \int_0^Q d\tilde{Q} V(\tilde{Q})$  we find for the potential energy on the island

$$E_{\text{pot}} = E_C N^2 - |e| N \sum_r \alpha_r V_r, \quad (6.3)$$

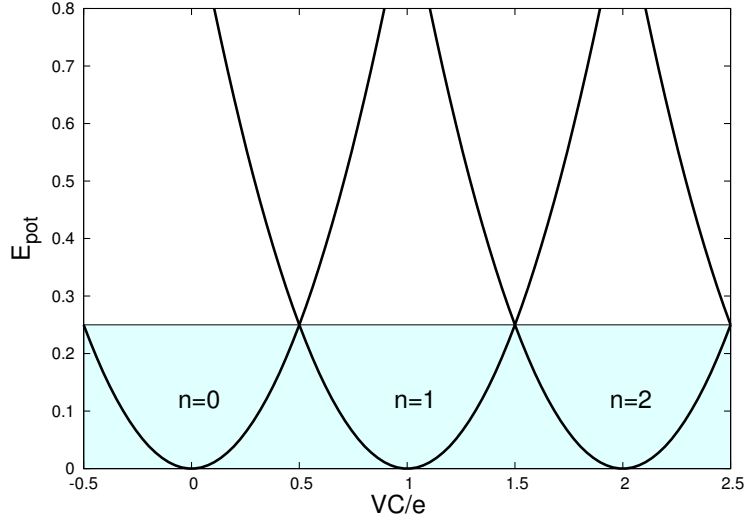


Figure 6.3: Electrostatic potential energy of the single electron box. The blue region marks the lowest energy region.

with  $\alpha_r = C_r/C$  and  $C = \sum_r C_r$ . For  $V_b = V_L - V_R = 0$  the number of excess electrons on the metallic island is zero. If the  $V_b$  is turned on, the number of electron charges changes in discrete steps  $N = \pm 1, \pm 2, \dots$ . Up to an  $N$  independent factor and assuming a symmetric bias voltage, Eq. 6.3 can be cast as [158]

$$E_{\text{pot}} \propto E_C \left( N + \frac{V_b C}{e} \right)^2. \quad (6.4)$$

This formula means that the number of electrons in the box jumps at certain voltages in order to keep the electrostatic potential energy as low as possible, see Fig. 6.3. At  $T = 0$  the electron charge of the system changes at each half-integer number of  $V_b \cdot C/e$ . For  $T > 0$  the steps where the charge changes become smoother.

### 6.1.3 Single electron transistor

The next logical step in the line of single electron devices is the *single electron transistor* [283]. An island is coupled via two junctions to a finite bias voltage  $V_b = V_L - V_R$  such that a finite current can flow. Further, the island is capacitively coupled to a gate electrode with a finite voltage  $V_g$ , which can be used to control the current through the device, hence the name transistor. The corresponding electric circuit is shown in Fig. 6.4.

For the electrostatic potential energy or charging energy for  $N$  electrons we find again

$$E_N = E_C N^2 - |e| N \sum_r \alpha_r V_r, \quad (6.5)$$

with  $C = \sum_r C_r$ ,  $\alpha_r = C_r/C$  and  $r \in \{L, R, g\}$ . Increasing the number of electrons on the dot as  $N - 1 \rightarrow N$  in a tunneling process, the charging energy changes by

$$\mu_N = E_N - E_{N-1} = (2N - 1)E_C - |e| \sum_r \alpha_r V_r, \quad (6.6)$$

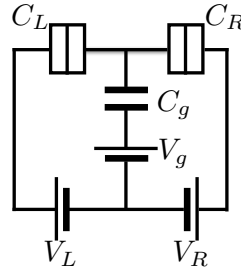


Figure 6.4: Replacement circuit of a single electron transistor.

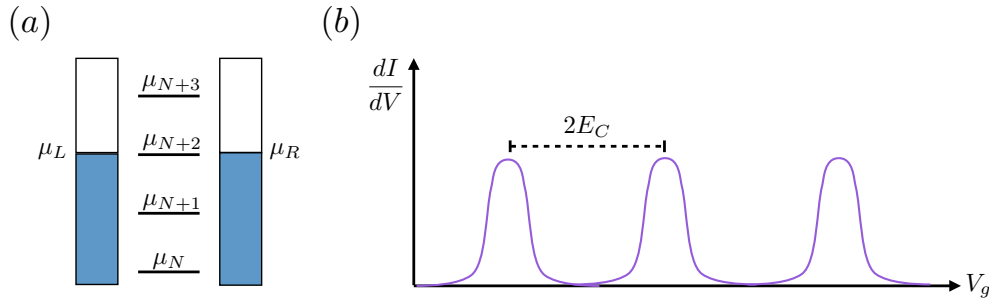


Figure 6.5: (a) Schematic drawing of the electrochemical potentials of the metallic island and of the leads' electrochemical potentials. (b) Whenever the gate voltage is tuned such that one of the  $\mu_N$  is in resonance with the leads chemical potentials a finite current will be measured. The broadening shown is due to the finite potential life-time of each quantum state and the temperature  $T$ .

which we denote by the electrochemical potential  $\mu_N$ . This can be tuned independent from the leads via the gate voltage and adjusts the position of the chemical potentials of the metallic island relative to the chemical potentials of the leads. The leads provide electrochemical potentials according to  $\mu_L = -|e|V_L$  and  $\mu_R = -|e|V_R$ . Assuming we fixed the chemical potential of the leads at the same value, whenever the leads chemical potentials are equal to one of the metallic island chemical potential  $\mu_N$ , see Fig. 6.5(a), electrons can tunnel and a finite current from electrons fluctuating on and from the island can be measured, see Fig. 6.5(b), and a Coulomb peak occurs. Depending on temperature and life-time of the respective state, the Coulomb peak will have a finite broadening. The distance between two neighboring Coulomb peaks is given by  $\mu_N - \mu_{N-1} = 2E_C$ , which is the so called *addition energy*. However, when no resonance condition between a metallic island chemical potential and the leads' chemical potentials is met the island is in the *Coulomb blockade*-regime.

### Transport versus Coulomb blockade

We now assume a finite symmetric bias voltage with  $V_L = -V_b/2$  and  $V_R = V_b/2$  and  $V_b \neq 0$ . If an island chemical potential has an energy lying between the two lead chemical potentials a finite current can flow, see. Fig. 6.6. However, if there is no island chemical potential in between transport can not occur and the device is in the Coulomb blockade regime, see Fig. 6.6(a). Whether the island is in that regime or not depends on the voltages applied and one can draw a

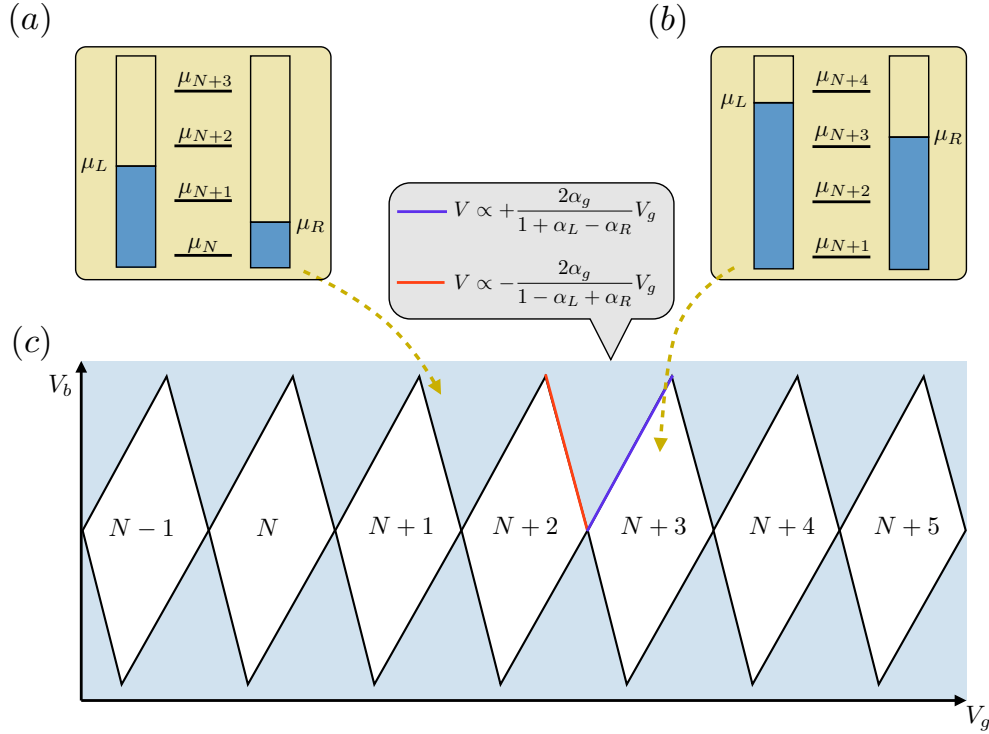


Figure 6.6: (a) Schematic drawing of the electrochemical potentials of the metallic island and of the leads in the transport regime, where the  $(N + 1)$ th electron is the transport electron. (b) The same for the Coulomb blockade regime. The island is filled up to the  $(N + 3)$ th electron and the next higher electrochemical potential of the island lies above the electrochemical potentials of the leads. (c) Stability diagram of the island with Coulomb diamonds, in which no transport occurs (white regions): Coulomb blockade. In the light blue regions a finite current is available.

so called *stability diagram* of the bias voltage versus the gate voltage, showing at which combinations of voltages a finite current occurs and when the device shows Coulomb blockade. From the resonance condition  $\mu_N = \mu_L$  and  $\mu_N = \mu_R$  one can deduce the lines in the stability diagram separating transport regimes from regimes with no transport. Evaluating these two conditions we find

$$V_b = \pm \frac{2\alpha_g}{1 \pm \alpha_L \mp \alpha_R} V_g. \quad (6.7)$$

The diagram shown in Fig. 6.6(c) shows diamond shaped regions, *Coulomb diamonds*, where current is suppressed. Outside the Coulomb diamond the current is not suppressed. We want to remark here that Eq. 6.7 changes, when the bias voltage is asymmetrically applied to the left and the right lead. Also the Coulomb diamond of the same physical system gain another shape then. Let us for example assume that  $V_L = 0$  and  $V_R = V_b$ . Then we find

$$V_b \propto \frac{\alpha_g}{1 - \alpha_R} V_g \quad \text{positive slope} \quad (6.8)$$

$$V_b \propto - \frac{\alpha_g}{\alpha_R} V_g \quad \text{negative slope} \quad (6.9)$$

Furthermore, if the bias voltage is sufficiently increased such that more than one chemical potential of the island fall into the transport window, the current is correspondingly increased, depending on the electron transport rate in the respective state.

### 6.1.4 Quantum dots

Any artificially structured physical system, in which the charge as well as the orbital degrees of freedom are quantized is called a *quantum dot* [167, 103]. Quantum dots are typically contacted the same way as the single electron transistor, but the number of gate electrodes can vary. Examples of quantum dot materials are single molecules [222], normal metals [230], superconductors [238, 55], ferromagnetic nanoparticles [95], self-assembled quantum dots [135], semiconductor lateral dots [283] and vertical dots [148], nanowires and carbon nanotubes [54, 187, 25] and graphene quantum dots [233].

Two effects dominate the physics of quantum dots. First, the Coulomb interaction between the electrons, which is an electrostatic effect. Second, the discrete energy spectrum due to the spacial confinement, which reproduces the behavior of an artificial atom. The simplest description of quantum dot systems is provided by the constant interaction model, introduced in the preceding section. The main attributes of this model are the constant capacitance  $C$  of the quantum dot, which is a sum of the capacitances participating in the formation of the dot, the energy spectrum of the quantum dot is independent of the capacitances and of the number of electrons on the dot.

However, deviations from this model occur quite often. The transport through a quantum dot is not necessarily ballistic anymore, since the electron scattering length might very well be smaller than the size of the dot. Further, the physics might be dominated in some parts of the spectrum by many-body effects, which goes beyond the standard constant interaction model, where the chemical part is only described by single-particle energy levels and the only many-body component is reflected in the electrostatic part by the Coulomb interaction. Therefore, effects of the electrodes and further electron interactions on the dot have to be taken into account separately to account for the true many-body spectrum.

Apart from ground states also excited states with the same number of particles, i.e., in the same particle sectors, occur and contribute to electron transport. Therefore the electrochemical potential describing the possible transitions have to be extended to account also for excited states:

$$\mu_N^{ab} = E_N^a - E_{N-1}^b, \quad (6.10)$$

where  $E_N^a$  is a many-body eigenenergy of the state  $a$  in particle sector  $N$  and  $E_{N-1}^b$  is a many-body eigenenergy of the state  $b$  in particle sector  $N - 1$ .

It is important to mention that tunnel processes mediated by a certain state are only possible, if this state has a finite possibility of being occupied [216, 103]. This is the reason why there is no current in the Coulomb blockade regime: All chemical potentials lie either above or below the transport window and therefore have a zero occupation probability.

Experimental transport measurements now offer the very useful potential of revealing the many-body spectrum of a quantum dot system - the so called *transport spectroscopy*. However,

the spectroscopy maps, typically in the form of differential conductances plotted in dependence of the bias and gate voltage, can be very complicated such that it is a difficult task to address certain measurements to physical effects or mechanisms. Therefore it is very helpful to calculate the current through a quantum dot in order to predict complicated spectroscopy maps and relate those to a physical model. The complexity arises from different tunnel couplings of different states, complicated dot Hamiltonians, selection rules, temperature effects and dissipation to the environment. These may result in effects such as negative differential conductance (NDC) or current suppression [312, 107] and so called fake resonances [249].

## 6.2 Model Hamiltonian and master equations of single electron transport

The description of the model Hamiltonian and the master equation approach for the description of single electron transport follows closely the presentation of the material in the book of Bruus and Flensberg [36].

### 6.2.1 Model Hamiltonian

The Hamiltonian describing the whole quantum dot setup can be written as

$$H = H_L + H_R + H_D + H_T \quad (6.11)$$

with the tunnel Hamiltonian

$$H_T = H_{TL} + H_{TR} \quad (6.12)$$

$$H_{TL} = \sum_{v_L v_D} \left( t_{L, v_L, v_D} c_{v_L}^\dagger c_{v_D} + t_{L, v_L, v_D}^* c_{v_D}^\dagger c_{v_L} \right) \quad (6.13)$$

$$H_{TR} = \sum_{v_R v_D} \left( t_{R, v_R, v_D} c_{v_R}^\dagger c_{v_D} + t_{R, v_R, v_D}^* c_{v_D}^\dagger c_{v_R} \right), \quad (6.14)$$

where  $c_{v_{L/R}}^{(\dagger)}$  annihilates (creates) an electron in the left/right lead in state  $|v_{L/R}\rangle$ .  $t_{r, v_r, v_D}$  is the corresponding tunnel matrix element from the dot to the lead and  $t_{r, v_r, v_D}^*$  from the lead to the dot.  $c_{v_D}^{(\dagger)}$  annihilates (creates) an electron on the dot in state  $|v_D\rangle$ .

The left lead Hamiltonian is defined as

$$H_L = \sum_{v_L} \epsilon_L c_{v_L}^\dagger c_{v_L} \quad (6.15)$$

and  $H_R$  is correspondingly defined.

The dot Hamiltonian  $H_D$  is some many-body Hamiltonian describing the quantum dot system.  $H_D$  has to be diagonalized and then we can write it as

$$H_D = \sum_{v_D} \xi_D c_{v_D}^\dagger c_{v_D}. \quad (6.16)$$

The eigenstates of  $H_D$  are many-body states and can incorporate complicated many-body effects.

### 6.2.2 Master equations of single electron transport

We assume that the coupling of the leads to the quantum dot is weak. Therefore the coherence time of the electrons  $\tau_{\text{coh}}$  is much smaller than the time between two tunneling events  $\tau_{\text{tunnel}}$ :

$$\tau_{\text{coh}} \ll \tau_{\text{tunnel}}. \quad (6.17)$$

Hence we can treat the quantum dot as an isolated system between the tunneling processes. We would like to know in which state  $|\alpha\rangle$  the system resides with which probability  $P(\alpha)$ . In equilibrium the answer is simply given by the Boltzmann distribution  $P(\alpha) = e^{E_\alpha/k_B T}/Z$ , where  $Z$  is the partition function.<sup>2</sup> In non-equilibrium the situation is different and we have to consider the tunneling rates into all states. Since the tunneling rate is small, coherent processes, which correspond to higher order tunneling processes will be suppressed and we can limit ourselves to first order in the tunneling rates described by *Fermi's golden rule*. The rate of a tunnel event between the left lead and the dot in a state  $|\alpha\rangle$  into a state  $|\beta\rangle$  is then given by

$$\Gamma_{\beta \leftarrow \alpha}^L = 2\pi \sum_{f_\beta i_\alpha} |\langle f_\beta | H_{TL} | i_\alpha \rangle|^2 W_{i_\alpha} \delta(E_{f_\beta} - E_{i_\alpha}), \quad (6.18)$$

where  $|i_\alpha\rangle$  is an initial state and  $|f_\beta\rangle$  a final state.  $W_{i_\alpha}$  is the thermal distribution function of the leads.

Since we have determined the rates by now, we can formulate the master equation:

$$\frac{d}{dt} P(\alpha) = - \sum_{\beta} \Gamma_{\beta \leftarrow \alpha} P(\alpha) + \sum_{\beta} \Gamma_{\alpha \leftarrow \beta} P(\beta), \quad (6.19)$$

where the first term on the right hand side describe tunneling out of state  $|\alpha\rangle$  and the second term describes tunneling into state  $|\alpha\rangle$ . This description is a semiclassical one, since the probabilities we deal with are classical probabilities. Here we are only interested in the steady state of the system, which is typically reached after all initial oscillatory processes have been damped out. Equation (6.19) simplifies to

$$\frac{d}{dt} P(\alpha) = 0 = - \sum_{\beta} \Gamma_{\beta \leftarrow \alpha} P(\alpha) + \sum_{\beta} \Gamma_{\alpha \leftarrow \beta} P(\beta). \quad (6.20)$$

Under the constriction  $\sum_{\alpha} P(\alpha) = 1$  we can solve this complete linear equations system. The complexity of the system depends on the number of states and electrons taken into account.

#### Rate equations for a quantum dot

We specify now Eq. (6.18) further with regard of an arbitrary quantum dot. As mentioned above in a quantum dot single many-body states are resolved. The tunneling rate given by Fermi's

<sup>2</sup>The dot can be assumed to be small compared to the environment, which allows for the use of the Boltzmann distribution.

golden rule can be written, e.g., for a tunneling event from the left lead on the dot, as

$$\Gamma_{\beta_{N+1} \leftarrow \alpha_N}^L = 2\pi \sum_{i_L v_L} \left| \langle \beta_{D,N+1} | \langle i_L | c_{v_L}^\dagger H_{TL} | \alpha_{D,N} \rangle | i_L \rangle \right|^2 W_{i_L} \delta(E_{\beta_{N+1}} - \varepsilon_{v_L} - E_{\alpha_N}), \quad (6.21)$$

where  $|\alpha_{D,N}\rangle |i_L\rangle$  is the initial state of the dot and the lead with  $N$  electrons on the dot and  $c_{v_L} |\beta_{D,N+1}\rangle |i_L\rangle$  is the final state with  $N+1$  electrons on the dot. Further, we have for the electrochemical potential of the dot  $\mu_{\beta_{N+1}, \alpha_N} = E_{\beta_{N+1}} - E_{\alpha_N}$ . The electron distribution in the leads is described by the Fermi function  $n_F(\varepsilon) = 1 / (e^{(\varepsilon - \mu)/k_B T} + 1)$ . Using this and the explicit tunnel Hamiltonian, we find

$$\Gamma_{\beta_{N+1} \leftarrow \alpha_N}^L = 2\pi \sum_{v_L} \left| \langle \beta_{D,N+1} | \sum_{v_D} t_{L,v_L,v_D}^* c_{v_D}^\dagger | \alpha_{D,N} \rangle \right|^2 n_F(\varepsilon_{v_L} - \mu_L) \delta(\mu_{\beta_{N+1}, \alpha_N} - \varepsilon_{v_L}). \quad (6.22)$$

The reverse tunnel event of an electron from the dot on the left lead is given by

$$\Gamma_{\beta_{N+1} \leftarrow \alpha_N}^L = 2\pi \sum_{v_L} \left| \langle \beta_{D,N-1} | \sum_{v_D} t_{L,v_L,v_D} c_{v_D} | \alpha_{D,N} \rangle \right|^2 (1 - n_F(\varepsilon_{v_L} - \mu_L)) \delta(\mu_{\beta_{N-1}, \alpha_N} - \varepsilon_{v_L}). \quad (6.23)$$

After the computation of all rates, we can write down the master equations and solve them numerically. Only the tunnel matrix elements have to be put in manually and desire for a reasonable estimate.

## 6.3 Carbon nanotubes and carbon nanotube peapods

In this section we want to introduce the basic properties of single-wall carbon nanotubes (SWCNT). The most comfortable way is to start with the explanation of *graphene*, which can be rolled up to SWCNTs.

### 6.3.1 Graphene

Graphene [224, 40] is the mother of a whole class of carbon-based materials, see Fig. 6.7. It is made out of carbon atoms arranged on a honeycomb lattice made out of hexagons. Fullerenes [8] can be thought of as wrapped graphene sheets with additionally introduced pentagons causing curvature defects. Carbon nanotubes (CNT) are rolled up graphene slices [256] such that tubes are formed. The underlying electronic properties of graphene also determines the electronic properties of the CNT. The daily use of graphite, which is made out of stacks of graphene, is found in the pencil [229] invented in 1564. It is astonishing that isolated graphene has been observed first only in 2004 by Novoselov and Geim<sup>3</sup> [206], who produced single graphene sheets by mechanical exfoliation of graphite.<sup>4</sup>

<sup>3</sup>Novoselov and Geim won the Nobelprize 2010 for their discovery.

<sup>4</sup>They used Scotch<sup>®</sup> tape for this purpose.

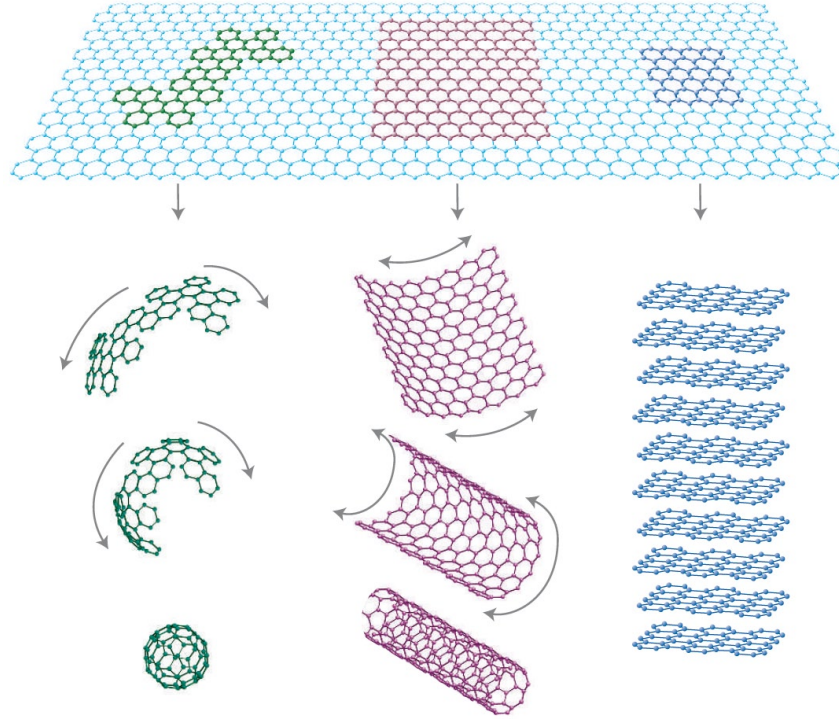


Figure 6.7: Mother graphene: On top a single graphene sheet is depicted. Cutting out a corresponding shape, a fullerene can be wrapped (most left), a CNT can be rolled up (middle) or a piece of graphite can be stacked (right). Figure is taken from [81].

The lattice structure of graphene is shown in Fig. 6.8. The lattice vectors are given by

$$a_1 = \frac{\sqrt{2}a}{2} (1, \sqrt{3}) \quad a_2 = \frac{\sqrt{2}a}{2} (-1, \sqrt{3}), \quad (6.24)$$

where  $a = 2.49 \text{ \AA}$  is the lattice constant of graphene and the nearest neighbor distance is  $a/\sqrt{3} = 1.44 \text{ \AA}$ . Each primitive unit cell consists of two atoms and therefore graphene can be decomposed into two sublattices. The reciprocal lattice vectors are given by

$$b_1 = \frac{2\pi}{3a} (\sqrt{3}, 1) \quad b_2 = \frac{2\pi}{3a} (-\sqrt{3}, 1). \quad (6.25)$$

The electronic structure of graphene is dominated by  $sp^2$  hybridization. In plane, from now on referred to as the  $(x,y)$ -plane, the atoms are strongly bound by  $\sigma$  bonds formed due to the hybridization of the  $s$  orbital with two of the  $p$  orbitals. The  $p_z$ -orbitals are therefore unaffected by the hybridization and form the so called  $\pi$  bands  $\pi$  and  $\pi^*$ . The lower  $\pi$  band is completely filled with electrons, while the upper  $\pi^*$  band is empty.

### Tight-binding dispersion relation

A simple tight-binding Ansatz [242, 308] leads to the dispersion relation of graphene. The fact that we have two electrons per unit cell will necessarily lead to two bands. In a tight-binding

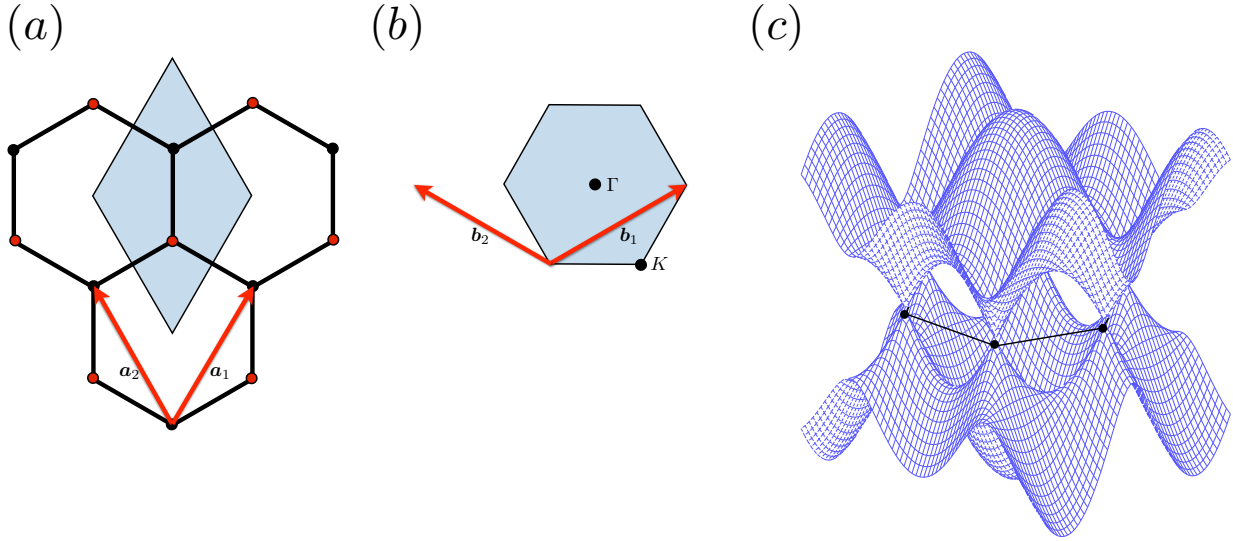


Figure 6.8: Lattice structure of graphene. (a) Real space lattice: The shaded region corresponds to the primitive unit cell and contains two atoms. (b) The first Brillouin zone of the reciprocal lattice. The reciprocal lattice is again a hexagonal one, but rotated by 30 degree. (c) The dispersion relation of graphene obtained from a tight-binding calculation.

calculation using Bloch's Theorem, treating the  $p_z$  orbitals locally and incorporating only nearest neighbor interaction we find

$$\epsilon_k = \pm \sqrt{1 + 4 \cos\left(\frac{3}{2}ak_y\right) \cos\left(\frac{\sqrt{3}}{2}ak_x\right) + \cos^2\left(\frac{\sqrt{3}}{2}ak_x\right)}, \quad (6.26)$$

which is depicted in Fig. 6.8. The two bands touch, where  $\epsilon_k = 0$ , which is the case at six points. But only 2 of these points are inequivalent and called *Dirac points*  $K$  and  $K'$ . Since the upper band is completely empty and the lower band filled, graphene is a *zero gap* semiconductor. Close to  $K$  or  $K'$  the dispersion relation can be linearized around the Fermi surface with a corresponding *Fermi velocity* of  $v_F = 3ta/2 \approx 1 \cdot 10^6$  m/s, where  $t$  is the intraband nearest neighbor hopping constant.

### Graphene as a quantum dot

The linear dispersion relation is one of the most striking properties of graphene. The electrons close to the Fermi surface can be treated as relativistic Dirac electrons, which are massless and have a constant velocity, which is the Fermi velocity  $v_F$  for graphene [40, 134] instead of the velocity of light in quantum electrodynamics [163]. However, this enables also the mechanism of *Klein tunneling* [136, 134] in graphene, which means perfect transparency of potential barriers, especially for normal incident electrons. The transparency condition is fulfilled for a potential barrier height  $V$  exceeding the rest mass of the electron. Since this is zero in graphene a sufficient large  $V$  is easily achieved and therefore electrostatic gating in order to define a quantum dot is not straightforward.

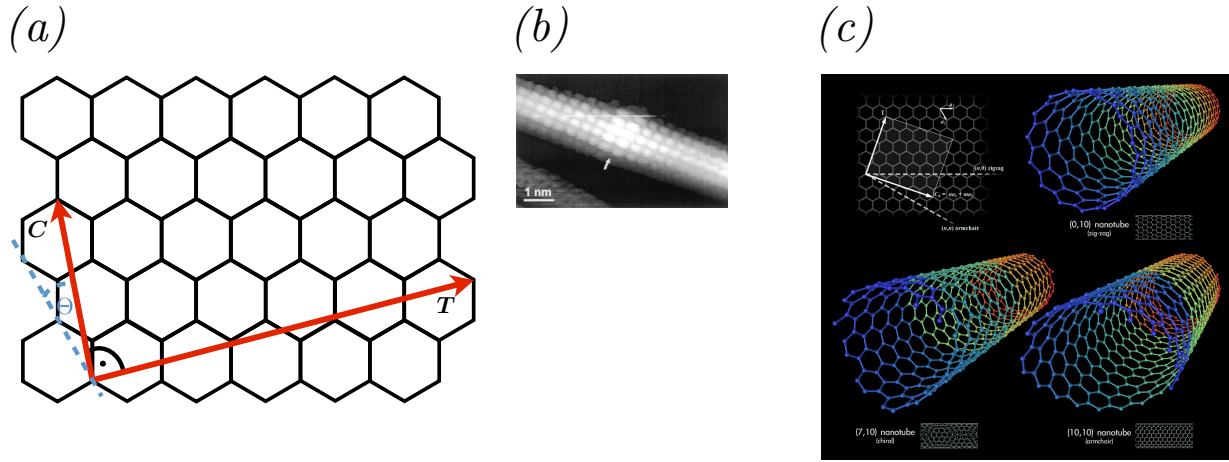


Figure 6.9: (a) Chiral vector  $C$ , chiral angle  $\Theta$  and translation vector  $T$  in a carbon nanotube. (b) Sequential electron tunneling micrograph taken from [219] showing an SWCNT. (c) Classification of zigzag (top right), chiral (bottom left) and armchair (bottom right) CNTs. The picture is published under [83].

In order to circumvent this problem it is suggested in [275] to consider bound states of electrons with a movement transversal to the boundaries of the quantum dot with respect to different boundaries. Further, non-uniform charge doping of the different layers in bi-layer graphene [225] provides a platform for assembling quantum dots in graphene structures, as well as introducing a gap in graphene nanoribbons [145].

### 6.3.2 Single-wall carbon nanotubes

Carbon nanotubes (CNT) have first been synthesized by Iijima<sup>5</sup> [121] using an arc discharging evaporation method. These first nanotubes have been of the *multi-wall carbon nanotube* type (MWCNT), where several nanotubes with different diameters each made from a mono-layer of carbon are put into each other. The diameter of a typical MWCNT is 3-10 nanometers [121, 170, 256].

More sophisticated and developed techniques [170, 128] allow for the controlled production of either MWCNTs or *single-wall carbon nanotubes* (SWCNT), which consist of a single tube. The structure and circumference of an SWCNT is defined by a pair of indices  $(n, m)$ , which determines the so called *chiral vector*  $C = na_1 + ma_2$ . The translation vector  $T$  times a positive integer  $l$  fixes the length of the nanotube, see Fig. 6.9. The chiral angle  $\theta$ , see Fig. 6.9(a) determines whether a SWCNT is for example one of the well-know types of SWCNT like a zigzag ( $\theta = 0^\circ$ ) or armchair ( $\theta = 30^\circ$ ) SWCNT.

SWCNT have a gapless band structure [42, 219, 194, 102, 51], if the Dirac points of graphene  $K$  are allowed and therefore  $k = K$ , where  $k$  is an arbitrary permitted momentum and can be expressed in terms of the reciprocal lattice vectors  $G$  and  $L$ , where  $L$  points into the directions of the tube axis. Due to the length of the tube,  $L$  can be tackled as quasi continuous and therefore the condition in the direction of  $L$  can always be fulfilled. Hence, only  $G$  is decisive and one

<sup>5</sup>Iijima called the nanotubes *microtubulus of graphitic carbon*.

finds

$$\frac{n-m}{3} \in \mathbb{Z}, \quad (6.27)$$

as a condition for a gapless band structure. However, it turns out in practice that only armchair SWCNT show true gapless behavior [42, 218], which is due to curvature effects [26] leading to an admixture of  $sp^3$  hybridization.

In this thesis we are especially interested in metallic carbon nanotubes and will restrict ourselves to these. The gap between different subbands in armchair nanotubes is approximately 1 eV  $\approx 10^4$  K, which makes SWCNTs true one dimensional systems. The decisive physics is furthermore determined from the bands crossing the Fermi surface in the  $K$  points, which can even be linearized for small temperatures and this results in the well known linear dispersion relation of armchair SWCNTs with a discretization due to the finite length of the tube and with respect to the open boundary conditions [144].

The one dimensionality makes carbon nanotubes ideal test candidates for the Luttinger liquid theory [65] and in [28, 329, 122] a power-law scaling of the conductance in agreement with Luttinger liquid theory has been found. Ballistic transport at low temperature in carbon nanotubes could be observed in [125, 13] allowing for an efficient implementation of field-effect transistors.

### Quantum dots from single wall carbon nanotubes

The first carbon nanotube quantum dot has been realized by contacting a bundle of SWCNTS [29] and transport measurements revealed clear indications of Coulomb charging effects modified by the discretized energy level structure of the tubes. A quantum dot with a single SWCNT has been assembled in [291]. The length of the quantum dot and therefore the electronic level quantization is determined by the position of the source and drain electrode ( $\approx 100$  nm). Due to the two bands of armchair SWCNTs and the discretization a typical four-fold repetition period of Coulomb diamonds would be expected in the transport map: Three small and one large diamond should alternate. However, this symmetry is often broken [257], which is captured in the extended constant interaction model [257, 212] often used for the description of the energy level structure of carbon nanotube systems. The model includes an intra-band energy splitting  $\Delta$ , an inter-band energy shift  $\delta$ , a spin exchange constant  $J$  and a correction  $dU$  to the charging energy, when a sub-band is doubly occupied. The parameters of the model can be extracted from measurements [64].

Apart from weak coupling transport measurements also the Kondo effect [208], Kondo correlations [124] and the non-equilibrium triplet Kondo effect [220] could be measured in SWCNTS. Also superconducting leads in combination with SWCNTs have been examined [23, 94]. The application of multi top gates to an SWCNT quantum dot leads to the formation of multi-quantum dot systems in a single SWCNT [258].

### Carbon nanotube peapods

*Carbon nanotube peapods* [150] are single-wall carbon nanotubes filled with  $C_{60}$  molecules, so called *fullerenes* [151]. These peapods have been observed first in a high resolution transmission

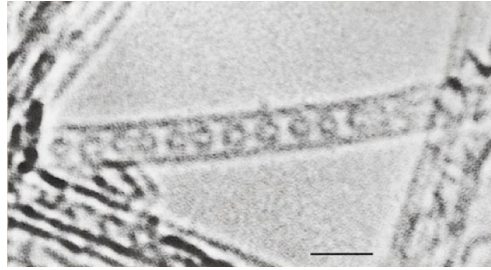


Figure 6.10: A single-wall carbon nanotube peapod. The scale bar is 2.0 nanometers. The picture is taken from [282].

electron microscopy experiment (HRTEM) [282]. Due to curvature effects of the SWCNT the binding energy of, e.g., a  $C_{60}$  inside the SWCNT is approximately 2 eV [150] and therefore six times larger than the corresponding binding energy of a  $C_{60}$  coupled to the SWCNT on the outside [88]. A review on peapod fabrication can be found in [196]. The filling can be either in-situ, where the SWCNT is filled while it is formed, or ex-situ, where the SWCNT is filled after it has formed. In the latter method, defects in the structure of the SWCNT play an important role, because there the fullerenes can enter the tube [175]. The characterization of peapods can be done via Raman scattering techniques [156], where basically an overlay of  $C_{60}$  and SWCNT scattering properties is found. The electronic properties of peapods are reviewed in [150]. In [210] a total-energy electronic structure calculation has been performed and it has been found that two additional bands close to the Fermi surface appear. Further, a strong hybridization between the lowest unoccupied molecular orbital of  $C_{60}$  and the SWCNT has been calculated [131]. By endohedrally filling the fullerenes with a spin carrying atom, e.g., N or Sc, the possibility is opened up for using such a sample as a quantum computational device, where the spin inside the fullerenes carries the quantum information [18]. Experiments using peapods as single electron transistors have been performed in [302, 235, 195].



# Chapter 7

## Transport via coupled states in a C<sub>60</sub> peapod quantum dot

In this chapter we review a sequential electron transport experiment performed on a carbon nanotube peapod device, see Sec. 6.3 and corresponding transport theory. Most of the material in this chapter has been published in

*A. Eliassen, J. Paaske, K. Flensberg, S. Smerat, M. Leijnse, M. R. Wegewijs, H. I. Jørgensen, M. Monthieux, J. Nygård — "Transport via coupled states in a C<sub>60</sub> peapod quantum dot" Phys. Rev. B **81**, 155431 (2010).*

Composite structures provide the possibility of tailored production of electronic devices on a nanometer scale. Peapods are devices, where the electronic properties might be constructed by the controlled placement of the fullerenes inside the SWCNT. In Chapter 8 we will give another example of such a composite structure, namely carbon nanotube ropes.

In the following we will first briefly introduce why peapods are interesting. Then we review the experiment and the modeling of the system. We close this chapter with a discussion about the nature of the observed features.

### 7.1 Introduction

In general, the interaction between quantum dot systems of different nature and the corresponding transport signatures are very interesting. A single-wall carbon nanotube peapod, which is an SWCNT with equidistantly placed fullerene molecules inside, is the next more complex system starting from a pure SWCNT. Since the advent of peapods [282] and the possibility of high-yield production of peapods [281] many experiments have been done. The aim of many of these experiments is to find a way to address the fullerenes inside the tube via the tube itself, e.g., by means of spin-exchange. Band structure calculations [210, 131, 172, 330, 59, 146] have shown that hybridization between an SWCNT and a metallic C<sub>60</sub> can form an additional electronic band, which crosses the Fermi-Energy depending on the chirality of the tube. But, there is no experimental evidence for this so far.

Scanning tunneling microscopy (STM) has been used in order to examine the electronic level structure, which is different in comparison to the pure SWCNT level structure [119].  $C_{60}$  molecules have a five times degenerate highest occupied molecular orbital (HOMO)  $h_u$  separated from the lowest three times degenerate unoccupied molecular orbital  $t_{1u}$  by a gap of  $\approx 2$  eV. While a negative STM sample bias voltage does not show any difference of the peapod compared to a pure SWCNT, a positive bias voltage clearly reveals the fullerenes influence inside the tube. Therefore only the unoccupied orbitals play a significant role. A semi-empirical model with coupling between the SWCNT  $\pi$ -orbitals and the  $t_{1u}$  states of the  $C_{60}$  can explain the observed features. The hybridization coupling constant is rather strong with 1.25 eV. Within the model in [119] the direct overlap of wave functions between two neighboring  $C_{60}$  turned out to be negligible. From density-functional calculations [172] a hybridization of  $\approx 0.1$  eV has been found. Photoemission experiments on peapod samples [272] even showed no evidence for hybridization between  $C_{60}$  molecules and tube.

The electronic level structure of peapods has also been examined in three terminal transport experiments [302, 235, 333, 195], but the results remain inconclusive. In [302, 235] the Coulomb diamond structures of the differential conductance map show no clear difference compared to a pure SWCNT conductance map. In [333, 195] irregular diamond patterns are measured and it is suggested that this is due to modulations caused by the encapsulated fullerenes. Since it is not possible to combine imaging techniques with transport measurements on the same sample, the structures measured in [302, 235, 333, 195] might be different. Therefore, more experiments on high-quality peapod devices are necessary in order to estimate the interaction between fullerenes and the encapsulating SWCNT. The question, whether a SWCNT peapod can be used in tailored nanoelectronic applications is still open.

In this chapter we report on a new set of detailed low-temperature measurements for a peapod quantum dot in the weakly coupled Coulomb blockade regime. As also in [302, 235] we find a very regular pattern of Coulomb diamonds resembling discretized charging effects. Furthermore, we also observe avoided crossings between two different gate coupled states in more than 400 diamonds. We can attribute these to a weak hybridization between the  $C_{60}$  molecules and the SWCNT. The different gate coupling is due to the electric screening of the fullerenes from the gate via the tube. The experimental findings can be reproduced in a transport calculation using transport theory in lowest order and a simple model incorporating the hybridization between the tube and the fullerene orbitals. We tentatively propose these signatures to relate to a short chain of  $C_{60}$ -molecules inside the CNT, residing close to one electrode.

## 7.2 Experimental results

### 7.2.1 The device

The single walled  $C_{60}$  peapods of purity grade 90-95% (see Ref. [302] for synthesis details), were suspended in dichloroethane by sonification and dispersed in the form of droplets onto an isolating  $SiO_2$  layer of thickness 500 nm, thermally grown on top of a highly doped silicon substrate. By use of atomic force microscopy imaging, individual tubes were identified and

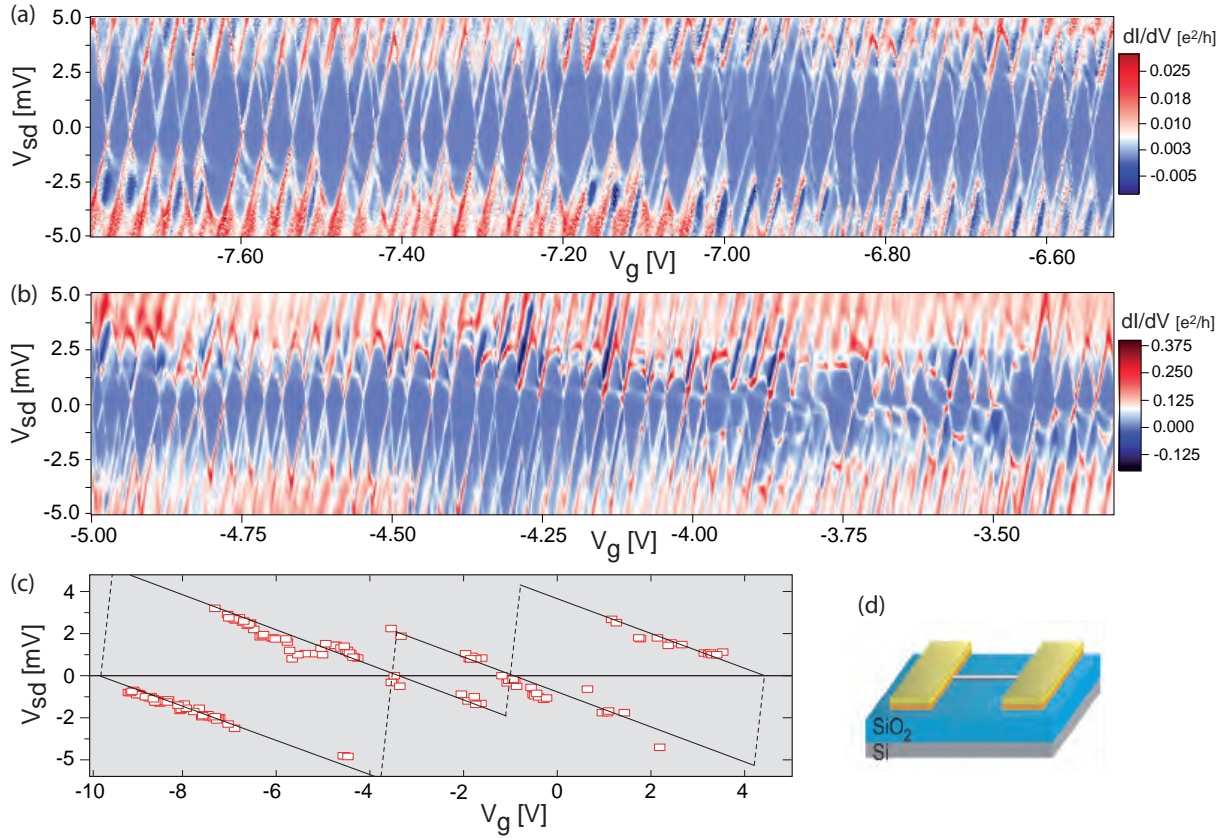


Figure 7.1: (a) and (b) Stability diagram, i.e., conductance ( $dI/dV_{sd}$ ) as a function of source-drain bias ( $V_{sd}$ ) and gate-voltage ( $V_g$ ) at 300 mK, showing a regular Coulomb blockade diamond pattern with four-electron shell structure throughout the measured gate-range. Diamonds are perturbed by a weakly gate-dependent feature superimposed on the entire structure. (c) Observed avoided crossings over the entire gate-range (red rectangles). Black lines are guides to the eye, outlining the edges of the "impurity diamond". (d) Sketch of the peapod quantum dot device.

then contacted by evaporated source and drain Ti/Au-electrodes (25 nm/25 nm) using e-beam lithography. The device layout, including the electrodes separated by  $L \approx 600$  nm, is shown schematically in Fig. 7.1d.

## 7.2.2 Transport measurements

We have performed electronic transport measurements down to 300 mK in a  $^3\text{He}$  cryostat, using standard lock-in techniques (AC source drain voltage  $50 \mu\text{V}$  RMS). Sweeping the gate-voltage  $V_g$  and measuring the linear conductance, we observe Coulomb blockade peaks in metallic peapod samples [302]. Here we concentrate on a single sample exhibiting highly regular Coulomb blockade peaks in the region  $-10 \text{ V} < V_g < 5 \text{ V}$ , representative gate-ranges being shown in Fig. 7.1a, b. We observe a clear four-electron shell structure similar to that of empty CNTs [37, 168, 257].

Unlike the device measured in Ref. [195], which also exhibited traces of a four-electron shell, there is no reason to believe that the device studied here has been accidentally partitioned into

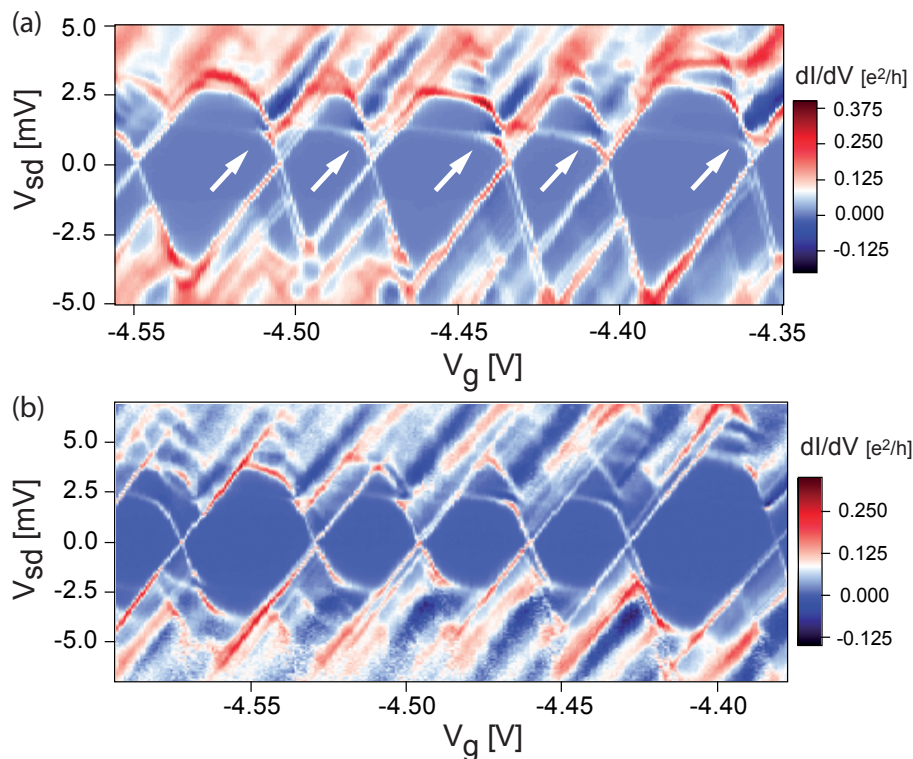


Figure 7.2: (a) Zoom in on a representative range of gate-voltages in Fig. 7.1b. At positive bias we observe a series of avoided crossings with a line of much lower gate-coupling than the main diamond edges. (b) The same device after suspension. Avoided crossings are seen at both negative and positive bias in the displayed gate-range.

smaller sub-systems. In Ref. [195], the presence of distinct gate-voltage regions with rather different, and surprisingly large diamond sizes ( $E_{add} \simeq 10 - 20$  meV for a peapod of length 500 nm), was interpreted as the tube being separated into two or more smaller 'dots'.

Having established the salient quantum dot features of these transport data presented in Fig. 7.1(a),(b) as essentially CNT-like, one notices a distinct perturbation of the entire stability-diagram: a very weakly gate-dependent resonance line passes through the diamonds at positive and/or negative bias, depending on the gate-voltage, and anti-crosses with the edges of the CNT Coulomb diamonds. Fig. 7.1c shows the gate- and bias-positions of these avoided crossings over the entire gate-range where such features were observed. The weakly gate-dependent resonance and the associated avoided crossings are seen more clearly in Fig. 7.2a, which zooms in on a representative gate-range in Fig. 7.1b. Due to the weak gate-dependence this line might have been assigned to inelastic cotunneling [53]. This would, however, be inconsistent with the observed avoided crossings with one side of the CNT diamond edges. Furthermore, the weakly gate-dependent resonance does not occur symmetrically at the same energy at positive and negative bias, as inelastic cotunneling resonances do, and for most gate-voltages it is only present either at positive or negative bias-voltage and strongly perturbs the single-electron tunneling (SET) region on the corresponding bias-side, showing broad regions of negative/positive differential conductance (NDC/PDC).

As will be further substantiated below, all of these observations are instead consistent with SET through a state which:

1. is much weaker coupled to the back-gate than are the levels of the CNT;
2. hybridizes with the levels of the CNT;
3. has a significant capacitive and tunnel coupling only to the source lead. We refer to this state as an "impurity orbital" to emphasize the general nature of the transport effect in the following analysis. After this we will argue that the impurity consists of a short chain of  $C_{60}$  molecules inside the tube.

## 7.3 Peapod model and transport calculations

Independent of the precise nature of the impurity we can formulate a general model invoking a SWCNT model and an impurity state and a connection between both. From transport calculations we can extract valuable information and the coupling to the SWCNT.

### 7.3.1 Extended constant interaction model

A constant interaction (CI) model describing SWCNTs has been proposed in [212, 64, 180, 257]. The energy of a SWCNT state in this CI model is given by

$$E^t = \sum_{\mu, \sigma, l} \varepsilon_{l\mu} n_{l\mu\sigma}^t + E_C^t N_t^2 + \delta U \sum_{\mu, l} n_{l\mu\uparrow} n_{l\mu\downarrow} + J \sum_{\mu\mu'} N_{\mu\uparrow} N_{\mu'\downarrow}, \quad (7.1)$$

where  $l$  numbers the states on sub-band  $\mu = A, B$  and  $\sigma = \uparrow, \downarrow$  is the spin index.  $n_{l\mu\sigma}^t$  is the number of electrons on the tube in state  $l$  on sub-band  $\mu$  with spin  $\sigma$ . The orbital energy is

$$\varepsilon_{l\mu} = \begin{cases} l \cdot \Delta & \mu = A \\ l \cdot \Delta + \delta & \mu = B \end{cases}, \quad (7.2)$$

where  $\Delta$  is the intra sub-band splitting and  $\delta$  is the inter sub-band shift. The Coulomb charging energy  $E_C^t$  of the SWCNT is as defined in Chapter 6.  $N_t = \sum_{\mu\sigma} N_{\mu\sigma}^t$  is the total number of excess electrons with  $N_{\mu\sigma}^t = \sum_l n_{l\mu\sigma}^t$ . Electrons on the same orbital cause an excess Coulomb energy  $\delta U$  and from spin flip processes an energy of  $J$  is gained. To account for the energy of an impurity inside the dot we assume that it has a charging energy  $E_C^i$  and that electrons on the SWCNT and the impurity influence each other via the tube-impurity Coulomb interaction  $E_C^{t-i}$ . For the impurity we find

$$E^i = E_C^i N_i^2 \quad (7.3)$$

and in total

$$E = \sum_{\mu, \sigma, l} \varepsilon_{l\mu} n_{l\mu\sigma}^t + E_C^t N_t^2 + \delta U \sum_{\mu, l} n_{l\mu\uparrow} n_{l\mu\downarrow} + J \sum_{\mu\mu'} N_{\mu\uparrow} N_{\mu'\downarrow} + E_C^i N_i^2 + E_C^{t-i} N_i \cdot N_t, \quad (7.4)$$

where  $N_i$  is the number of electrons on the impurity. Equation 7.4 describes what we call the *extended constant interaction model* (eCI).

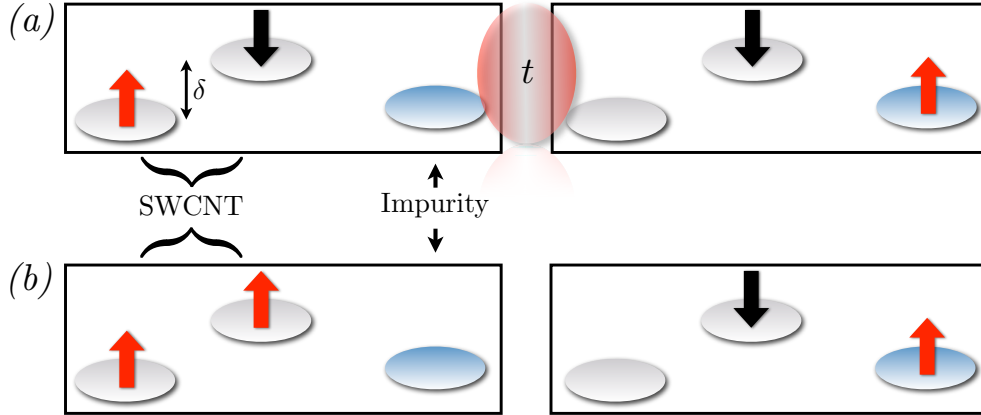


Figure 7.3: (a) Each box (left and right, respectively) contains a possible spin state configuration of the tube-impurity system. If the energy of the two states adjusted by gate and bias voltage is close the two states hybridize. A single electron hopping process will transform the right state into the left state and vice versa. (b) Hybridization is disallowed in this case, since the total quantized spin of the two state configurations is different. A hopping event cannot transform the states into each other.

### Explicit model

The explicit model we use is shown in Fig. 7.4(b). We use two orbitals from the SWCNT, one of each sub-band. These two orbitals are therefore split by the inter sub-band shift  $\delta$ . Further we employ one impurity orbital. The justification of using only one impurity level is given in Fig. 7.1(c) from the extremely different size of the Coulomb diamonds of the impurity, which suggests a very large level spacing of the impurity orbitals and therefore it suffices to take only the lowest one into account.

### Hybridization

As we will see below, the observed transport features can only be explained, if we allow that electrons can tunnel from the tube to the impurity and vice versa. In molecular physics this phenomenon is also well known under the name *hybridization*. This leads to non-zero off-diagonal matrix elements in the Hamiltonian, if hybridization between two states is possible, see Fig. 7.3. Assuming a system with at least two states, which hybridize, we would find in a matrix representation

$$H = \begin{pmatrix} \ddots & & & & \\ & E_i(V_b, V_g) & & & \\ & & \ddots & & \\ & & & t & \\ & & & & E_j(V_b, V_g) & \\ & & & & & \ddots \end{pmatrix}, \quad (7.5)$$

where the energies  $E_i(V_b, V_g)$  and  $E_j(V_b, V_g)$  can depend differently on the gate and bias voltage. Therefore the energies can be brought into resonance, which results in noticeable hybridization

effects. In the differential conductance map hybridization leads to an avoided crossing of two excitation lines at the point where they would cross without hybridization.

The eCI and the hopping of electrons form our *many-body peapod model*. The Hamiltonian of the model has to be diagonalized exactly for every gate- and bias-voltage point.

### Parameters

The parameters of the eCI can be extracted directly from the experimental measurements, see Fig. 7.2. We find

- $E_C^t = 2.9$  meV (charging energy),
- $\delta = 1.2$  meV (subband splitting),
- $dU = 0$  meV (excess Coulomb energy) and
- $J = 0$ .

Extracting  $J$  is very difficult since it invokes excited states. Therefore we set  $J = 0$  making sure that no qualitative differences occur.

The charging energy of the impurity is

- $E_C^i = 2.5$  meV,

which can be read off from the smaller diamond in the middle of Fig. 7.1. The strength of the hybridization can be read off from the avoided crossings and we find

- $t \approx 0.15$  meV.

The tube-impurity charging energy is estimated as

- $E_C^{t-i} \approx 0.1$  meV.

### Gate- and bias coupling

In the experiment, see Figs. 7.1 and 7.2, the bias voltage is only applied to the source and the drain lead is grounded:

$$V_{sd} = V_s \propto -|e|\mu_s \quad (7.6)$$

$$V_d = 0. \quad (7.7)$$

The voltage dependence of the energy of the states fulfills the proportionality

$$\varepsilon_m \propto -|e|\alpha_g^m V_g - |e|\alpha_s^m V_{sd}, \quad (7.8)$$

with  $m = 1, 2$  for the two orbitals of the SWCNT, respectively, and  $m = i$  for the impurity orbital. Furthermore, the coupling constants are defined as  $\alpha_k^m = \frac{C_k^m}{C^m}$  and  $C^m = C_s^m + C_d^m + C_g^m$ . In Fig. 7.4c a schematic Coulomb diamond including avoided crossings is shown. From the slopes of the respective excitation lines one can extract the coupling constants. Therefore reading off the slopes of the respective excitation lines in the experimentally measured conductance map we extract for the SWCNT coupling constants

- $\alpha_g^{1,2} = 0.104$
- $\alpha_s^{1,2} = 0.298$ .

Extracting the impurity coupling constants is much more difficult. The experiment reveals only the excitation line which is due to the drain resonance. This is simply not enough to read off the couplings. Furthermore, the very steep slopes, which one could divine in Fig. 7.1 are not convenient for this purpose, since the error is too large. However, we have another line at hand, the NDC/PDC feature, which is depicted in Fig. 7.4(c) as a grey broad band, which is not necessarily parallel to the Coulomb diamond edges. Making use of this slope we can extract

- $\alpha_g^i = 0.0055$
- $\alpha_s^i = 0.99$ .

From this we can assume that the impurity chemical potential is pinned to the source chemical potential. Further, the impurity has to be of a local nature and is situated very close to the source.

### Tunnel couplings to the leads

The tunnel couplings to the leads can not be read off from the differential conductance map or any other experimental transport measurement. Therefore, we have to employ extensive numerical studies to estimate the tunnel couplings. For the SWCNT we find

- $\Gamma_s^t = \Gamma_d^t$

to be suitable. We checked further that small deviations from this symmetry do not change the qualitative findings of our calculations. For the impurity we find corresponding to the local nature and its settling close to the source

- $\Gamma_s^i = 4\Gamma_{s,d}^t$
- $\Gamma_d^i = 0$ .

### 7.3.2 Transport calculation results

We will show now, that standard master equations, i.e., lowest order perturbation theory in the tunnel coupling to the leads, see also Sec. 6.2.2, suffice to explain the significant transport signatures observed in the experiment.

The agreement between the experiment shown in Fig. 7.2(a) and the theory calculation shown in Fig. 7.4(a) is striking. We will now explain significant transport signatures occurring in the experiment as well as in the model calculation.

1. The nearly horizontal conduction line, which passes through the Coulomb diamonds at positive bias voltage shows strengthened avoided crossings with the source SET resonances (white arrows in Fig. 7.2(a)). These avoided crossings are due to hybridization, which occurs if the impurity orbital and an SWCNT orbital share one electron and if the two corresponding many-body states are in resonance with each other.

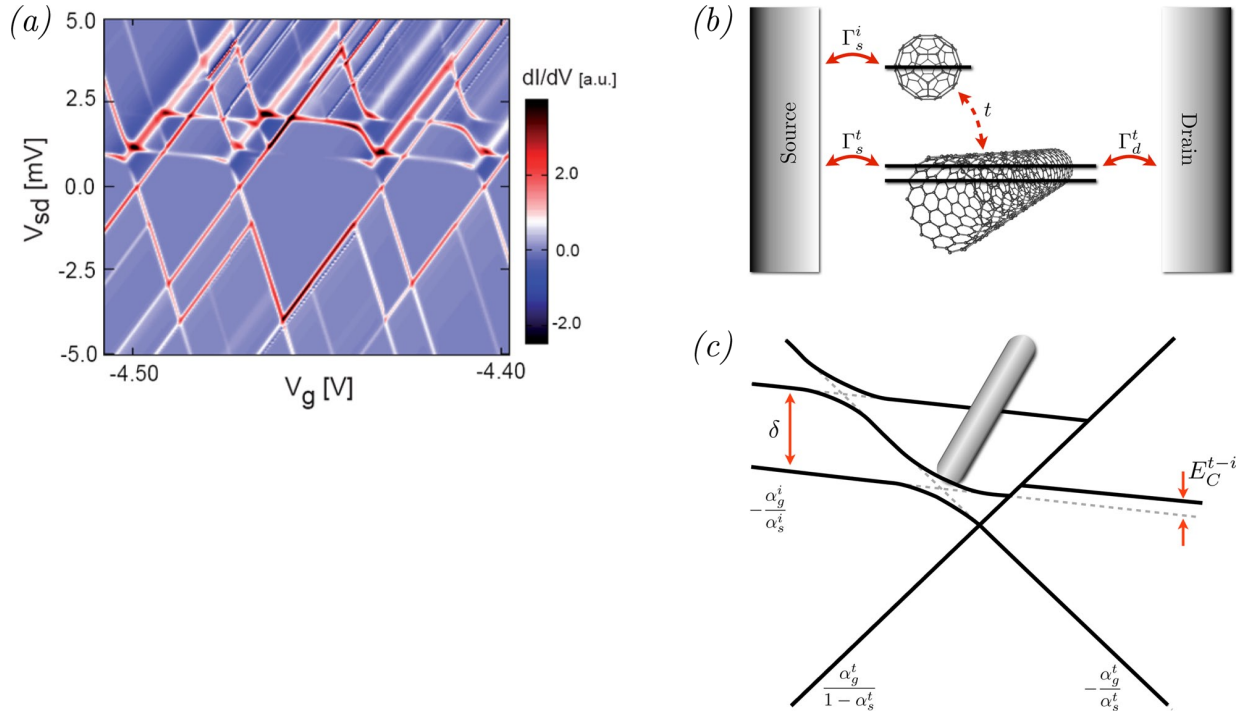


Figure 7.4: (a) Calculated stability diagram showing  $dI/dV_{sd}$  as a function of source-drain bias ( $V_{sd}$ ) and gate-voltage ( $V_g$ ) for a gate-voltage range corresponding to the three central diamonds in Fig. 7.2a. In the calculation we use the experimental temperature  $T = 300$  mK, but neglect tunnel broadening. Therefore all resonances are somewhat sharper than in the experiment. (b) Model system used in the calculation. The impurity level hybridizes with both CNT subbands (amplitude  $t$ ), but is only tunnel coupled to the source (rate  $\Gamma_s^i$ ). Both CNT subbands are coupled with the same rate to source and drain ( $\Gamma_s^t = \Gamma_d^t$ ). (c) Sketch of avoided crossings. The capacitances associated with the tube and impurity can be read off from the slope of the resonance lines far from the avoided crossing.

2. Within the SET region we find a broad structure consisting of a positive differential conductance (PDC) followed by a negative differential conductance (NDC), nearly parallel to one of the Coulomb diamond edges. These features emerge from the avoided crossings and along these broad lines, also indicated in Fig. 7.4(c) as a broad grey line, the energies of the two states causing the avoided crossing are resonant. This leads to an interference terms in the tunnel rates causing Fano resonance [67] shaped variations of the differential conductance. It is important to note that this does not correspond to the usual resonance of a dot chemical potential with one of the lead chemical potentials. It corresponds to a resonance between the SWCNT and the encapsuled impurity.
3. The nearly horizontal impurity conduction line is not visible at negative bias, which is due to the source coupling of the impurity chemical potential. Therefore a very high energy would be needed to shift the impurity state into the transport window at negative bias.
4. There is an obvious even-odd effect of the avoided crossings going from one diamond to the next: The magnitude of the gap is alternating in each subsequent diamond. In the

large diamond in the middle of Fig. 7.4(a) the gap is smaller than in the two neighboring diamonds on the left and on the right. This is due to a stronger hybridization of filled SWCNT sub-bands with the impurity orbital.

5. The impurity conduction line is not running straight through all diamonds, but makes a small jump at each drain resonance Coulomb diamond edge, because a finite capacitive coupling between the SWCNT and the impurity exists, which we denoted above as the tube-impurity charging energy and can be estimated from the jump at the Coulomb diamond edge as 0.1 meV.
6. The magnitude of the impurity conduction line strongly depends on the applied voltages. Especially, further away from the avoided crossings the line fades out. This is another piece of evidence that the impurity is local and located close to the source and has no coupling to the drain. A finite drain coupling would enable transport through the impurity alone, but with a zero drain coupling transport channels along the impurity run dry away from the avoided crossings, where hybridization allows transport through the impurity.
7. We also find higher lying excitation inside the Coulomb diamonds. These correspond to  $\delta = 1.2$  meV and corresponds to tunneling with excited states of the SWCNT. This is possible, since hybridization causes an effective coupling between the sub-bands.

## 7.4 Nature of the impurity state

Up to now we have considered a general impurity without specifying its concrete nature. The simplest idea would be an accidental impurity residing outside the tube. This would be similar to the explanation given in [120], without fullerenes.

However, after the transport measurements the device has been modified: It has been covered with PMMA and the center of the CNT has been suspended with electron beam lithography followed by wet etching in a buffered solution of hydrogenic acid. This has created a 5 nm deep trench in the  $SiO_2$  layer, reducing effects from inhomogeneities. Performing low temperature measurements for second time gives the result shown in Fig. 7.2(b), which is very similar to the result in Fig. 7.2(b). Especially, we see the conduction line inside the Coulomb diamonds, which we would not expect if an impurity outside the tube had been removed. Further, the order of magnitude of the hybridization constant and all the other parameters have not changed. Therefore it is highly unlikely that the impurity is outside the tube.

Another possibility would be a defect in the CNT causing a separation into two quantum dots. This can be excluded by our numerical studies, where a symmetric coupling of the tube to the leads has been necessary to obtain results similar to the experimental measurements. This would not be expected if a defect would separate the CNT like dot from one of the leads.

Even if we have no final prove at hand we are confident of the scenario that a chain of  $C_{60}$  is residing inside the tube close to the source lead. This explains best the screening from the gate electrode and also the independence from exterior purification procedures.

## 7.5 Conclusion

In this chapter we reviewed an experiment and the corresponding theory on low temperature electron transport through a carbon nanotube peapod quantum dot. We observe conduction lines inside the Coulomb diamonds showing a small dependence on the gate voltage and form avoided crossings with the standard Coulomb diamond edges. We ascribe this additional conduction line to an impurity orbital which is capacitively and tunnel coupled to the carbon nanotube orbitals. Such impurity states appear in many nano-device systems. For example the measurements in [216] and [235] show some features which are similar to the features observed here. In this chapter the impurity is most probably formed by a chain of  $C_{60}$  molecules at one end of the SWCNT. The results found are important for addressing certain states of coupled quantum dot systems in a controlled way.



# Chapter 8

## Spin-dependent electronic hybridization in a rope of carbon nanotubes

The work presented in this chapter follows the paths of Chapter 7. Here, sequential electron transport is performed in a carbon nanotube rope, which is a bundle of in this case less than 10 carbon nanotubes forming at least three quantum dots. Most of the material presented in this chapter has been published in

*K. Goß, S. Smerat, M. Leijnse, M. R. Wegewijs, C. M. Schneider, C. Meyer*  
"Spin-dependent electronic hybridization in a rope of carbon nanotubes"  
*submitted to Phys. Rev. Lett, arXiv:1011.4004.*

In modern electronics and further in molecular spintronics it is an essential issue to obtain nano-sized objects with tailored functionalities. While Chapter 7 focuses on general properties of such devices we examine here the functionalization of nano-devices in nano-electronics, especially by means of a magnetic field which assists in addressing spin explicitly. We will first briefly introduce the reader by means of recent literature into the field of molecular electronics. Second, we describe the experiment performed and the corresponding model calculations. We end this chapter with a short discussion of the results.

### 8.1 Introduction

The idea of molecular electronics and spintronics is to enable the manipulation of spin and charges in electronic nano-devices containing one or more molecules [31]. These devices simply exploit the fact that electron current is a composite of spin up and spin down particles differently acting with magnetic materials. However, assembling nano-devices is still a tricky task and asks for sophisticated methods and new ideas. In [214] such devices have been constructed based on an approach developed in [221, 84]. A nanowire made out of gold is exposed to a large current, which causes a break of the wire forming a gap with two electrodes. Molecules are deposited from a solution thus forming a three-terminal device with the two electrodes and a back gate. The contact conditions of each sample will be different due to the randomness of the

molecule deposition procedure, but constructing many devices results in many different contact conditions and it has been found in [214] that devices appear with weak (incoherent tunneling), intermediate (coherent tunneling, but Coulomb diamonds are found) and strong coupling to the leads (Coulomb diamonds vanish for the benefit of higher order processes). It is also possible to construct multi quantum dots out of a single carbon nanotubes as has been shown in [30], where magnetic nanoparticles dispersed in a solution have been deposited on a carbon nanotube thus forming a controlled number of quantum dots depending on the time the nanotube has been plunged in the solution.

Carbon nanotubes turned out to be particularly suitable as nano-electric devices. Nuclear spins can be completely eliminated, which cause spin relaxation and decoherence and a strong spin-orbit interaction [152] allows all-electrical control over spin degrees of freedom, while long spin relaxation and decoherence times are preserved [38, 207]. Furthermore, they can be produced ultraclean [287] and assembled to three terminal devices forming double quantum dots with negligible distortion allowing for precise control over single electrons down to a single excess electron on the dot. Carbon nanotubes can also be used as electromechanical resonators of high quality [286, 120, 165], which have potential applications in sensing, cooling, and mechanical signal processing. The resonator motion is typically coupled to the charges inside and this can be resolved in electron transport measurements.

Carbon nanotubes also have remarkable spin properties. The phenomenon of *spin-orbit coupling*, coupling of orbital motion and spin of electrons, leads to the well known fine structure in atomic spectra. In [152] it has been shown in an electron transport measurement that electrons in SWCNTs show a significant spin-orbit coupling. Due to this the circumferential quantization of the momentum of electrons in a SWCNT quantum dot with spin parallel/antiparallel aligned to a magnetic field aligned parallel to the tube axis is different. This leads to an energy splitting between electrons with different spins, which can be observed in transport and is proportional to the magnitude of the spin-orbit coupling. This provides a mechanism for all-electrical control of spins in SWCNTs [152]. For a sufficient strong coupling to the leads, the Kondo effect can be observed in SWCNTs [124]. Using ferromagnetic leads makes it possible to observe the tunneling magneto resistance (TMR) effect, which is important to build spin valves [255]. Also separation of spin and charge transport channels has been found [292].

Furthermore, SWCNTs might also be applied in quantum information processing devices. For this purpose spin relaxation times  $T_1$  and spin dephasing times  $T_2^*$  have been measured in a  $^{13}\text{C}$ -nanotube [44]. It could be confirmed that the dominating mechanism is the hyperfine interaction with the finite spin on the carbon atoms.

In order to employ single molecules as nano-electronic devices it is necessary to understand their interactions with the environment, e.g., the interaction with contacts and also with neighboring molecules [215]. These interactions can be studied by scanning near-field optical microscopy [21], tip-enhanced Raman spectroscopy [106, 105] or scanning tunneling spectroscopy (STS) [218]. However, in-situ characterization of actual devices, e.g., field-effect transistors, is difficult to implement and only STS can detect spin dependent phenomena.

In the experiment described in this chapter, we used electron transport spectroscopy, similar to Chapter 7, where the device is capacitively coupled to a back gate. It is also interesting to observe bundled SWCNTs with this technique, since it is expected that the respective tubes

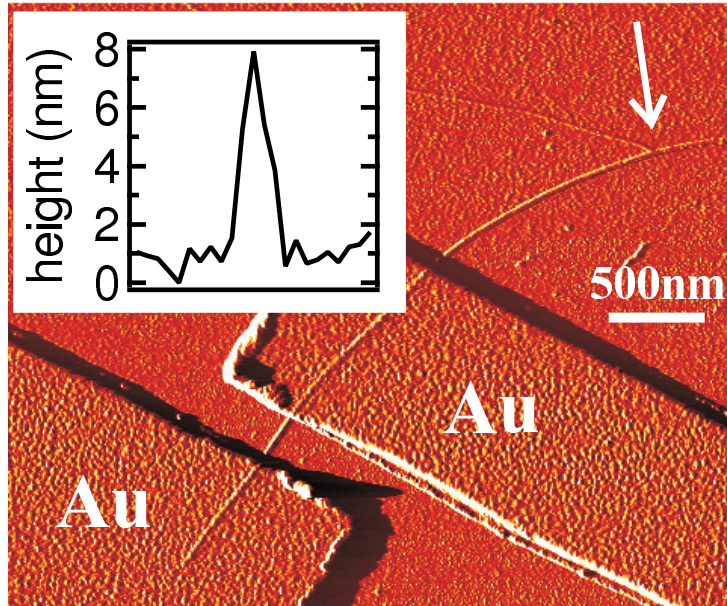


Figure 8.1: AFM picture of the measured device, in whose vicinity one or more CNTs split off (arrow) from the contacted rope. Due to stacking faults in the metal deposited on top, the CNT is also visible underneath the contacts. Inset: AFM height profile running perpendicular to the CNT in the QD region.

couple differently to the gate electrode [130] due to electrostatic effects, like screening. Low-temperature electron transport measurements are capable of resolving these gating effects, allowing the study of interactions between coupled nanoscale conductors.

In this chapter we will first describe the performed experiment. Then we determine the strength of the hybridization and the electrostatic interaction between different quantum dots within the SWCNT rope. By means of transport calculation we can furthermore determine the sign of the hybridization. In a final step we examine the influence of a magnetic field on the rope. Furthermore, the SWCNT dominating the electron transport can be altered by applying a magnetic field and the electronic hybridization is selectively suppressed due to spin effects and this offers prospects for accessing individual charge and spin degrees of freedom in coupled carbon-based molecular systems.

## 8.2 The sample and the experiment

The bundle of SWCNTs, an *SWCNT rope*, has been grown by means of chemical vapor deposition at  $920^\circ$  on a Si back-gate with an insulating  $\text{SiO}_2$  layer in between. As catalyst Fe/Mo has been used and methane as a precursor [147]. In this process mainly SWCNTs arise and only a few MWCNTs [285]. The electrodes consist of 5 nm Ti and 60 nm Au and have been patterned using electron beam lithography forming a quantum dot of 360 nm with highly-doped silicon as the back gate. An AFM imaging technique shows the device, see Fig. 8.1, and reveals the corresponding height profile of the SWCNT rope. It turns out that the device has a diameter of 7 nm.

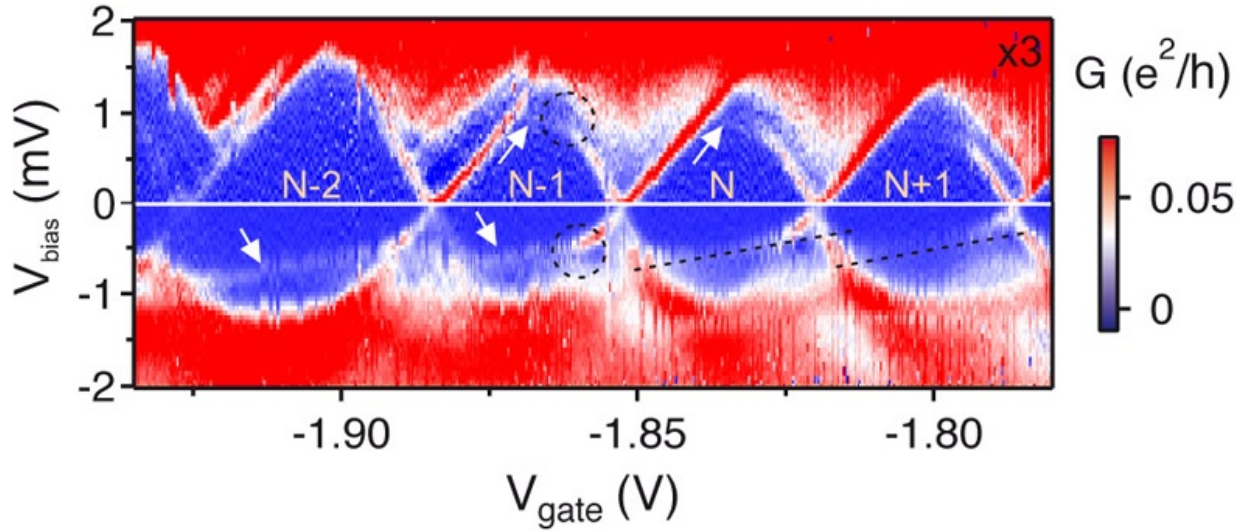


Figure 8.2: (color online) The differential conductance plotted versus gate and bias voltage showing four complete Coulomb diamonds. Secondary resonances, indicated by white arrows and dashed lines, cross the region of Coulomb blockade. Circles indicate the anticrossings. To clearly display all features, the conductance at positive bias has been multiplied by three.

Furthermore, we have found that a single carbon nanotube splits away from the rope, indicating that we really deal with a rope of SWCNTs and not with a MWCNT.

At room temperature the device behaves as a metallic conductor with an ohmic resistance of 290 k $\Omega$ . At a base temperature of  $\approx 30$  mK in a dilution refrigerator the device shows highly non-linear transport properties, see Fig. 8.2, i.e., single-electron charging effects. The electron temperature has been determined as  $\approx 600$  mK.

We have found regular Coulomb diamonds on a large gate voltage range from  $-2.4$  V up to 1.3 V, which proves that a stable quantum dot has formed inside the rope. Furthermore, we observe the following remarkable features in Fig. 8.2:

1. Additional conductance lines inside the Coulomb diamonds. Under Coulomb blockade conditions conduction lines should not appear inside the Coulomb diamonds;
2. These lines have a small slope compared to the Coulomb diamond edges and therefore suggest that the corresponding states have a small gate dependence;
3. They appear at positive and negative bias voltages with different slopes, intensities and asymmetrically. The intensity of the lines is weaker far away from the Coulomb diamond edges and increases on approaching. The additional conductance lines at positive bias voltage lie at nearly 1 meV, while at negative bias voltage at approximately  $-0.5$  meV;
4. At the crossing points with the Coulomb diamond edges of the same slope these additional conductance lines form avoided crossings;
5. At each subsequent diamond the additional conductance lines jump abruptly. The height of the jump is different for negative and positive bias voltage.

### 8.3 Model, transport calculation and results

From the asymmetry in bias voltage we can conclude that inelastic co-tunneling [53] can be excluded as a possible explanation for the occurrence of the two conduction lines inside the Coulomb diamonds. Therefore, we conclude from the measurement data that several, but at least three, quantum dots are coupled in parallel to the leads. One of the dots causes the main Coulomb diamond scheme in the conductance map and two additional dots are responsible for the conduction lines inside the Coulomb diamonds. All dots feel differently the electric field generated by the gate electrode. Furthermore, electrons may hop between the different quantum dots.

For the transport calculations we employ standard master equations [36], which account for electron tunneling processes to and from the leads in lowest order. The electrochemical potential on the dot is given by

$$\mu_{v\xi}^i \propto -|e|\alpha_s^i V_b - |e|\alpha_g^i V_g \quad (8.1)$$

with  $i = m, s$  denoting the dot,  $v$  the target state and  $\xi$  the initial state.  $\alpha_{s,d,g}^i = C_{s,d,g}^i / C^i$ , where  $C^i = C_s^i + C_d^i + C_g^i$  is the total capacitance of the system. Tuning the voltages one can exactly adjust the number of electrons on the dot.

We assume in our model, shown in Fig. 8.3(a) that two quantum dots exist, one main quantum dot, labelled with  $m$ , and a side quantum dot, labelled with  $s$ . The model is similar to the eCI model in Chapter 7. Summarizing, both dots are coupled to both leads. Electrons can hop from the main dot to the side dot and vice versa causing hybridization of states. If hybridization would be negligible the thermal and tunnel broadening would be larger than the hopping constant  $t$  and the conduction lines which form avoided crossings in our measurements would simply cross each other [215]. If  $t$  is significant avoided crossings will occur between the conduction lines, as already argued in Chapter 7. The rates from the leads on the dot can be different for the two dots and for the two leads. Furthermore, the gate coupling is different and an inter-dot Coulomb interaction  $U^{ms}$  exists, causing an additional charging energy when both dots are occupied. Proceeding from one diamond to the next with increasing  $V_g$  the main dot will be charged with another electron. This increases the electrostatic field on the side dot causing an energy offset  $U^{ms}$  in the differential conductance map.

A typical calculated differential conduction map is shown in Fig. 8.3(b). We find Coulomb diamonds caused by the main dot. The weakly gate electrode voltage dependent side dot is responsible for the occurrence of the conduction line inside the Coulomb diamonds. These lines form avoided crossings, where they would intersect the Coulomb diamond edges with the same slope. Fano resonances can also be observed, which do not appear in the experimental data. A jump of the conductance line inside a Coulomb diamond happens at each Coulomb diamond edge due to  $U^{ms}$ .

At the energetic resonance of two states, the hybridized bonding  $|-\rangle$  and anti-bonding  $|+\rangle$  states are generated, which are split in energy by  $2|t|$  (see the inset of Fig. 8.3b). Figure 8.3b shows that the calculations reproduce the experimentally observed features very well. The bonding and anti-bonding states contribute very differently to the conductance, which is seen from

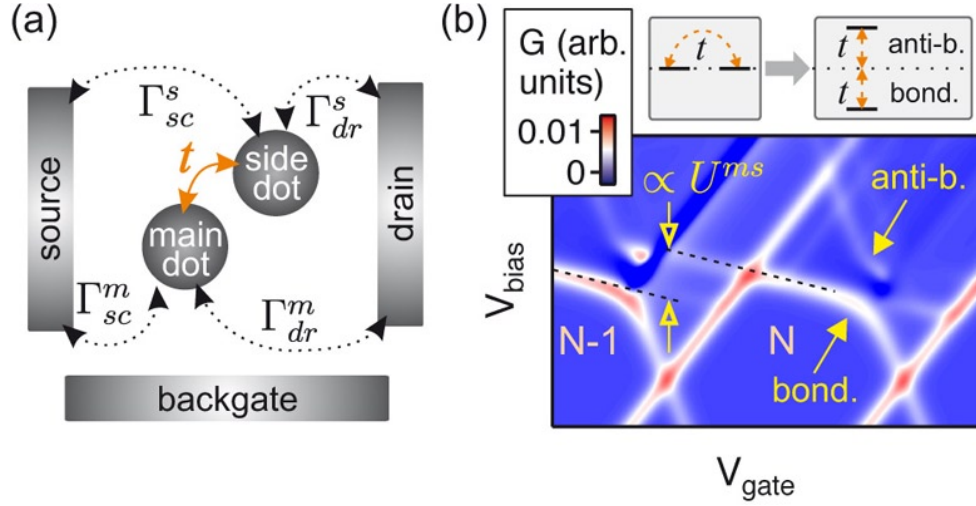


Figure 8.3: (color online) (a) Sketch of the transport model: Two QDs are contacted in parallel with different gate coupling strength. Electrons tunnel with rates  $\Gamma$  from the leads into and out of the QDs. The QDs are connected due to hybridization with an amplitude  $t$ . (b) Calculated stability diagram accounting for one orbital on each QD. *Inset*: The hybridization of two orbitals generates a bonding and an anti-bonding eigenstate.

the very different intensity of the conduction lines. This relates to the sign of  $t$ , as shown in the following.

We consider a simplified case here: The hybridized eigenstates for a single electron in the coupled quantum dot system are

$$\begin{aligned} |+\rangle &= \cos\theta|m\rangle + \sin\theta|s\rangle \\ |-\rangle &= -\sin\theta|m\rangle + \cos\theta|s\rangle, \end{aligned} \quad (8.2)$$

where  $|m\rangle$  and  $|s\rangle$  are the original states on the main dot and the side dot with the energies  $\pm\varepsilon = \pm\varepsilon(V_b, V_g)$  taken relative to their resonance energy. The hybridized states depend on the applied voltages through  $\theta$ , where  $\tan\theta = \frac{\sqrt{\varepsilon^2 + t^2} - \varepsilon}{t}$ , and their corresponding eigenenergies are  $\pm\sqrt{\varepsilon^2 + t^2}$ . This analysis can be extended to more electrons in the system. The rate for the tunneling of an electron from the leads into the  $|\pm\rangle$  state is proportional to the corresponding tunnel matrix elements  $T_{\pm}$ :

$$\Gamma_{\pm} \propto |T_{\pm}|^2 = T_{m/s}^2 \cos^2\theta + T_{s/m}^2 \sin^2\theta \pm T_m T_s \cos\theta \sin\theta. \quad (8.3)$$

Here  $T_m$  and  $T_s$  are the matrix elements for tunneling into  $|m\rangle$  or  $|s\rangle$ , respectively, whose sign we take to be the same since the single SWCNT from the rope form a single junction.

According to Eq. 8.3 the sign of the hybridization constant  $t$  determines whether the bonding state or the anti-bonding state is enhanced. This can be confirmed in a model calculation, see Fig. 8.4. In the left panel of Fig. 8.4(a) we chose  $t > 0$  and find an enhanced anti-bonding state, whereas in the right panel the bonding state is enhanced for  $t < 0$ . Comparing with the experimental measurements, see Fig. 8.3 and Fig. 8.4, we find that the bonding state is enhanced

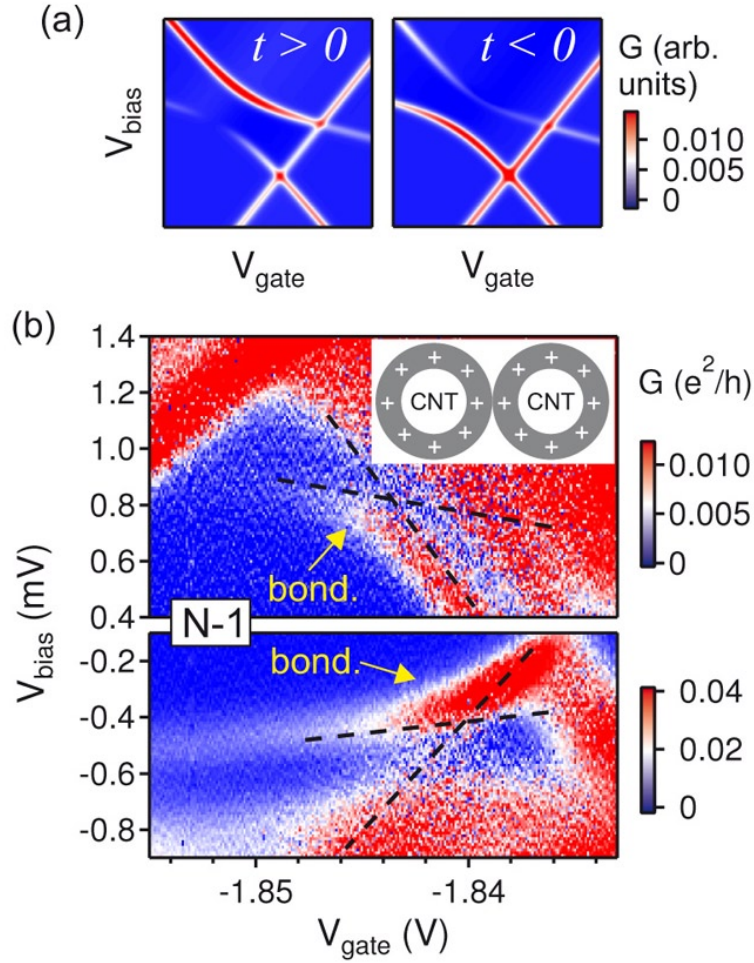


Figure 8.4: (color online) (a) Calculated stability diagrams showing anticrossings for opposite signs of the hybridization integral  $t$ . (b) High resolution measurement of the anticrossings marked by circles in Fig. 8.2. The dashed lines indicate the resonance positions as extrapolated from Fig. 8.2. *Inset*: Sketch of the sign of the overlapping CNT QD wavefunctions.

and therefore that the sign of  $t$  is negative. In conclusion, the overlap of the wave functions of the two adjacent SWCNTs has to be positive as depicted in Fig. 8.4(b) in the inset.

For the additional conduction line at positive bias voltage we find a negative slope. From this we can deduce a small gate voltage coupling. Since we do not find any signature of the corresponding second diamond edge belonging to this conduction line, we can safely assume that the absolute value of the slope of the second diamond edge is so large that it is not measurable. This, together with the small negative slope, suggests a strong bias coupling of the corresponding orbital. With the same line of arguments, we can conclude that the additional conduction line at negative bias voltage is strongly drain coupled and weakly gate coupled.

### Parameters

For the inter-dot charging energy we find

- at positive bias voltage:  $U_{\text{pos}}^{ms} = 0.4$  meV;
- at negative bias voltage:  $U_{\text{neg}}^{ms} = 0.2$  meV.

The magnitude of the hybridization constant is determined as

- at positive bias voltage:  $t_{\text{pos}} = -0.1$  meV;
- at negative bias voltage:  $t_{\text{neg}} = -0.075$  meV.

In an exhaustive numerical survey we estimate the coupling of the side dot orbital to the source for the additional conduction line at positive bias voltage as  $\alpha^s = 0.7 - 1$  and the drain coupling at negative bias voltage as  $\alpha^d = 0.7 - 1$ .

From the difference in the strength of the hybridization, the inter-dot charging energy and the asymmetry in the coupling to the leads we can justify the following assumptions:

1. The orbitals corresponding to the additional conduction lines at positive and negative bias voltage belong to two different quantum dots, which differently couple to gate, source and drain.
2. Both quantum dots, referred to as side dots, couple to the main dot via a hopping constant  $t_{\text{neg}}$  and  $t_{\text{pos}}$ , respectively.
3. Probably, the side dots are located in different SWCNTs as part of the rope, because of the significantly different gate coupling, which is a result of electrostatic screening.
4. Furthermore, due to the asymmetric coupling to source and drain electrode of the two side dots, one can assume that the side dots are located at opposite ends of the rope.

We have to note further, that the values for the hybridization constants and the inter-dot charging energies are upper bounds of the real values due to the source and drain coupling. Still, the order of magnitude is correct.

## 8.4 Magnetic field measurements

By means of an applied magnetic field it is possible to determine its influence on the spin degrees of freedom and especially on the hybridization.

At 10 T we find the experimental measurement result shown in Fig. 8.5(a) with several significant signatures. Transport through the main dot is highly suppressed at positive and negative bias voltages. Transport through the side dot at positive bias voltage is strongly enhanced, while transport through the other side dot completely vanishes. From the hybridization strength, the inter-dot charging energy and the gate, source and drain coupling we conclude that the side dot

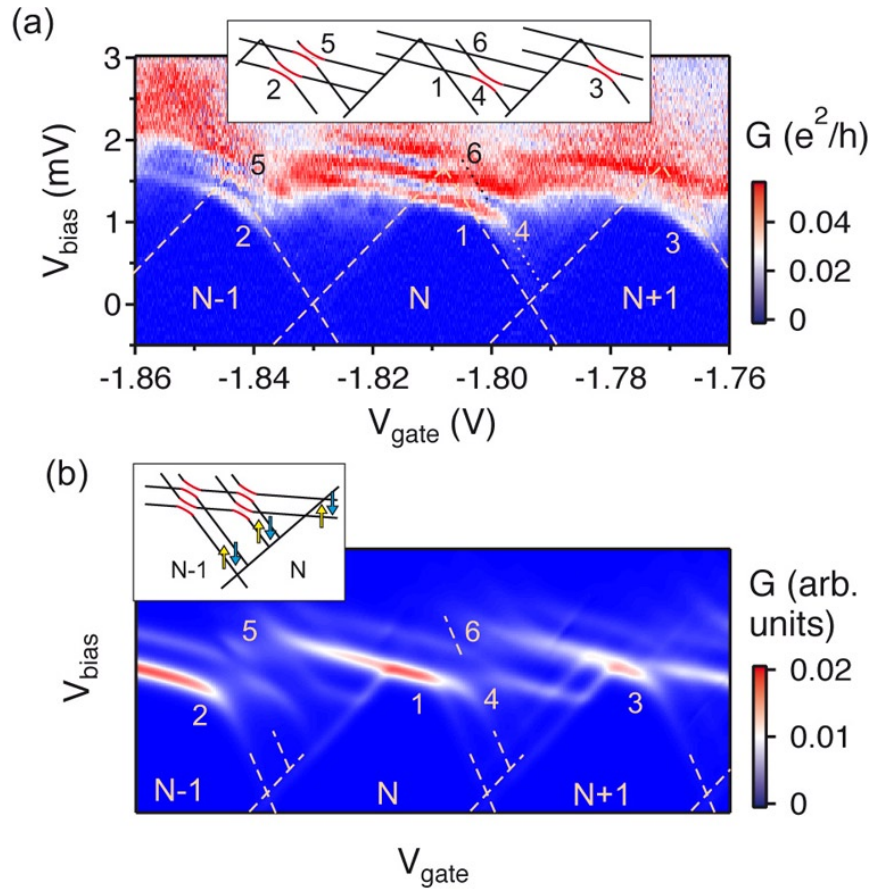


Figure 8.5: (color online) (a) Crossings and anticrossings at  $B = 10$  T (same charge states of the main dot as in zero field). The dashed lines indicate the extrapolated diamond edges. *Inset*: Guide to the measurements. The anti-bonding states are included in the sketch for completeness. (b) Calculated stability diagram with  $N = 1$  according to the model sketched in the inset. Coupling parameters are taken from the experiment and tunneling rates are adjusted accordingly. *Inset*: Schematic stability diagram for different states on the quantum dots. Arrows indicate spin split states.

is the same as before. Furthermore, we find as in the 0 T that the bonding state is enhanced and in addition we observe several excited states. At position 1 in Fig. 8.5(a) we see a clear crossing, where we would expect a avoided crossing from the 0 T measurements.

A model calculation can reproduce the measurement very well, see Fig. 8.5(b). We observe at position 1 again the crossing. This is due to different quantum numbers, most probably different spin of the two resonating states. Therefore, the states can not hybridize and stay independent. At position 2 and 3 we observe hybridizing states and again a crossing at position 6. Avoided crossings with higher lying states can be found at positions 4 and 5.

Tuning gate and bias voltage enables the concrete addressing of certain spin states of the quantum dot, which is a key issue of quantum information processing and spintronics.

## 8.5 Discussion

In this chapter we examined a quantum dot system formed in different SWCNTs of a carbon nanotube rope system. The system consists at least of three interacting quantum dots. The interaction is due to hybridization of states and we could determine the magnitude and the sign of the afore mentioned. Further, we could estimate the electrostatic interaction between the dots. The transport has been found to be enhanced through the bonding states, while it is suppressed in the anti-bonding states. Due to conserved quantum numbers, i.e., spin, the hybridization between states in a magnetic field is selectively suppressed. All measurements are confirmed with a standard master equations transport calculation. Our findings might also be relevant for other systems, i.e., graphene quantum dots interacting with carbon nanotubes or other single molecules. It has been shown that hybridization, in general, might enable addressing in a controlled way well defined spin and charge states of quantum dot systems.

# Bibliography

- [1] G. Aeppli und Z. Fisk, *Comments Cond. Mat. Phys.* **16** (1992), 155.
- [2] I. Affleck, T. Kennedy, E.H. Lieb und H. Tasaki, *Physical Review Letters* **59** (1987), 799.
- [3] K. Al-Hassanieh, A. Feiguin, J. Riera, C. Büsser und E. Dagotto, *Physical Review B* **73** (2006).
- [4] L. Amico, R. Fazio, A. Osterloh und V. Vedral, *Reviews of Modern Physics* **80** (2008), 517.
- [5] M. Amman, K. Mullen und E. BenJacob, *Journal of Applied Physics* **65** (1989), 339.
- [6] S. Andergassen, V. Meden, H. Schoeller, J. Splettstoesser und M.R. Wegewijs, *Nanotechnology* **21** (2010), 272001.
- [7] P. Anderson, *Physical Review* **109** (1958), 1492.
- [8] W. Andreoni: *The Physics of Fullerene-Based and Fullerene-Related Materials (Physics and Chemistry of Materials with Low-Dimensional Structures)*. Springer, 2000.
- [9] D.N. Aristov, *Physical Review B* **55** (1997), 8064.
- [10] J. Audretsch: *Verschränkte Systeme: Die Quantenphysik Auf Neuen Wegen (German Edition)*. Wiley-VCH Verlag GmbH, 2005.
- [11] B Derrida et al. *Exact solution of a 1D asymmetric exclusion model using a matrix formulation*, 1993.
- [12] M. Bañuls, M. Hastings, F. Verstraete und J. Cirac, *Physical Review Letters* **102** (2009), 240603.
- [13] A. Bachtold, M. Fuhrer, S. Plyasunov, M. Forero, E. Anderson, A. Zettl und P. McEuen, *Physical Review Letters* **84** (2000), 6082.
- [14] J. Bardeen, L.N. Cooper und J.R. Schrieffer, *Physical Review* **108** (1957), 1175.
- [15] T. Barthel, C. Kasztelan, I. McCulloch und U. Schollwöck, *Physical Review A* **79** (2009).

- [16] T. Barthel, U. Schollwöck und S. White, *Physical Review B* **79** (2009), 245101.
- [17] S.A. Basylko, P.H. Lundow und A. Rosengren, *Physical Review B (Condensed Matter and Materials Physics)* **77** (2008), 73103.
- [18] S.C. Benjamin, A. Ardavan, G.A.D. Briggs, D.A. Britz, D. Gunlycke, J. Jefferson, M.A.G. Jones, D.F. Leigh, B.W. Lovett, A.N. Khlobystov, S.A. Lyon, J.J.L. Morton, K. Porfyrakis, M.R. Sambrook und A.M. Tyryshkin, *Journal of Physics: Condensed Matter* **18** (2006), S867.
- [19] H. Benthien, *Physical Review B* **75** (2007).
- [20] H. Benthien, F. Gebhard und E. Jeckelmann, *Physical Review Letters* **92** (2004), 256401.
- [21] E. Betzig und R.J. Chichester, *Science (New York, N.Y.)* **262** (1993), 1422.
- [22] L.C. Biedenharn und J.D. Louck: *Angular Momentum in Quantum Physics (Encyclopedia of Mathematics and Its Applications, Vol 8)*. Cambridge University Press, 1984.
- [23] M.J. Biercuk, S. Garaj, N. Mason, J.M. Chow und C.M. Marcus, *Nano Letters* **5** (2005), 1267.
- [24] G. Binasch, P. Grünberg, F. Saurenbach und W. Zinn, *Physical Review B* **39** (1989), 4828.
- [25] M.T. Björk, C. Thelander, A.E. Hansen, L.E. Jensen, M.W. Larsson, L.R. Wallenberg und L. Samuelson, *Nano Letters* **4** (2004), 1621.
- [26] X. Blase, L. Benedict, E. Shirley und S. Louie, *Physical Review Letters* **72** (1994), 1878.
- [27] I. Bloch, J. Dalibard und W. Zwerger, *Reviews of Modern Physics* **80** (2008), 885.
- [28] M. Bockrath, D.H. Cobden, J. Lu, A.G. Rinzler, R.E. Smalley, L. Balents und P.L. McEuen, *Nature* **397** (1999), 598.
- [29] M. Bockrath, D.H. Cobden, P.L. McEuen, N.G. Chopra, A. Zettl, A. Thess und R.E. Smalley, *Science* **275** (1997), 1922.
- [30] L. Bogani, R. Maurand, L. Marty, C. Sangregorio, C. Altavilla und W. Wernsdorfer, *Journal of Materials Chemistry* **20** (2010), 2099.
- [31] L. Bogani und W. Wernsdorfer, *Nature materials* **7** (2008), 179.
- [32] E. Boulat, H. Saleur und P. Schmitteckert, *Physical Review Letters* **101** (2008).
- [33] B. Braunecker, P. Simon und D. Loss, *arXiv:0808.4063v1 [cond-mat.mes-hall]* (2008).
- [34] B. Braunecker, P. Simon und D. Loss, *Physical Review Letters* **102** (2009), 116403.
- [35] P. Bruno, *Physical Review Letters* **87** (2001), 137203.

- [36] H. Bruus und K. Flensberg: *Many-Body Quantum Theory in Condensed Matter Physics: An Introduction (Oxford Graduate Texts)*. Oxford University Press, USA, 2004.
- [37] M.R. Buitelaar, A. Bachtold, T. Nussbaumer, M. Iqbal und C. Schönenberger, *Phys. Rev. Lett.* **88** (2002), 156801.
- [38] D. Bulaev, B. Trauzettel und D. Loss, *Physical Review B* **77** (2008), 235301.
- [39] S. Caprara, *Nuclear Physics B* **493** (1997), 640.
- [40] A. Castro Neto, F. Guinea, N. Peres, K. Novoselov und A. Geim, *Reviews of Modern Physics* **81** (2009), 109.
- [41] M. Cazalilla und J. Marston, *Physical Review Letters* **88** (2002).
- [42] J.C. Charlier und J.P. Issi, *Applied Physics A: Materials Science & Processing* **67** (1998), 79.
- [43] M.C. Chung und I. Peschel, *Physical Review B* **64** (2001).
- [44] H. Churchill, F. Kuemmeth, J. Harlow, A. Bestwick, E. Rashba, K. Flensberg, C. Stwertka, T. Taychatanapat, S. Watson und C. Marcus, *Physical Review Letters* **102** (2009).
- [45] H.O.H. Churchill, A.J. Bestwick, J.W. Harlow, F. Kuemmeth, D. Marcos, C.H. Stwertka, S.K. Watson und C.M. Marcus, *Nature Physics* **5** (2009), 321.
- [46] W. Coish, J. Fischer und D. Loss, *Physical Review B* **77** (2008).
- [47] W. Coish und D. Loss, *Physical Review B* **70** (2004).
- [48] P. Coleman: *Heavy Fermions: electrons at the edge of magnetism*, Band 1 von *Handbook of Magnetism and Advanced Magnetic Materials*. John Wiley and Sons, 2007.
- [49] M. Cramer, A. Flesch, I. McCulloch, U. Schollwöck und J. Eisert, *Physical Review Letters* **101** (2008).
- [50] W. Dahmen und A. Reusken: *Numerik für Ingenieure und Naturwissenschaftler (Springer-Lehrbuch) (German Edition)*. Springer, 2008.
- [51] H. Dai, E.W. Wong und C.M. Lieber, *Science* **272** (1996), 523.
- [52] A.J. Daley, C. Kollath, U. Schollwöck und G. Vidal, *Journal of Statistical Mechanics: Theory and Experiment* **2004** (2004), P04005.
- [53] S. De Franceschi, S. Sasaki, J. Elzerman, W. van der Wiel, S. Tarucha und L. Kouwenhoven, *Physical Review Letters* **86** (2001), 878.
- [54] C. Dekker, *Phys. Today* **52** (1999), 22.

- [55] J. von Delft und D. Ralph, *Physics Reports* **345** (2001), 61.
- [56] M. Devoret, *Physical Review Letters* **64** (1990), 1824 .
- [57] L. Dias da Silva, F. Heidrich-Meisner, A. Feiguin, C. Büsser, G. Martins, E. Anda und E. Dagotto, *Physical Review B* **78** (2008).
- [58] T. Dittrich, P. Hänggi, G.L. Ingold, B. Kramer, G. Schön und W. Zwerger: *Quantum Transport and Dissipation*. Wiley-VCH, 1998.
- [59] O. Dubay und G. Kresse, *Phys. Rev. B* **70** (2004), 165424.
- [60] C. Eckart, *Reviews of Modern Physics* **2** (1930), 305.
- [61] D.M. Edwards, S. Ejima, A. Alvermann und H. Fehske, *Journal of Physics: Condensed Matter* **22** (2010), 435601.
- [62] J. Eisert und T. Osborne, *Physical Review Letters* **97** (2006), 150404.
- [63] S. Ejima, *Physical Review B* **80** (2009).
- [64] A. Eliassen: *Electronic transport in C60 Peapods*. University of Copenhagen, Dissertation, 2007.
- [65] F D M Haldane. 'Luttinger liquid theory' of one-dimensional quantum fluids. I. Properties of the Luttinger model and their extension to the general 1D interacting spinless Fermi gas, 1981.
- [66] M. Fannes, B. Nachtergaele und R.F. Werner, *Communications in Mathematical Physics (1965-1997)* **144** (1992), 443.
- [67] U. Fano, *Physical Review* **124** (1961), 1866.
- [68] A. Feiguin und S. White, *Physical Review B* **72** (2005), 220401.
- [69] D.K. Ferry, S.M. Goodnick und J. Bird: *Transport in Nanostructures*. Cambridge University Press, 2009.
- [70] J. Fischer und D. Loss, *Science (New York, N.Y.)* **324** (2009), 1277.
- [71] D. Fisher, *Physical Review Letters* **69** (1992), 534.
- [72] D. Fisher, *Physical Review B* **51** (1995), 6411.
- [73] Z. Fisk, *Physica B: Condensed Matter* **206-207** (1995), 798.
- [74] A. Flesch, M. Cramer, I. McCulloch, U. Schollwöck und J. Eisert, *Physical Review A* **78** (2008), 033608.

- [75] A. Friedrich: *Time-dependent Properties of one-dimensional Spin-Systems: A DMRG-Study*. RWTH Aachen, Dissertation, 2006.
- [76] A. Friedrich, A. Kolezhuk, I. McCulloch und U. Schollwöck, *Physical Review B* **75** (2007), 094414.
- [77] T.A. Fulton und G.J. Dolan, *Physical Review Letters* **59** (1987), 109.
- [78] R.M. Fye und D.J. Scalapino, *Phys. Rev. Lett.* **65** (1990), 3177.
- [79] E. Gagliano und C. Balseiro, *Physical Review Letters* **59** (1987), 2999.
- [80] D.J. Garcia, K. Hallberg, B. Alascio und M. Avignon, *Phys. Rev. Lett.* **93** (2004), 177204.
- [81] A.K. Geim und K.S. Novoselov, *Nature materials* **6** (2007), 183.
- [82] A. Georges, G. Kotliar, W. Krauth und M. Rozenberg, *Reviews of Modern Physics* **68** (1996), 13.
- [83] C.C. (GFDL). *Creative Commons (GFDL)*.
- [84] S. Ghosh, H. Halimun, A.K. Mahapatro, J. Choi, S. Lodha und D. Janes, *Applied Physics Letters* **87** (2005), 233509.
- [85] I. Giaever, *Physical Review Letters* **20** (1968), 1504 .
- [86] T. Giamarchi: *Quantum Physics in One Dimension (The International Series of Monographs on Physics)*. Oxford University Press, USA, 2003.
- [87] P. Giannozzi, *Applied Numerical Mathematics* **4** (1988), 273.
- [88] L. Girifalco und M. Hodak, *Physical Review B* **65** (2002), 125404.
- [89] S. Girvin, L. Glazman, M. Jonson, D. Penn und M. Stiles, *Physical Review Letters* **64** (1990), 3183.
- [90] D. Gobert, C. Kollath, U. Schollwöck und G. Schütz, *Physical Review E* **71** (2005).
- [91] D. Gobert, M. Schechter, U. Schollwöck und J. von Delft, *Physical Review Letters* **93** (2004), 186402.
- [92] C. Gorter, *Physica* **17** (1951), 3.
- [93] H. Grabert. *Single charge tunneling: A brief introduction*, 1991.
- [94] K. Grove-Rasmussen, H. Jørgensen, B. Andersen, J. Paaske, T. Jespersen, J. Nygård, K. Flensberg und P. Lindelof, *Physical Review B* **79** (2009).
- [95] S. Guéron, M. Deshmukh, E. Myers und D. Ralph, *Physical Review Letters* **83** (1999), 4148.

- [96] M. Gulácsi, *Advances in Physics* **53** (2004), 769.
- [97] M. Gulacsi, A. Bussmann-Holder und A.R. Bishop, *Physical Review B (Condensed Matter and Materials Physics)* **71** (2005), 214415.
- [98] C. Guo, A. Weichselbaum, S. Kehrein, T. Xiang und J. von Delft, *Physical Review B* **79** (2009).
- [99] F.D.M. Haldane, *Journal of Physics C: Solid State Physics* **14** (1981), 2585.
- [100] K. Hallberg, *Physical Review B* **52** (1995), R9827.
- [101] K.A. Hallberg, *Advances in Physics* **55** (2006), 477.
- [102] N. Hamada, S.i. Sawada und A. Oshiyama, *Physical Review Letters* **68** (1992), 1579.
- [103] R. Hanson, J.R. Petta, S. Tarucha und L.M.K. Vandersypen, *Reviews of Modern Physics* **79** (2007), 1217.
- [104] M. Hartmann, J. Prior, S. Clark und M. Plenio, *Physical Review Letters* **102** (2009).
- [105] A. Hartschuh, E. Sánchez, X. Xie und L. Novotny, *Physical Review Letters* **90** (2003).
- [106] N. Hayazawa, *Chemical Physics Letters* **335** (2001), 369.
- [107] H. Heersche, Z. de Groot, J. Folk, H. van der Zant, C. Romeike, M. Wegewijs, L. Zobbi, D. Barreca, E. Tondello und A. Cornia, *Physical Review Letters* **96** (2006), 206801.
- [108] F. Heidrich-Meisner, A.E. Feiguin und E. Dagotto, *Physical Review B* **79** (2009).
- [109] F. Heidrich-Meisner, A.E. Feiguin, U. Schollwöck und W. Zwerger, *Physical Review A* **81** (2010).
- [110] F. Heidrich-Meisner, I. González, K. Al-Hassanieh, A. Feiguin, M. Rozenberg und E. Dagotto, *Physical Review B* **82** (2010).
- [111] F. Heidrich-Meisner, G. Orso und A.E. Feiguin, *Physical Review A* **81** (2010), 053602.
- [112] R.T. Henriques, L. Alcacer, J.P. Pouget und D. Jerome, *Journal of Physics C: Solid State Physics* **17** (1984), 5197.
- [113] A.C. Hewson: *The Kondo Problem to Heavy Fermions (Cambridge Studies in Magnetism)*. Cambridge University Press, 1997.
- [114] M. Hochbruck und C. Lubich, *SIAM Journal on Numerical Analysis* **34** (1997), 1911.
- [115] A. Holzner: *Dissertation*. LMU München, Dissertation, 2010.
- [116] A. Holzner, A. Weichselbaum, I.P. McCulloch, U. Schollwöck und J. von Delft. *Chebyshev expansion of spectral functions in DMRG* (2010).

- [117] G. Honner und M. Gulácsi, *Phys. Rev. Lett.* **78** (1997), 2180.
- [118] G. Honner und M. Gulácsi, *Physical Review B* **58** (1998), 2662.
- [119] D.J. Hornbaker, S.J. Kahng, S. Misra, B.W. Smith, A.T. Johnson, E.J. Mele, D.E. Luzzi und A. Yazdani, *Science* **295** (2002), 828.
- [120] A.K. Hüttel, B. Witkamp, M. Leijnse, M.R. Wegewijs und H.S.J. van der Zant, *Phys. Rev. Lett.* **102** (2009), 225501.
- [121] S. Iijima, *Nature* **354** (1991), 56.
- [122] S. Ilani, L.A.K. Donev, M. Kindermann und P.L. McEuen, *Nature Physics* **2** (2006), 687.
- [123] J. Dukelsky et al. *Equivalence of the variational matrix product method and the density matrix renormalization group applied to spin chains*, 1998.
- [124] P. Jarillo-Herrero, J. Kong, H.S.J. van der Zant, C. Dekker, L.P. Kouwenhoven und S. De Franceschi, *Nature* **434** (2005), 484.
- [125] A. Javey, J. Guo, Q. Wang, M. Lundstrom und H. Dai, *Nature* **424** (2003), 654.
- [126] E. Jeckelmann, *Phys. Rev. B* **66** (2002), 45114.
- [127] S. Jin, T.H. Tiefel, M. McCormack, R.A. Fastnacht, R. Ramesh und L.H. Chen, *Science (New York, N.Y.)* **264** (1994), 413.
- [128] A. Jorio: *Carbon Nanotubes: Advanced Topics in the Synthesis, Structure, Properties and Applications (Topics in Applied Physics)*. Springer, 2007.
- [129] R. Jullien und P. Pfeuty, *Journal of Physics F: Metal Physics* **11** (1981), 353.
- [130] K. Kaasbjerg und K. Flensberg, *Nano letters* **8** (2008), 3809.
- [131] C.L. Kane, E.J. Mele, A.T. Johnson, D.E. Luzzi, B.W. Smith, D.J. Hornbaker und A. Yazdani, *Phys. Rev. B* **66** (2002), 235423.
- [132] T. Kasuya, *Progress of Theoretical Physics* **16** (1956), 45.
- [133] C. Kasztelan: *Doktorarbeit Christian Kasztelan*. LMU München, Dissertation, 2010.
- [134] M.I. Katsnelson, K.S. Novoselov und A.K. Geim, *Nature Physics* **2** (2006), 620.
- [135] D.L. Klein, P.L. McEuen, J.E.B. Katari, R. Roth und A.P. Alivisatos, *Applied Physics Letters* **68** (1996), 2574.
- [136] O. Klein, *Zeitschrift für Physik* **53** (1929), 157.
- [137] A. Kleine: *Simulating Quantum Systems on Classical Computers with Matrix Product States*. RWTH Aachen, Dissertation, 2009.

- [138] A. Kleine, C. Kollath, I. McCulloch, T. Giamarchi und U. Schollwöck, *Physical Review A* **77** (2008).
- [139] A. Kleine, C. Kollath, I.P. McCulloch, T. Giamarchi und U. Schollwöck, *New Journal of Physics* **10** (2008), 045025.
- [140] A. Klümper. *Equivalence and solution of anisotropic spin-1 models and generalized t-J fermion models in one dimension*, 1991.
- [141] A. Klümper, A. Schadschneider und J. Zittartz, *Zeitschrift für Physik B Condensed Matter* **87** (1992), 281.
- [142] M. Kohno, *Physical Review Letters* **105** (2010).
- [143] C. Kollath, U. Schollwöck und W. Zwerger, *Physical Review Letters* **95** (2005).
- [144] S. Koller: *Spin transport in Carbon nanotubes*. Universität Regensburg, Dissertation, 2006.
- [145] S. Koller, L. Mayrhofer und M. Grifoni, *Europhysics Letters (EPL)* **88** (2009), 57001.
- [146] H. Kondo, H. Kino und T. Ohno, *Physical Review B* **71** (2005), 115413.
- [147] J. Kong, H.T. Soh, A.M. Cassell, C.F. Quate und H. Dai, *Nature* **395** (1998), 878.
- [148] L.P. Kouwenhoven, D. Austing und S. Tarucha. *Few-electron quantum dots*, 2001.
- [149] I.V. Krive, R.I. Shekhter und M. Jonson, *Low Temperature Physics* **32** (2006), 887.
- [150] I.V. Krive, R.I. Shekhter und M. Jonson, *Low Temperature Physics* **32** (2006), 887.
- [151] H.W. Kroto, J.R. Heath, S.C. O'Brien, R.F. Curl und R.E. Smalley, *Nature* **318** (1985), 162.
- [152] F. Kuemmeth, S. Ilani, D.C. Ralph und P.L. McEuen, *Nature* **452** (2008), 448.
- [153] T. Kühner, S. White und H. Monien, *Physical Review B* **61** (2000), 12474.
- [154] T.D. Kühner und S.R. White, *Phys. Rev. B* **60** (1999), 335.
- [155] I. Kulik und R.I. Shekhter, *Zh. Eksp. Teor. Fic.* **68** (1975), 623.
- [156] H. Kuzmany, R. Pfeiffer, M. Hulman und C. Kramberger, *Philosophical transactions. Series A, Mathematical, physical, and engineering sciences* **362** (2004), 2375.
- [157] C. Lacroix, *Solid State Communications* **54** (1985), 991.
- [158] P. Lafarge, H. Pothier, E.R. Williams, D. Esteve, C. Urbina und M.H. Devoret, *Zeitschrift für Physik B Condensed Matter* **85** (1991), 327.

- [159] J. Lambe, *Physical Review Letters* **22** (1969), 1371 .
- [160] C. Lanczos, *Journal of Research of the National Bureau of Standards* **45** (1950), 255.
- [161] C. Lanczos, *J Research Nat. Bur. Standards* **45** (1950), 255.
- [162] C. Lanczos, *J Research Nat. Bur. Standards* **49** (1952), 33.
- [163] L.D. Landau und E.M. Lifschitz: *Lehrbuch der theoretischen Physik, 10 Bde., Bd.4, Quantenelektrodynamik*. Deutsch (Harri), 1991.
- [164] S. Langer, F. Heidrich-Meisner, J. Gemmer, I. McCulloch und U. Schollwöck, *Physical Review B* **79** (2009), 214409.
- [165] B. Lassagne, Y. Tarakanov, J. Kinaret, D. Garcia-Sanchez, D. Garcia-Sanchez und A. Bachtold, *Science (New York, N.Y.)* **325** (2009), 1107.
- [166] J.I. Latorre und V. Picó, *Journal of Physics A: Mathematical and Theoretical* **42** (2009), 265302.
- [167] M. Leijnse: *Transport spectroscopy and control of molecular quantum dots*. RWTH Aachen, Dissertation, 2009.
- [168] W. Liang, M. Bockrath und H. Park, *Phys. Rev. Lett.* **88** (2002), 126801.
- [169] K. Likharev, *IEEE TRANSACTIONS ON MAGNETICS* **23** (1987), 1138.
- [170] A. Loiseau, P. Launois-Bernede, J.P. Salvetat, S. Roche und P. Petit: *Understanding Carbon Nanotubes: From Basics to Applications (Lecture Notes in Physics)*. Springer, 2009.
- [171] D. Loss und D. DiVincenzo, *Physical Review A* **57** (1998), 120.
- [172] J. Lu, S. Nagase, S. Zhang und L. Peng, *Phys. Rev. B* **68** (2003), 121402.
- [173] H. Luo, T. Xiang und X. Wang, *Physical Review Letters* **91** (2003), 049701.
- [174] J.M. Luttinger, *Phys. Rev.* **119** (1960), 1153.
- [175] D. Luzzi, *Carbon* **38** (2000), 1751.
- [176] O. Madelung, M. Schulz und H. Weiss: *Landolt-Bornstein Group III (Volume 17, Subvolume C Semiconductors : Technology of Si, Ge and Sic)*. Springer.
- [177] J. Makhoul, *Proc. IEEE* **63** (1975), 561.
- [178] M.A. Martin-Delgado und G. Sierra, *International Journal of Modern Physics A* **11** (1996), 3145.
- [179] M. Matos, G. Bonfait, R. Henriques und M. Almeida, *Physical Review B* **54** (1996), 15307.

- [180] L. Mayrhofer und M. Grifoni, *Eur. Phys. J. B* **63** (2008), 43.
- [181] I.P. McCulloch: *Collective phenomena in strongly correlated electron systems*. Australian National University, Dissertation, 2001.
- [182] I.P. McCulloch, *Journal of Statistical Mechanics: Theory and Experiment* **2007** (2007), P10014.
- [183] I.P. McCulloch, *arxiv:0804.2509* (2008).
- [184] I.P. McCulloch und M. Gulácsi, *Europhysics Letters (EPL)* **57** (2002), 852.
- [185] I.P. McCulloch, A. Juozapavicius, A. Rosengren und M. Gulacsi, *Phil. Mag. Lett.* **81** (2001), 869.
- [186] I.P. McCulloch, A. Juozapavicius, A. Rosengren und M. Gulacsi, *Phys. Rev. B* **65** (2002), 52410.
- [187] P. McEuen, *Phys. World* **13** (2000), 31.
- [188] A. Meister: *Numerik linearer Gleichungssysteme*. Vieweg+Teubner Verlag, 2007.
- [189] N.D. Mermin und H. Wagner, *Physical Review Letters* **17** (1966), 1133.
- [190] S. Methfessel und D.C. Mattis: *Magnetismus*, Band 18 von *Handbuch der Physik*. H. P. J. Wijn, 1968.
- [191] W. Metzner und D. Vollhardt, *Physical Review Letters* **62** (1989), 324.
- [192] R. Millikan, *Physical Review (Series I)* **32** (1911), 349 .
- [193] A. Millis, P. Littlewood und B. Shraiman, *Physical Review Letters* **74** (1995), 5144.
- [194] J.W. Mintmire, B.I. Dunlap und C.T. White, *Physical Review Letters* **68** (1992), 631.
- [195] J. Mizubayashi, J. Haruyama, I. Takesue, T. Okazaki, H. Shinohara, Y. Harada und Y. Awano, *Physical Review B (Condensed Matter and Materials Physics)* **75** (2007), 205431.
- [196] M. Monthioux, *Carbon* **40** (2002), 1809.
- [197] S. Moukouri und L.G. Caron, *Phys. Rev. B* **52** (1995), R15723.
- [198] S. Moukouri und L.G. Caron, *Phys. Rev. B* **54** (1996), 12212.
- [199] K. Mullen, *Physical Review B* **37** (1988), 98 .
- [200] M.A. Nielsen und I.L. Chuang: *Quantum Computation and Quantum Information*. Cambridge University Press, 2001.

- [201] S. Nishimoto, *Physical Review B* **77** (2008).
- [202] S. Nishimoto, F. Gebhard und E. Jeckelmann, *Journal of Physics: Condensed Matter* **16** (2004), 7063.
- [203] S. Nishimoto und E. Jeckelmann, *Journal of Physics: Condensed Matter* **16** (2004), 613.
- [204] S. Nishimoto, T. Pruschke und R.M. Noack, *Journal of Physics: Condensed Matter* **18** (2006), 981.
- [205] Y. Nishiyama, *The European Physical Journal B* **12** (1999), 547.
- [206] K.S. Novoselov, A.K. Geim, S.V. Morozov, D. Jiang, Y. Zhang, S.V. Dubonos, I.V. Grigorieva und A.A. Firsov, *Science (New York, N.Y.)* **306** (2004), 666.
- [207] K.C. Nowack, F.H.L. Koppens, Y.V. Nazarov und L.M.K. Vandersypen, *Science (New York, N.Y.)* **318** (2007), 1430.
- [208] J. Nygard, D.H. Cobden und P.E. Lindelof, *Nature* **408** (2000), 342.
- [209] M. Ogata und H. Shiba, *Physical Review B* **41** (1990), 2326.
- [210] S. Okada, S. Saito und A. Oshiyama, *Phys. Rev. Lett.* **86** (2001), 3835.
- [211] K. Okunishi, Y. Akutsu, N. Akutsu und T. Yamamoto, *Physical Review B* **64** (2001), 104432.
- [212] Y. Oreg, K. Byczuk und B. Halperin, *Physical Review Letters* **85** (2000), 365.
- [213] T. Osborne, *Physical Review Letters* **97** (2006), 157202.
- [214] E.A. Osorio, T. Bjørnholm, J.M. Lehn, M. Ruben und H.S.J. van der Zant, *Journal of Physics: Condensed Matter* **20** (2008), 374121.
- [215] E.A. Osorio, K. Moth-Poulsen, H.S.J. van der Zant, J. Paaske, P. Hedegård, K. Flensberg, J. Bendix und T. Bjørnholm, *Nano letters* **10** (2010), 105.
- [216] E.A. Osorio, K. O'Neill, M. Wegewijs, N. Stuhr-Hansen, J. Paaske, T. Bjørnholm und H.S.J. van der Zant, *Nano Letters* **7** (2007), 3336.
- [217] S. Östlund und S. Rommer, *Physical Review Letters* **75** (1995), 3537.
- [218] M. Ouyang, J.L. Huang, C.L. Cheung und C.M. Lieber, *Science (New York, N.Y.)* **292** (2001), 702.
- [219] M. Ouyang, J.L. Huang und C. Lieber, *Physical Review Letters* **88** (2002), 066804.
- [220] J. Paaske, A. Rosch, P. Wölfle, N. Mason, C.M. Marcus und J. Nygård, *Nature Physics* **2** (2006), 460.

- [221] H. Park, A.K.L. Lim, A.P. Alivisatos, J. Park und P.L. McEuen, *Applied Physics Letters* **75** (1999), 301.
- [222] J. Park, A.N. Pasupathy, J.I. Goldsmith, C. Chang, Y. Yaish, J.R. Petta, M. Rinkoski, J.P. Sethna, H.D. Abruña, P.L. McEuen und D.C. Ralph, *Nature* **417** (2002), 722.
- [223] S. Pati, S. Ramasesha, Z. Shuai und J. Brédas, *Physical Review B* **59** (1999), 14827.
- [224] L. Pauling: *The Nature of the Chemical Bond and the Structure of Molecules and Crystals; An Introduction to Modern Structural Chemistry. (George Fisher Baker Non-Resident Lec)*. Cornell University Press, 1960.
- [225] J.M. Pereira, P. Vasilopoulos und F.M. Peeters, *Nano letters* **7** (2007), 946.
- [226] R. Pereira, S. White und I. Affleck, *Physical Review Letters* **100** (2008), 027206.
- [227] I. Peschel, *Journal of Statistical Mechanics: Theory and Experiment* **2004** (2004), P12005.
- [228] I. Peschel, K. Hallberg, M. Kaulke und X. Wang: *Density-Matrix Renormalization - A New Numerical Method in Physics: Lectures of a Seminar and Workshop held at the Max-Planck-Institut für Physik komplexer ... 18th, 1998 (Lecture Notes in Physics)*. Springer, 1999.
- [229] H. Petroski: *The Pencil: A History of Design and Circumstance*. Knopf, 1990.
- [230] J. Petta und D. Ralph, *Physical Review Letters* **87** (2001), 266801.
- [231] P. Pfeuty, *Physics Letters A* **72** (1979), 245.
- [232] L. Pollet, C. Kollath, U. Schollwöck und M. Troyer, *Physical Review A* **77** (2008), 023608.
- [233] L.A. Ponomarenko, F. Schedin, M.I. Katsnelson, R. Yang, E.W. Hill, K.S. Novoselov und A.K. Geim, *Science (New York, N.Y.)* **320** (2008), 356.
- [234] T. Prosen und M. Žnidarič, *Journal of Statistical Mechanics: Theory and Experiment* **2009** (2009), P02035.
- [235] C.H.L. Quay, J. Cumings, S.J. Gamble, A. Yazdani, H. Kataura und D. Goldhaber-Gordon, *Physical Review B (Condensed Matter and Materials Physics)* **76** (2007), 73404.
- [236] C. Raas und G. Uhrig, *Physical Review B* **79** (2009), 115136.
- [237] C. Raas, G. Uhrig und F. Anders, *Physical Review B* **69** (2004), 041102.
- [238] D.C. Ralph, C.T. Black und M. Tinkham, *Physical Review Letters* **74** (1995), 3241.
- [239] S. Ramasesha, S.K. Pati, H.R. Krishnamurthy, Z. Shuai und J.L. Bredas, *Synth. Met.* **85** (1997), 1019.

- [240] N. Read und D.M. Newns, *J. Phys. C* **16** (1983), 3273.
- [241] N. Read, D.M. Newns und S. Doniach, *Phys. Rev. B* **30** (1984), 3841.
- [242] S. Reich, J. Maultzsch, C. Thomsen und P. Ordejón, *Physical Review B* **66** (2002), 035412.
- [243] F. Reininghaus: *Decoherence Effects in Nonequilibrium Transport Through Mesoscopic Systems*. RWTH Aachen, Dissertation, 2009.
- [244] F. Reininghaus, T. Korb und H. Schoeller, *Phys. Rev. Lett.* **97** (2006), 26803.
- [245] T.M. Rice und K. Ueda, *Phys. Rev. Lett.* **55** (1985), 995.
- [246] T.M. Rice und K. Ueda, *Phys. Rev. B* **34** (1986), 6420.
- [247] P. Richmond, *Journal of Physics C: Solid State Physics* **3** (1970), 2402.
- [248] V. Rodrigues, J. Bettini, P. Silva und D. Ugarte, *Physical Review Letters* **91** (2003), 096801.
- [249] C. Romeike, M. Wegewijs und H. Schoeller, *Physical Review Letters* **96** (2006), 196805.
- [250] S. Rommer und S. Östlund, *Physical Review B* **55** (1997), 2164.
- [251] G. Roux, T. Barthel, I. McCulloch, C. Kollath, U. Schollwöck und T. Giamarchi, *Physical Review A* **78** (2008), 023628.
- [252] M.A. Ruderman und C. Kittel, *Phys. Rev.* **96** (1954), 99.
- [253] Y. Saad: *Iterative Methods for Sparse Linear Systems (The Pws Series in Computer Science)*. Pws Pub Co, 1996.
- [254] Y. Saad und M.H. Schultz, *SIAM Journal on Scientific and Statistical Computing* **7** (1986), 856.
- [255] S. Sahoo, T. Kontos, J. Furer, C. Hoffmann, M. Gräber, A. Cottet und C. Schönenberger, *Nature Physics* **1** (2005), 99.
- [256] R. Saito: *Physical Properties of Carbon Nanotubes*. World Scientific Publishing Company, 1998.
- [257] S. Sapmaz, P. Jarillo-Herrero, J. Kong, C. Dekker, L.P. Kouwenhoven und H.S.J. van der Zant, *Phys. Rev. B* **71** (2005), 153402.
- [258] S. Sapmaz, C. Meyer, P. Beliczynski, P. Jarillo-Herrero und L.P. Kouwenhoven, *Nano letters* **6** (2006), 1350.
- [259] J. Schliemann, A. Khaetskii und D. Loss, *Journal of Physics: Condensed Matter* **15** (2003), R1809.

- [260] P. Schmitteckert, *Physical Review B* **70** (2004).
- [261] U. Schollwöck, *Rev. Mod. Phys.* **77** (2005), 259.
- [262] U. Schollwöck, *Annals of Physics* **In Press**, (2010), .
- [263] J.R. Schrieffer und P.A. Wolff, *Phys. Rev. B* **149** (1966), 491.
- [264] N. Schuch, M. Wolf, F. Verstraete und J. Cirac, *Physical Review Letters* **100** (2008), 030504.
- [265] Y.V. Sharvin, *Soviet Physics - JETP* **21** (1965), 655.
- [266] B.S. Shastry und D.C. Mattis, *Phys. Rev. B* **24** (1981), 5340.
- [267] S.Q. Shen, *Physical Review B* **53** (1996), 14252.
- [268] J.F. Sherson, C. Weitenberg, M. Endres, M. Cheneau, I. Bloch und S. Kuhr, *Nature* **467** (2010), 68.
- [269] N. Shibata, *Journal of the Physics Society Japan* **66** (1997), 2221.
- [270] N. Shibata und K. Ueda, *Journal of Physics: Condensed Matter* **11** (1999), R1.
- [271] N. Shibata, K. Ueda, T. Nishino und C. Ishii, *Phys. Rev. B* **54** (1996), 13495.
- [272] H. Shiozawa, H. Ishii, H. Kihara, N. Sasaki, S. Nakamura, T. Yoshida, Y. Takayama, T. Miyahara, S. Suzuki, Y. Achiba, T. Kodama, M. Higashiguchi, X.Y. Chi, M. Nakatake, K. Shimada, H. Namatame, M. Taniguchi und H. Kataura, *Physical Review B (Condensed Matter and Materials Physics)* **73** (2006), 75406.
- [273] M. Sigrist, H. Tsunetsugu und K. Ueda, *Phys. Rev. Lett.* **67** (1991), 2211.
- [274] M. Sigrist, H. Tsunetsugu, K. Ueda und T.M. Rice, *Phys. Rev. B* **46** (1992), 13838.
- [275] P. Silvestrov und K. Efetov, *Physical Review Letters* **98** (2007), 016802.
- [276] P. Simon, B. Braunecker und D. Loss, *Physical Review B (Condensed Matter and Materials Physics)* **77** (2008), 45108.
- [277] P. Simon und D. Loss, *Physical Review Letters* **98** (2007), 156401.
- [278] J. Sirker, *Physical Review B* **71** (2005).
- [279] S. Smerat, H. Schoeller, I.P. McCulloch und U. Schollwöck, *accepted for publication in Phys. Rev. B* (2011).
- [280] S. Smerat, U. Schollwöck, I. McCulloch und H. Schoeller, *Physical Review B* **79** (2009).
- [281] B. Smith, *Chemical Physics Letters* **321** (2000), 169.

- [282] B.W. Smith, M. Monthioux und D.E. Luzzi, *Nature* **396** (1998), 323.
- [283] L.L. Sohn, G. Schön und L.P. Kouwenhoven: *Mesoscopic Electron Transport (NATO Science Series E: (closed))*. Springer, 1997.
- [284] Z.G. Soos und S. Ramasesha, *The Journal of Chemical Physics* **90** (1989), 1067.
- [285] C. Spudat, C. Meyer, K. Goss und C.M. Schneider, *physica status solidi (b)* **246** (2009), 2498.
- [286] C. Stampfer, A. Jungen, R. Linderman, D. Obergfell, S. Roth und C. Hierold, *Nano letters* **6** (2006), 1449.
- [287] G.A. Steele, G. Gotz und L.P. Kouwenhoven, *Nature nanotechnology* **4** (2009), 363.
- [288] D. Stewart und T. Leyk, *Journal of Computational and Applied Mathematics* **72** (1996), 10.
- [289] L. Tagliacozzo, T. de Oliveira, S. Iblidir und J. Latorre, *Physical Review B* **78** (2008), 024410.
- [290] H. Takasaki, T. Hikihara und T. Nishino, *Journal of the Physical Society of Japan* **68** (1999), 1537.
- [291] S.J. Tans, M.H. Devoret, H. Dai, A. Thess, R.E. Smalley, L.J. Geerligs und C. Dekker, *Nature* **386** (1997), 474.
- [292] N. Tombros, S. van Der Molen und B. van Wees, *Physical Review B* **73** (2006), 233403.
- [293] S. Trebst, H. Monien, A. Grzesik und M. Sigrist, *Phys. Rev. B* **73** (2006), 165101.
- [294] S. Trebst, U. Schollwöck, M. Troyer und P. Zoller, *Physical Review Letters* **96** (2006), 250402.
- [295] M. Troyer und D. Würtz, *Phys. Rev. B* **47** (1993), 2886.
- [296] H. Tsunetsugu, Y. Hatsugai, K. Ueda und M. Sigrist, *Phys. Rev. B* **46** (1992), 3175.
- [297] H. Tsunetsugu, M. Sigrist und K. Ueda, *Phys. Rev. B* **47** (1993), 8345.
- [298] H. Tsunetsugu, M. Sigrist und K. Ueda, *Rev. Mod. Phys.* **69** (1997), 809.
- [299] A. Tsvetik, *Physical Review Letters* **72** (1994), 1048.
- [300] K. Ueda, T. Nishino und H. Tsunetsugu, *Phys. Rev. B* **50** (1994), 612.
- [301] T. Ulbricht und P. Schmitteckert, *Europhysics Letters (EPL)* **89** (2010), 47001.
- [302] P. Utke, J. Nygård, M. Monthioux und L. Noé, *Applied Physics Letters* **89** (2006), 233118.

- [303] F. Verstraete und J. Cirac, *Physical Review B* **73** (2006), 094423.
- [304] F. Verstraete, J. García-Ripoll und J. Cirac, *Physical Review Letters* **93** (2004), 207204.
- [305] F. Verstraete, D. Porras und J. Cirac, *Physical Review Letters* **93** (2004), 227205.
- [306] G. Vidal, *Physical Review Letters* **91** (2003), 147902.
- [307] G. Vidal, *Physical Review Letters* **93** (2004), 040502.
- [308] P. Wallace, *Physical Review* **71** (1947), 622.
- [309] X. Wang und T. Xiang, *Physical Review B* **56** (1997), 5061.
- [310] Z. Wang, X.P. Li und D.H. Lee, *Physical Review B* **47** (1993), 11935.
- [311] B. van Wees, H. van Houten, C. Beenakker, J. Williamson, L. Kouwenhoven, D. van der Marel und C. Foxon, *Physical Review Letters* **60** (1988), 848.
- [312] M.R. Wegewijs und K.C. Nowack, *New Journal of Physics* **7** (2005), 239.
- [313] D. Wharam, T. Thornton, R. Newbury, M. Pepper, H. Ahmed, J. Frost, D. Hasko, D. Peacock, D. Ritchie und G. Jones, *Journal of Physics C: Solid State Physics* **21** (1988), L209.
- [314] S. White, *Physical Review B* **72** (2005), 180403.
- [315] S. White und I. Affleck, *Physical Review B* **77** (2008), 134437.
- [316] S. White und A. Feiguin, *Physical Review Letters* **93** (2004), 076401.
- [317] S.R. White, *Phys. Rev. Lett.* **69** (1992), 2863.
- [318] S.R. White, *Phys. Rev. B* **48** (1993), 10345.
- [319] S.R. White und A.E. Feiguin, *Phys. Rev. Lett.* **93** (2004), 76401.
- [320] W. van der Wiel, S. De Franceschi, J. Elzerman, T. Fujisawa, S. Tarucha und L. Kouwenhoven, *Reviews of Modern Physics* **75** (2002), 1.
- [321] E. Wigner, *Zeitschrift für Physik* **43** (1927), 624.
- [322] E.P. Wigner: *Group Theory and its Application to the Quantum Mechanics of Atomic Spectra, Expanded Edition*. Academic Press, 1959.
- [323] K. Wilson, *Reviews of Modern Physics* **47** (1975), 773.
- [324] J. Xavier und E. Miranda, *Physical Review B* **78** (2008), 144406.
- [325] J.C. Xavier und E. Miranda, *Phys. Rev. B* **70** (2004), 75110.

- 
- [326] J.C. Xavier, E. Novais und E. Miranda, *Phys. Rev. B* **65** (2002), 214406.
- [327] J.C. Xavier, R.G. Pereira, E. Miranda und I. Affleck, *Phys. Rev. Lett.* **90** (2003), 247204.
- [328] T. Yanagisawa und K. Harigaya, *Physical Review B* **50** (1994), 9577.
- [329] Z. Yao, H.W.C. Postma, L. Balents und C. Dekker, *Nature* **402** (1999), 273.
- [330] Y.G. Yoon, M.S.C. Mazzoni und S.G. Louie, *Applied Physics Letters* **83** (2003), 5217.
- [331] K. Yosida, *Phys. Rev.* **106** (1957), 893.
- [332] C.C. Yu und S.R. White, *Phys. Rev. Lett.* **71** (1993), 3866.
- [333] H.Y. Yu, D.S. Lee, S.H. Lee, S.S. Kim, S.W. Lee, Y.W. Park, U. Dettlaff-Weglikowska und S. Roth, *Applied Physics Letters* **87** (2005), 163118.
- [334] W. Yu und S. Haas, *Physical Review B* **63** (2000), 024423.
- [335] G. Yule, *Philos. Trans. R. Soc. London, Ser. A* **226** (1927), 267.
- [336] O. Zachar, S. Kivelson und V. Emery, *Physical Review Letters* **77** (1996), 1342.
- [337] C. Zhang, E. Jeckelmann und S. White, *Physical Review B* **60** (1999), 14092.



# Acknowledgments

I am grateful to Prof. Ulrich Schollwöck for giving me the opportunity to work in his group during my diploma and phd thesis. I especially enjoyed his way of introducing me to the field of numerical physics and strongly correlated systems. Furthermore, he encouraged me to follow collaborations in (from his standpoint) off-topic fields. For this I am very grateful.

I owe many thanks to Prof. Herbert Schoeller for co-refereeing my thesis and spending time with me discussing Kondo lattice physics, quantum dot physics and for giving me an insight into and a feeling for analytical methods, which helped me to understand my own results.

I appreciated to work together with Prof. Maarten Wegewijs, who explained me how Coulomb blockade works and convinced me that also this field of theoretical physics is really exciting. Martin Leijnse helped me out with any question I had concerning KinEq and I owe special thanks to him for the fruitful collaborations.

I examined about 1000 conduction lines together with Karin Goss and learned a lot about experimental physics from her. I enjoyed her motivating spirit and thank her for our fruitful collaboration.

For our work together on Econophysics I owe many thanks to Ludwig Ohl. During his diploma work at the LMU Munich we wondered several times why economics, especially stock markets, work at all and do not crash every few seconds.

For all the coffee breaks, discussions and fun we had together in Aachen I thank all the people from the third and fourth floor: Georg Bannasch (also for his nice saxophone play), Thomas Barthel, Stefan Depenbrock, Andreas Friedrich, Georg Harder, Martin Holtschneider, Severin Jakobs, Boris Kastening, Adrian Kleine, Alexei Kolezhuk, Thomas Korb, Andre Kriner, Stephan Langer, Kerstin Lorenz, Hai-Bo Ma, Ian McCulloch, David Peters, Felix Reckermann, Frank Reininghaus and Guillaume Roux.

For reading parts of this thesis I thank Andreas Holzner, who helped me with valuable comments and corrections.

Special thanks I owe to Christian Kasztelan who has been a great office mate during the Munich time and unbelievably we also shared an apartment, which lead to discussion about everything at nearly any time - 24/7. Maybe it can be summarized best as: "Da trittst Du nur gaaanz vorsichtisch aufs Gas und BÄNG haste die Schallmauer gebrochen... ", oder "Tankfüllung ist inkl!"

I thank also the wonderful secretaries Gaby Kramp-Salecker (Aachen) and Cordula Weber (Munich), who patiently helped me with every question concerning administrative stuff.

I would also like to thank the Munich group for the nice atmosphere all the time: Robert

Bamler, Fabian Heidrich-Meissner, Tassilo Keilmann and Giuliano Orso.

I thank the German Research Foundation (Deutsche Forschungsgemeinschaft) supporting me during my phd thesis financially.

I am especially grateful to my family for the support in all the little and big things concerning life and all the love they gave to me. Without them I would never have come so far.

Finally, I would like to thank Anne for all her love and just being the way she is.

# Curriculum vitae

*Name* Sebastian Smerat  
*Date of birth* 01/01/1982  
*Place of birth* Leverkusen, Germany  
*Nationality* German  
*Adress* Elsenheimerstr. 12a  
80687 München, Germany

## Education

10/2007 - 03/2011 Doktorarbeit (Ph.D. studies) with Prof. Dr. U. Schollwöck  
LMU München  
*“Ground state and dynamical properties of the finite Kondo lattice model  
and transport through carbon based nanodevices”*

09/2006 - 08/2007 Diploma thesis with Prof. Dr. U. Schollwöck  
Rheinisch-Westfälische technische Hochschule Aachen  
*“Das magnetische Polaron im Kondogittermodell”*

04/2002 - 08/2007 Studies of physics  
Rheinisch-Westfälische technische Hochschule Aachen

07/2001 - 04/2002 Civil service

06/2001 Abitur (high school diploma)  
Nicolaus-Cusanus Gymnasium, Bergisch Gladbach

Munich, 08. February 2011



# Erklärung

Hiermit versichere ich, die hier vorliegende Dissertation selbstständig und nur unter Verwendung der im Literaturverzeichnis angegebenen Quellen und Hilfsmittel angefertigt zu haben. Die den benutzten Werken wörtlich oder inhaltlich entnommenen Stellen sind als solche kenntlich gemacht.

München, den 08.02.2011

Sebastian Smerat